Università degli Studi di Ferrara

UCA Universidad de Cádiz

INTERNATIONAL DOCTORAL COURSE IN
"EARTH AND MARINE SCIENCES (EMAS)"

CYCLE 35

COORDINATOR Prof. PAOLO CIAVOLA

Paleoclimate reconstructions of Upper Cretaceous shallow-water carbonates of the Adriatic carbonate platform based on rudist bivalves: a combined approach using $\delta^{18}O$ and clumped isotope paleothermometers

Scientific/Disciplinary Sector (SDS) GEO-02

Candidate
Barbora Křížová

Supervisor
Prof. Gianluca Frijia

Years 2019-2023

Acknowledgments

I am deeply indebted to my supervisor, Gianluca Frijia, for all that he taught me, for all the awesome field trips, and last but not least, for opening the door to the world of stratigraphy and geochemistry to me. I would also like to express my deepest gratitude to Niels de Winter for mentoring me, and for the great deal of work he has done reviewing and commenting on my thesis. I would like to express my appreciation to Martin Ziegler and the Clumped isotope lab working group at Utrecht University for welcoming me to their inspirational and caring working environment.

This endeavor would not have been possible without Katharina Schmitt, who taught me how to act in the lab and led me through my first stable isotope measurements. I am also very grateful to my colleague, Sahara Cardelli, who helped me to navigate through the often-confusing life of an Italian Ph.D. student. Many thanks to Lorenzo Consorti for his great help with the biostratigraphy and manuscript preparation, and for all the great time we spent together in the field. I would like to extend my sincere thanks to Giorgio Tunis, who shared his enormous knowledge about the geology and localities of the Friuli karst and Istria and always took kind care of me during the fieldwork.

Special thanks are owed to Valentina Brombin for performing the stable isotope analysis, Deborah Arbulla and Alceo Tarlao for providing the rudist specimens, to Sandro Venturini for a kind consultation and sharing his data on the thermal history of the Istria region, and to Philippe Claeys and Steven Goderis for performing the μXRF measurements. Thanks should also go to Sara Tomás Lafaja for taking the time and effort when reviewing my thesis. I am also thankful to Marco Franceschi and Lorenzo Bonini from the University of Trieste for their help with fieldwork and manuscript preparation. Furthermore, I would like to acknowledge the financial aid from the SEPM Foundation.

I am extremely grateful to my partner Šimon for reminding me that science is fun when I needed it the most, and for his enormous emotional support that kept me sane. I could not have undertaken this journey without the love from my family, especially Mom and Dad, who bravely supported my decisions, even though they often had other opinions.

Lastly, I would like to thank the Veronese family for their warm welcome to Ferrara and for being there for me.

Abstract

The Late Cretaceous was an interval characterized by abrupt climate perturbations, recording some of the warmest temperatures in Earth history. The greenhouse climate reached its 'hothouse' stage at the Cenomanian-Turonian Boundary interval when the sea surface temperatures (SSTs) attained over 35 °C in low and mid-latitudes, coinciding with the highest sea level stands of Phanerozoic. Under these conditions, an extinct order of bivalves, rudists, thrived on tops and margins of carbonate platforms, significantly contributing to global carbonate production. Their low-Mg calcite outer shell layers provide valuable archives of the Cretaceous climatic conditions, allowing for paleoenvironmental interpretations, both at a short time scale (*e.g.*, years; by analyzing shell increments through their growth profile) and long time scale (by analyzing shell isotopic variations over sedimentary successions).

The most widely used method for 'measuring' past temperatures is the $\delta^{18}O$ paleothermometer. Nevertheless, this method suffers from several problems, the main being the uncertainty of the original isotopic composition of the seawater from which the studied shells precipitated. The clumped isotope thermometer is a promising tool for overcoming this issue since it gives paleotemperature estimates independently of the original $\delta^{18}O_{seawater}$.

The presented thesis focuses on paleotemperature and paleoenvironmental reconstructions in shallow-water carbonates of the Adriatic Carbonate Platform using rudist shells, applying two different thermometers (oxygen and clumped isotope analyses). Sampled section and rudist specimens come from two regions: 1) Friuli karst area (NE Italy) and 2) southern Istria (Croatia). A reference section of upper Cenomanian-middle Turonian carbonates was sampled in the Friuli region, and a precise stratigraphic framework was developed using biostratigraphy, combined with carbon and Sr-isotope chemostratigraphy. A high-resolution paleotemperature profile was constructed based on the $\delta^{18}O$ analysis of rudist shells and bulk rock material. The Late Cretaceous thermal maximum has been identified in the Lower Turonian strata, with calculated temperatures reaching as much as 41-45 °C. Subsequently, clumped isotope analysis was applied to selected rudists from the Friuli and Istria regions, investigating the diagenetic processes influencing the clumped isotope thermometer, such as the solid-state reordering. Finally, clumped isotope and $\delta^{18}O$ analyses of two well-preserved rudist specimens from the Istria region were used for paleotemperature calculations, estimates of seasonal temperature variations, and, for the first time, for $\delta^{18}O_{seawater}$ calculations of Turonian and middle Coniacian seas covering the Adriatic Carbonate Platform.

Riassunto

Il Cretaceo Superiore è stato un intervallo stratigrafico caratterizzato da significative perturbazioni climatiche, registrando alcune delle temperature più calde della storia della Terra. Un clima di tipo “greenhouse” raggiunse il suo stadio di "hothouse" nell'intervallo al limite Cenomaniano-Turoniano, quando le temperature della superficie degli oceani (SST) raggiunsero oltre 35 °C alle basse e medie latitudini, in coincidenza con i massimi livelli marini del Fanerozoico. In queste condizioni, un ordine estinto di bivalvi, le rudiste, prosperava negli ambienti di piattaforma interna e sui margini delle piattaforme carbonatiche, contribuendo in modo significativo alla produzione globale di carbonato di calcio. Gli strati esterni delle loro conchiglie composti da calcite basso magnesiasca (low-Mg) si sono rivelati preziosi archivi delle condizioni climatiche del Cretaceo, consentendo interpretazioni paleoambientali, sia a breve scala temporale (ad esempio anni; analizzando gli incrementi di crescita attraverso il profilo della conchiglia) che a lunga scala (analizzando le variazioni isotopiche della conchiglia nelle successioni sedimentarie).

Il metodo più utilizzato per "misurare" le temperature del passato è basato sulle analisi del $\delta^{18}O$ nella calcite. Tuttavia, questo metodo soffre di diversi problemi, il principale dei quali è l'incertezza della composizione isotopica originale dell'acqua marina da cui sono precipitate le conchiglie studiate. Un secondo nuovo metodo chiamato “clumped-isotopes” è uno strumento promettente per superare questo problema, poiché fornisce stime della paleotemperatura indipendentemente dal valore originale del $\delta^{18}O$ dell'acqua marina.

La tesi qui presentata si concentra sulle ricostruzioni delle paleotemperature e paleoambientali nei carbonati mare basso della Piattaforma Carbonatica Adriatica utilizzando conchiglie di rudiste, applicando due diversi termometri (analisi dell'ossigeno e “clumped-isotopes”). I campioni di rudiste analizzati provengono da due regioni: 1) Carso Goriziano del Friuli (NE Italia) e 2) Istria meridionale (Croazia). Una sezione di riferimento del Cenomaniano superiore- Turoniano medio è stata campionata nella regione friulana, e uno schema stratigrafico preciso è stato sviluppato utilizzando la biostratigrafia in combinazione con la chemostratigrafia del carbonio e degli isotopi dello Sr (SIS). È stato, poi, costruito un profilo di paleotemperatura ad alta risoluzione basato sull'analisi del $\delta^{18}O$ nelle conchiglie di rudiste e nella roccia totale (“bulk”). Il massimo termico del Cretaceo superiore è stato identificato negli strati del Turoniano inferiore, con temperature calcolate che raggiungono i 41-45 °C. Successivamente, le analisi dei “clumped-isotopes” sono state applicate a rudiste

selezionate provenienti dalle regioni del Friuli e dell'Istria, con lo scopo di studiare i processi che influenzano questo metodo di paleotermometria isotopica (es. diagenesi e "solid-state reordering"). Infine, l'analisi degli dei "cluped isotopes" e del δ18O di due esemplari di rudiste ben preservate provenienti dalla regione istriana è stata utilizzata per il calcolo della paleotemperatura, per la stima delle variazioni stagionali di temperatura e, per la prima volta, per il calcolo del $\delta^{18}O$ dell'acqua marina del Turoniano e del Coniaciano medio che ricopriva la Piattaforma Carbonatica Adriatica.

Table of Contents

1 Introduction

1.1 Late Cretaceous paleotemperatures

The Cretaceous system (143.1 to 66.1 Ma according to GTS 2020) was characterized by abrupt climate perturbations and significant global warming, making it one of the warmest periods in the Earth history (Fig.1.1). Data compilation by O'Brien et al. (2017) indicates maximum surface ocean water temperatures (SSTs) of over 35 °C during the thermal maximum, and SSTs above 30 °C for the mid-Cretaceous; values significantly higher than those of the modern oceans. Global cooling that started in the Coniacian caused the SSTs to drop below 30 °C in the late Santonian or early Campanian (O'Brien et al., 2017) and was punctuated by short-term hot snaps (Wiese and Voigt, 2002).

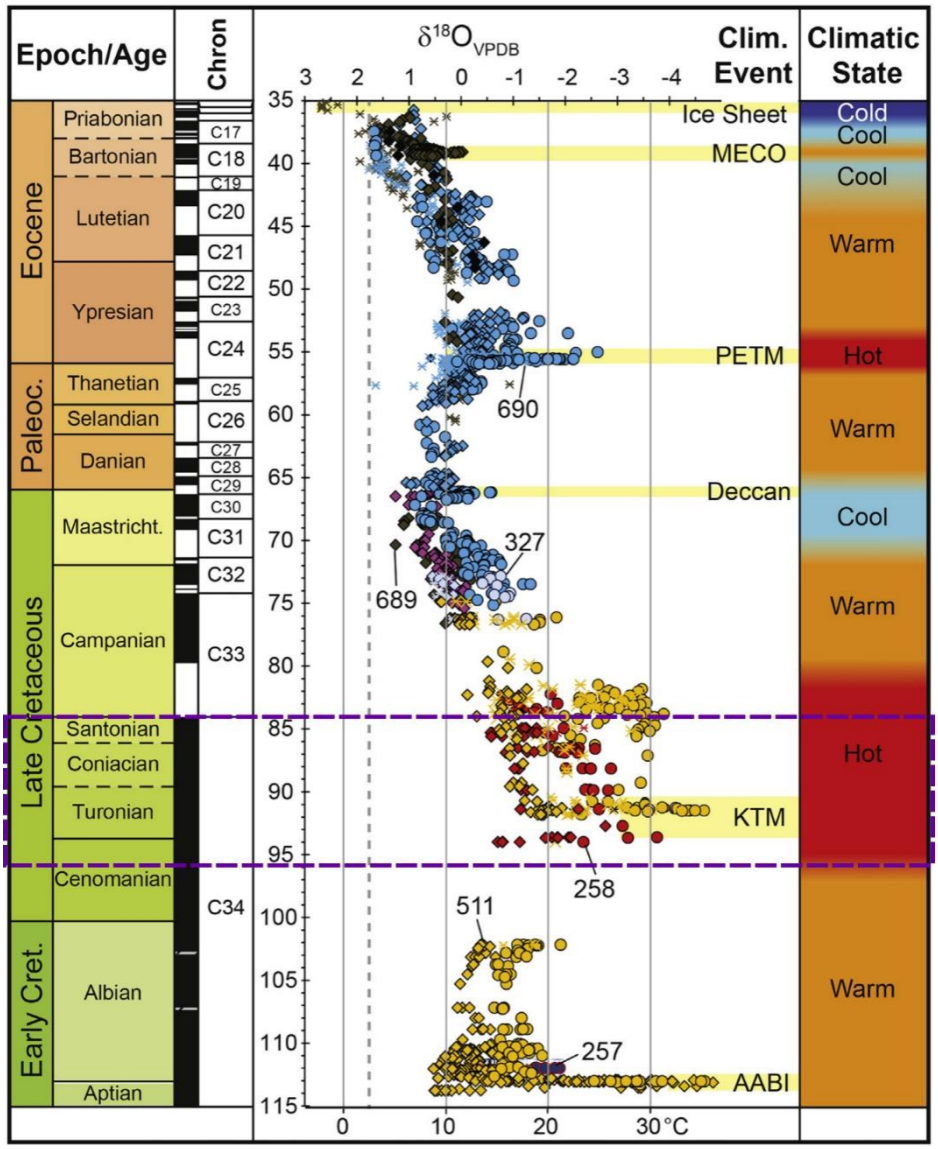

Fig.1.1. Paleotemperature evolution from the Early Cretaceous to Eocene with Climatic stages interpreted. The Paleotemperatures are based on $\delta^{18}O$ analyses of planktic foraminifera. Note the KTM (Cretaceous Thermal Maximum) in Early Turonian. From Huber et al. (2018). The dashed rectangle marks the interval that is subject to the presented thesis.

The timing of the culmination of the Late Cretaceous climatic warming is debated. The Cenomanian-Turonian boundary is reported to be the warmest time of the Cretaceous by some authors (Friedrich et al., 2012; Grossman and Joachimski, 2022; Huck and Heimhofer, 2021) whereas other authors report the early–mid-Turonian interval to be the warmest stage of Cretaceous (Huber et al., 2018; Stoll and Schrag, 2000). Recent paleoclimatic studies report the warmest Cretaceous SSTs of over 35 °C occurring from the late Cenomanian to Turonian (O'Brien et al., 2017). Regardless of the timing, there is a consensus indicating the Turonian was the warmest stage of the Cretaceous (MacLeod et al., 2013).

Long-lasting warm temperatures along with paleogeographic and geodynamic changes resulted in an increase in global sea levels (Haq, 2014; Fig. 1.2). The latest Phanerozoic sea level compilations show a sea level maximum in the early Turonian (Haq, 2014), although the estimates of the magnitude of this peak vary when based on different approaches, and from author to author. Compilations of previously published data estimate the earliest Turonian sea level maximum of ~50-70 meters (Miller et al., 2004) and ~240-250m above the present day (Haq, 2014). $^{87}Sr/^{86}Sr$-derived sea-level curve of (van der Meer et al., 2017), resulted in an estimated maximum of ~150m before mid-Turonian. Marcilly et al. (2022) used paleogeographic flooding maps, showing an increase from about 28 m to ~280 at 80 Ma (end of early Turonian).

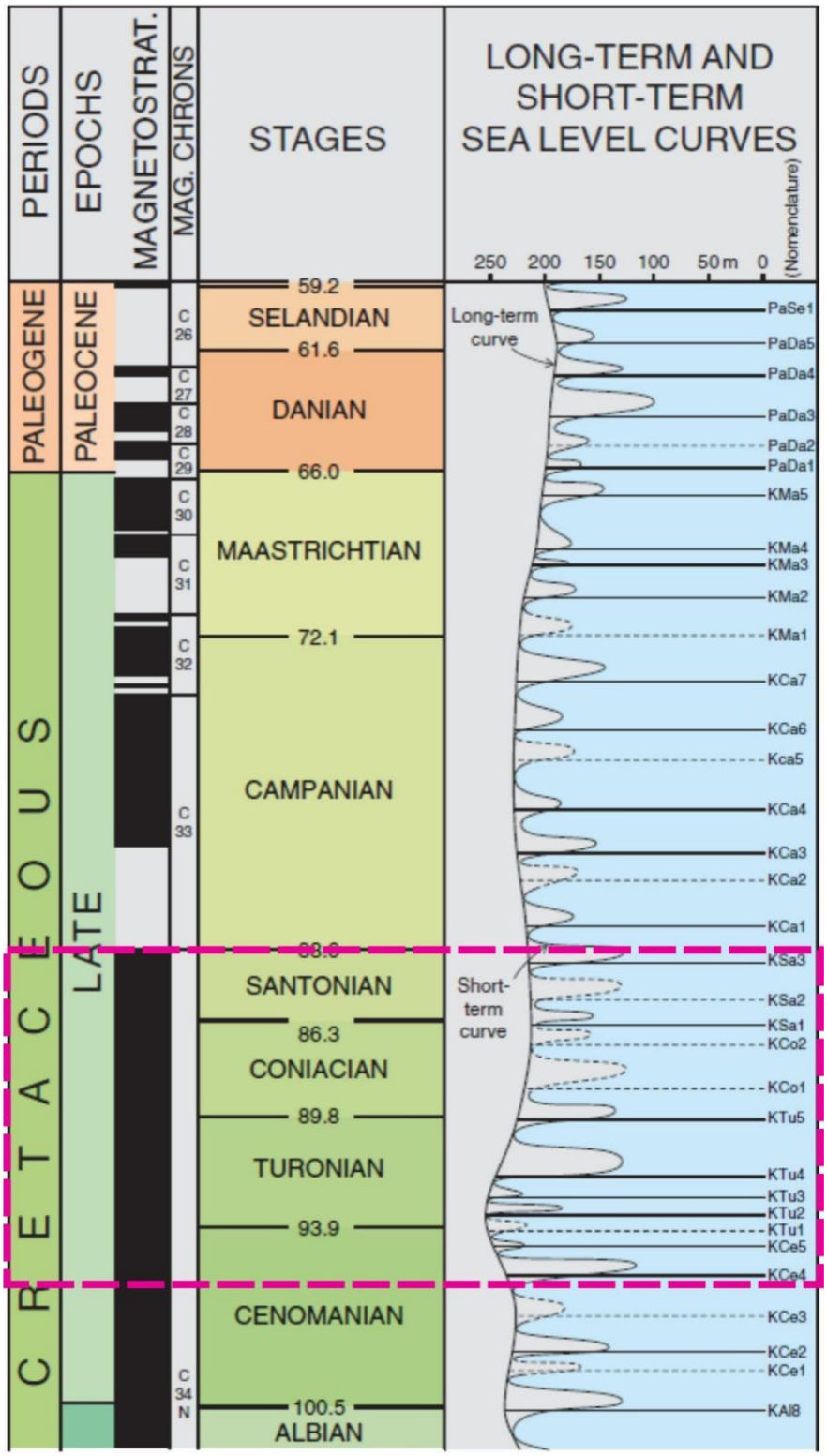

Fig.1.2. Sea level fluctuations during the Late Cretaceous. After Haq, 2014. The dashed rectangle marks the interval that is subject to the presented thesis.

The highstand of sea levels resulted in widespread epicontinental seas and large shelf areas covered with seawater which become areas of active carbonate factories (Fig.1.3).

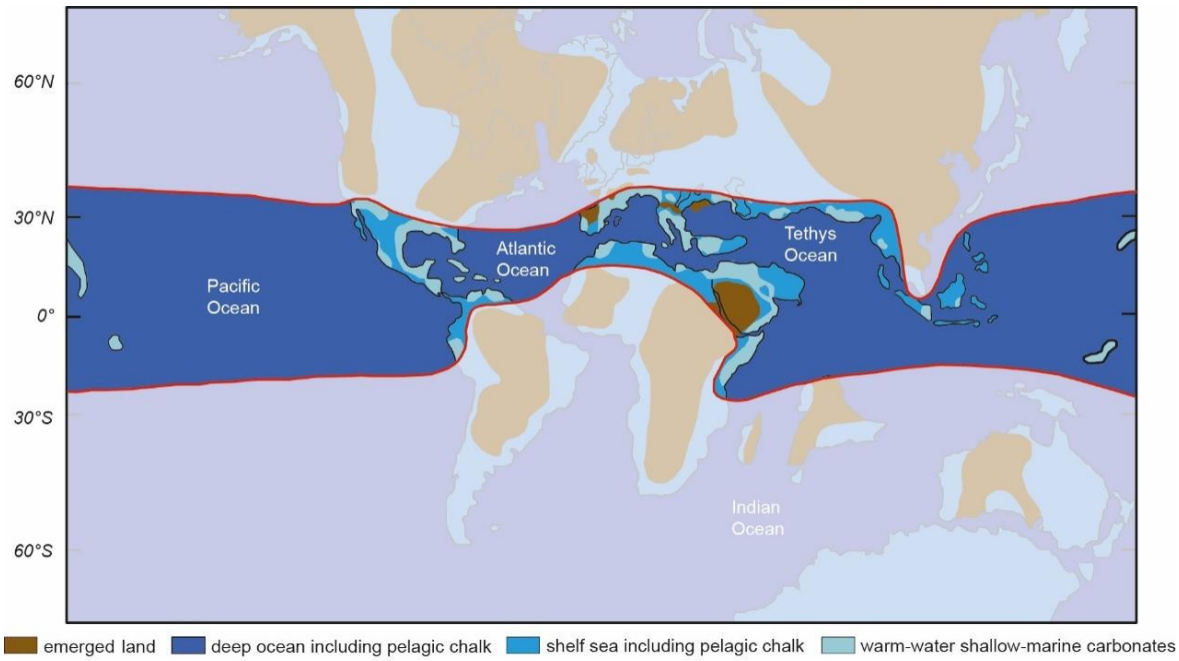

Fig.1.3. Shallow marine carbonate platforms (light blue) during the Late Cretaceous (98 Ma). From Schmitt (2019).

1.2 Paleothermometers in carbonate rocks

1.2.1 $\delta^{18}O$ paleothermometry

Since the discoveries of Urey (1947), expanded by Urey et al. (1951) and Lowenstam and Epstein (1954), which suggested the potential use of stable oxygen isotope ratios in carbonates to reconstruct paleotemperatures, oxygen isotope analyses of biogenic carbonates are one of the most widely used methods of reconstructions of environmental conditions of past marine environments (see a review of Wierzbowski, 2021 and Grossman and Joachimski, 2022). This is possible due to the temperature dependence of the oxygen isotope ratio ($\delta^{18}O$) between calcium carbonate ($CaCO_3$) and the water from which it is precipitated (Pearson, 2012; Urey, 1947; Wierzbowski, 2021).

Oxygen naturally occurs in three stable isotopes: ^{16}O, ^{17}O, and ^{18}O, with relative abundances of 99.757, 0.038, and 0.205 % respectively (Pearson, 2012; Rohling, 2013). Oxygen isotope geochemistry represented by the $^{18}O/^{16}O$ ratio relies on the higher abundance and greater mass difference between the two species (Rohling, 2013). Therefore, the isotopic ratio, R, is defined as the abundance of the heavier over the lighter isotope. The global average proportion is expressed as follows (Pearson, 2012; equation 1):

$R = {}^{18}O/{}^{16}O = 0.205/99.757 = 0.002055$ (1)

Oxygen isotope ratios (like for other isotope measurements) are quoted in δ notation, which expresses the deviation of the measured ratio of ^{18}O to ^{16}O from a standard substance (for carbonates the international VPDB standard; Grossman, 2012). The results are reported in parts per thousand (per mille; ‰; Pearson, 2012; Grossman, 2012; equation 2).

$$\delta^{18}O = [(R_{sample} - R_{standard})/R_{standard}] \times 1000 \quad (2)$$

Thus, if a sample has a positive $\delta^{18}O$, it is enriched in the heavy isotope relative to the standard and, if negative, it is depleted relative to the standard. Two different standard values are used: Vienna Standard Mean Ocean Water (VSMOW) and Vienna Pee Dee Belemnite (VPDB), which is used in studies of carbonates (for oxygen, as well as for stable carbon isotope analyses; Pearson, 2012; Grossman, 2012; Rohling, 2013).

Oxygen isotope fractionation processes that affect oxygen isotopes in water are evaporation, atmospheric vapor transport, precipitation, and subsequent return of freshwater to the ocean (through precipitation and runoff or ice melting; Rohling, 2013). Because molecules containing heavy isotopes have slightly greater bond strengths and lower vibrational frequencies than lighter isotopes, they are slightly less reactive. Therefore, the light isotope ^{16}O is slightly preferred in water vapor, whereas, during condensation, the heavy ^{18}O is preferred. In the case of mixing two water masses with different $\delta^{18}O$ (e.g., in delta environments), the produced water will have an intermediate oxygen ratio (Pearson, 2012). Additionally, the difference in reactivity between the heavier and lighter oxygen isotopes is influenced by the ambient temperature. An increase in temperature lowers the difference in reaction rates (Pearson, 2012).

Therefore, the oxygen isotope paleothermometry is based on glacial-interglacial cyclicity in the $\delta^{18}O$ in carbonates. The growth of ice sheets leaves the ocean isotopically enriched and consequently the marine carbonates ($\delta^{18}O$ depleted water is stored in the glacial ice), and conversely, higher temperatures leading to deglaciation, recirculate the isotopically depleted fresh water (which lowers the seawater $\delta^{18}O$ and produces lower marine carbonate $\delta^{18}O$ values during ice-free intervals; Grossman, 2012; Pearson, 2012; Fig.1.4).

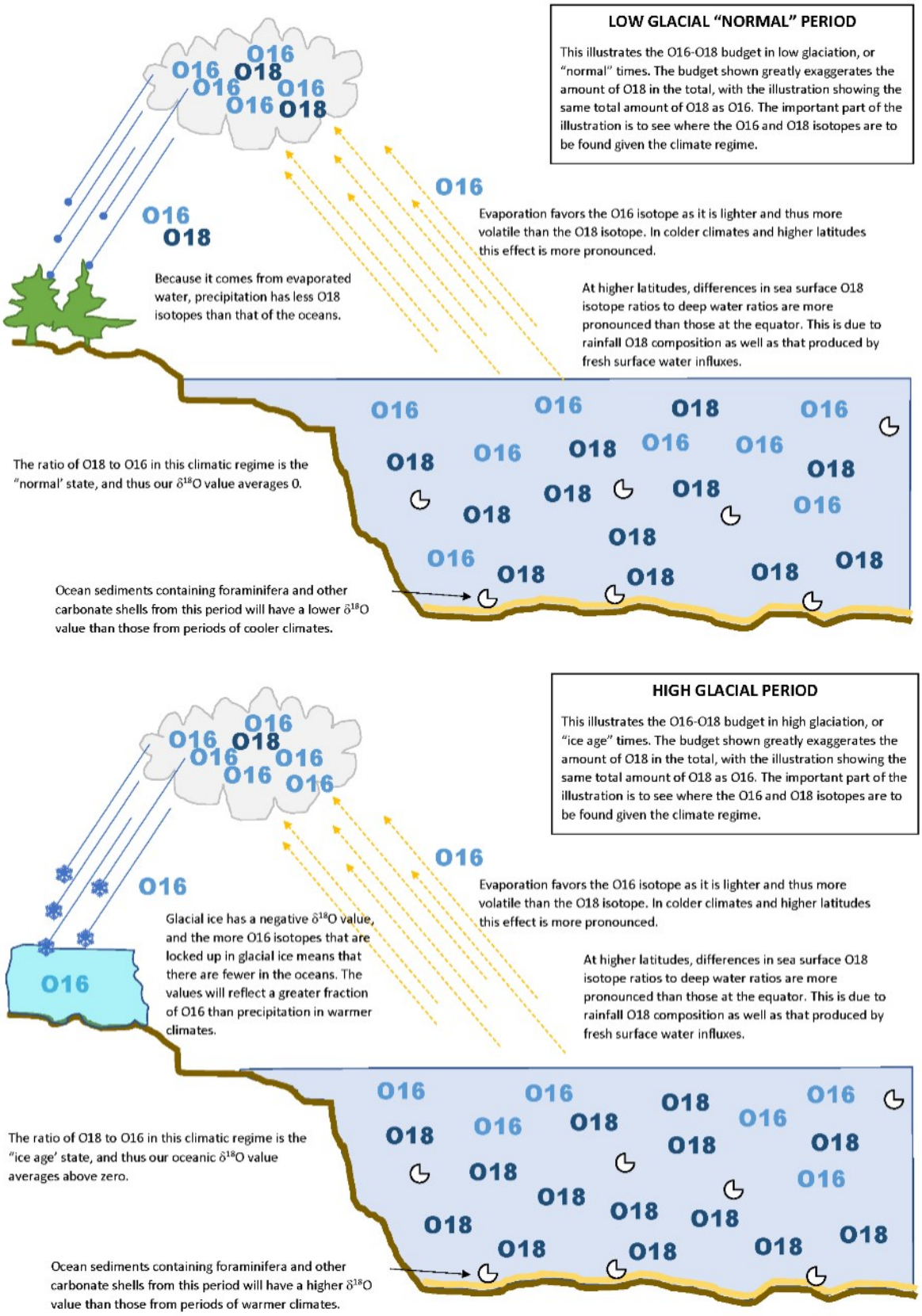

Fig.1.4. Oxygen isotope thermometer principles based on glacial-interglacial periods. From Hasenberg (2018).

To derive temperatures from Oxygen isotope data several equations have been generated which are related to different carbonate components. The equation for paleotemperature calculations based on $\delta^{18}O$ has undergone some changes since its first use (Epstein et al., 1953; Urey et al., 1951), resulting in the following form used for biogenic aragonite and calcite (Anderson and Arthur, 1983; Grossman, 2012; Wierzbowski, 2021; equation 2):

$$T(°C) = 16.0 - 4.14 \times (\delta^{18}O_{calcite} - \delta^{18}O_{water}) + 0.13 \times (\delta^{18}O_{calcite} - \delta^{18}O_{water})^2 \quad (3)$$

Where $\delta^{18}O_{calcite}$ [VPDB] is the oxygen isotope composition of the analyzed carbonate and $\delta^{18}O_{water}$ [VSMOW] is the oxygen isotope composition of water which the carbonates precipitated from.

However, as already highlighted in the pioneering studies of Urey (1947) and Urey et al. (1951), in order to derive paleotemperatures from biogenic carbonates, three main factors must be evaluated/assumed: the value of past-seawater $\delta^{18}O$, vital-effect fractionations vs. precipitation in equilibrium with sea-water, and the preservation of the biogenic material through geologic time (possible diagenetic alterations of the carbonates).

As clearly shown in the paleotemperature equations presented above, the major complicating factor of using $\delta^{18}O$ as a paleotemperature indicator is that it relies on the $\delta^{18}O$ of the seawater from which the carbonate precipitated (Urey et al., 1951; Grossman, 2012, Pearson, 2012). Temperature is only constrained if the $\delta^{18}O$ of both phases (mineral-seawater) are known. However, for much of the sedimentary record, the $\delta^{18}O$ of the ancient seawater is unknown (Eiler, 2007; Watkins et al., 2014).

The principal controlling factor of the regional $\delta^{18}O$ of modem surface seawater is the local evaporation-precipitation (E-P) balance. The salinity of seawater depends on the same E-P balance, therefore, the two are often correlated. Variability in E-P is sometimes referred to as a salinity effect on $\delta^{18}O$ (Pearson, 2012). This is not very accurate because $\delta^{18}O$ of seawater varies according to other factors as well. The oxygen isotope ratio is influenced by precipitation, which changes systematically with latitude, river freshwaters flowing into the ocean, iceberg melting, the local climate, and advection (Pearson, 2012; Rohling, 2013; Fig.1.5).

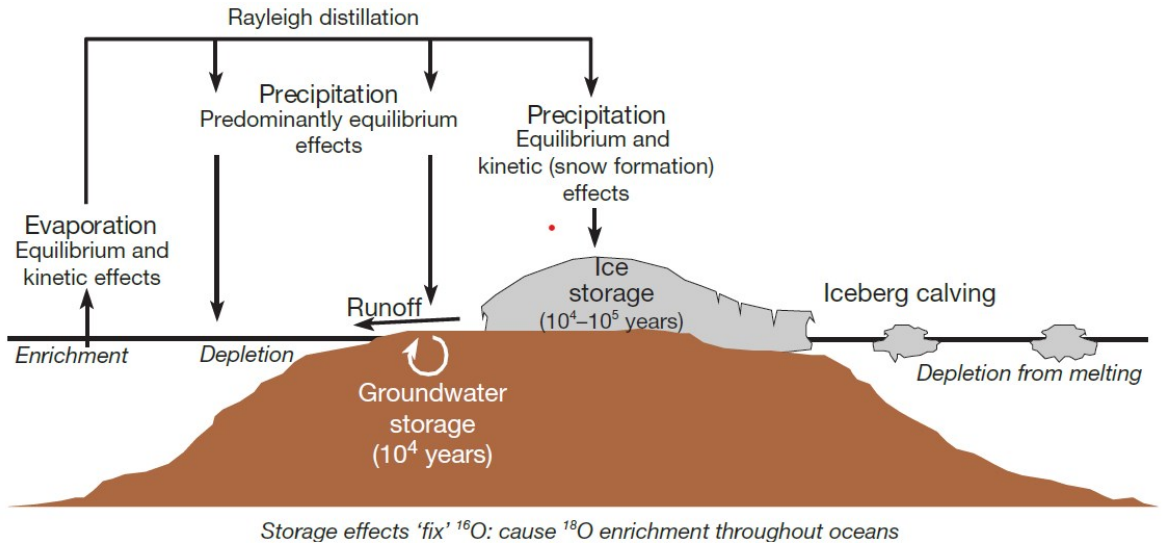

Fig.1.5. Schematic presentation of factors influencing oxygen isotope ratios. Effects on seawater are described in italics. Comment below this figure refers to the storage of preferentially ^{16}O-enriched precipitations in ice sheets and groundwater, which causes a relative $\delta^{18}O$-enrichment of the oceans. From Rohling (2013).

The modern variability of surface ocean $\delta^{18}O$ ranges from about -1.5 to +1.5 ‰ VSMOW in open ocean waters (Pearson, 2012; Fig.1.6). In restricted marine environments, such as the Arctic Ocean, Mediterranean Sea, and the Red Sea, the oxygen isotope composition varies from roughly -2 to +2 ‰ (Pearson, 2012 and references therein, Fig.1.6). Differences of $\delta^{18}O$ of 3 ‰ correspond to a temperature of over 12 °C. This is an important issue in using $\delta^{18}O$ to establish patterns of sea-surface temperatures in the geologic past (Pearson, 2012).

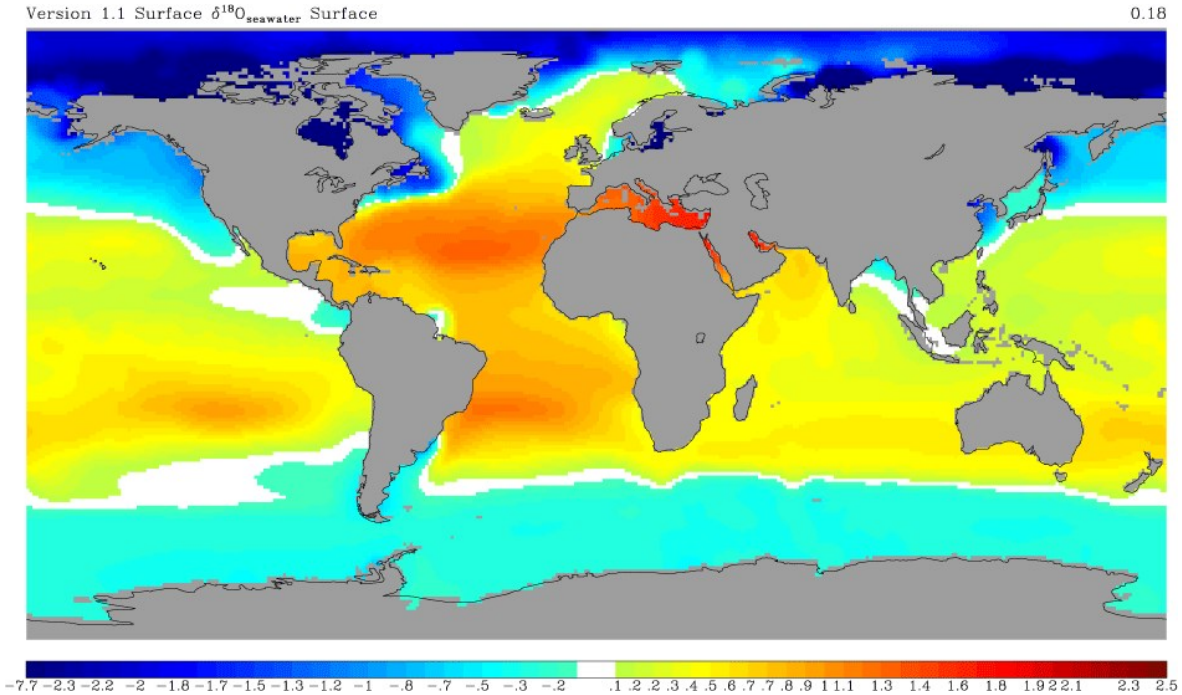

Fig.1.6. Global compilation of $\delta^{18}O$ measurements [‰, VSMOW]. From LeGrande and Schmidt (2006).

To correct for the effects of latitudinal variation in P-E, Zachos et al. (1994) developed an empirical relationship for Southern Hemisphere surface seawaters (0-70°), which describes the present-day distribution of $\delta^{18}O_{seawater}$ as a function of latitude (equation 4):

$$\delta^{18}O_{seawater}\ (‰VSMOW) = 0.576 + 0.041x - 0.0017x^2 + 1.35*10^{-5}x^3 \qquad (4)$$

Where x is the latitude in degrees.

In the studies of greenhouse climate periods (such as the Late Cretaceous), the lack of permanent ice cover needs to be considered when estimating the $\delta^{18}O_{seawater}$. The difference in global $\delta^{18}O_{seawater}$ between the modern world and the ice-free world is estimated using mass-balance calculations based on $\delta^{18}O$ of the ocean and continental glaciers (Grossman, 2012). These estimates are almost exactly -1 ‰ VSMOW (Grossman, 2012; Pearson, 2012).

Many calcifying species produce their shells in oxygen-isotopic equilibrium with seawater. However, the kinetic effects, grouped under the term 'vital effects,' cause disequilibrium in some taxa (Ravelo and Hillaire-Marcel, 2007; Rohling, 2013; Watkins et al., 2014), which can, ultimately, bias the calculations of the paleotemperatures (Walliser and Schöne, 2020). These vital effects were largely observed in some foraminifera taxa, where they seem to be related to the photosynthetic activity of symbiotic algae (Ravelo and Hillaire-Marcel, 2007). In general, mollusks, brachiopods, sclerosponges, and many smaller foraminifera typically secret their calcitic skeletons at or near the oxygen isotopic equilibrium, whereas corals, echinoderms, and larger benthic foraminifera skeletons can differ as much as -3 ‰ from the equilibrium values (Grossman, 2012 and references therein).

Finally, sample preservation is a very important issue to consider for any temperature reconstructions in the fossil record. The $\delta^{18}O$ compositions in fossil skeletons can be altered through oxygen exchange with diagenetic waters. Alteration is enhanced by higher temperatures and pressures of burial (Grossman, 2012) as well as by a high ratio of fluid/rock interaction.

Low-magnesium calcite is a carbonate mineral phase that is more resistant to diagenesis than high-Mg calcite or aragonite and thus can better preserve its original chemical/structural composition in the sedimentary record (Grossman, 2012; Veizer and Prokoph, 2015). As a result, only a few groups of organisms are available for Phanerozoic reconstructions of temperatures: brachiopods, foraminifera, belemnites, and bivalves (Veizer and Prokoph, 2015; Fig.1.7).

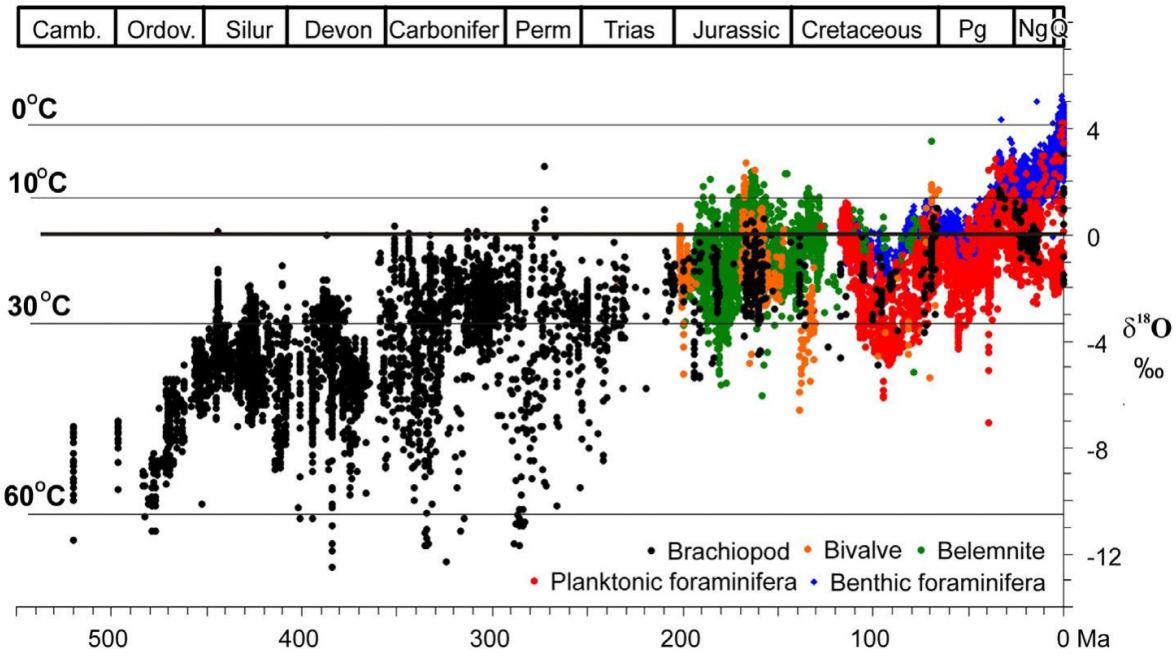

Fig.1.7. $\delta^{18}O$ of Phanerozoic low-Mg calcitic fossils. The temperature estimates are based on the Visser et al. (2003) transfer function, assuming the present-day $\delta^{18}O$ value of 0 ‰ SMOW for seawater. In the Paleozoic, $\delta^{18}O$ paleotemperatures are based on brachiopods, whereas since the Cretaceous, planktonic foraminifera is the major source of $\delta^{18}O$ thermometry. From Veizer and Prokoph (2015).

1.2.2 Clumped isotope paleothermometry

Clumped isotope thermometry in carbonates has developed into an important tool for paleoenvironmental studies since its first application. Ghosh et al. (2006) and Schauble et al. (2006) introduced a new paleothermometer based on the 'clumping' of ^{13}C and ^{18}O in the carbonate mineral lattice into bonds with each other.

Carbonate minerals are molecular crystals, consisting of separate CO_3^{2-}carbonate groups with strong internal C-O bonds, which are bound to the crystal lattice by weaker cation-oxygen (Ca^{2+}-O in calcite) bonds (Schauble et al., 2006; see Fig.1.8).

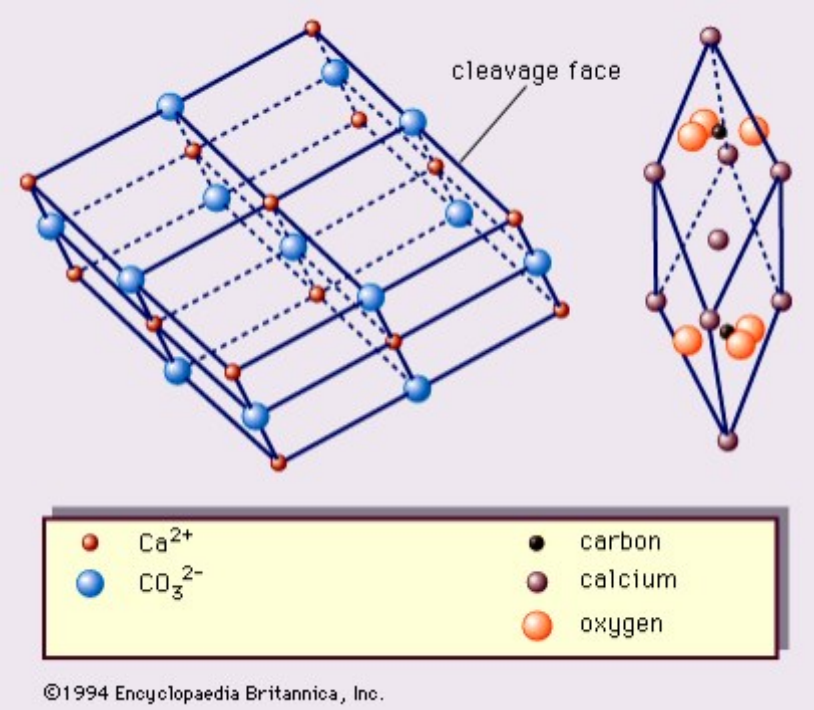

Fig.1.8. Calcite crystal structure.

Carbonate minerals contain 20 isotopic variations (isotopologues) of the carbonate ion group (Ghosh et al., 2006); see Table 1.1.

Tab.1.1. Abundances of isotopologues of CO_2, assuming bulk $^{13}C/^{12}C$ ratios equal to PDB, bulk $^{18}O/^{17}O/^{16}O$ ratios equal to SMOW, and a stochastic (random) distribution of isotopes. From Ghosh et al. (2006).

CO_2	Mass	Abundance
Isotopologue		
$^{16}O^{12}C^{16}O$	44	98 %
$^{16}O^{13}C^{16}O$	45	1.10 %
$^{17}O^{12}C^{16}O$	45	730 ppm
$^{18}O^{12}C^{16}O$	46	0.40 %
$^{17}O^{13}C^{16}O$	46	8.19 ppm
$^{17}O^{12}C^{17}O$	46	135 ppb
$^{18}O^{13}C^{16}O$	47	45 ppm
$^{17}O^{12}C^{18}O$	47	1.5 ppm
$^{17}O^{13}C^{17}O$	47	1.5 ppb
$^{18}O^{12}C^{18}O$	48	4.1 ppm
$^{17}O^{13}C^{18}O$	48	16.7 ppb
$^{18}O^{13}C^{18}O$	49	46 ppb

The most abundant isotopologue $^{12}C^{16}O_3^{2-}$ (~98.4 %) contains no rare isotopes. Following in abundance, three isotopologues: $^{13}C^{16}O_3^{2-}$ (~1.1 %), $^{12}C^{18}O^{16}O_2^{2-}$ (~0.6 %), and $^{12}C^{17}O^{16}O_2^{2-}$ (~0.11 %) contain one rare isotope (are singly substituted). These four isotopologues contribute together as much as ~99.99 % to the carbonate ion groups in natural carbonates. The remaining 100 ppm are doubly, triply, and quadruply substituted isotopologues; each of them having unique vibrational properties, and therefore differ in thermodynamic stability (Ghosh et al., 2006).

The clumped isotope studies are based on the exchange of ^{13}C, ^{18}O, and ^{17}O between carbonate molecules (Shauble et al., 2006):

$$^{12}C^{18}O^{16}O_2^{2-} + {}^{13}C^{16}O_3^{2-} \rightleftharpoons {}^{13}C^{18}O^{16}O_2^{2-} + {}^{12}C^{16}O_3^{2-} \quad (5)$$

and

$$^{12}C^{17}O^{16}O_2^{2-} + {}^{12}C^{18}O^{16}O_2^{2-} \rightleftharpoons {}^{12}C^{18}O^{17}O^{16}O^{2-} + {}^{12}C^{16}O_3^{2-} \quad (6)$$

The clumped isotope thermometry focuses on the former (5) because it involves the most abundant (~96 %) doubly substituted isotopologue: $^{13}C^{18}O^{16}O_2^{2-}$, of the mass-47 signal in CO_2 generated by phosphoric acid digestion (Schauble et al., 2006; Ghosh et al., 2006). In other words, this paleotemperature proxy is based on a homogenous isotope reaction (Eiler, 2011; Fig.1.9).

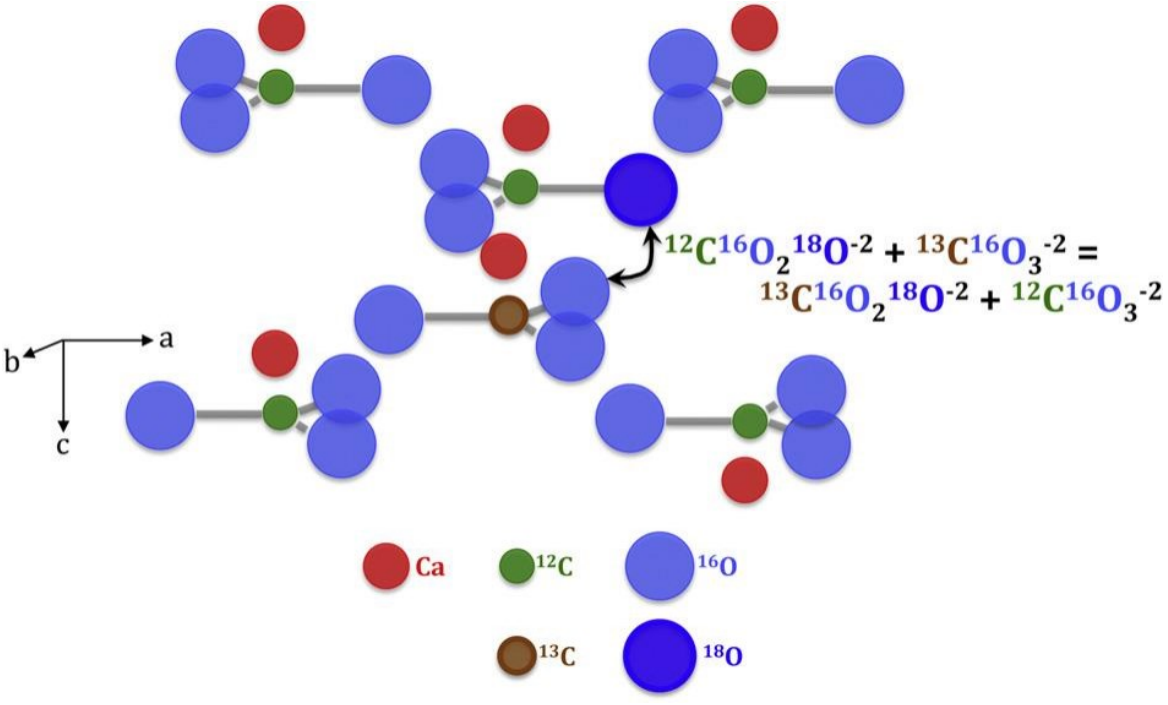

Fig.1.9. Atomic structure of the calcite lattice, illustrating the homogeneous isotope exchange reaction between carbonate ion groups on which carbonate clumped isotope thermometry is based. From Eiler (2011).

The clumped isotope analysis is based on the thermodynamic principle – molecules with heavy isotopologues have lower vibrational energies than molecules containing lighter isotopes (Urey, 1947). Therefore, the ordering of ^{13}C and ^{18}O into bonds (clumping) with each other in the carbonate minerals is temperature-dependent (Ghosh et al., 2006). When system entropy increases at higher temperatures, clumping decreases. Consequently, in the decreasing temperatures of carbonates growth, the heavy isotopologues (with an M/Z of 47) become more abundant (Eiler, 2007; 2011; Ghosh et al., 2006; Schauble et al., 2006). Temperature dependence corresponds to a balance between enhanced thermodynamic stability of ^{13}C and ^{18}O isotopologue of the carbonate vs the random isotopic distributions (Eiler 2007; 2011).

The abundances of the clumped isotopologues are measured as ratios of mass-47 to mass-44 (R^{47}). In reporting abundances of mass-47 in measured CO_2, Eiler and Schauble (2004) defined the variable Δ_{47} as the difference between the measured value of R^{47} and the value of R^{47} expected in that sample if its carbon and oxygen isotopes are randomly distributed (referred to as stochastic distribution; equation 7):

$$\Delta_{47} = (R^{47}_{measured} / R^{47}_{stochastic} - 1) \times 1000 \qquad (7)$$

Values of Δ_{47} are reported in units per mil and vary between 0 and 1 ‰. Principally, they reflect the 'super-abundance of $^{13}C^{18}O^{16}O$ (Eiler, 2011).

Most paleoclimatological studies deal with temperatures of ~0-40 °C. The published calibrations in calcite, aragonite, carbonate-apatite, and a wide range of phyla from various environments show remarkable coherence (Eiler, 2011; Fig.1.10).

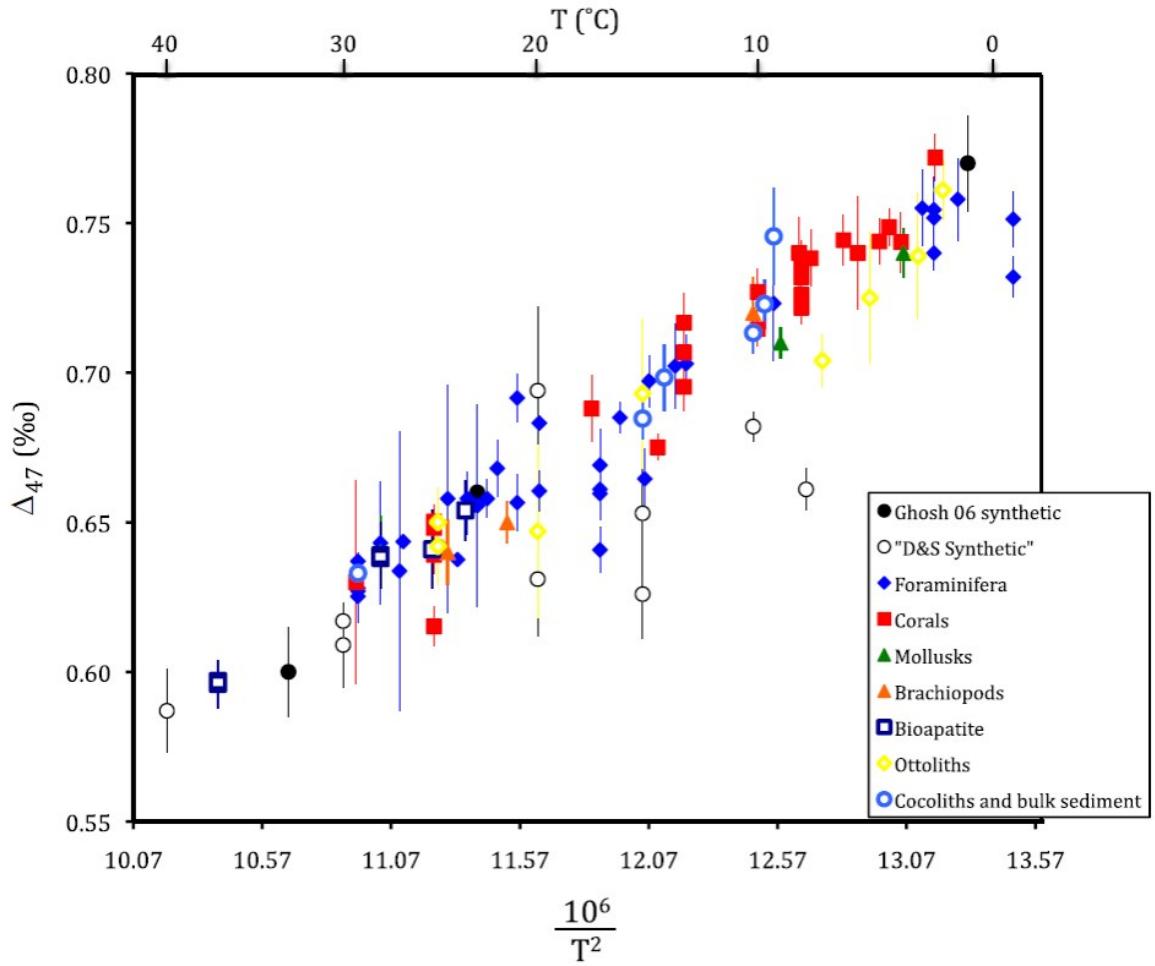

Fig.1.10. Calibrations of the carbonate clumped isotope thermometer between temperatures of 0-40 °C. From Eiler, 2011.

The latest clumped isotope thermometer calibration was performed by Anderson et al. (2021). It covers the broadest range of temperatures, includes diverse carbonates (laboratory precipitates, foraminifera calcite), replicates measurements several times, and uses carbonate standardization (Fig.1.11; equation 8):

$$\Delta_{47(\text{I-CDES90°C})} = 0.0391 \pm 0.0004 \times (10^6/T^2) + 0.154 \pm 0.004 \quad (r^2 = 0.97) \qquad (8)$$

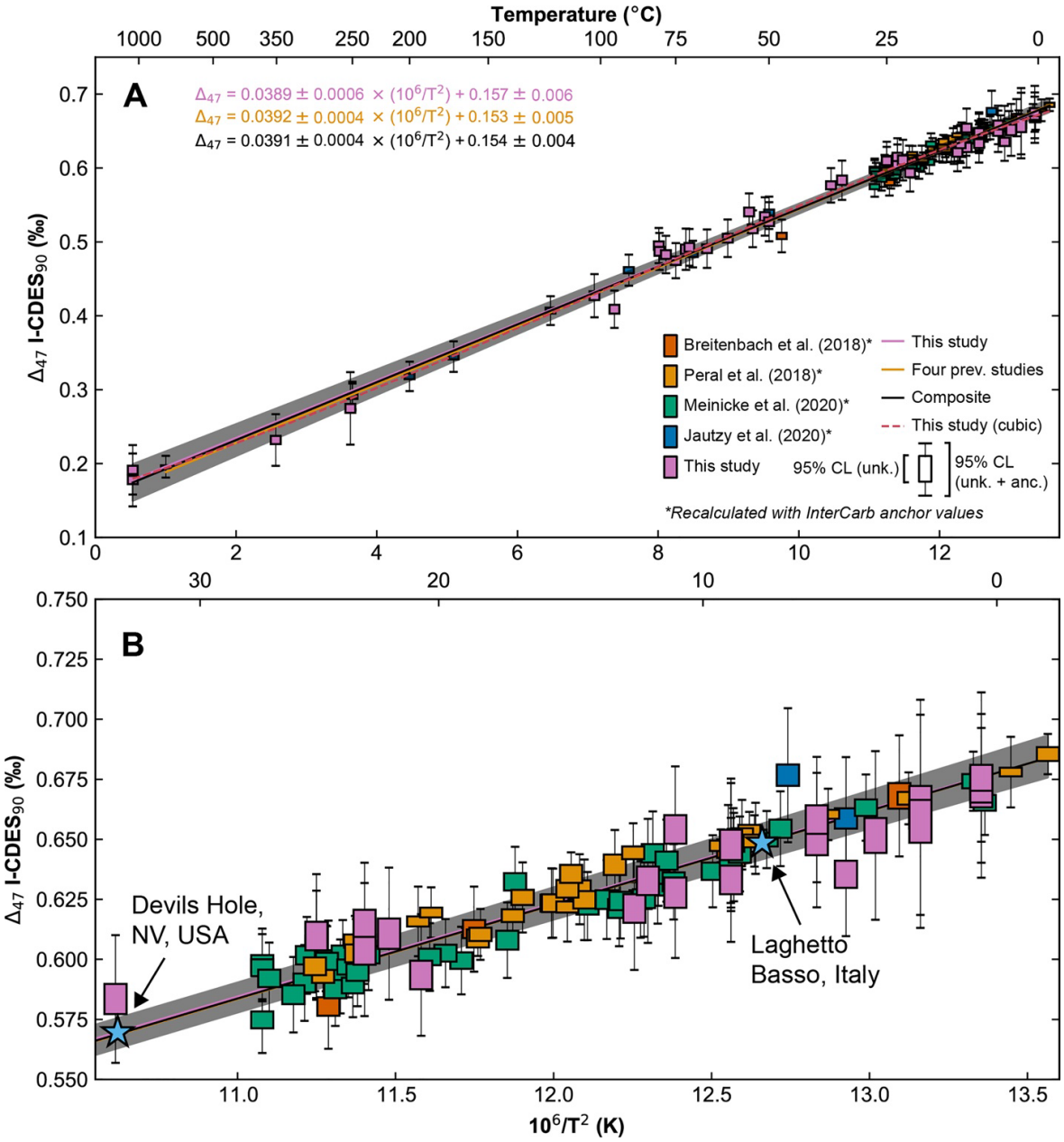

Fig.1.11. (**A**) All Δ_{47} results from the study of Anderson et al. (2021) are shown with data from four recent studies using carbonate-based standardization. Error bars correspond to 95 % confidence limits. The regressions through the study correspond well with the dataset. (**B**) Inlet (A) from 0-30 °C. The results from two localities (blue stars) presented in the study are precisely on the regression lines. From Anderson et al. (2021).

Δ_{47} in carbonates can be measured with external precision as good as 0.01–0.02 ‰ (depending on sample size and the number of measured repetitions), and so clumped isotope thermometer can constrain growth temperatures with precision as good as ± 2 °C. This uncertainty is large but sufficient for resolving many problems in paleoclimate research, meteoritics, and the thermal history of soils and shallow crustal rocks (Ghosh et al., 2006).

Two main concerns were raised by Ghosh et al. (2006): 1. If carbonate grows at low temperatures and is later heated without re-crystallization, at what temperatures and after what times will it re-equilibrate at the new, higher temperature? And 2. If carbonate grows at a high temperature and then cools, what will be the temperature at which the examined reaction stops re-equilibrating? The second question is of particular importance when applying the clumped isotope thermometer to high-temperature metamorphic rocks (Ghosh et al., 2006). Nevertheless, for the scope of this thesis, concern nr. 1 needs to be considered.

Solid-state reordering of C–O bonds in the lattice of carbonate minerals can alter the Δ_{47} without influencing shell microstructure and trace element concentrations – features usually used to determine the preservation of the samples (Henkes et al., 2014).

Henkes et al. (2014) developed a model responding to hypothetical burial and exhumation history, explained in Fig.1.12.

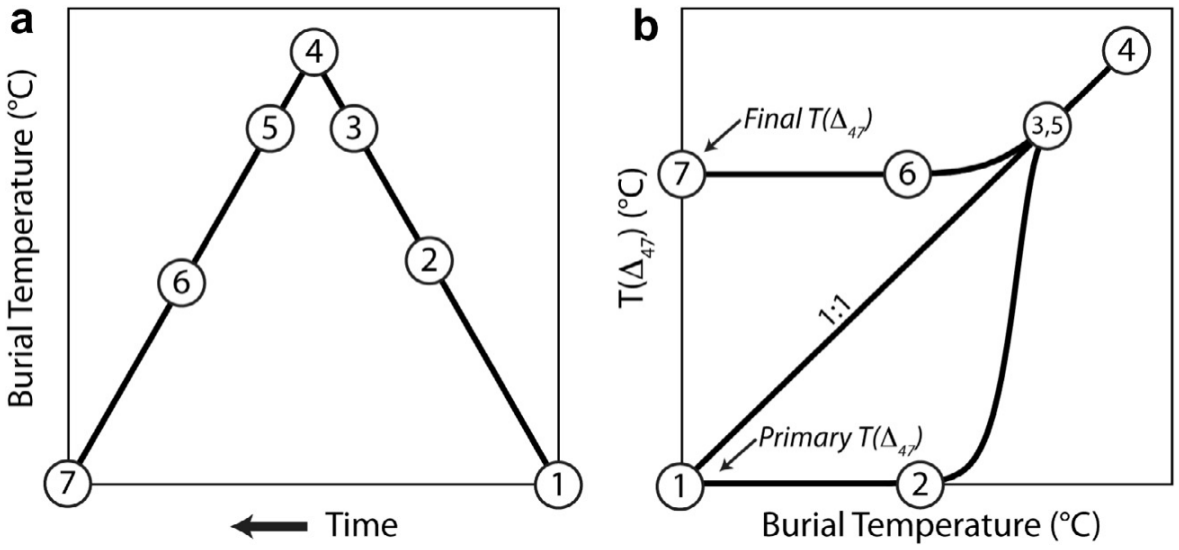

Fig.1.12. (**a**) A schematic picture of the features of the burial history, and (**b**) T(Δ_{47})-burial temperature trajectories. Points 1-2: A period where clumped isotope record does not undergo reordering and original Δ_{47} values do not change. 2-3: When a sample is buried and experiences temperatures sufficiently high, a period of rapid activation of reordering takes place (Δ_{47} approaches equilibrium with the burial environment). 3-4: Increasing temperature causes Δ_{47} to reach equilibrium with the ambient temperature. 4-5: A sample in apparent thermal equilibrium will remain in equilibrium with the burial environment during retrograde cooling. 5-6: During the cooling, reordering remains active but is 'closing (apparent T(Δ_{47})>burial temperature). 6-7: A sample cools to a point when reordering becomes inactive; the mineral remains in an apparent T(Δ_{47}) value. From Henkes et al. (2014).

This issue is very important to be considered when using clumped isotopes for paleotemperature reconstructions in the fossil record where sedimentary sequences might have experienced several phases of burial and exhumation.

Importantly, the main advantage of clumped isotope thermometer is that it is based on a homogenous equilibrium, therefore, it is defined based only on measurements of the carbonate minerals (Ghosh et al., 2006; Schauble et al., 2006). In other words, it is not dependent on the isotopic composition of water (Eiler, 2011), as is the case of the previously discussed $\delta^{18}O$ paleothermometer.

Clumped isotope thermometry provides a unique insight into some of the main complications of $\delta^{18}O$ thermometry. The $\delta^{18}O$-based paleotemperature calculations depend on knowledge of the $\delta^{18}O$ composition of the seawater from which the carbonate minerals precipitated (Grossman, 2012; Pearson, 2012). Since the clumped isotope thermometry is independent of the original isotopic composition of the seawater, it can be used (with the $\delta^{18}O$ measured in the same sample) to calculate the $\delta^{18}O_{seawater}$ (e.g., Cummins et al., 2014).

1.3 Main carbonate producers of Late Cretaceous carbonate platforms, Rudist bivalves

Rudists, an order of inequivalved, thick-shelled, heterodont sessile bivalves (Skelton, 2018), evolved during the Late Jurassic (Oxfordian; Dechaseaux et al., 1969) and went extinct at the end of the Cretaceous (Maastrichtian; Skelton, 2018; Steuber et al., 2002). They were the main carbonate producers on the margins and tops of the carbonate platforms in the Late Cretaceous (Gili et al., 1995; Kauffman and Johnson, 1988). Rudist fossils are found in low-latitude tropics mainly but extend to as much as 50-55°N and 40-45°S paleolatitudes (Johnson et al., 2001 and references therein).

Rudist shells are often large and robust compared to modern bivalves. The lower (attached) valve is usually larger, whereas the upper (free) valve tends to be smaller in most rudist families (Hernandez, 2011). The rudist shell morphology is graphically illustrated in Fig.1.13 and 1.14.

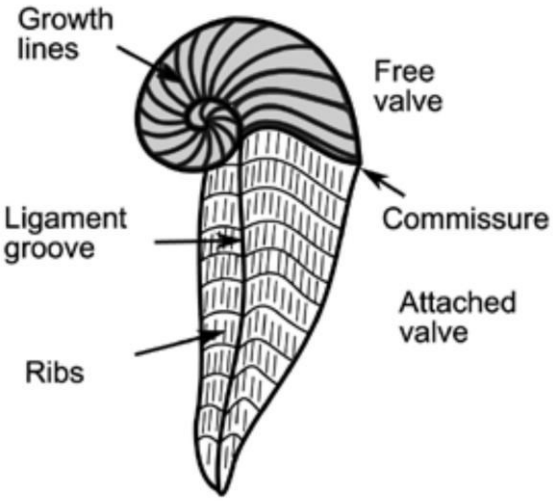

Fig.1.13. External rudist shell morphology. From Hernandez (2011).

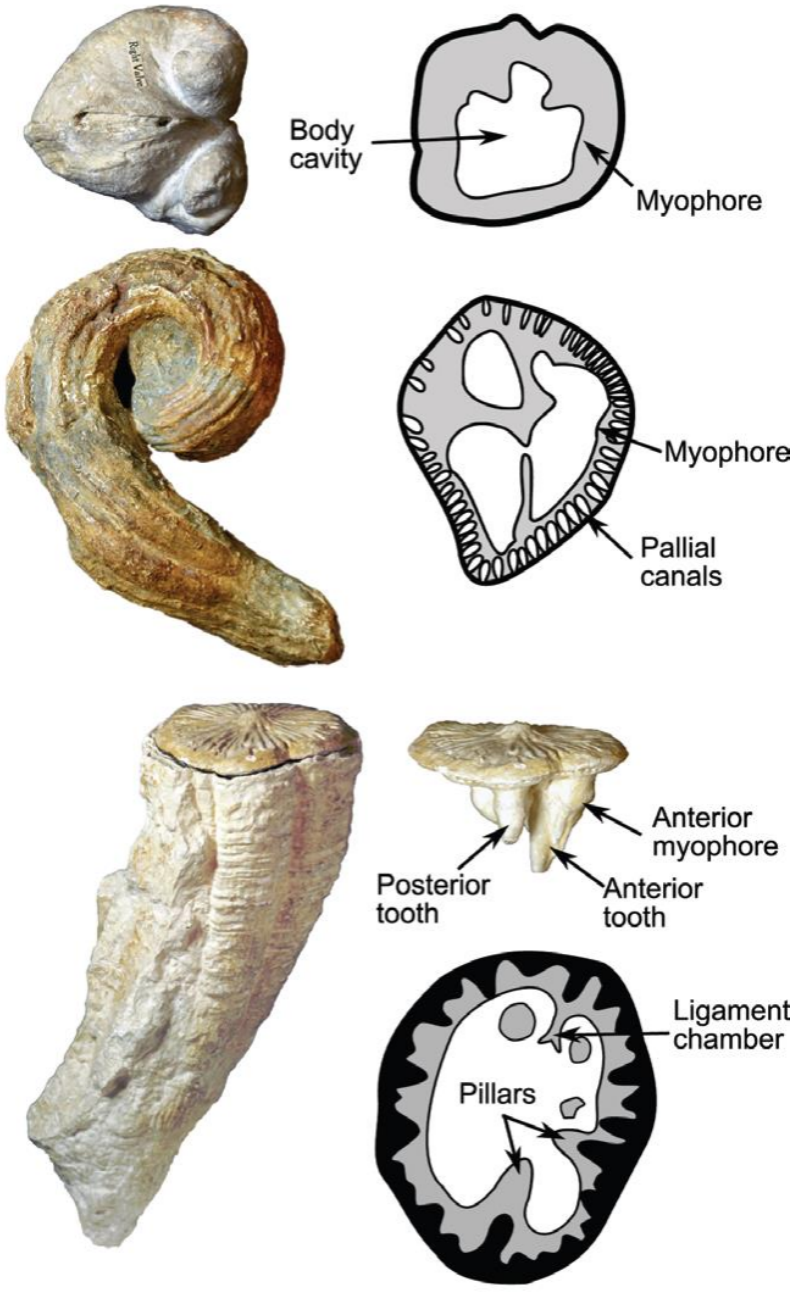

Fig.1.14. Examples of rudists internal morphology. The inner aragonite (grey) and outer calcitic (black) layers of the shells are shown. From Hernandez (2011).

During their evolution, they have grown in an extraordinary variety of morphologies (Fig.1.15; Skelton, 2018). This morphological diversity of growth forms is linked to the nature of the substrate they inhabited (Skelton, 2018), allowing them to thrive under a wide range of conditions: from hard to soft substrate, quiet to tractive current activities, from none to moderate sediment accumulation that could have been continuous to spasmodic (Skelton and Gili, 2002). Consequently, understanding the relationship between the substrate, water dynamics, and rudist shell morphology allows for paleoenvironmental analyses based on the mere presence of the rudist fossils.

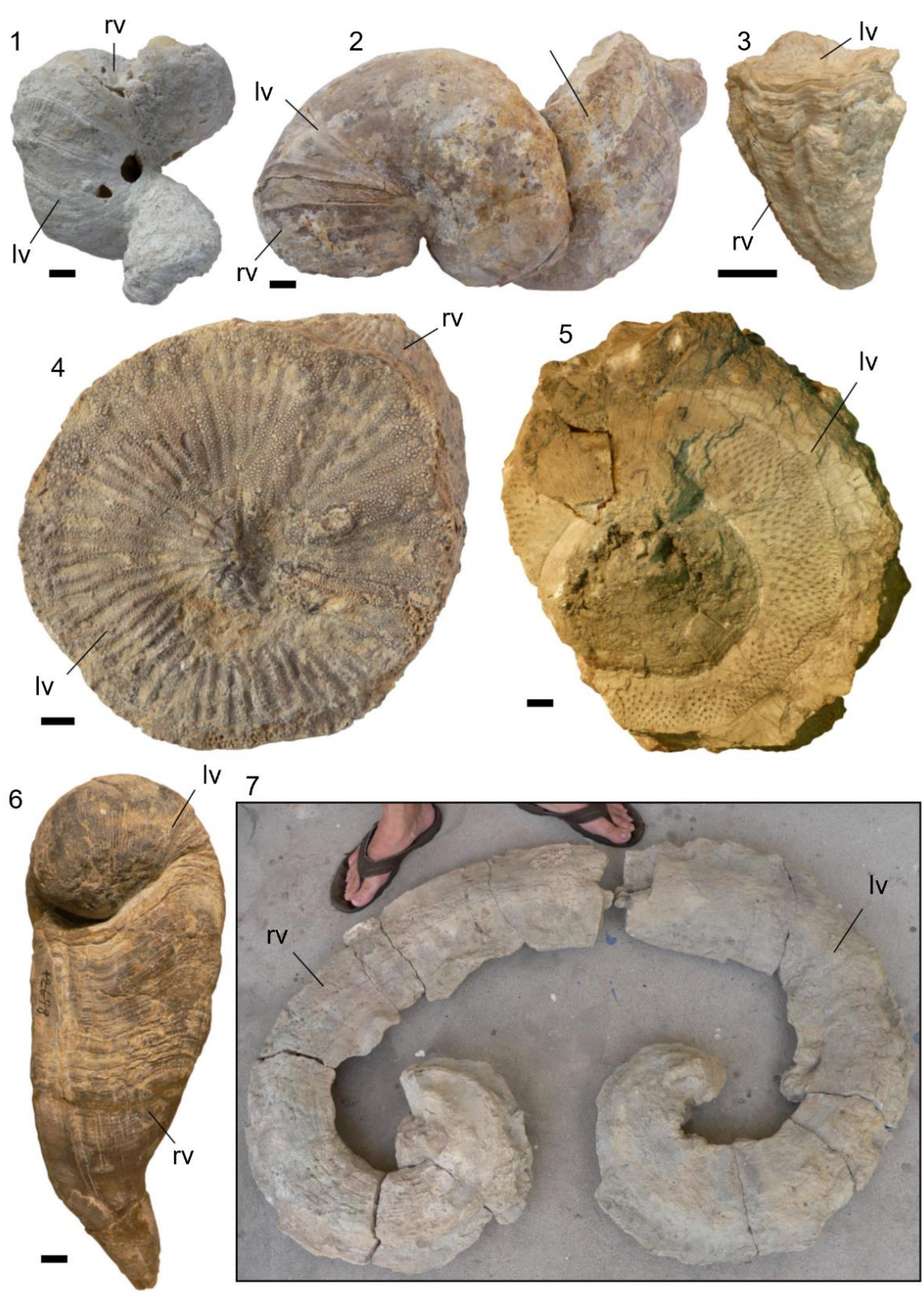

Fig.1.15. Morphological diversity in different families of rudist bivalves. 1. *Epidiceratidae*, 2. *Requieniidae*, 3. *Radiolitidae*, 4. *Hippuritidae*, 5. *Radiolitidae*, 6. *Plagioptychidae*, 7. *Antillocaprinidae*. lv, left valve, rv, right valve; scale bars: 10mm. After Skelton (2018).

The functional requirements of rudist shell growth were possibly twofold: 1. Presentation of the feeding apparatus to feeding and respiratory water currents, and 2. Stabilization of the shell in/on the substratum so that the requirement nr. 1 could be maintained (Gili and Götz, 2018). The resulting paleoecological morphotypes were defined by Skelton and Gili (2002) and revised by Gili and Götz (2018; Fig.1.16).

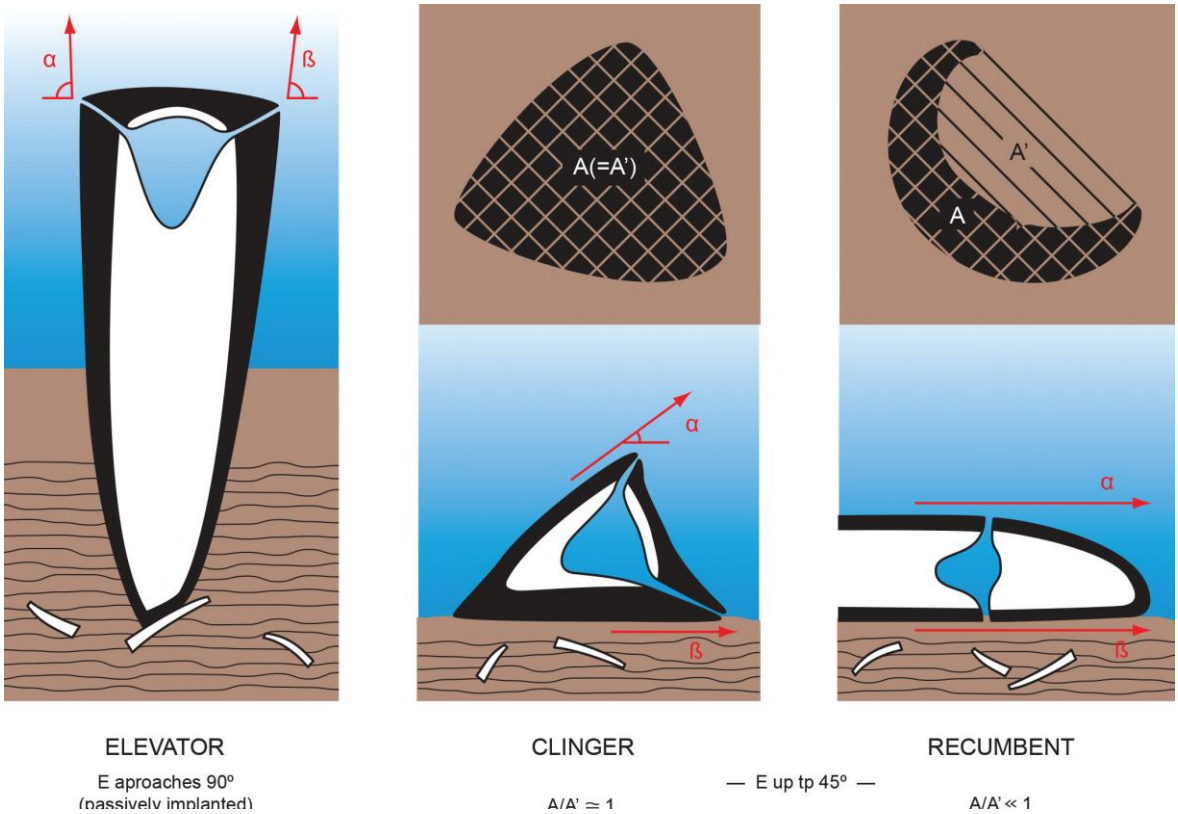

Fig.1.16. Rudist paleoecological morphotypes. All shell types are shown in the vertical section and Clinger and Recumbent morphotypes are additionally shown in plain view. A, the surface area of basal contact; A', the virtual area of support; E, mean angle of elevation; α, maximum and β, minimum inclination. E tends towards 90° in Elevators, whereas in Clingers and Recumbents, E<45°. From Gili and Götz (2018).

The Elevator morphotype is most often associated with muddy (wackestone to packstone) substrates. The stability of the upward growth was achieved by passive embedding of the attached, lower valve in accumulating sediment. Therefore, their occurrences point to environments with net positive sediment accumulation (Gili and Götz, 2018). The most closely aggregative rudists (many representatives of families *Hippuritidae* and *Radiolitidae*) were Elevators (Skelton and Gili, 2002).

In the ecological morphotype Clinger, a broad basal area of frictional or adherent contact was achieved by the margin overgrowth of the attached valve (Gili and Götz, 2018). This allowed for achieving stability on firm or hard substrates with condensed or spasmodic sedimentation

(Skelton and Gili, 2002). In contrast, the Recumbent morphotype shells were not attached (in adults), and the surface area of basal contact (A, Fig.1.16) was not the main stabilization feature. Recumbents' shells resisted overturning by currents and reduced the possibility of sediment burial by expanding their virtual area of support (A', Fig.1.16; Gili and Götz, 2018). Hence, they were adapted for stabilization upon high energy, mobile substrata frequently swept by traction currents (Skelton and Gili, 2002).

Hernandez (2011) broadly divides the evolutionary history of rudists into three diversification-extinction episodes (Fig.1.17). 1. The origination of rudists in Oxfordian (family *Diceratidae*) and their diversification, until the extinction of diceratids in the Valanginian (Early Cretaceous). 2. The times of the family *Caprinidae*, which retained primitive features such as mainly aragonitic shells with a thin layer of calcite but acquired novel adaptive morphologies such as hollow pallial canals within the shell walls allowing for larger sizes of their shells. 3. The diversification of the mainly calcitic families *Hippuritidae* and *Radiolitidae* into massive elevators or facultative recumbents with thick outer calcite shell layers, occupying a broad array of ecological niches after the rudist extinction event at the end of the Cenomanian (Philip and Airaud-Crumiere, 1991).

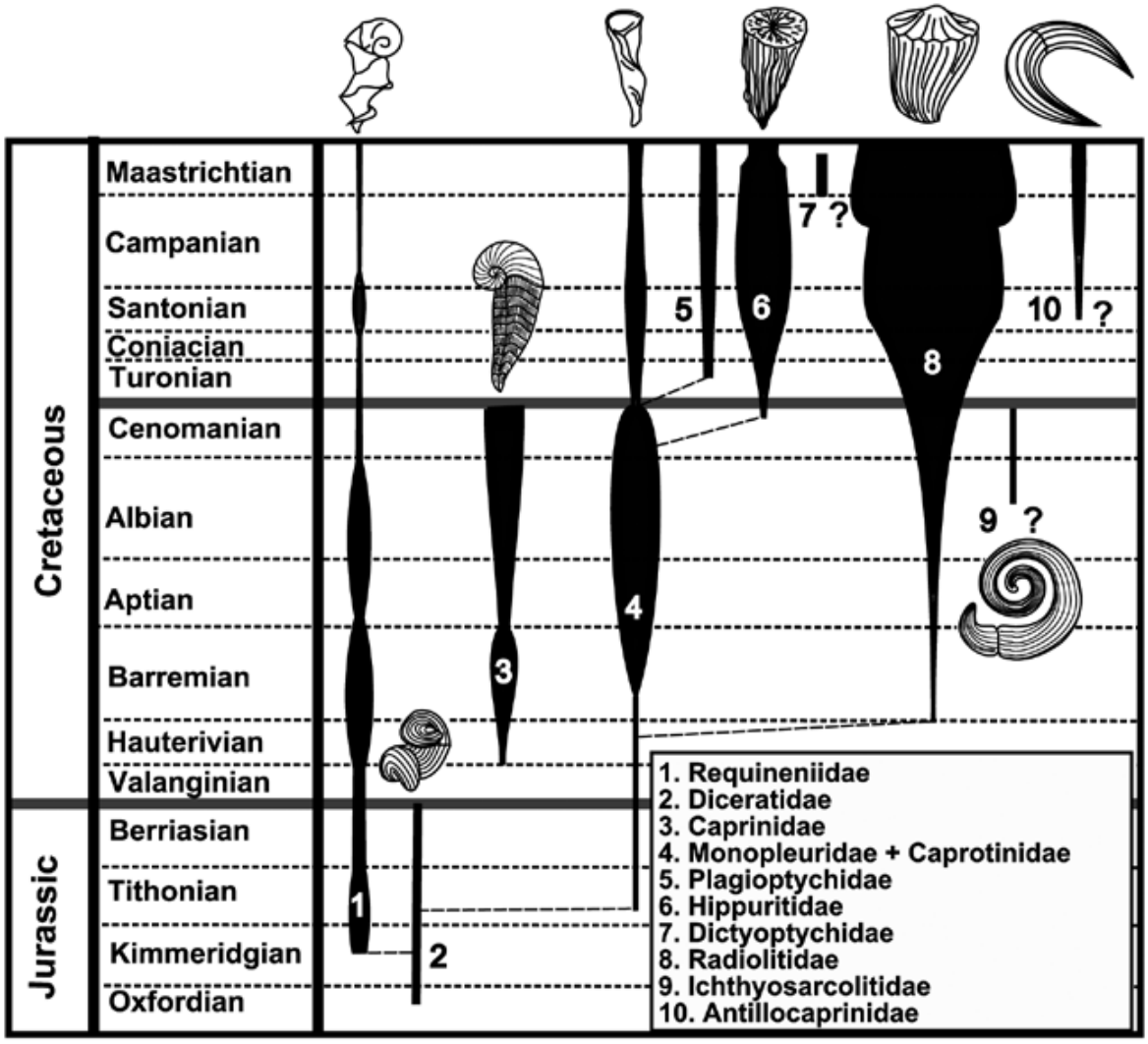

Fig.1.17. Evolutionary history of rudists. From Hernandez, 2011 (modified after Skelton, 2003).

Steuber et al. (2016) presented general patterns of diversification and extinction of rudists with improved stratigraphic and taxonomic precision (Fig.1.18). They identified an increase in the number of rudist genera from Oxfordian to the Campanian, with peaks in the early Aptian, late Albian, late Cenomanian, and late Campanian, and two major reductions in the number of genera in the mid-Aptian and at the Cenomanian/Turonian boundary.

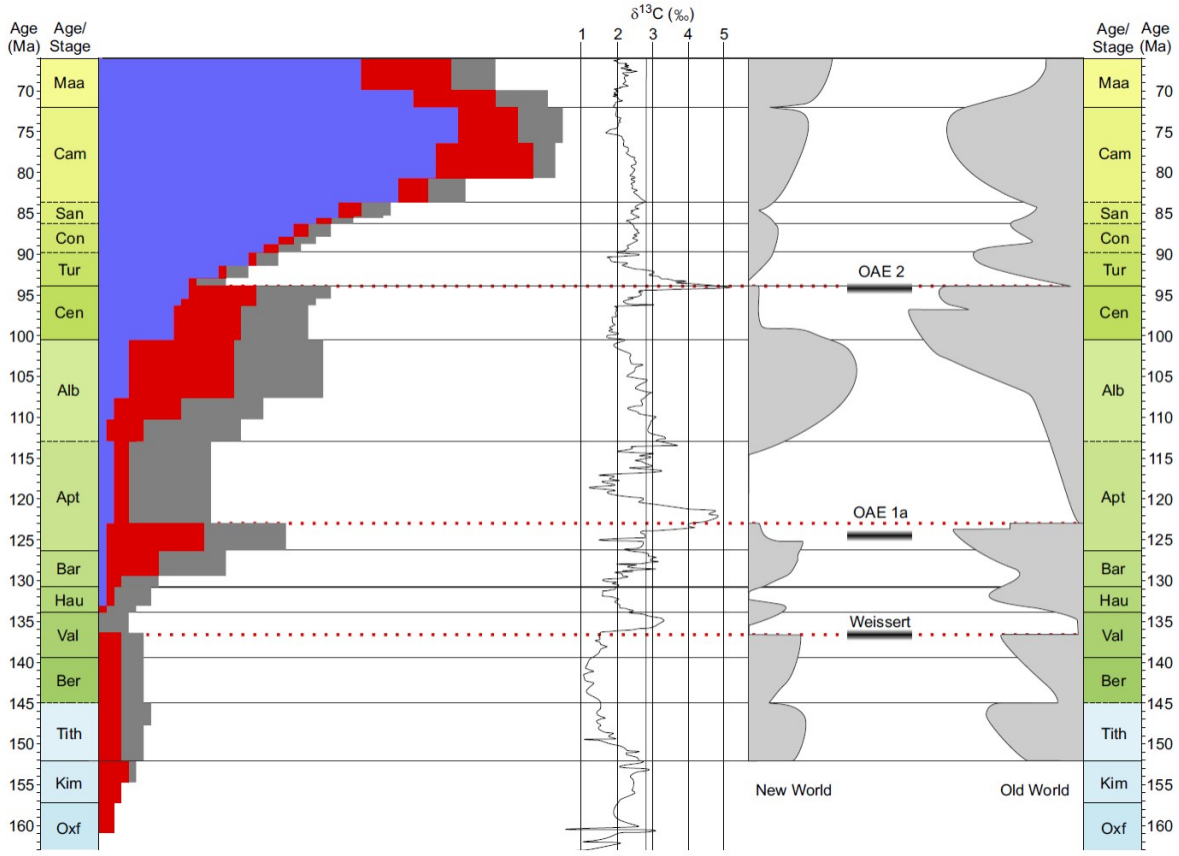

Fig.1.18. Number of rudist genera with calcite-dominated shells (blue), aragonite-dominated shells (red), and with a dominance of neither calcite nor aragonite (gray), compared to the carbon-isotopic composition of marine carbonates and the extent of carbonate platforms in the Americas (New World) and Europe, North Africa, and Arabia (Old World). Red dotted lines, major extinction events among rudists. Grey bars, Oceanic anoxic events. Note that the aragonite-dominated taxa were predominantly affected during the extinction events, whereas the calcite-dominated taxa (e.g., family *Radiolitidae*) continued to radiate. From Steuber et al. (2016).

Mollusk shells are known as archives of paleoenvironmental conditions for more than 50 years (Gröcke and Gillikin, 2008). The calcite-dominated shells of rudist bivalves have been proven as suitable for climate reconstruction in the Cretaceous (de Winter et al., 2017a; Huck and Heimhofer, 2021; Schmitt et al., 2022; Steuber, 1996; Steuber et al., 2005b). The thick low-Mg calcitic outer layer of their shells allows quantitative analyses of ontogenetic oxygen isotope variations, sometimes even at seasonal resolution (Fig.1.19; Steuber, 1996; Steuber et al., 2005; de Winter et al., 2017; Schmitt et al., 2022), referred to as chemical sclerochronology (Gillikin et al., 2019). Chemical sclerochronology (or sclerochemistry) is focused on the isotope and element signatures in biological carbonates (Gillikin et al., 2019). For the purposes of this thesis, an oxygen isotope thermometer was applied to rudist shells sampled throughout an outcrop (long-term paleotemperature variations were reconstructed), as well as to sampled rudist sclerochronological profiles to reconstruct seasonal paleotemperature variations.

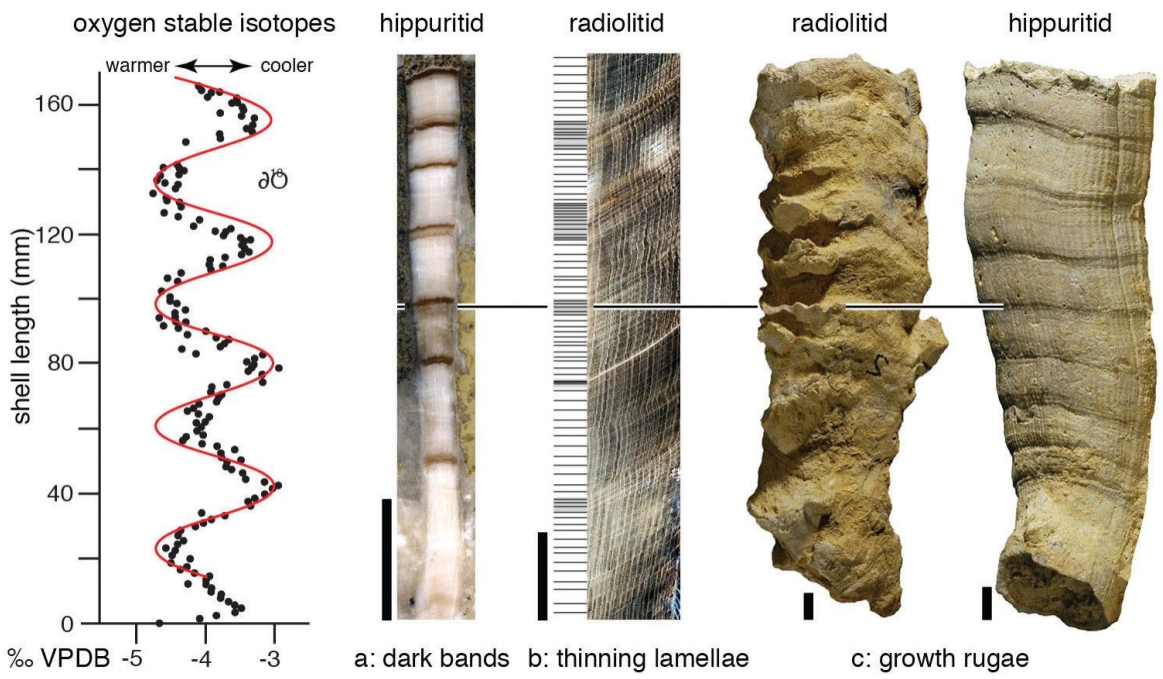

Fig.1.19. The oxygen-isotope variations in rudist shells are interpreted as seasonal variations in temperatures through the years. a. and b. longitudinal sections of rudists depicted in the figure (c). a. hippuritid rudist showing dark, organic-rich bands, b. radiolitid rudist showing thinned growth lamellae. c. growth rugae in hippuritids and radiolitids. Scale bars, 1cm. From Gili and Götz (2018).

With the recent increase in using the novel method of clumped isotope thermometry, the first studies using calcitic shells of rudist bivalves were made for paleoclimate reconstructions of the Cretaceous (de Winter et al., 2017; Huck et al., 2012; see Fig.1.20).

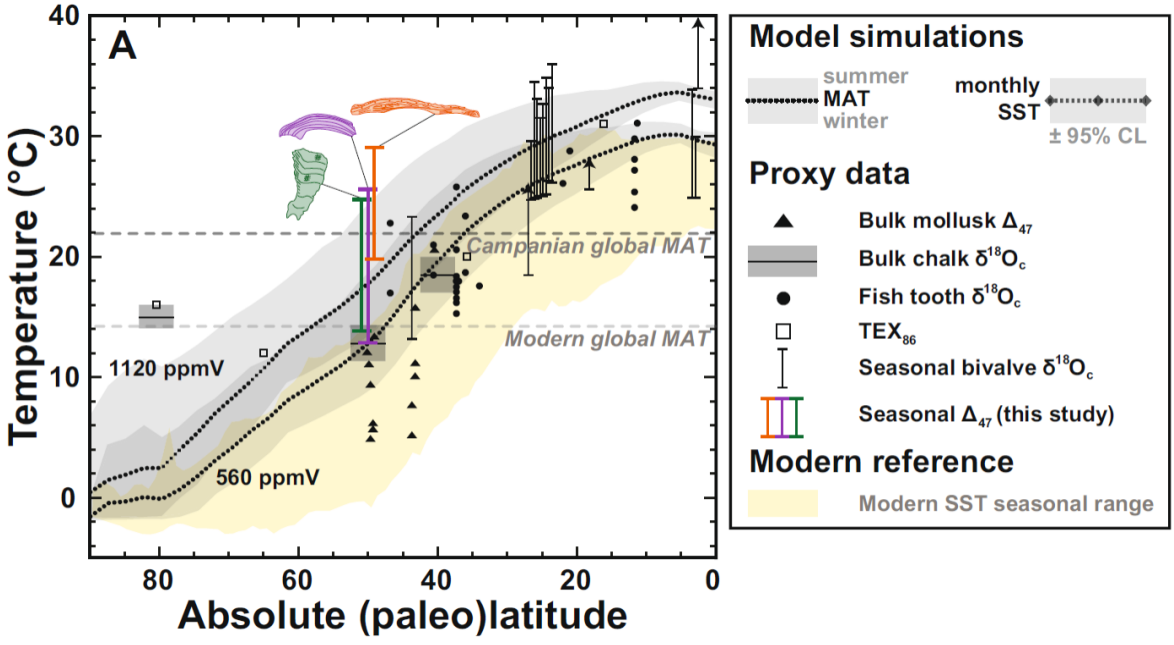

Fig.1.20. Comparison between modeled and reconstructed sea surface temperatures in Campanian. Vertical orange, purple, and green bars show seasonality reconstructions and dashed black lines indicate modeled mean annual temperatures (560 ppmV = 2×preindustrial and 1120 ppmV= 4× preindustrial CO_2 pressure) with grey envelopes representing seasonality. From de Winter et al. (2021).

The properties of rudist shells described above, as well as the above-mentioned examples of their ongoing research, illustrate the great potential rudist bivalves have in the reconstructions of the Cretaceous climate.

1.4 Aims of Study

The main objectives of this Ph.D. thesis are:

- Building, for the first time, a high-resolution paleotemperature curve (using $\delta^{18}O$ analysis of rudist shells and micritic bulk rock) in the Upper Cretaceous shallow-water carbonates of the western Tethys using a key section (Devetachi, Friuli region) and producing high-resolution stratigraphic framework (using biostratigraphy, $\delta^{13}C$- and $^{87}Sr/^{86}Sr$-chemostratigraphy).
- Studying the faunal (rudist and benthic foraminifera) and facies evolution in the analyzed stratigraphic interval and comparing these records with the observed paleotemperature fluctuations.
- Investigating the rudist bivalves from the Friuli and Istria regions as a proxy for clumped isotope paleothermometry.
- Using clumped isotope thermometry for absolute paleotemperature estimates, and, in combination with the $\delta^{18}O$ results, inferring the oxygen isotopic composition of the seawater that the studied rudists precipitated the shells from.
- Reconstructing paleotemperature records using Δ_{47}, and $\delta^{18}O$ analyses through the sclerochronological profiles of the best-preserved specimens, aiming for precise reconstruction of the seasonal paleotemperature fluctuations.

2 Methodology

2.1 Samples collection and preparation

Extensive fieldwork included sedimentological, stratigraphic, and paleontological analyses, at the decimeter scale. 500 samples were collected and over 100 thin sections were prepared and studied. Samples of bulk rock and, where possible, rudist or other bivalve shells were collected at intervals not exceeding 1 meter, where allowed by outcrop conditions. All samples were cut and polished to a maximum of 600µm and micro-drilled under a binocular microscope with a hand-operated dental drill. Bulk rock powder samples were obtained by a tungsten carbide drill bit of 0.5 mm in diameter, whereas the shell samples were obtained by a drill bit of 0.3mm in diameter. Areas for drilling bulk rock material were carefully selected to obtain a micritic matrix where possible. Cement-filled cavities, veins, and areas showing diagenetic alterations were avoided. Rudist and other bivalve shell fragments were carefully selected and micro-drilled under the microscope, avoiding any areas showing evidence of recrystallization or bioerosion. Only shells with visible original microstructure were drilled for powder samples. Polished slabs were obtained to check directly under the microscope the pristine preservation state of analyzed rudist shells by the occurrence of low-Mg calcite prisms arranged in well-distinguishable growth increments (Huck and Heimhofer, 2021).

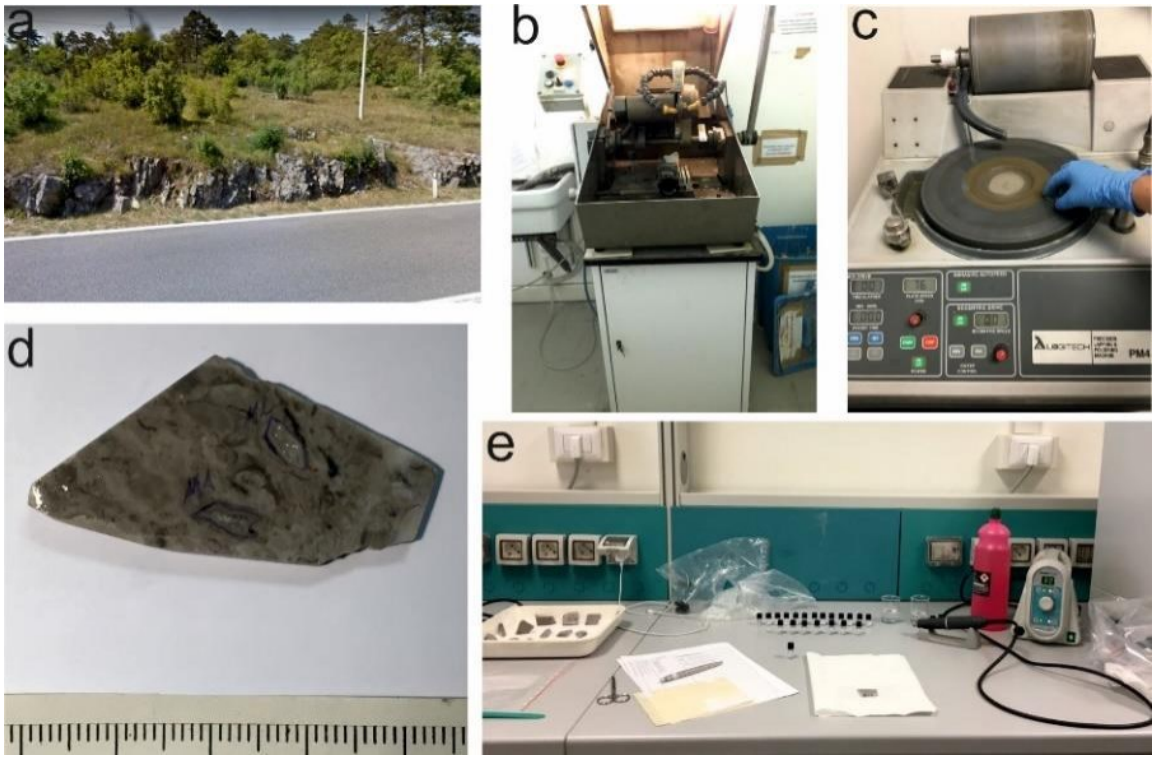

Fig.2.1. **a.** Example of outcrop conditions (Devetachi section, Friuli, NE Italy). **b.** Cutting and **c.** polishing hand specimens. **d.** polished rock slab ready for micro-drilling. e. microdrill settings in the Laboratory of Paleoclimatology and Isotopic Stratigraphy at the University of Ferrara.

2.2 Stable carbon and oxygen isotope analyses

The carbon and oxygen isotopic analysis was performed in the Laboratory of Paleoclimatology and Isotopic Stratigraphy of the Department of Physics and Earth Sciences of the University of Ferrara, using isoFLOW (Elementar©) operating in continuous flow with a PrecisION IRMS (Elementar©). 454 samples were analyzed in total, comprising ~300 bulk rock samples and ~150 rudists and bivalve samples. Vials containing powder samples of 150±30 µg were flushed with He and reacted with viscous water-free orthophosphoric acid (3 hours at 50 °C), releasing CO_2. The released sample-CO_2 was transferred to the IRMS, and simultaneous analysis of $\delta^{13}C$ and $\delta^{18}O$ was performed. In the IRMS, the sample-CO_2 molecules are ionized by the source and pass through a magnet, which deflects and sorts them into beams with distinctive mass/charge ratios (m/z). Arriving in the collector, three Faraday cups detect the ions with masses 44, 45, and 46 (the detection is bracketed between masses of the calibrated reference gas. In Faraday cups, ions' impact is translated into an electrical signal forming peaks with areas proportional to the number of incident ions. The isotopic ratio is then calculated through peak definition and integration using the ionOS software. Single-point calibration was performed using the in-house MAQ-1 standard, and the consistency of the measurements was monitored by two control standards (IAEA 603 and Carrara Marble). isoFLOW external precision is 0.08 ‰, with analytical uncertainties in order of ± 0.1 ‰. Carbon and oxygen isotope ratios were expressed in δ notation ($\delta^{13}C$ and $\delta^{18}O$), in per mille (‰) units, relative to VPDB.

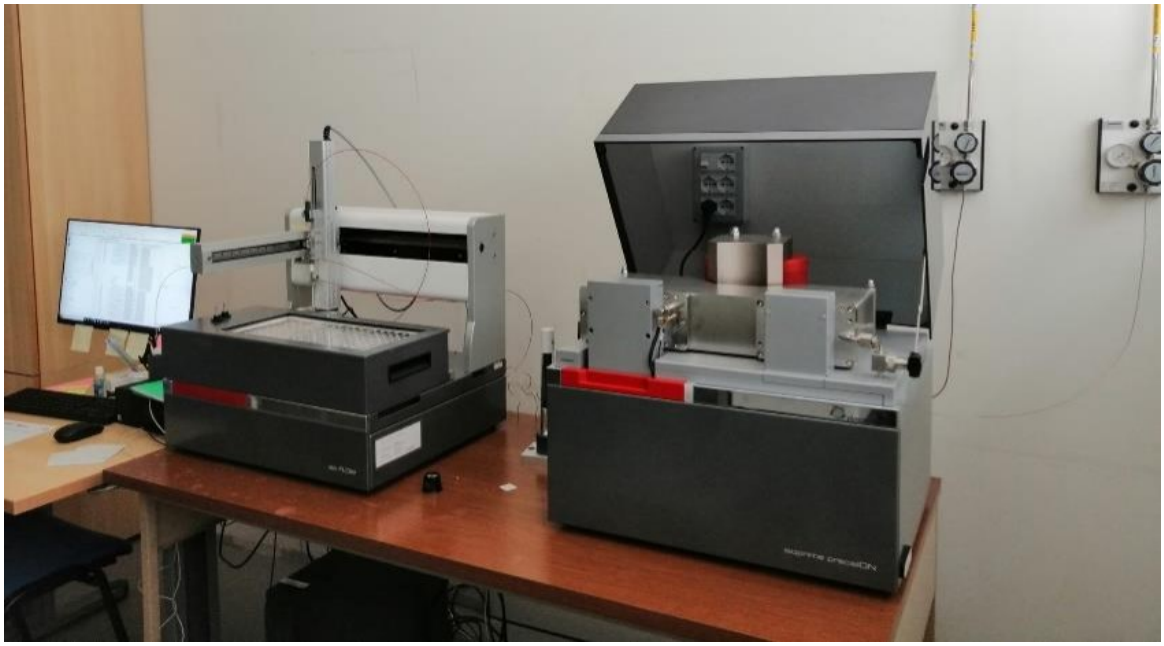

Fig.2.2. PrecisION IRMS (Elementar©). Laboratory of Paleoclimatology and Isotopic Stratigraphy, University of Ferrara.

2.3 Clumped isotope analyses

Clumped isotope analyses were performed in the Stable Isotope lab at Utrecht University using Kiel IV carbonate devices coupled to a MAT 253 or 253 Plus IRMS. Carbonate aliquots (70-150 µg) were reacted with nominally anhydrous (103 %) phosphoric acid at 70 °C for 300s. The produced CO_2 gas was led through two liquid nitrogen-cooled (−196 °C) cryogenic traps and a PoraPak™ Q trap (Merck KGaA, Darmstadt, Germany) kept at −50 °C through a custom-built external cooling unit (Dennis and Schrag, 2010). The purified CO_2 gas was analyzed in micro-volume mode using the LIDI workflow with 400 s integration time against a clean CO_2 working gas ($\delta^{13}C$ = −2.82 ‰; $\delta^{18}O$ = −4.67 ‰) and corrected for pressure baseline effects (Bernasconi et al., 2013; Meckler et al., 2014; Müller et al., 2017). Clumped isotope values were corrected to the Intercarb-Carbon Dioxide Equilibrium Scale (I-CDES) by creating an empirical transfer function (ETF) using measurements of ETH standards (ETH-1, -2 and -3) and their accepted Intercarb values (Bernasconi et al., 2021). The results were expressed with Δ notation (in ‰ units).

Fig.2.3. Kiel IV carbonate device (left) coupled to a 253 Plus IRMS in the Stable Isotope lab (right), Utrecht University.

2.4 $^{87}Sr/^{86}Sr$ analyses

A total of 30 shell fragments of rudists were sampled for Strontium Isotope Stratigraphy (SIS). Where possible, multiple samples were collected from each analyzed stratigraphic level, to test the internal consistency of the data. The samples were selected in the field by a preliminary assessment of their preservation with a low-magnification hand lens. Laboratory preparation and further screening of the selected shell fragments followed the method described in Frijia and Parente (2008). To assess the preservation of the original shell microstructure, the samples were passed through a petrographic screening (optical microscopy). Shells were selected based on the preservation of the prismatic microstructure, and/or growth lines visible under the microscope. A further screening step was performed by analyzing the elemental (Mg, Sr, Mn, and Fe) composition of the shells.

Strontium isotope analysis was performed at the Institute for Geology, Mineralogy, and Geophysics of Ruhr University (Bochum, Germany). After strontium separation by standard ion-exchange methods, strontium-isotope ratios were analyzed on a Finnigan MAT 262 thermal-ionization mass spectrometer and normalized to an $^{87}Sr/^{86}Sr$ value of 0.1194. The $^{87}Sr/^{86}Sr$ ratios of the samples were adjusted to a value of 0.709175 for the USGS EN-1 standard, to be consistent with the normalization used in the compilation of the ‘‘look-up’’ table of McArthur et al. (2020; version 6). Where more than one sample was available for one stratigraphic level a mean value was calculated. When more than one level was sampled in a thin interval (less than 15 m), with no evidence of intervening stratigraphic gaps, the numerical age was derived from the mean value of all the samples following the methodology of Frijia et al. (2015). The precision of the $^{87}Sr/^{86}Sr$ mean values for each stratigraphic level is given as 2

s.e. of the mean when the number of samples (n) is 4. When n < 4, the precision is considered not to be better than the average precision of a single measurement (2 s.e. ¼ ±0.000007) and is calculated from the standard deviation of the mean value of the standards run with the samples. The numerical ages of the samples analyzed in this study were derived from the look-up table of McArthur and Howarth (2020, version 6), which is tied to the Geological Time Scale of Gradstein et al. (2020; herein after GTS2020). Minimum and maximum ages were obtained by combining the statistical uncertainty (2 s. e.) of the mean values of the Sr-isotope ratios of the samples with the uncertainty of the seawater curve.

2.5 Elemental analyses

The concentration of Mg, Sr, Fe, and Mn was measured at the Institute for Geology, Mineralogy, and Geophysics of Ruhr University (Bochum, Germany), using Inductively Coupled Plasma Optical Emission Spectrometer (ICP-OES, Thermo Fisher Scientific iCAP 6500 DUO). About 1.5 mg of the produced sample powder was weighed in with a balance of the type XPR6UD5 (Mettler Toledo) with a reading precision of 0.5 mg and a reproducibility of ±0.25 mg (n = 10). The sample was subsequently dissolved in 1ml 3 M HNO_3. The reaction time was 24hrs and subsequently, 2ml of H_2O was added. The samples were then measured using the ICP-OES, and the results were expressed in parts per million (ppm) units.

Additionally, elemental composition of two rudist shells (*Hippurites nabresinensis*, Friuli, and *Praeradiolites ciryi*, Istria region) was measured using Tornado M4 micro-X-ray fluorescence (µXRF) scanner (Bruker nano GmbH, Berlin, Germany) hosted at the Analytical, Environmental and Geochemistry research group of the Vrije Universiteit (Brussel). The µXRF scanner is equipped with an Rh source and two X Flash 430 Silicon Drift detectors. The methodology presented herein is after Schmitt et al. (2022).

Semi-quantitative µXRF-maps showing relative differences in elemental compositions were created to assess the distribution of major and trace elements across the surface of shell fragments. Polished shell surfaces were scanned in the µXRF mapping mode using a short acquisition time of 1 ms per pixel. Maps were created by focusing the X-ray beam on a circular spot with a diameter of 25 µm and dragging the beam across the polished surface, collecting µXRF spectra every 50 µm in X and Y directions. This procedure yielded ~106 µXRF spectra per sample, which allowed semi-quantitative maps of elemental distribution (magnesium, iron, and strontium) to be created based on differences in the area of peaks in the µXRF spectrum associated with elements (ROI counts; see de Winter and Claeys, 2016).

Quantitative point-by-point μXRF line scans were performed more or less perpendicular to the growth axis in the studied rudist specimens with a sampling resolution of 50 μm. Point-by-point line scans allow the X-ray beam to remain on each point for 60 s at maximized energy settings (50 kV, 600 μA, no source filter). This time of analysis represents the ideal compromise between lowering the signal-to-noise ratio (by increasing measurement time) and increasing the spatial sampling resolution (by increasing the number of measurements). This causes the signal-to-noise ratio of individual spectra to be high enough to allow quantification of individual spectra to produce accurate and reproducible measurements of concentrations of a range of major and trace elements (see discussion in de Winter et al. 2017b). Therefore, XRF spectra in line scans yield quantitative major and trace element profiles, contrary to spectra of pixels in XRF maps, which can only be used to measure relative changes in element abundances.

3 Paleotemperature reconstructions and biota evolution in the Cenomanian-Turonian (Upper Cretaceous) interval of the Adriatic Carbonate Platform (Friuli; NE Italy)

Krizova B., Consorti L., Cardelli S., Schmitt K. E., Brombin V., Franceschi M., Tunis G., Bonini L., Frijia G.

Submitted to Palaeogeography, Palaeoclimatology, Palaeoecology

3.1 Introduction

The Late Cretaceous (100.5 Ma to 66.4 Ma, Gradstein et al., 2020) was characterized by extremely high temperatures in the oceans and continents. The modeled CO_2 concentration in the atmosphere was among the highest of the entire Phanerozoic (e.g., Bice et al., 2006; Burgener et al., 2023; Hay and Floegel, 2012; O'Brien et al., 2017), and it has been considered the main driver of the warm Cretaceous climate (e.g., Hay and Floegel, 2012). Numerous studies evidenced a reduced equator-to-pole temperature gradient during the Late Cretaceous (Hay, 2008; O'Connor et al., 2019 among others), but the presence of latitudinal variations similar to the modern ones has also been proposed (de Winter et al., 2021; Pucéat et al., 2007). A gradual warming started in the Albian and culminated during the Cretaceous Thermal Maximum (KTM) across the late Cenomanian and Early Turonian (O'Brien et al., 2017), where sea-surface temperatures (SSTs) reached ≥30 °C in the tropics and ≥20 °C in the southern mid-to-high latitudes (Friedrich et al., 2012; Huber et al., 2018; O'Brien et al., 2017; Scotese et al., 2021; Song et al., 2019b). A few studies suggested possible glacial episodes during the middle Turonian (Bornemann et al., 2008; Galeotti et al., 2009; Miller et al., 2004), but this theory has been recently questioned by high-resolution SST reconstructions showing extreme warmth during the whole Turonian even at the high latitudes (Huber et al., 2018; MacLeod et al., 2013; O'Connor et al., 2019). Concurrently, the sea level rose to its Cretaceous maximum (Haq, 2014; Miller et al., 2004), thus flooding large portions of continents created shallow water environments suitable for carbonate platform establishments (Pohl et al., 2019). The KTM was followed by a long-term gradual cooling which lasted until the Maastrichtian (Clarke and Jenkyns, 1999; Friedrich et al., 2012; O'Brien et al., 2017; O'Connor et al., 2019; Steuber et al., 2005b). Despite the Cretaceous climate is among those better studied in the geological past, mechanisms and forcing factors of heat transfer in the different ocean settings are still unclear and uncertainty still exists concerning the pole-to-equator temperature gradients.

Cretaceous paleoclimatology has been mostly based on deep-water carbonates via $\delta^{18}O$ analyses of bulk rock, and planktonic as well as benthic foraminifera (Clarke and Jenkyns, 1999; Friedrich et al., 2012; Huber et al., 2018, 2002; Petrizzo et al., 2022 among others), or using the organic geochemical paleothermometer TEX_{86} (*e.g.*, O'Brien et al., 2017; O'Connor et al., 2019). Neritic carbonate successions, despite being important archives of climate and environmental changes, have been largely overlooked thus representing a major gap in understanding the Late Cretaceous climate and biota evolution, considering the extensive presence of shallow water carbonate environments in the Late Cretaceous world.

The few studies on Cretaceous climatic reconstructions from neritic settings are based on rudist bivalves, the major calcifiers in the Late Cretaceous shallow seas, because of their compact low-Mg calcite outer shell layer and the possibility to sample intra-shell $\delta^{18}O$ variations (Steuber, 1996, Steuber et al., 2005). During the Late Cretaceous, rudist bivalves as well as other important shallow-marine calcifying organisms such as benthic foraminifera experienced episodes of demise and extinctions (Steuber, 2003; Steuber et al., 2023). It is still unclear, however, whether the temperature variations had a major role in impacting neritic faunas or acted in connection with other environmental perturbations associated with the oceanic anoxic events (OAEs; Steuber et al., 2023). Recent data suggest that the majority of the extinction events during the Phanerozoic coincided with the extreme warming or cooling phases (Song et al., 2021). Therefore, understanding seasonal temperature variability, latitudinal temperature gradients, and absolute temperatures throughout the Late Cretaceous from different areas and depositional settings is crucial. This potentially helps to elucidate the forcing mechanisms of heat transfer, ocean circulation, and the response of biota to temperature perturbations. A high-resolution intra-shell sampling of rudist shells from different locations has allowed for the estimation of seasonal variability during the Cretaceous (de Winter et al., 2021; Huck and Heimhofer, 2021; Steuber et al., 2005; Walliser and Schöne, 2020; Schmitt et al., 2022) contributing to a better understanding of the oceanic heat transfer dynamics. This research, however, focuses either on a single specimen or provides a compilation of isotopic data from rudists of different ages and locations. Thus, it does not allow a resolution high enough to assess a direct correlation between temperature changes and shallow-water biota evolution.

This study aims to provide high resolution paleotemperatures reconstruction based on $\delta^{18}O$ analysis of bulk-rock data and well-preserved rudists through the Cenomanian-Turonian shallow-water carbonates of an expanded succession cropping out in the Friuli region (Italy). Facies analyses and sedimentological observations were used to reconstruct biota evolution

and depositional settings. Biostratigraphy and isotope stratigraphy ($\delta^{13}C$ and $^{87}Sr/^{86}Sr$) allowed for building a precise chronostratigraphic framework.

Paleotemperature trends and absolute estimates were then compared with published deep-water and shallow-water data to evaluate the local vs. global signatures. Finally, the reconstructed temperatures were correlated with rudist and benthic foraminifera distribution throughout the studied interval to highlight possible causal relationships.

3.2 Geological settings

The Devetachi section is located on a road cut of the SS n. 47, which drives from Trieste to Gorizia (45.86 N, 13.57 E) and belongs to the so-called Friuli Carbonate Platform (FCP). This carbonate platform was situated at the NW corner of the larger Adriatic Carbonate Platform (AdCP), which was part of a Mesozoic peri-Adriatic Mediterranean archipelago of isolated carbonate shelves bordered by pelagic and/or hemipelagic basins. FCP borders the Belluno basin to the west and the Slovenian basin to the northeast (Sanders, 2001; Vlahović et al., 2005). Shallow-water carbonate deposits of the FCP are made of a thick rock pile of Mesozoic, Palaeocene, and breccia, and are overlain by a Middle Eocene siliciclastic succession of flysch containing, in some localities, large carbonate olistoliths (Consorti et al., 2021; Jurkovšek et al., 2016). The platform succession displays evidence of multiple subaerial short and/or longer exposures, recorded by paleokarst features, especially throughout the Mesozoic, that were driven by a combined influence of paleotectonics and eustatic oscillations (Otoničar, 2007). The geological settings is the result of the Dinaric and Alpine orogeny, starting with the Late Cretaceous fore-bulging which continued through the Palaeocene, whereas, in the Middle Eocene, the onset of foredeep settings associated with the advancement of the Dinaric chain is testified by siliciclastic rocks of the flysch succession (Otoničar, 2007). Several authors have proposed the lithostratigraphic nomenclature of the outcropping Meso-Cenozoic carbonate units (*e.g.,* Consorti et al., 2021; Cucchi et al., 1987; Jurkovšek et al., 2016; Martinis, 1962). The studied section, located near the Devetachi village, is part of the "Aurisina limestone" unit (upper Cenomanian to Lower Campanian age). In particular, the stratigraphic interval investigated in this study comprises the upper part of the "Zolla member" unit and the lower part of the "Aurisina limestone" that includes the Cenomanian-Turonian transition (Fig.1), similar to other records reported in the surroundings of the study area (Melis et al., 2000).

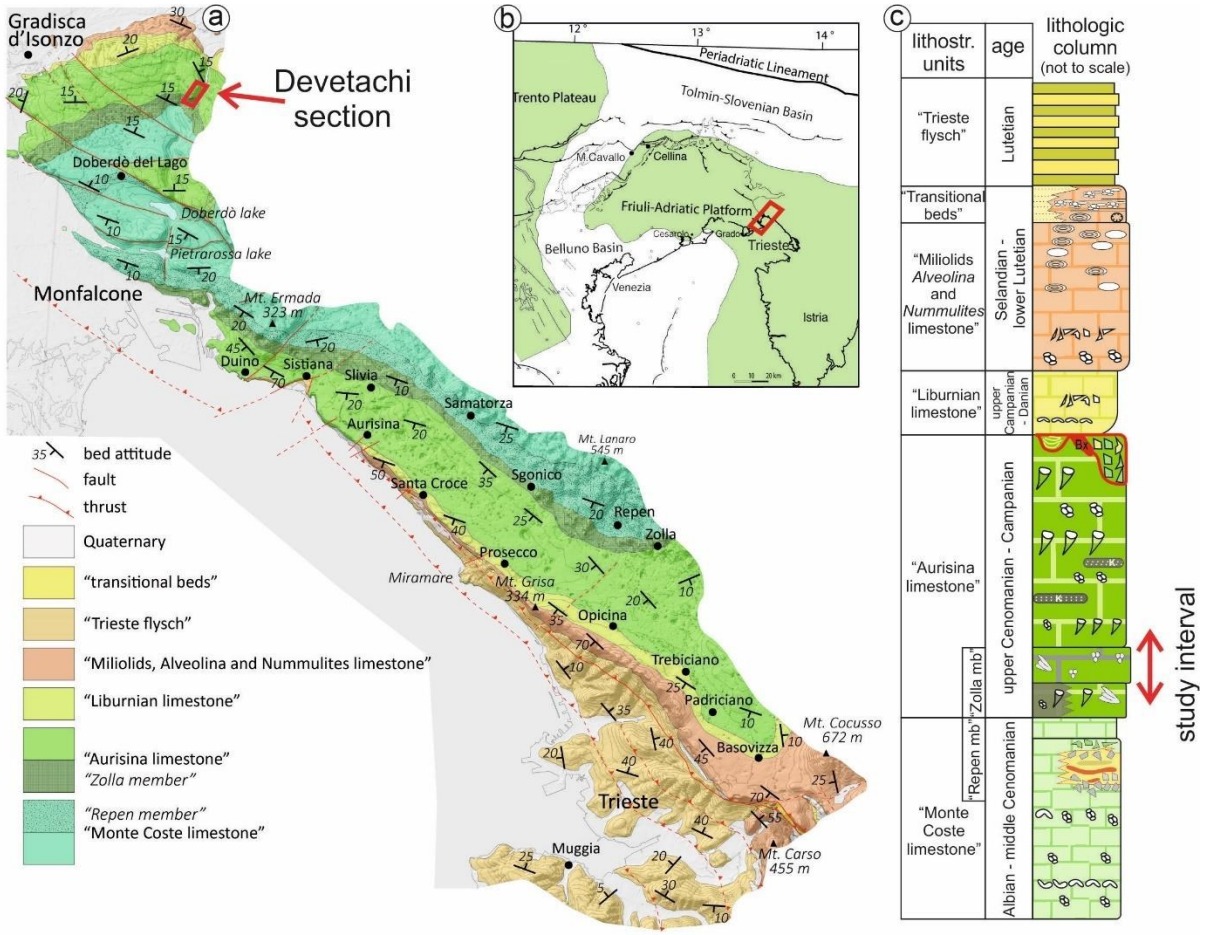

Fig.1. Location and geology of the studied area (modified from Consorti et al., 2021). **1a.** Geological map of the Italian Karst (simplified from Jurkovšek et al., 2016). **1b.** Cretaceous paleogeographic map.**1c.** Lithostratigraphic units and lithological columns of the studied area (modified from Picotti et al., 2019).

3.3 Material and methods

The studied section covers a thickness of almost 150 m of shallow water carbonates. Extensive fieldwork and close-spaced sampling (mostly up to 50 cm and not exceeding 1 m) have been performed for lithological, sedimentological, and biostratigraphic analyses and geochemical purposes. Over 100 thin sections were studied for facies analyses and biostratigraphy. All samples (bulk-rock and bivalves) were cleaned, cut, polished and microdrilled. The obtained powders were used to run stable $\delta^{13}C$ and $\delta^{18}O$ analyses (on bulk rock and shell material), and Sr-isotope analyses (on selected shells). Bulk rock powder samples were obtained by microdrilling polished rock slabs with a tungsten carbide drill bit of 0.5 mm in diameter. Shell sample powders were obtained using a drill bit of 0.3mm in diameter. Areas for drilling bulk rock material were carefully selected to collect micrite. Cement-filled cavities, veins, and areas showing diagenetic alterations were avoided. Most rudists and other bivalve shells were preserved in the form of fragments. The best-preserved shells were selected based on the

following criteria: 1. Visible growth increments, 2. compact prismatic microstructure of the outer shell layer, and 3. negligible impact of bioerosion and recrystallization. The larger radiolitid rudist fragments often preserved a cellulоprismatic structure in the outer shell layer (Pons and Vicens, 2008) which was avoided during drilling. A few *Chondrodonta* shell fragments from the lower part of the section as well as requinid rudist fragments were also sampled and analyzed. $\delta^{13}C$ and $\delta^{18}O$ analyses were performed at the Paleoclimatology and isotope stratigraphy lab of the University of Ferrara. 285 samples of bulk rock and 133 samples of rudists and 2 *Chondrodonta* fragments were analyzed using isoFLOW (Elementar©) operating in continuous flow with a PrecisION IRMS (Elementar©).

For each analysis, approximately 150 µg of homogenous powder sample was weighted into vials. Each vial was flushed with He to replace the atmospheric air in the vial with pure He. After that in each vial, the powder reacted with hot viscous water-free orthophosphoric acid for 3 h at 50 °C, triggering the release of CO_2 from the powder sample. The released CO_2 sample gas was extracted and transferred into the IRMS for the simultaneous analysis of $\delta^{13}C$ and $\delta^{18}O$. The isotope ratio was calculated using the ionOS software. For the single-point calibration, the in-house MAQ-1 standard was used. In addition, the measurement was monitored by two control standards (IAEA 603 and Carrara Marble). The external precision for the isoFLOW is 0.08 ‰. Analytical uncertainties (1 sigma) for the isotope analyses were in the order of ±0.1 ‰ for $\delta^{13}C$ and $\delta^{18}O$. The $^{13}C/^{12}C$ and $^{18}O/^{16}O$ isotopic ratios are expressed in the δ notation (in ‰ units) relative to VPDB.

22 samples of radiolitid rudists were selected for Sr-isotope stratigraphy (SIS). Their low-Mg calcite compact outer layer proved to be suitable for SIS (Frijia et al., 2015; Frijia and Parente, 2008; Steuber et al., 2005a). Samples were collected in regular spacing across the section in intervals not exceeding 20 m. The samples were selected in the field by a preliminary assessment of their preservation with a low-magnification hand lens. Laboratory preparation and further screening of the selected shell fragments followed the method described in Frijia and Parente (2008). To assess the preservation of the original shell microstructure, the samples were screened using optical microscopy. A further screening step was performed by analyzing the elemental (Mg, Sr, Mn, and Fe) composition of the shells. Strontium isotope and elemental analyses were performed at the Institute for Geology, Mineralogy, and Geophysics of Ruhr University (Bochum, Germany). After strontium separation by standard ion-exchange methods, strontium-isotope ratios were analyzed on a Finnigan MAT 262 thermal-ionization mass spectrometer and normalized to an $^{87}Sr/^{86}Sr$ value of 0.1194. The $^{87}Sr/^{86}Sr$ ratios of the

samples were adjusted to a value of 0.709175 for the USGS EN-1 standard, to be consistent with the normalization used in the compilation of the 'look-up' table of McArthur and Horwath (2020; version 6). Where more than one sample was available for one stratigraphic level, the mean value was calculated. When more than one level was sampled in a thin interval (less than 15 m), with no evidence of intervening stratigraphic gaps, the numerical age was derived from the mean value of the samples, following the approach of (Frijia et al., 2015). The precision of the $^{87}Sr/^{86}Sr$ mean values for each stratigraphic level is given as 2 s.e. of the mean when the number of samples (n) is 4. When n< 4, the precision is considered not to be better than the average precision of a single measurement (2 s.e. ±0.000007) and is calculated from the standard deviation of the mean value of the standards run with the samples (see methodology in Frijia et al., 2015). The numerical ages of the samples analyzed in this study were derived from the look-up table of McArthur and Howarth (2020, version 6), which is tied to the Geological Time Scale of Gradstein et al. (2020; herein after GTS2020). Minimum and maximum ages were obtained by combining the statistical uncertainty (2 s.e.) of the mean values of the Sr-isotope ratios of the samples with the uncertainty of the seawater curve.

For measuring the concentrations of Mg, Sr, Fe, and Mn, about 1.5 mg of the produced sample powder was dissolved in 1 ml 3 M HNO3. Subsequently, 2 ml of H_2O was added, and the samples were left to react for 24hrs before being analyzed. The elemental concentrations (Mg, Sr, Fe, Mn) were measured with an Inductively Coupled Plasma Optical Emission Spectrometer (ICP-OES, Thermo Fisher Scientific iCAP 6500 DUO).

3.4 Results

3.4.1 Facies analyses

Based on semi-quantitative petrographic analyses of thin sections evenly distributed over the studied profile, seven main lithofacies associations were identified and interpreted in terms of depositional environment (Fig.2, 3). They can all be ascribed to inner platform settings and were identified based on texture, components, and sedimentary structures.

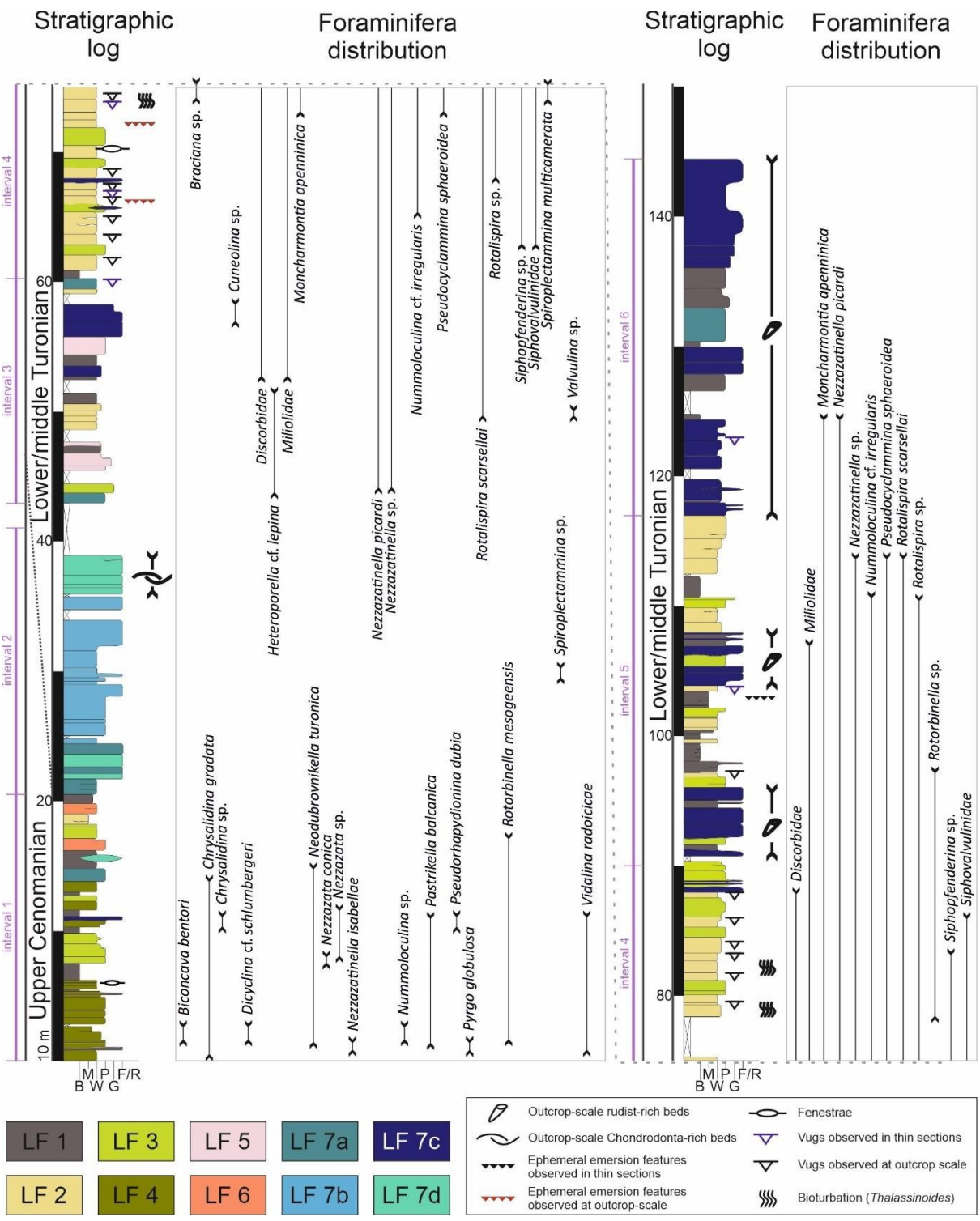

Fig.2. Lithological-sedimentological log, biostratigraphy, and chronostratigraphy of the Devetachi section. The chronostratigraphic calibration is constrained by biostratigraphy.

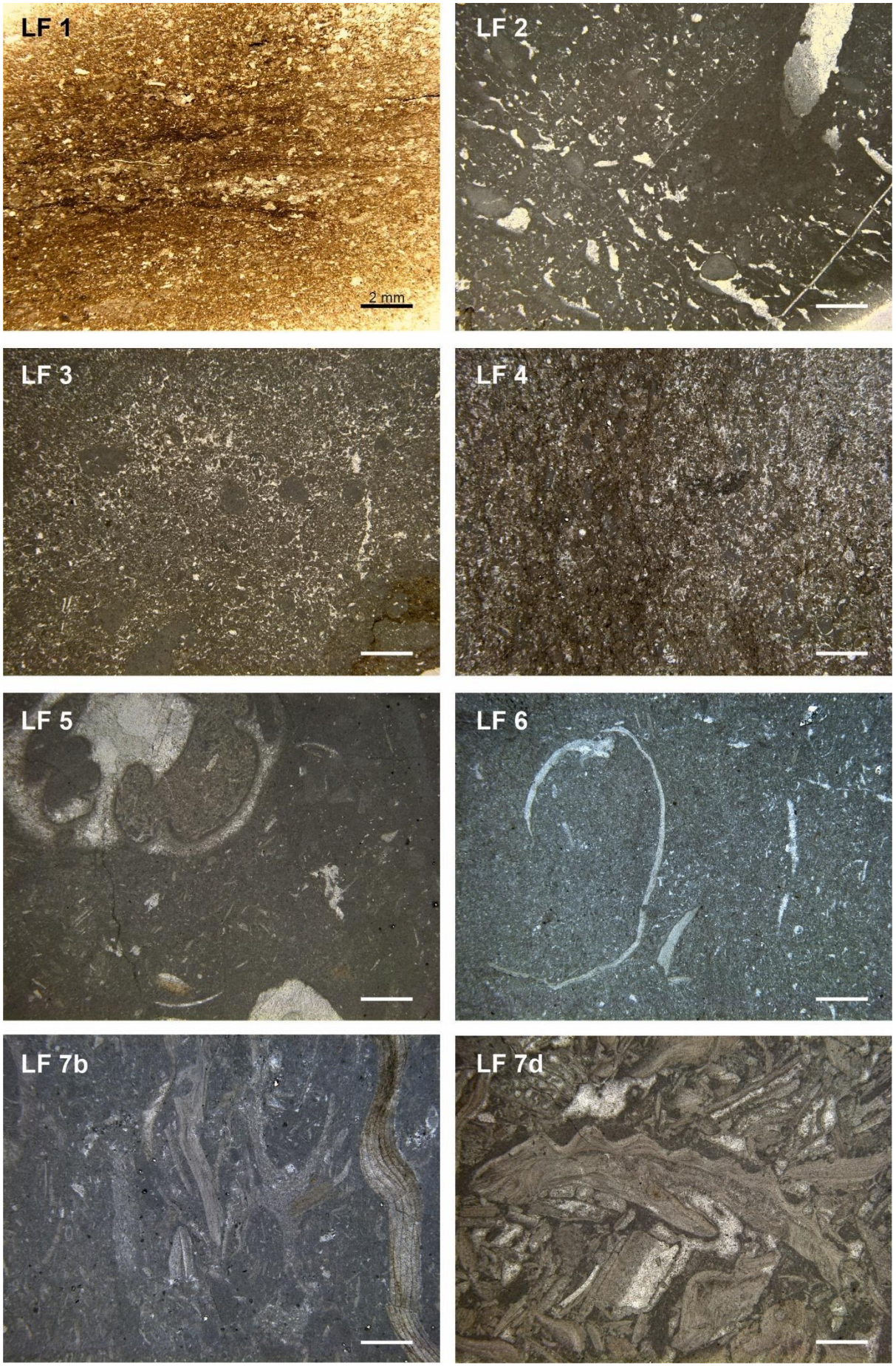
LF 1
2 mm
LF 2
LF 3
LF 4
LF 5
LF 6
LF 7b
LF 7d

Fig.3. Some representative microfacies of the studied sections. LF1 Laminated micropeloidal wackestone to bindstone; LF2 Mudstone-wackestone to packstone often with fenestrae and/or vugs; LF3 Peloidal packstone to grainstone; LF4 Foraminifera 804 wackestone-packstone with peloids: LF5 Gastropod packstone to floatstone; LF6 Microbioclastic-bivalve wackestone packstone with calcispheres; LF7b Rudist packstone-rudstone with highly fragmented, thin elongated fragments of radiolitid rudists and subordinated Chondrodonta shell fragments; LF7c Rudist wackestone to floatstone/rudstone with large shell fragments. Scale bar is 2 mm for all the photographs.

LF1- Laminated wackestone to bindstone. This facies occurs mostly in thin beds of 10 to 20cm. It is dominated by micropeloids, often organized in clots, moderate micritic intraclasts, and subordinate skeletal grains. These are composed of rare bivalve/rudists fragments, ostracods, small benthic foraminifera, gastropods. This facies is blackish in appearance and often slightly argillaceous showing faint irregular/crinkly lamination. The crinkly laminae are rich in organic matter. Occasionally, a calcimicrobial texture (*e.g.*, Schlagintweit et al., 2015) mostly with small rotaliid (including discorbids) benthic foraminifera, thin-shelled miliolids, and sparse ostracods is present. The interpreted depositional settings of this facies is a restricted intertidal to a very shallow subtidal lagoon. In the lower part of the section from 10 to 15 m calcispheres are occasionally present in this LF.

LF2- Mudstone-wackestone to packstone often with fenestrae and/or vugs. This LF is composed mainly of mudstone-wackestone textures but packstones can also be found. Micropeloids are abundant whereas the skeletal content is made by sparse ostracods, *Thaumatoporella*, small agglutinated benthic foraminifera, nubecularids, cyanobacterial filaments, and nodules. Dascycladaceans and small recrystallized bivalve fragments are occasionally found. This facies presents frequent evidence of micro dissolution with vugs (often with geopetal structures) and birds-eyes. Rarely, fenestral fabric is found. The interpreted depositional setting of this facies is restricted intertidal to a shallow subtidal lagoon.

LF3- Peloidal packstone to grainstone. This facies type is dominated by peloids, rare fragments of bivalves, small benthic foraminifera, ostracods, and *Thaumatoporella*. Rare micritic intraclasts are found and cement-filled vugs. The possible depositional setting of this facies is a shallow subtidal lagoon.

LF4- Foraminifera wackestone-packstone. The main components are represented by small and large-sized benthic foraminifera of diverse assemblages of porcelaneous, agglutinating, and rotaliid benthic foraminifera, *Thaumatoporella*, and moderate bivalve fragments (mainly

rudists) are common. Among the non-skeletal grains, peloids are abundant to common. The depositional setting of this facies was probably a more or less open subtidal lagoon.

LF5- Gastropod packstone to floatstone. Large gastropods (0.5 to a few cm) dominated these facies with subordinate green algae, peloids, and some rare fragments of rudists. This facies occurs only in a limited interval of Devetachi section between meters 40 and 60, forming ~30 cm thick beds. The depositional settings of this facies were probably similar to LF4, a subtidal lagoon.

LF6- Microbioclastic-bivalve wackestone-packstone with calcispheres. These facies are composed of microbioclastic debris, a few large and thin bivalve shells often with articulated valves and abundant small shell fragments, in place recrystallized. Calcispheres are also present together with rare small gastropods and coral fragments. The depositional setting of this facies was an open lagoon but possibly indicating a deeper environment compared to facies LF4 and 5 with low to moderate water energy.

LF7- Bivalve packstone-rudstone. This facies usually occurs in beds with thicknesses ranging from 30 cm up to 1 m. According to the texture, components, and sedimentary, it is further subdivided in:

a) Bivalve wackestone-packstone with highly fragmented small undetermined bivalve shells and echinoderm fragments.

b) Rudist packstone-rudstone with highly fragmented, thin-elongated fragments of radiolitid rudists and subordinated *Chondrodonta* shell fragments.

c) Rudist wackestone to floatstone/rudstone with large shell fragments. The texture of the matrix in the floatstones and rudstones is a packstone-grainstone made of peloids small fragments of rudists and rare foraminifers.

d) *Chondrodonta* floatstone-rudstone with subordinated rudist shells.

The depositional settings of LF7 facies was probably a subtidal open lagoon with moderate to high water energy. LF7c-d probably reflects the deposition in a slightly deeper environment than LF7a-b.

Based on the sedimentological and lithological characteristics, the section was subdivided into 6 intervals (Fig.2).

Interval 1 (0-20 m): This interval is dominated by lagoonal deposits of LF4 in the first 5 - 7 m, followed by bindstones of LF1 and peloidal packstone/grainstone of LF3, which become increasingly abundant upwards, intercalated to LF4, for the next 10 m. Two levels of LF1 with sporadic calcispheres are found from meter 10 to 15. The last 5 m of this interval represent a shift to slightly deeper conditions with the occurrence of LF7a-d and LF4. Few levels of microbioclastic-bivalve packstone with few calcispheres of LF6 are found from meter 15 to 19.

Interval 2 (20-40 m): This interval is dominated by medium (40-50cm) to thick strata (up to 80 cm) of LF7. *Chondrodonta* (LF7d) are abundant in the lower and upper part of the interval and highly fragmented rudist packstone-rudstone (LF7b) with very poorly preserved foraminifera dominating the middle part.

Interval 3 (40-60m): This interval consists of an alternation of very shallow subtidal LF1 and LF2 with the sporadic occurrence of large gastropods-dominated LF 5 at meters 46 and 55, forming beds of a maximum of 30cm. Upwards, the interval is capped by 1.5 m of thin beds of rudist LF7c.

Interval 4 (60-90m): This interval is characterized by the shallowest depositional conditions of the entire section. It is dominated by LF2 intercalated with LF3. Fenestrae, cemented vugs, and evidence of at least two emersion surfaces (at 66 and 72 m) are found in thin sections and outcrop. Bioturbation with *Thalassinoides*-like ichnofacies is found in the middle of this interval.

Interval 5 (90-117m): This interval is composed of two 10-13m thick cycles whose base is composed of medium-thickness rudists beds of LF7c passing upwards to LF1-LF2 and LF3 with evidence of ephemeral emersions represented by micro dissolutions features and cemented vugs. The occurrence of closely spaced thick-bedded rudist strata of LF7c marks the top of this interval.

Interval 6 (115-145m): The last interval is dominated by thick (up to 1 m) rudist-rich beds of LF7c. Rudist shells are mainly fragmented and with variable sizes (up to 4-7 cm). Rare complete shells were observed in the outcrop. Rudists are chaotically distributed within the beds, even in rare cases of thin intervals with shells oriented parallel to the stratification. Occasionally, on the top of LF7c, LF1 occurs.

3.4.2 Biostratigraphy

The biostratigraphic frame was approached by analyzing the vertical distribution of the benthic foraminifera identified in thin sections. The inferred age refers to published records of the peri-Mediterranean carbonate platforms (Chiocchini et al., 2012; Schroeder and Neumann, 1985; Velić, 2007) where the assemblage zones, although reliable in terms of relative occurrences, are not definitively anchored to the chronostratigraphic scale. The stratigraphic range of some of the identified taxa bears a finer constrain obtained by correlating their distribution in the section with published records calibrated with chemostratigraphic tools (Arriaga et al., 2016; Frijia et al., 2015). Moreover, this study highlights new records of benthic foraminifera that have not been reported from this stratigraphic position. The most relevant identified taxa are figured in Fig 4.

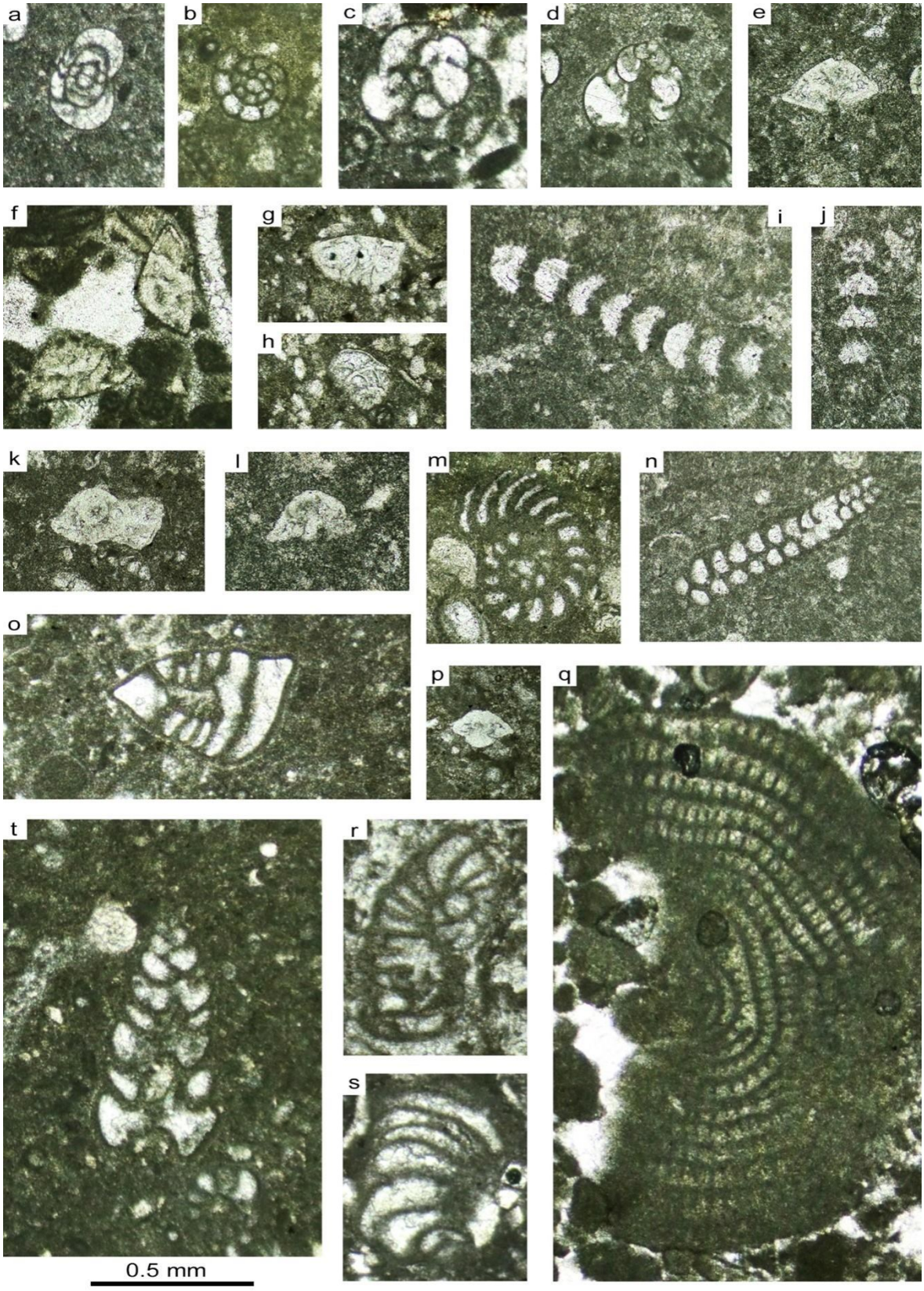

Fig.4. Selected foraminifera specimens from the Devetachi section. **a, b**) *Moncharmontia apenninica*. **c, d**) *Siphopfenderina* sp. **e, k**) *Rotalispira* sp. **f**) *Rotorbinella* sp. **g, h**) *Rotalispira scarsellai*. **i, j**) *Braciana* sp. **l**) *Rotorbinella* sp. (=*Eponides hemisphaericus* in Chiocchini et al., 2012). **m**) *Pseudocyclammina sphaeroidea*. **n**)

Spiroplectammina multicamerata. **o**) *Nezzazatinella picardi*. **p**) *Rotorbinella mesogeensis*. **q**) *Pastrikella balcanica*. **r, s**,) *Neodubrovnikella turonica*. **t**) *Valvulina* sp. Scale equals 0.5 mm for all the specimens.

The first 20 m of the section (interval 1) contain *Pastrikella balcanica* (Cherchi, Radoičić & Schroeder) *Rotorbinella mesogeensis* (Tronchetti), *Chrysalidina gradata* d'Orbigny, *Pseudorhapydionina dubia* (De Castro) and *Vidalina radoicicae (*Cherchi & Schroeder), that can be considered as a reliable proxy of the upper Cenomanian substage (Frijia et al., 2015; Schroeder and Neumann, 1985). Through this stratigraphic interval, accompanying fauna is presented by *Nummoloculina sp.*, *Nezzazata isabellae* Arnaud-Vanneau&Sliter, *Nezzazata conica* (Smout), and *Dicyclina cf. schlumbergeri* Munier-Chalmas. This interval is followed by about 25 m barren of foraminifera, where just sporadically some small miliolids and discorbidae were observed, whereas, towards the upper part, the green algae *Heteroporella cf. lepina* occurs.

A new foraminiferal assemblage starts diversifying at meter 40 (interval 3). It is composed, up to meter 90, of *Moncharmontia apenninica* (De Castro), *Braciana sp*. and *Rotalispira sp*., *Rotorbinella sp*., *Nezzazatinella sp*. (resembling *N. aegyptiaca*), *Nezzazatinella picardi* (Henson), *Siphopfenderina sp*., *Pseudocyclammina sphaeroidea* Gendrot, *Spiroplectammina multicamerata* Said & Kenawy, *Valvulina sp.*, and *Nummoloculina cf. irregularis*, along with miliolidae and discorbidae. Based on correlations with Sr-isotope stratigraphy (SIS) data from the Apennine Carbonate Platform of Arriaga et al. (2016) and Frijia et al. (2015), and the occurrence of the index assemblage *Nezzazatinella*, *M. apenninica,* and *P. sphaeroidea*, it is possible to assign this stratigraphic interval to the Lower-middle Turonian.

From meter 90 (interval 5) to the top of the section, the foraminiferal assemblage is characterized by the co-occurrence of *Nezzazatinella picardi*, *Pseudocyclammina sphaeroidea*, *Rotorbinella sp*. (very close to *Eponideshemisphaericus* in Chiocchini et al., 2012), *Rotalispira scarsellai* (Torre), *Moncharmontia apenninica* and *Nummoloculina cf. irregularis*, along with miliolidae and discorbidae. On this basis and considering both SIS and classical biostratigraphy (Arriaga et al., 2016; Chiocchini et al., 2012; Frijia et al., 2015) it was possible to place the upper part of the studied section in the middle Turonian.

Interesting stratigraphic records concern the occurrences identified in open nomenclature as *Braciana sp*. and *Siphopfenderina sp*. here found associated with Lower to mid-Turonian fauna. These taxa have been, so far, reported from younger levels of the |Lower Campanian of the Adriatic Carbonate Platform, cited as *Braciana jelaskai,* Schlagintweit and CvetkoTešović,

and *Siphopfenderina sp*., respectively (Schlagintweit and Cvetko Tešović, 2017; Schlagintweit and Septfontaine, 2022). It could be thus possible to extend the stratigraphic distribution of these two genera through the Turonian-Campanian period. Further studies could unravel their exact systematics and the relative stratigraphic range for each species.

3.4.3 Isotope analyses

Closely spaced sampling allowed for building a high-resolution $\delta^{13}C$ and $\delta^{18}O$ record both from bulk-rock and bivalve shell samples (Fig.5). The bulk-rock curve represents $\delta^{13}C$ and $\delta^{18}O$ values averaged per strata and superimposed five-points moving averages were used to remove "noises" and small wiggles.

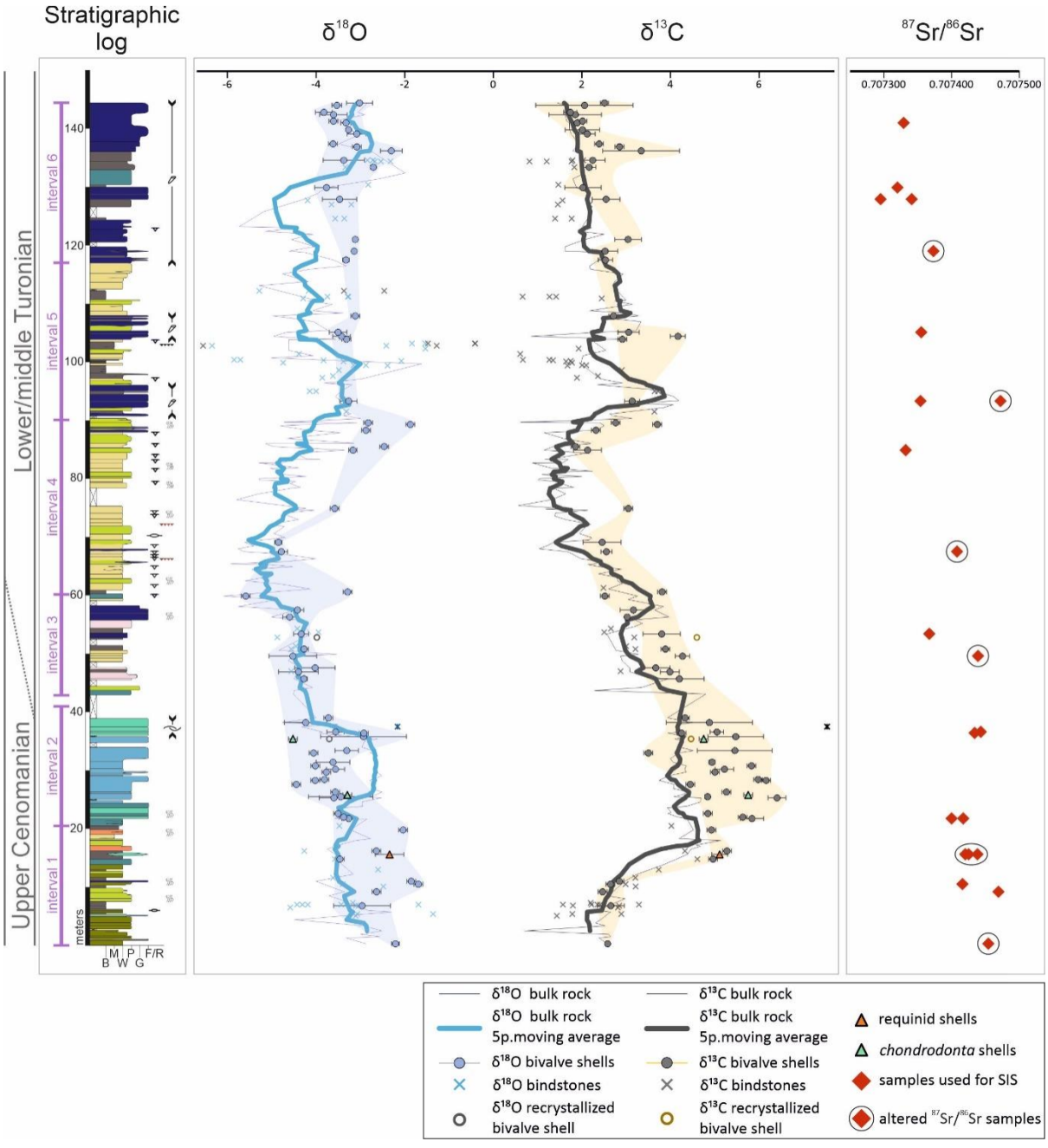

Fig.5. Geochemical results (δ18O, δ13C, 87Sr/86Sr). δ18O and δ13C bulk rock values (thin lines) and 5 points moving averages (thick lines) are marked. Bulk shell values (single points) were averaged when more specimens were analyzed from the same rock bed (error bars show the standard deviation of the average) and an envelope was drawn to highlight the secular isotopic trends. Values corresponding to LF1 are reported (crosses) but are excluded from the stable isotope curves, as well as samples from levels with evidence of emersions (see text for discussion). Shell samples with evidence of recrystallization were also excluded from the envelope of the isotopic profiles. Results of Sr-isotope analyses of all individual measured samples are reported. Altered shells are marked with a black circle. Chronostratigraphy is based on foraminifera distribution.

In both $\delta^{13}C$ and $\delta^{18}O$ records, marked negative peaks occur, corresponding to vuggy/ fenestral facies or close to emersion surfaces (Fig.5). These values were not considered in the calculation of the moving averages. Also, the laminated carbonates of LF1 were not considered for the moving average curves following results found in Frijia et al. (2019, see discussion below). The $\delta^{13}C$ averaged values of bulk rock material span from a minimum of 2.73‰ to a maximum of 5.14‰, whereas the $\delta^{18}O$ values span from a minimum of -6.09‰ to a maximum of -1.62‰. The shell values were obtained mainly from well-preserved fragments of radiolitid rudists, with one level containing requinid rudists, and two levels of *Chondrodonta* shell fragments. The $\delta^{13}C$ shell values span from 1.28‰ to 6.55‰, and in $\delta^{18}O$ from -5.59‰ to a maximum of -1.69‰. The resulting secular trends of bulk rock and shell material $\delta^{13}C$ and $\delta^{18}O$ are impressively similar with shell fragments generally yielding slightly more positive $\delta^{13}C$ and $\delta^{18}O$ values.

At the base of the section (intervals1 and 2), the smoothed bulk-rock $\delta^{13}C$ isotope curve (Fig.5, thick grey line) shows a pronounced positive excursion starting around meter 13 where values of 2 ‰ increase rapidly to a maximum value of 4.64 ‰ above meter 20. At this level, the $\delta^{13}C$ in the shells records a maximum value of 6.40 ‰. For the following 20 m, the $\delta^{13}C$ shows the highest values of the whole section, which stays around 4.2 ‰ for bulk rock and ranges from 3.50 ‰ to 6.40 ‰ for the shells. From meter 40 to 90 (intervals 3 and 4), the carbon isotope profiles present a regular decrease, with superimposed minor positive fluctuations (slightly less than 1 ‰), reaching a minimum of 0.8 ‰ just below the base of interval 5 where the onset of rudist-rich facies LF7c occurs. Continuing upwards, in the first meters of interval 5, the $\delta^{13}C$ curve increases rapidly, making a positive peak of 4 ‰ at 95 m. After this point, the isotopic profile is characterized by a regular and limited decrease of the values until the top of the section with the minim values of 1.45 ‰ in the bulk curve with some minor superimposed positive fluctuations.

The $\delta^{18}O$ profile of both bulk and shells shows a general decreasing trend from the base of the section where values around -2.5 ‰ are found, to the minimum of the whole section between 60 and 70 meters (interval 4) represented by values around -5.5 ‰. This general trend is interrupted by a positive fluctuation in interval 2 which is evident in the bulk rock curve whereas it appears less pronounced in the shell isotopic record. A gradual increase follows until meter 100 before a slightly negative trend (more pronounced in the bulk rock than in the shell isotopic trend) occurs from meter 110 to 130. From meter 130 to the top of the section, the values rise until around -3 ‰ and they stay constant.

3.4.4 Sr-isotope stratigraphy (SIS)

22 samples of rudist shell fragments were selected, throughout the section, from 15 stratigraphic intervals and measured for $^{87}Sr/^{86}Sr$ (Fig.5; Tab.1). Several studies have shown that the low-Mg calcite rudist shells are among the material most suitable for SIS (Frijia et al., 2015 and references therein). The analyzed rudist samples show excellent preservation of the original prismatic microstructure (Fig.6). To obtain further insight into the diagenetic processes, concentrations of major and trace elements (Sr, Mg, Fe, and Mn) were measured (Fig.7). A threshold for Sr content of 800 ppm for well-preserved rudist shells (Frijia et al., 2015; Huck and Heimhofer, 2015; Steuber, 2003, 1999; Steuber et al., 2005b) was used to determine samples preservation. Four samples having Sr content below 800 ppm were excluded from further $^{87}Sr/^{86}Sr$-based age calculations. Considering the very consistent and low concentration of Mn (>8 ppm) and Fe (>25 ppm) in all analyzed samples (well below a limit of 50 and 300 ppm reported for diagenetic biotic carbonates for Mn and Fe respectively; see Frijia et al., 2015 and reference therein), one sample with Fe content of ~60 ppm was also considered altered and not used in further interpretations despite its Sr content.

Tab.1. Results of the strontium isotope, elemental, and stable isotope analyses. Age was calculated for the well-preserved samples, using the 'look-up' table of McArthur and Horwath (2020; version 6).

	Analyses						Age			Elemental analyses				Stable isotope analyses	
Meters from the base	$^{87}Sr/^{86}Sr$ measured	± 2 s mean	87Sr/86Sr corrected	Preservation	87Sr/86Sr mean	± 2 s mean	Min. [Ma]	Preferred [Ma]	Max. [Ma]	Mg [ppm]	Sr [ppm]	Fe [ppm]	Mn [ppm]	$\delta^{18}O$ [‰ VPDB]	$\delta^{13}C$ [‰ VPDB]
0.3	0.707455	0.000005	0.707454	altered	0.707454	0.000018				2152	313	9.315	1.68	-2.27	2.59
9.2	0.707496	0.000006	0.707469	altered	0.707469	0.000018				3399	885.9	n.d.	3.46	-2.64	2.47
10.5	0.707423	0.000005	0.707416	preserved; CTBE	0.707416	0.000018				n.d.	n.d.	n.d.	n.d.	-1.69	2.64
15.6	0.707439	0.000005	0.707438	altered; CTBE						1546	572.1	11.32	6.27	-2.52	5.02
15.6	0.707426	0.000005	0.707425	altered; CTBE						1771	655.1	7.336	5.76	-2.68	5.02
15.6	0.707427	0.000005	0.707420	altered; CTBE	0.707428	0.000013				1433	628.3	7.988	6.54	-2.21	5.38
21.75	0.707401	0.000005	0.707400	preserved; CTBE						1775	982.6	6.725	0.323	-3.17	5.55
21.75	0.707418	0.000005	0.707417	preserved; CTBE	0.707417	0.000017				1905	921.3	0.084	0.18	-3.44	6.07
36.4	0.707435	0.000007	0.707434	altered; CTBE						3437	982.3	12.68	1.1	-2.92	4.25
36.6	0.707444	0.000007	0.707443	altered; CTBE	0.707439	0.000009				2310	1233	5.163	0.681	-3.43	4.94
49.6	0.707440	0.000006	0.707439	altered	0.707448	0.000018				2759	1304	n.d.	1.44	-4.90	4.39
53.4	0.707370	0.000005	0.707367	**preserved**	0.707367	0.000018	93.06	**93.803**	94.65	3113	1148	3.19	0.744	-4.22	4.10
67.5	0.707411	0.000005	0.707408	altered	0.707419	0.000018				2686	1077	1.829	0.219	-4.89	2.46
84.9	0.707339	0.000005	0.707332	**preserved**	0.707332	0.000018	91.92	**92.700**	93.45	3391	901.9	21.23	0.959	-3.18	2.13
93.3	0.707499	0.000006	0.707472	altered	0.707472	0.000018				2733	987	58.31	2.21	-3.18	2.99
93.3	0.707357	0.000005	0.707354	**preserved**						3051	1048	2.148	0.74	-3.13	3.08
105.1	0.707358	0.000005	0.707355	**preserved**	0.707355	0.000001	93.21	**93.420**	93.65	2267	924.3	11.27	2.03	-3.36	2.89
119	0.707381	0.000004	0.707373	altered	0.707389	0.000018				1828	959.9	2.321	0.796	-3.15	2.45
127.9	0.707353	0.000005	0.707341	**preserved**						1078	1054	0.882	0.247	-2.99	2.41
127.9	0.707322	0.000005	0.707295	**preserved**						1657	1092	1.374	0.272	-3.71	2.99
129.9	0.707322	0.000004	0.707320	**preserved**	0.707319	0.000033	na	**92.285**	93.49	1424	1071	1.613	0.779	-3.95	2.31
141	0.707336	0.000005	0.707329	**preserved**	0.707329	0.000018	91.78	**92.604**	93.35	n.d.	n.d.	n.d.	n.d.	-3.28	2.01

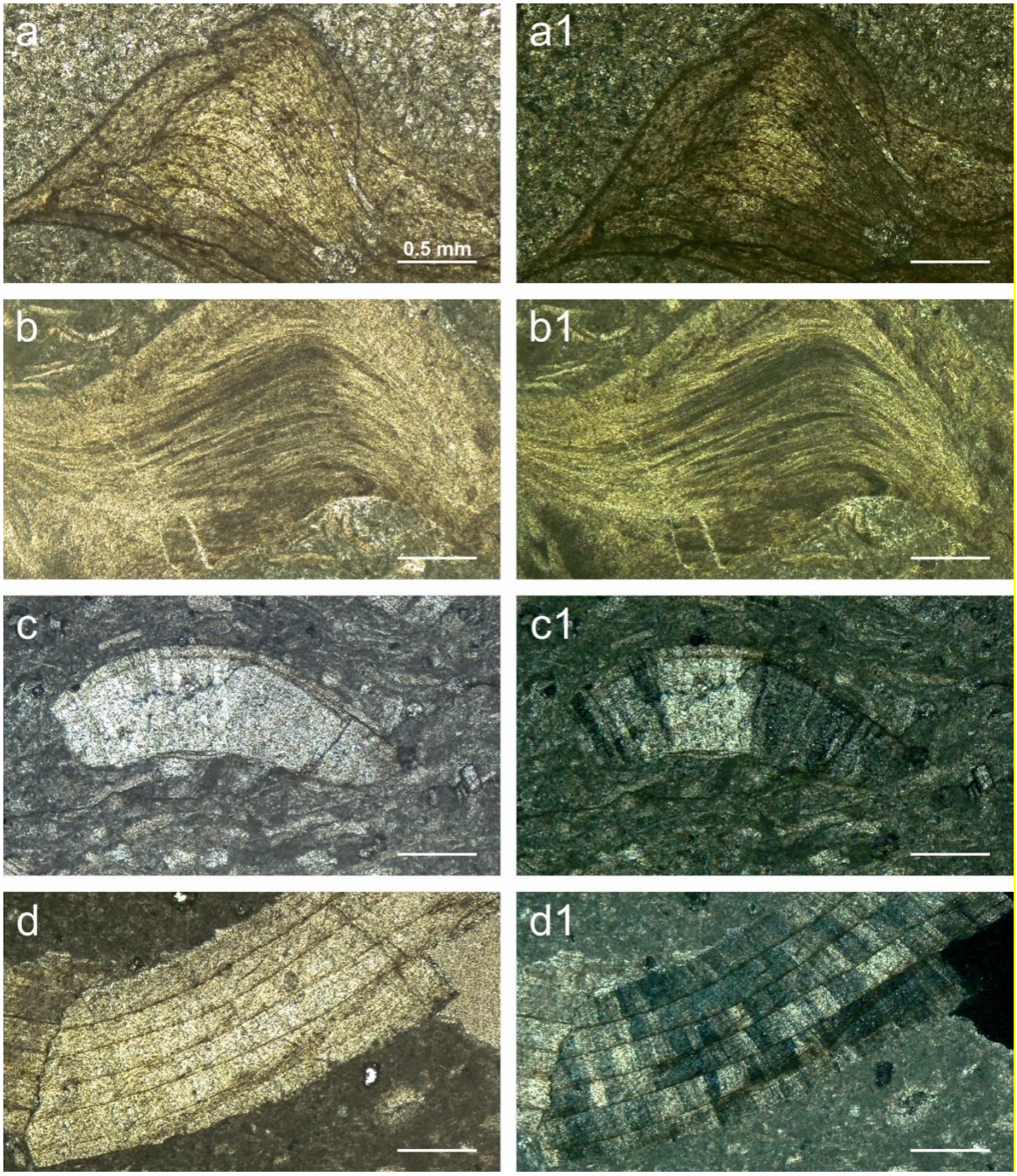

Fig.6. thin sections of rudist shells and chondrodonta. **a-b** well cross foliated microstructure of chondrodonta shell (**a1-b1** cross-polarized light); **c-d** compact portion of the outer shell layer of two different radiolitid shells. Figure **c1** (cross-polarized light) show slight recrystallization of the prismatic microstructure, figure **d1** shows well preserved prismatic structure and growth lines. Scale bars equal 0.5 mm.

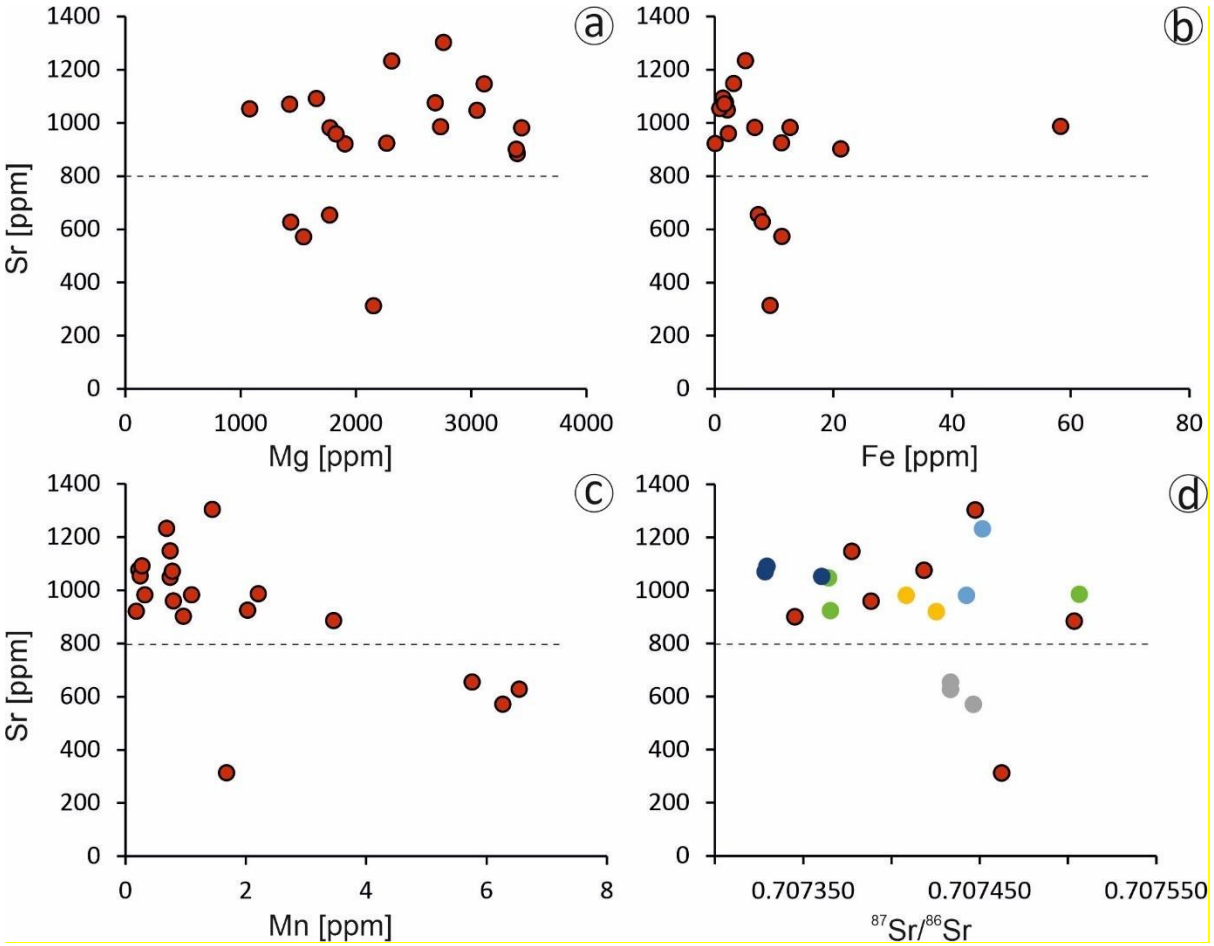

Fig.7. Cross-plots of Mg, Fe, and Mn. Vs Sr concentrations and Sr vs. $^{87}Sr/^{86}Sr$. The dashed horizontal line indicates the threshold Sr concentration (800 ppm) used in this study after Steuber et al (2005b) and Frijia et al. (2015). Above this value, it is assumed that the original marine Sr-isotopic ratio has been retained (see text for further details). Note that most of the rudist samples analysed for this study have very low Fe and Mn concentrations except for one sample with a Fe concentration of 58 ppm, which was excluded from Sr-isotope stratigraphy (see text for details). The cross-plot of Sr concentrations vs $^{87}Sr/^{86}Sr$ (**d**) shows single measurements for bed in red, and multiple samples from the same bed in colors (same color = same bed).

Furthermore, 3 samples were excluded from the SIS database as their isotopic $^{87}Sr/^{86}Sr$ values are more radiogenic than samples from the nearby interval, considering that diagenesis usually rises $^{87}Sr/^{86}Sr$ signal (Boix et al., 2011; McArthur, 1994, p. 19). Furthermore, the $^{87}Sr/^{86}Sr$ values of these samples are inconsistent with their stratigraphic position considering the profile of the Sr-isotopes reference curve in the late Cenomanian-late Turonian interval (see below, McArthur and Horwath, 2020).

Among the samples selected for SIS, the highest Sr isotope values are found in the lower part of the section (intervals1 and 2; upper Cenomanian) where they range from 0.707416 to 0.707417. Until the top of the section, the following samples show a regular decrease of the

Sr- isotopic values until a minimum of 0.707319 is reached (interval 6). This trend mirrors the descending branch of Sr-isotope values, which characterizes the late Cenomanian-late Turonian interval of the global marine Sr-isotope secular curve (McArthur and Horwath, 2020). Interestingly, the Sr-isotope values from the lower part of the Devetachi section (interval 1-2) are comparable to those found in the upper Cenomanian shallow-water carbonates of the Apennine Carbonate Platform from Frijia and Parente (2008). As highlighted by these authors, the lack of correspondence between the Sr-isotopic record across the late Cenomanian and the modeled Sr-isotopes reference curve hampers the use of SIS for this stratigraphic interval (Frijia and Parente, 2008). Therefore, we did not attempt to translate the $^{87}Sr/^{86}Sr$ values from the lower part of the Devetachi section in numerical ages. The calculated SIS ages from the selected post-Cenomanian beds are reported in Tab. 1 and discussed in the next paragraphs together with the $\delta^{13}C$-isotope stratigraphy.

3.5 Discussion

3.5.1 Reliability of $\delta^{13}C$ and $\delta^{18}O$ geochemistry

The $\delta^{13}C$ and $\delta^{18}O$ composition of shallow-water carbonates is known to be potentially affected by syn- and post-depositional diagenetic alteration (Marshall, 1992), biological fractionation, and local environmental processes which can cause the isotopic signal to deviate from the global open ocean value (Del Viscio et al., 2022 and references therein). The positive covariance between $\delta^{13}C$ and $\delta^{18}O$ bulk rock values enables inferring the diagenetic alteration due to the meteoric water influx in the mixing zone (Allan and Matthews, 1982) as well as decreasing alteration in the freshwater phreatic zone (Swart and Oehlert, 2018). Although the lack of covariance between $\delta^{13}C$ and $\delta^{18}O$ alone has been proposed as indicative of the unaltered nature of the isotopic signal (Grotzinger et al., 2011), recent studies point out that changes in the sediment source through time can also produce paired shifts in $\delta^{13}C$ and $\delta^{18}O$ values (Oehlert and Swart, 2019; Swart and Oehlert, 2018).

In the Devetachi section, cross-plots of $\delta^{13}C$ and $\delta^{18}O$ for single facies show that they plot within the field of Cretaceous well-preserved low-latitude biotic calcite (after Veizer and Prokoph, 2015; Fig.8a), apart from the LFs 6, 7b, and 7d that show higher $\delta^{13}C$ values. These LFs are composed of abundant bivalve shell material (mainly rudists) and, possibly, their high values correspond to the wide range of variability of C-isotopes in mollusk shells, due to the metabolic activity (Walliser and Schöne, 2020) and their response to perturbed C-cycle associated to Oceanic Anoxic Event 2 (see next paragraph).

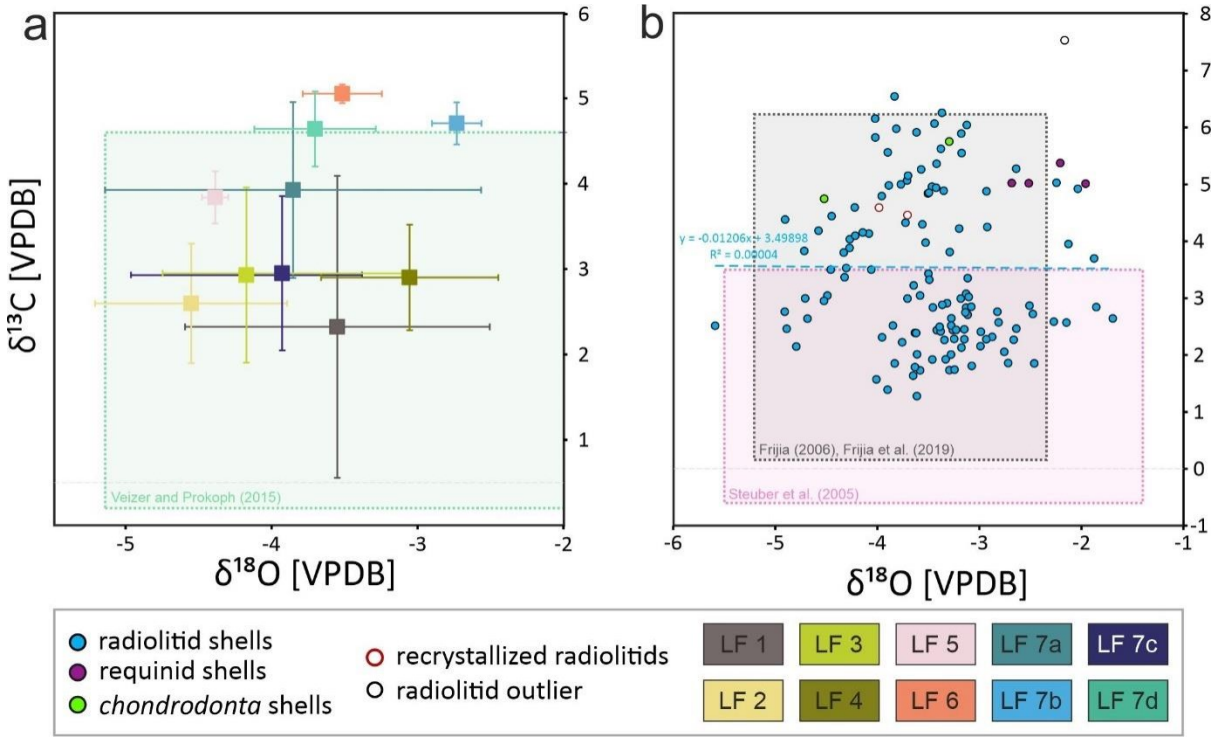

Fig.8. Cross-plot of $\delta^{18}O$ vs $\delta^{13}C$ values for the studied section. **a.** Average $\delta^{18}O$ and $\delta^{13}C$ of individual lithofacies (error bars indicate the standard deviation of the averages). The rectangle represents the well-preserved biotic calcite of shallow marine tropical-subtropical carbonates (after Veizer and Prokoph, 2015; in green); **b.** Individual bivalves (rudists and *Chondrodonta*) $\delta^{18}O$ vs $\delta^{13}C$. Note the lack of covariance between $\delta^{18}O$ and $\delta^{13}C$. Analysed bivalves plot in the field of well-preserved Late Cretaceous rudists (Steuber et al., 2005a; in pink), and well-preserved late Cenomanian-Campanian radiolitids (Frijia, 2006; Frijia et al.,2019; in black).

The most depleted $\delta^{13}C$ and $\delta^{18}O$ values (Fig.8a) are found in LF1 and LF2. These laminated carbonates of LF1 are likely of a bacterial origin/influence, and do not preserve the original isotopic signature of the seawater due to their metabolic processes as shown for similar facies by Frijia et al. (2019) in the Apennine Carbonate Platform.

LF2 shows values depleted in $\delta^{13}C$ and $\delta^{18}O$ (Fig.8a). This lithofacies contains some spar-filled fenestrae and vugs, indicating deposition in an intertidal-restricted environment that was possibly subject to short-lasting subaerial exposure episodes. Despite this possible slight meteoric alteration, the $\delta^{13}C$ and $\delta^{18}O$ values are not uniformly low in this lithofacies but rather show scattered values (see Fig.5 and 8a). Lithofacies representing shallow subtidal-restricted lagoonal conditions are, in general, those showing relatively lowest $\delta^{13}C$ and $\delta^{18}O$ values (see above). Nevertheless, they fall well within the field of values of well-preserved biotic calcite of shallow marine tropical-subtropical carbonates (after Veizer and Prokoph, 2015). Finally, the inverted "J" stable isotope pattern, typical of carbonates affected by meteoric diagenesis

(Allan and Matthews, 1982; Lohmann, 1988) is not present in the analyzed samples dataset, indicating that the isotope patterns did not suffer from significant meteoric alteration.

The reliability of the bulk rock isotopic curves can be strengthened by their comparison to the shell isotopic profile. Well-preserved rudist shells are considered to record the $\delta^{13}C$ and $\delta^{18}O$ of the water they grew in. There is a consensus that fractionation for $\delta^{18}O$ occurs in equilibrium with the fluid, whereas a more variable $\delta^{13}C$ signal can be found, due to metabolic processes (Steuber, 1999; Walliser and Schöne, 2020).

Nonetheless, we consider the radiolitid shell isotopic record presented in this study to reflect the original isotopic composition of the seawater, considering that: 1) radiolitids proved to precipitate their shells in equilibrium with sea-water $\delta^{13}C$ and $\delta^{18}O$ (Schmitt et al., 2022), 2) the isotopic values of the radiolitid shells in this study are comparable with the data of (Frijia, 2006; Frijia et al., 2019) for the Late Cenomanian-Campanian interval of the Apennine Carbonate Platform (Fig.8b) and with the $\delta^{18}O$ composition of well-preserved Late Cretaceous rudists of Steuber et al., (2005b) 3) The analyzed radiolitids show very good preservation of their prismatic outer shell layer (Fig.6).

The close resemblance of bulk rock $\delta^{13}C$ and $\delta^{18}O$ profiles with the shell $\delta^{13}C$ and $\delta^{18}O$ profiles suggests good preservation of the original marine isotopic signal in the bulk rock material. These last findings are impressive, considering that the oxygen isotopic records in shallow marine carbonates are easily altered by diagenetic processes (Marshall, 1992).

3.5.2 Chemostratigraphy ($\delta^{13}C$, $^{87}Sr/^{86}Sr$)

A correlation among the major features of the carbon-isotope profile from the Devetachi section, the Late Cretaceous marine $\delta^{13}C$ reference curve (Cramer and Jarvis, 2020), and a Turonian pelagic carbon-isotope curve of Jarvis et al. (2015) from the Bohemian Cretaceous Basin is shown in Fig.9.

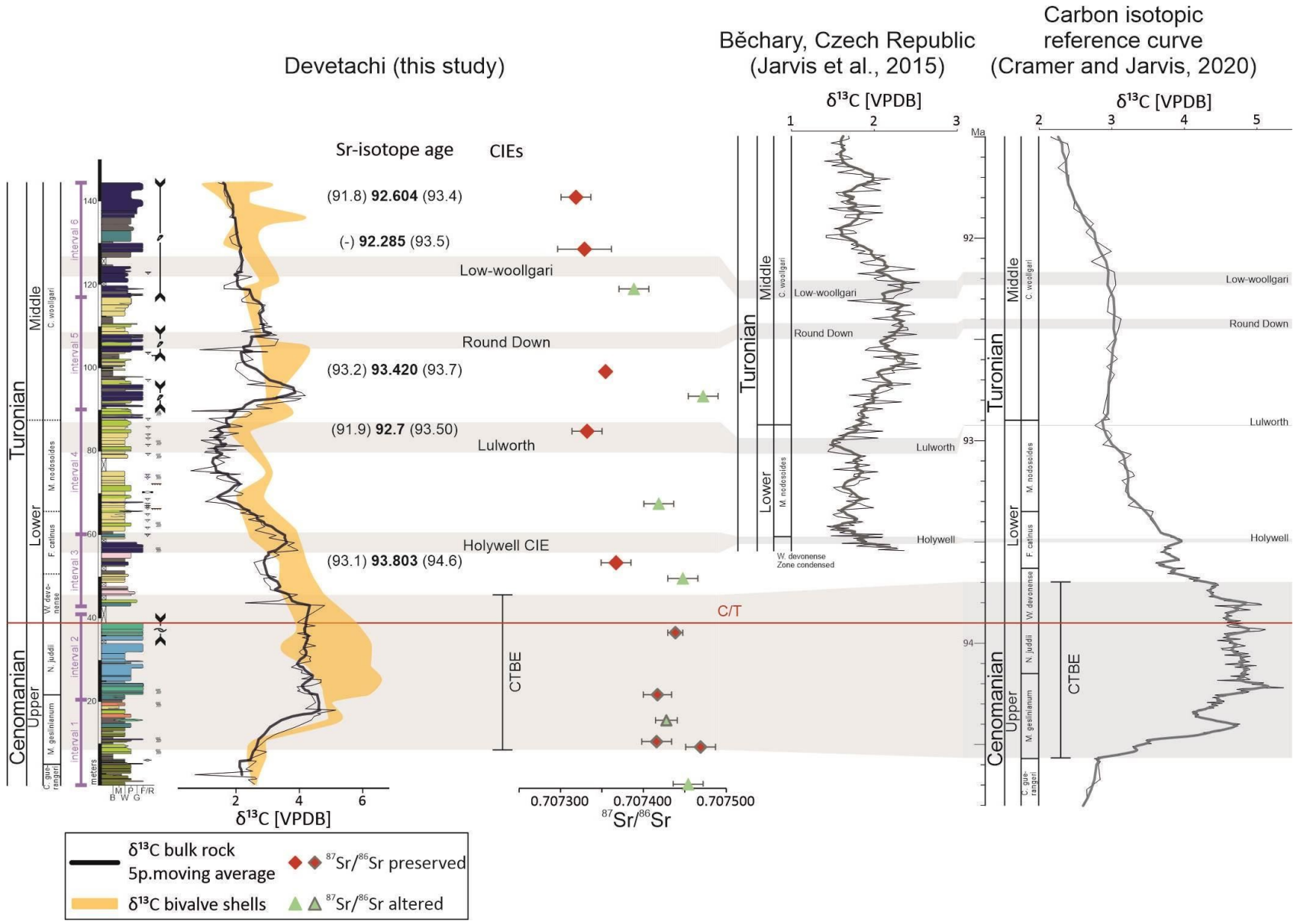
Devetachi (this study)
Sr-isotope age
CIEs
(91.8) 92.604 (93.4)
(-) 92.285 (93.5)
Low-woollgari
Round Down
(93.2) 93.420 (93.7)
(91.9) 92.7 (93.50)
Lulworth
Holywell CIE
(93.1) 93.803 (94.6)
C/T
CTBE
Turonian
Cenomanian
Middle
Lower
Upper
C. woollgari
M. nodosoides
F. catinus
W. devonense
N. juddii
M. gesninianum
C. guerangeri
interval 1
interval 2
interval 3
interval 4
interval 5
interval 6
meters
δ13C [VPDB]
87Sr/86Sr
0.707300
0.707400
0.707500
Běchary, Czech Republic
(Jarvis et al., 2015)
W. devonense Zone condensed
Carbon isotopic
reference curve
(Cramer and Jarvis, 2020)
Ma
92
93
94
δ13C bulk rock
5p.moving average
δ13C bivalve shells
87Sr/86Sr preserved
87Sr/86Sr altered

Fig.9. C and Sr-isotope stratigraphy (SIS) of Devetachi section. C-isotope correlation of the studied section from the Friuli Carbonate Platform with the Late Cretaceous C-isotope reference curve of the English Chalk (Cramer and Jarvis, 2020) and the Turonian carbon isotope profile of the Bohemian Cretaceous Basin (Jarvis et al., 2015). Black bold numbers next to the Devetachi C-isotope curves indicate the preferred SIS age, whereas the numbers in brackets refer to the upper and lower age limits (see text for details). Chronostratigraphy of Devetachi section is now constrained by chemostratigraphy correlations and dating.

The reference curve of Cramer and Jarvis (2020) shows a very prominent positive carbon-isotope excursion (CIE) of about 3 ‰ at the Cenomanian-Turonian boundary event (CTBE) interval (Fig.9), corresponding to the Oceanic Anoxic Event 2 (OAE2, Bonarelli event, Paul et al., 1999; Tsikos et al., 2004). The following positive CIEs are short-lasting and smaller in amplitude, occurring during the early (Holywell event) and middle Turonian (Round Down and Low-woollgari events). Matching of the Devetachi carbon-isotope curve with the reference/pelagic records was constrained by cross-correlating the CIEs and by independent tie-points, derived from biostratigraphy and SIS. The very prominent $\delta^{13}C$ positive excursion beginning right below meter 10 in the Devetachi section, reaching values of 4 to 6 ‰, can be correlated with the CTBE in the reference curve. The SIS data further support this correlation. In Devetachi, the Sr-isotopic values measured within the CTBE interval are comparable to those reported by Frijia and Parente (2008, set 1 to 3) across the CTBE in the Apennine Carbonate Platform. Above the CTBE, the $\delta^{13}C$ curve in Devetachi shows a descending trend similar to the reference curve of Cramer and Jarvis (2020), interrupted by a positive $\delta^{13}C$ fluctuation at around 60 m which correlates with the Early Turonian Holywell event (Fig.9). This correlation is also strengthened by SIS which gives the age of 93.80 Ma (from a level ~12 m below the Holywell event), corresponding to the base of the Lower Turonian (Gradstein et al., 2020). The next match between the $\delta^{13}C$ curve in the Devetachi and the reference/pelagic sections is at around meter 80, where the curve reaches its minimum values. This interval can be correlated with the Early/middle Turonian Lulworth event negative CIE; a correlation reinforced by the SIS ages (Tab.1 and Fig.9) and by biostratigraphy. The first occurrences (FO) of the benthic foraminifera *M. apenninica* and *P. sphaeroidea* (FO of which is in the upper part of the Early Turonian according to Frijia et al., 2015; Arriaga et al., 2016) a few meters below the CIE supports the position of Lulworth event CIE in the Devetachi section. Following upwards in the Devetachi carbon-isotope curve, the Round Down event can be tentatively identified between meters 90 and 105, where the isotopic profile registers a positive fluctuation of up to 1 ‰.

The last identified CIE in the Devetachi section, placed between meters 120 and 130, is correlated to the middle Turonian Low-woollgari event. SIS from levels a few meters above gives an age interval of 92.3-92.6 Ma, corresponding to the middle Turonian (Gradstein et al., 2020). Above this event, the carbon-isotope correlation becomes more problematic, nevertheless, the SIS data suggest that the top of the section is not younger than the middle Turonian (Fig.9).

3.5.3 Oxygen isotopes and $\delta^{18}O$ paleothermometry

Water temperatures and climatic fluctuations of ancient waterbodies can be reconstructed using $\delta^{18}O$ in biotic carbonates if the organism produces its mineralized parts in isotopic equilibrium with the surrounding water (Epstein et al., 1953). The studies of the Late Cretaceous sea surface temperatures (SSTs) generally rely on $\delta^{18}O$ analyses of planktonic foraminifera (Friedrich et al., 2012; Huber et al., 2018; MacLeod et al., 2013), whereas shallow-water carbonates are seldom considered because of often less continuous sedimentary record and potential impact of local environmental conditions and diagenesis on the isotopic values (Marshall, 1992; Schmitt et al., 2022). However, the results from the Devetachi section suggest that this section preserves a fairly complete isotopic record across the upper Cenomanian-middle Turonian and that the $\delta^{18}O$ signal (in both, the bulk rock and shell fragments) has not been markedly altered.

A comparison of the Devetachi $\delta^{18}O$ record with pelagic sections from two sections (Běchary, Czech Republic (Jarvis et al., 2015), and Kent, UK (Jenkyns et al., 1994; Fig.10)), shows remarkable similarities. A warming trend highlighted by a gradual decrease of the $\delta^{18}O$ values is visible, in the Devetachi section, from the upper Cenomanian to the Lower Turonian, just below the base of the *M. nodosoides* ammonite zone where minimum $\delta^{18}O$ values (the warmest interval) occur (Fig.10, marked in red). This $\delta^{18}O$ minimum is well-visible in the Kent section within the same stratigraphic interval.

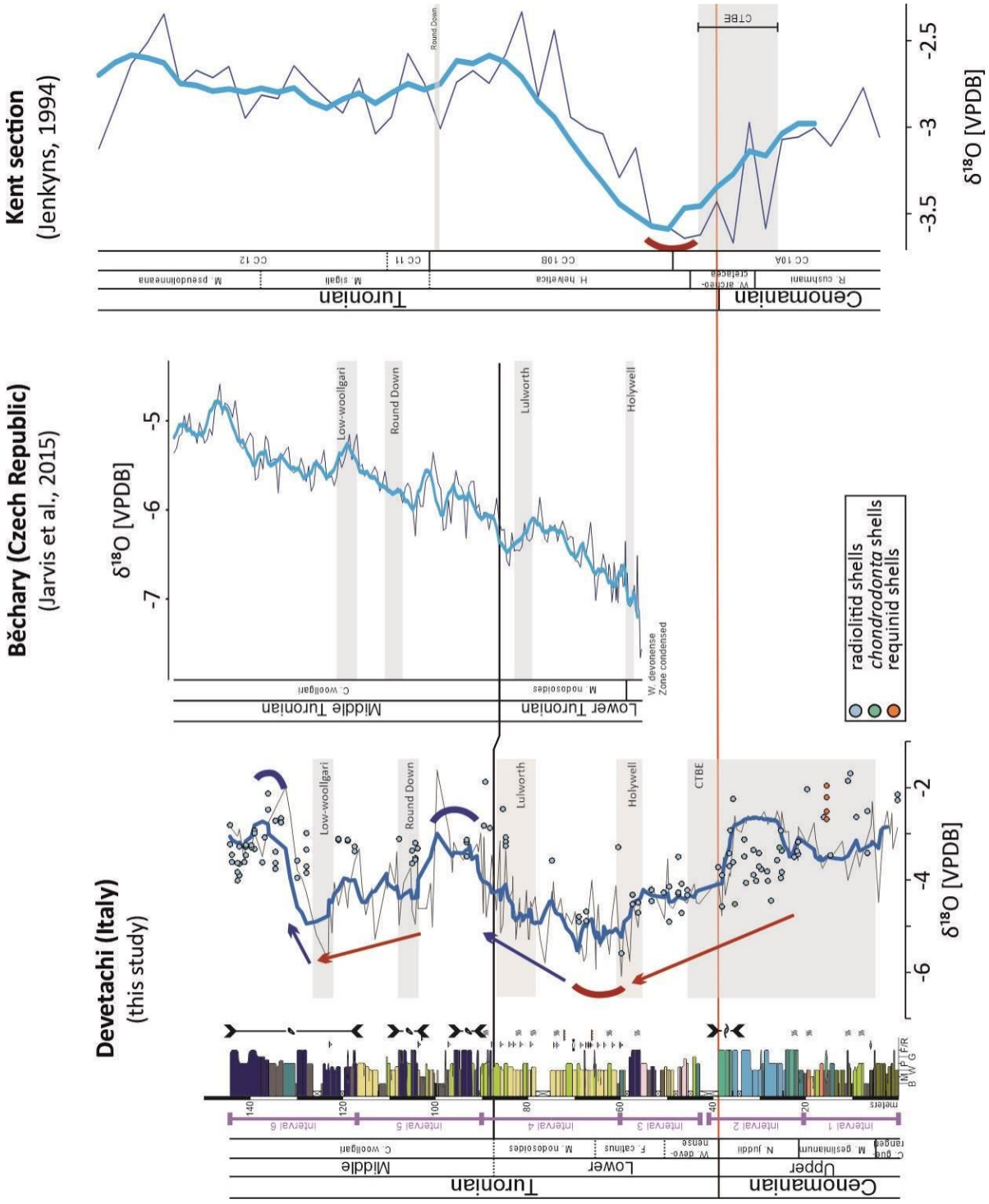

Fig.10. Correlation of Devetachi $\delta^{18}O$ curve with $\delta^{18}O$ profiles of pelagic sections from Běchary (Jarvis et al., 2015), and Kent sections (Jenkyns et al., 1994). Stratigraphic correlations are made according to the chronostratigraphy framework developed in the Devetachi section, and C-isotopes correlations among the three sections. Carbon isotopic Events (CIEs) are after the reference curve of Cramer and Jarvis (2020). Note the warmest phase in the Lower Turonian followed by a general cooling trend.

After that minimum, all curves show a gradual increase which testifies to a cooling trend, although interrupted by a few intervals of sharp and short fluctuations toward negative $\delta^{18}O$ values that could be indicative of warming phases (warmth events are well visible in the data of Jarvis et al., 2015, Fig.10). A recent exhaustive compilation of Late Cretaceous SSTs using $\delta^{18}O$ in foraminifera and Tex_{86} data indicates the late Cenomanian-Turonian interval as the warmest time of the whole Cretaceous (O'Brien et al., 2017), followed by regular cooling. Climate reconstructions of the Cretaceous super-greenhouse suggest the most pronounced warming (KTM) at the Cenomanian-Turonian interval (O'Brien et al., 2017 and references therein; O'Connor et al., 2019). The recent data compilations of Huber et al. (2018) and O'Brien et al. (2017) indicate the peak warmth in the Early Turonian. This is in accordance with the bulk rock and shell data from the Devetachi section. The temperature trend of the Devetachi section comparable to the global temperature evolution suggests an important impact of global water circulation and heat transfer, across oceans and neritic-closed oceanic settings, likely influencing the shallow marine environment more than local environmental processes.

Absolute paleotemperatures in the Devetachi section have been estimated using the high-resolution $\delta^{18}O$ record obtained from the shell fragments of radiolitid rudists and a few other bivalves. Rudists are considered a suitable shallow marine neritic SST archive (Huck and Heimhofer, 2021; Schmitt et al., 2022; Steuber, 1996; Steuber et al., 2005b). Detailed analyses of sclerochornological profiles of rudists allowed for the identification and quantification of seasonal temperature changes in shallow water settings of the Cretaceous world (Huck and Heimhofer., 2021; Steuber et al., 2005). On the contrary, the rudist fragments analyzed in this study would represent annual averages at best and thus would not provide information on seasonal variations. However, they provide high-resolution data on larger-scale temperature evolution in a critical time interval of the Cretaceous. We calculated paleotemperatures based on rudist shell material using the equation (1) from Anderson and Arthur (1983):

$$(1)\ T\ ^{\circ}C = 16.0 - 4.14 * (\delta^{18}O_{calcite} - \delta^{18}O_{seawater}) + 0.13 * (\delta^{18}O_{calcite} - \delta^{18}O_{seawater})^2$$

The challenging aspect when estimating water temperatures based on equation (1) is that the $\delta^{18}O_{seawater}$ must be assumed. Most Late Cretaceous paleoclimatic studies use an average value of –1 ‰VSMOW assuming an ice-free world (*e.g.,* Grossman, 2012; Wallisser and Schone, 2020). This value is often corrected to account for latitudinal variation (Zachos et al., 1994).

However, recent clumped isotope thermometry data and the Cretaceous climate simulations have demonstrated that the assumption of a constant $\delta^{18}O_{seawater}$ of –1 ‰VSMOW may not be valid in all the Cretaceous oceans (Dennis et al., 2013; Zhou et al., 2008 among others). Using a global average $\delta^{18}O_{seawater}$ value does not consider either the spatial heterogeneity in water isotope signatures of the Cretaceous or the different paleoenvironment (open vs. restricted ocean circulation, local evaporation-precipitation balance). In shallow-marine settings, the oxygen isotopic composition of the water depends on the evaporation-precipitation balance and the freshwater contribution (Dennis et al., 2013; Steuber, 1999; Steuber et al., 2005b). Modeled $\delta^{18}O_{seawater}$ suggests values between +0.3 and +0.5 ‰ for the low- to mid-latitudes Tethyan surface waters in the Late Cretaceous (Zhou et al., 2008). Applying unrealistic $\delta^{18}O_{seawater}$ values leads to under- or overestimations of the absolute paleotemperatures. To account for these shortcomings, we calculated paleotemperatures using two approaches: 1) an average $\delta^{18}O_{seawater}$ of -1‰ corrected to account for latitudinal changes (considering a paleolatitude of 28°N for the studied section according to Barrier et al. (2018), using the equation of Zachos et al. (1994), and 2) $\delta^{18}O_{seawater}$ +0.3‰ modeled for western Tethys surface waters (Zhou et al., 2008). According to these two scenarios, the $\delta^{18}O$ data from Devetachi rudist shells suggest temperature ranges from 22 to 41°C for scenario 1 and from 25 to 45 °C for scenario 2 (Fig.11). The warmest paleotemperature, coinciding with the negative $\delta^{18}O$ peak in the bulk rock data, is found in the Early Turonian with extremes of 41 and 45°C (scenarios 1 and 2 respectively). Temperatures >40°C from low-latitude sites are also reconstructed by O'Brien et al. (2017) for the "hot" Early Turonian age. Estimated temperatures during the CTBE interval in Devetachi vary between 23 and 37 °C and 26 to 39 °C (scenarios 1 and 2 respectively). These values agree with calculated paleotemperatures across the CTBE (31 to 37 °C) obtained using the Tex_{86} proxy by Forster et al. (2007) from low-latitude ODP sites. Finally, middle Turonian temperatures reconstructed in the Devetachi section range from 24-33 °C and 27-36 °C according to the two $\delta^{18}O_{seawater}$ scenarios considered herein. These paleotemperature calculations match the middle–late Turonian maximum seasonal temperature changes of 24-35 °C (Walliser and Schöne, 2020) and 28-35 °C (Steuber et al., 2005) considering $\delta^{18}O_{seawater}$ of -1‰. Furthermore, Walliser and Schöne, (2020), using the modeled $\delta^{18}O_{seawater}$ of Zhou et al. (2008) calculated annual mean SSTs of 37 °C during the middle-late Turonian which is comparable with the maximum temperature for this interval in the Devetachi section. Finally, paleotemperatures of ca 35 °C have been obtained using the Tex_{86} paleothermometry from low paleolatitude sites during the late Turonian-Early Coniacian interval (O'Brien et al., 2017).

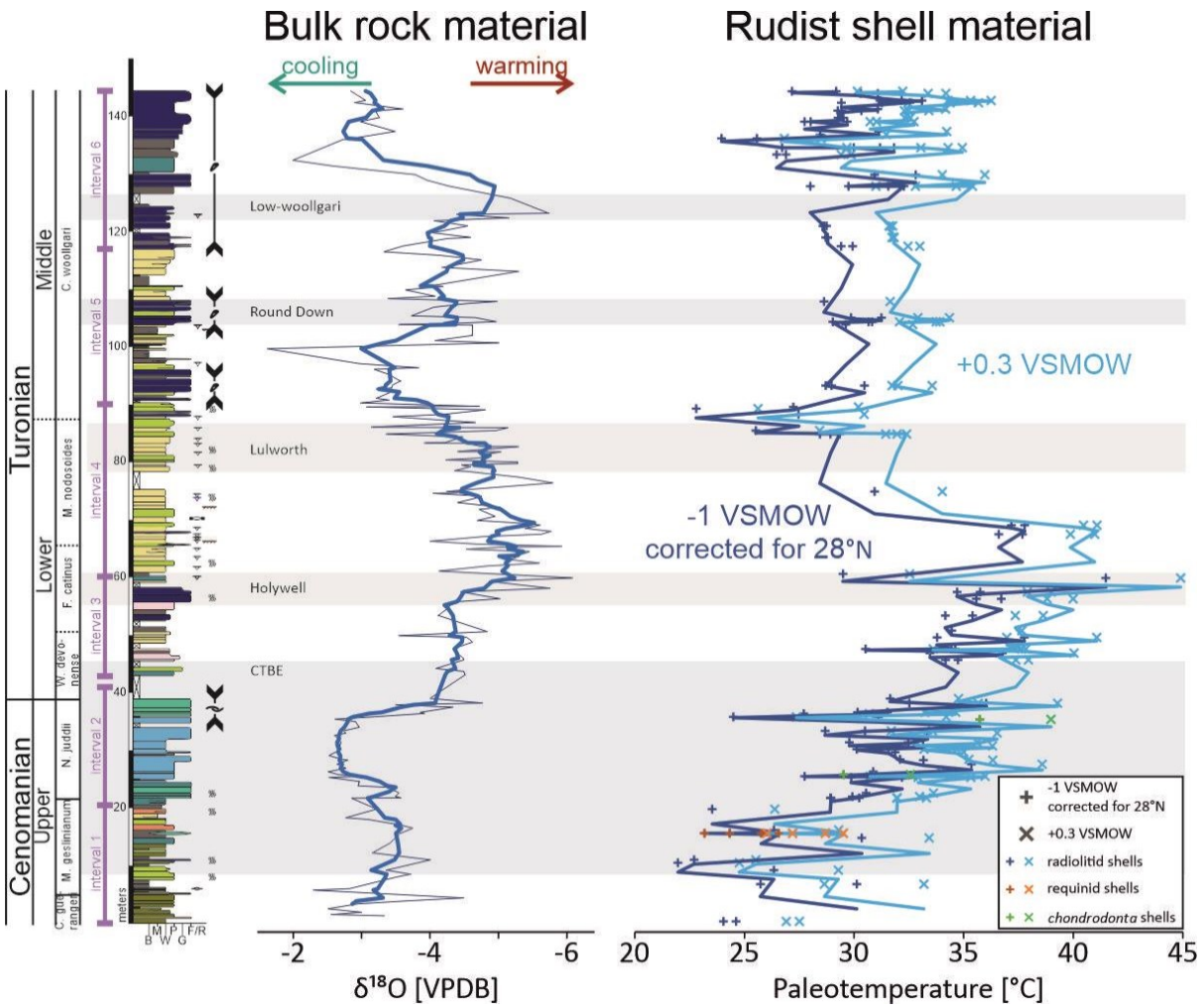

Fig.11. Paleotemperature reconstruction on Devetachi section based on well-preserved rudist shells. Bulk rock $\delta^{18}O$ profile is also reported (thick line represents 5 points moving average). Paleotemperature estimates were obtained using a $\delta^{18}O_{seawater}$ of -1‰ corrected for paleolatitude after Zachos et al. (1994) (dark blue) and a $\delta^{18}O_{seawater}$ of +0.3% modeled for the mid-Cretaceous western Tethyan ocean (Zhou et al., 2008; light blue, see text for further details). Crosses and exes represent individual shell results, thin blue lines are 3 points moving averages. Note paleotemperature in excess of 40 °C in the Lower Turonian.

3.5.4 Biota evolution and paleotemperatures changes

Using the high-resolution stratigraphic framework developed herein allows for evaluating the possible impacts of the reconstructed paleotemperatures on the distribution of benthic foraminifera and rudists in the Friuli Carbonate Platform. This dataset (Devetachi) has been further increased by comparing the benthic foraminiferal stratigraphic distribution and semi-quantitative analysis of rudist abundance from the Apennine Carbonate Platform using the data from Frijia et al. (2015; Fig.12). Unlike in benthic foraminifera, the lack of complete rudist specimens did not allow for a systematic study and biostratigraphy of these bivalves. However, to understand the effects of reconstructed temperature fluctuations on these fossils, the relative

rudist bed richness observed in the outcrop was considered (Fig.12). This allowed for estimating major changes in rudist abundance through the studied stratigraphic interval. Following the approach of Frijia et al. (2014), which considered a relative richness in rudists within a single bed, the thickness of rudist-rich beds, and the spacing between the individual rudist-rich beds as an indication of their abundance.

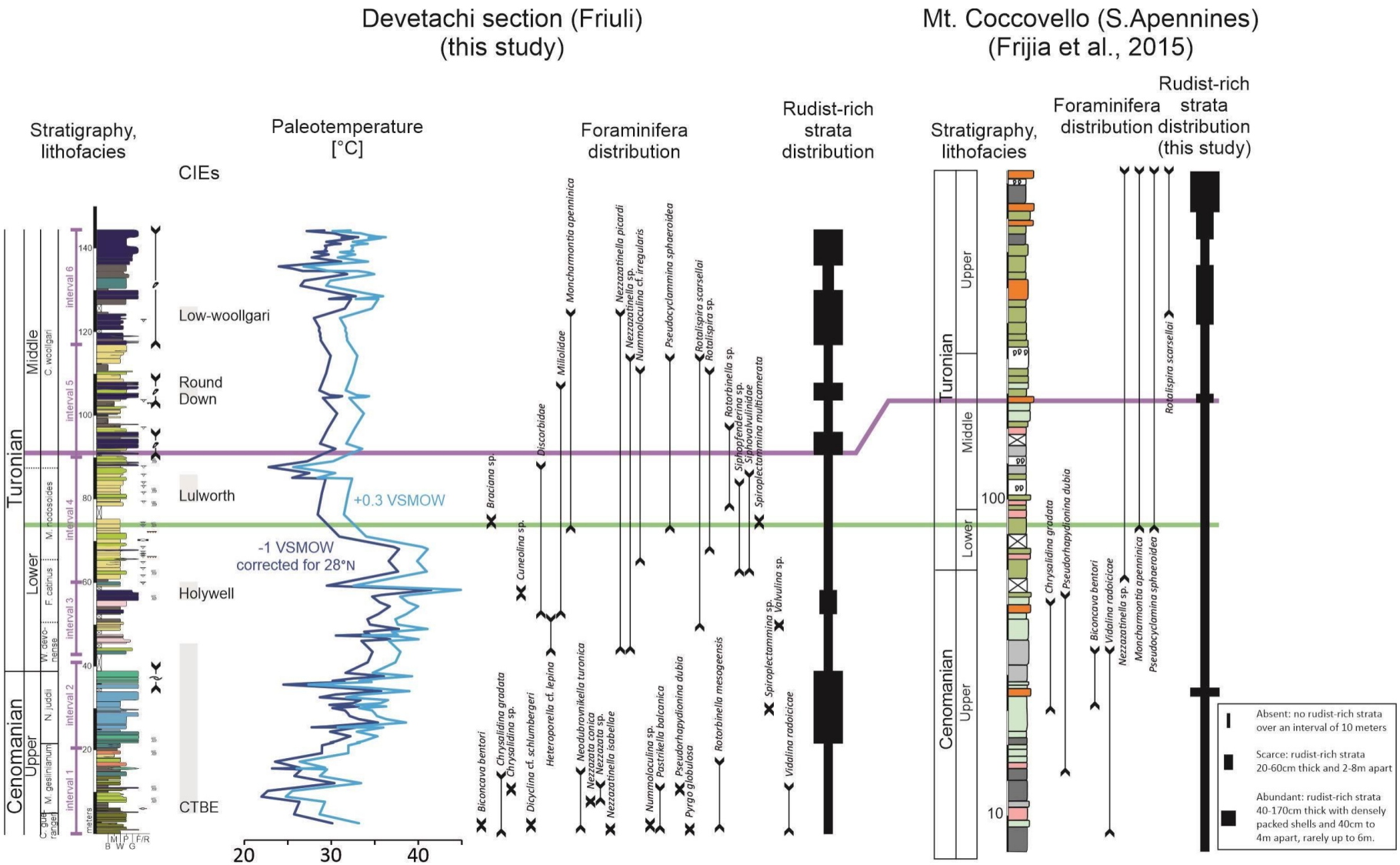
Devetachi section (Friuli)
(this study)
Mt. Coccovello (S.Apennines)
(Frijia et al., 2015)
Stratigraphy, lithofacies
Paleotemperature [°C]
CIEs
Foraminifera distribution
Rudist-rich strata distribution
Turonian
Cenomanian
Upper
Middle
Lower
W. devonense
M. gesimanum
N. juddii
C. gulrajesi
F. catinus
M. rodosoides
C. woollgari
interval 1
interval 2
interval 3
interval 4
interval 5
interval 6
meters
M P F/R
B W G
Low-woollgari
Round Down
Lulworth
Holywell
CTBE
+0.3 VSMOW
-1 VSMOW corrected for 28°N
20
30
40
Biconcava bentori
Chrysalidina gradata
Chrysalidina sp.
Dicyclina cf. schlumbergeri
Heteroporella cf. lepina
Neodubrovnikella turonica
Nezzazata conica
Nezzazata sp.
Nezzatinella isabellae
Nummoloculina sp.
Pastrikella balcanica
Pseudorhapydionina dubia
Pyrgo globulosa
Rotorbinella mesogeensis
Valvulina sp.
Vidalina radoicicae
Braciana sp.
Cuneolina sp.
Discorbidae
Miliolidae
Moncharmontia apenninica
Nezzatinella picardi
Nezzatinella sp.
Nummoloculina cf. irregularis
Pseudocyclammina sphaeroidea
Rotalispira scarsellai
Rotalispira sp.
Rotorbinella sp.
Siphoptenderina sp.
Siphovalvulinidae
Spiroplectammina multicamerata
Spiroplectammina sp.
Absent: no rudist-rich strata over an interval of 10 meters
Scarce: rudist-rich strata 20-60cm thick and 2-8m apart
Abundant: rudist-rich strata 40-170cm thick with densely packed shells and 40cm to 4m apart, rarely up to 6m.

Fig.12. Benthic foraminifera and rudists distribution/abundance in the Devetachi section (Friuli Carbonate Platform) and Mt. Coccovello (Apennine carbonate platform, Frijia et al., 2015) across the upper Cenomanian-middle Turonian interval compared to the reconstructed temperature fluctuations in Devetachi. Black bars represent semiquantitative rudist abundance estimations following the approach from Frijia et al. (2014, see text for details). Continuous green and purple lines mark the re-occurrence of high diversity foraminifera assemblages and rudist-dominated facies respectively after the CTBE/OAE-2. Note that these bioevents occur after the Lower Turonian Thermal Maximum in both carbonate platform areas.

The CTBE dramatically impacted the shallow water fauna resulting in the extinction of several shallow marine groups (recent review in Steuber et al., 2023). Published data report a major crisis among the main Late Cretaceous shallow-water carbonate producers, such as benthic foraminifera (Frijia and Parente, 2008) and rudist bivalves (*e.g.*, Steuber et al., 2016; Steuber and Schlüter, 2012; Steuber et al.,2023 and reference therein). The high diversity of the large and structurally complex late Cenomanian benthic foraminifera species vanished slightly before the Cenomanian-Turonian boundary. An Early Turonian assemblage composed of small and morphologically simple r-strategist taxa follows. Such foraminifera assemblages are reported from a few persisting resilient platforms of the Early Turonian age (Parente et al., 2008, Arriaga et al., 2016, Consorti et al., 2021, Consorti and Schlagintweit, 2021). The extinction mainly affected larger foraminifera with an extreme or moderate K-strategy lifestyle, like alveolinids, orbitolinids, and soritoideans. In several areas, the stratigraphic record of carbonate platforms at the CTBE is represented by late Cenomanian shallow-water carbonates overlain by hemipelagic facies indicating the placement of the carbonate platform beneath the photic zone (Elrick et al., 2009; Korbar et al., 2012). Where the shallow-water carbonate platforms were resilient to the environmental/climate perturbations during the CTBE, some small and little complex Cenomanian benthic foraminifera have been observed thriving across the CTBE, establishing the foundations for the flourishment of the late Cretaceous assemblages (Consorti et al., 2016; Schlagintweit and Yazdi-Moghadam, 2021; Yazdi-Moghadam and Schlagintweit, 2021). The CTBE aftermath features the presence of the first newcomers, accompanied by smaller or structurally simple Cenomanian survivors such as the genera *Dicyclina* and *Rotorbinella* (Arriaga et al., 2016). The data from the Devetachi section provide a similar picture and further detailed insights on the CTBE and the Early Turonian. The studied section shows the disappearance of larger Cenomanian foraminifera (*P. balcanica*, *C. gradata*, among others) at the onset of the CTBE. This bioevent is overlain by around 10 m of an interval barren of benthic foraminifera. An oligotypic foraminiferal association composed of small r-strategists such as miliolids, discorbidae, *Nezzazatinella picardi,* and *Siphopfenderina sp.*

appears just above and continues for ~40 m. This assemblage correlates with increased warming from the upper Cenomanian to the Lower Turonian, which culminates in the highest paleotemperatures reconstructed by $\delta^{18}O$ data (Fig.12), representing an increase of around 10 °C from the upper Cenomanian strata. A well-diversified benthic foraminifera association, even if in part composed of small r-strategists, appears at meter 75 and it is characterized by some long-lasting Late Cretaceous benthic foraminifera taxa (Frijia et al., 2015; Velić, 2007): *Moncharmontia apenninica*, *Nezzazatinella* sp., *Pseudocyclammina sphaeroidea*, *Rotalispira* sp., *Rotorbinella* sp., *Rotalispira scarsellai*, *Braciana* sp., *Spiroplectammina sp.* and suggests the establishment of improved environmental conditions. The occurrence of these assemblages coincides with the onset of a cooling trend resulting in a temperature decrease of around 7 °C with respect to the warmest Lower Turonian peak. Frijia et al. (2015) and Arriaga et al. (2016) report a similar benthic foraminifera distribution from the Apennine Carbonate Platform where the r-strategists dominate during the latest Cenomanian-Early Turonian and the first occurrence of a more diversified assemblage dominated by *M. apenninica* and *P. sphaeroidea* from the middle/upper part of the Lower Turonian. The paleotemperature reconstructions presented in this study suggest that the dramatic temperature increase across the CTBE, possibly in association with the other paleoenvironmental changes associated with the CTBE (Parente et al., 2008), was harmful to the more specialized benthic foraminifera and that during the warmest Turonian interval only simple r-strategic forms could thrive. Only when the temperatures cooled down for more than 5 °C, the benthic foraminifera started to diversify again.

The trend in the rudist abundance is remarkably similar to that of the benthic foraminifera. Rudist-rich beds occurrence both in the Friuli Carbonate Platform and in the Apennine Carbonate Platform sharply decreases from the upper Cenomanian interval and become almost absent in the uppermost Cenomanian-lowermost Turonian, where only a few beds with rare and small rudist fragments have been found. This pattern is seen in many locations around the world and represents a major drop in rudist communities and extinction of several families across the CTBE (Johnson and Kauffman, 1990; Philip and Airaud-Crumiere, 1991). Rudist declines have been attributed to regional climate changes, such as climate events that may have caused less oxygen in neritic setting (Steuber and Löser 2000) and to other environmental perturbations associated with the CTBE/OAE-2 (Steuber et al., 2023 and references therein). The rudist-poor interval in Devetachi coincides with the warmest phase indicated by the $\delta^{18}O$ reconstructed paleotemperature. Rudist-dominated strata reappear and become increasingly

more abundant, in both the Apennine and Friuli Carbonate platforms, in the middle Turonian where our data show a temperature decrease of 8-9°C (Fig.12, purple line).

Temperature is a critical factor limiting the ranges of most marine species, playing a significant role in influencing marine animals' evolution (Scotese et al., 2021). Laboratory experiments and oceanographic studies show that marine organisms experienced enhanced mortality rates when temperatures record significant increases/decreases reaching the upper/lower thermal limits for the individual species. Moreover, rapid changes in temperatures can create large habitat loss due to the inability of the ecosystem to adapt to the changed conditions (Song et al., 2021 and references therein). Maximum SST estimates obtained in this study are exceptionally warm indicating > 40 °C in the Early Turonian. de Winter et al. (2017) also found similar temperature maxima, reconstructing seasonality variations in well-preserved Campanian rudist from Oman. These extreme values would question whether the rudists and the benthic foraminifera could tolerate such heat stress. Recent mollusks and foraminifera show a drastic increase in mortality concurred in high-temperature conditions. Modern organisms cannot survive when the seawater temperatures reach 40°C (Garrabou et al., 2009 and references therein), even though laboratory experiments on mollusks and foraminifera proved that some species can live at temperatures as high as 40 °C, even if for a limited time (Schmidt et al., 2016; Seuront et al., 2019). Finally, Veizer and Prokoph (2015) suggested preferred temperature ranges between 14 and 28°C for fossil Phanerozoic bivalves. The ecological requirements of the studied rudists and foraminifera are difficult to assess and doing so is beyond the scope of this study. Furthermore, the reconstructed temperatures could have been biased by an incorrect assumption of the $\delta^{18}O_{seawater}$. Hence, more studies using different paleotemperature proxies independent of $\delta^{18}O_{seawater}$ are needed to correctly evaluate the absolute paleotemperatures, such as clumped isotope analysis (de Winter et al., 2021).

Despite the absolute temperature maxima estimates for the Devetachi section, the close match between rudist and foraminifera stratigraphic changes and temperature fluctuations suggests a strong causal relationship. Song et al. (2021) proved a marked correlation between climate changes, large mass extinction, and small intervals of biodiversity loss. These authors suggest that temperature changes with a magnitude of >5.2 °C and a rate >10 °C/Ma represented a critical threshold in determining mass extinction/biodiversity loss. The data from the Devetachi section record an increase of around 8-10 °C from the upper Cenomanian to the Lower Turonian KTM in less than 1 Ma and a decrease of 7-9 °C when a high diversified foraminifera

assemblage and rudist-dominated facies reappear. Such results agree with the thresholds suggested by Song et al. (2021). We conclude that despite the possible co-occurrence of several other environmental stressing factors (*e.g.*, nutrients fluxes, acidification events, anoxia) on shallow water communities during the Late Cenomanian-Turonian interval (*e.g.,* OAE-2, see review in Steuber et al., 2023), the temperature played a major role in controlling shallow water biota evolution on a relatively short time scales (>1Ma). Further studies comparing different stressing mechanisms in the Late Cretaceous shallow-water carbonates from different regions will be needed to understand if temperature alone was the main factor controlling carbonate platform evolution and at what time scale.

3.6 Conclusions

In this study, a combined sedimentological, stratigraphic, and geochemical approach has been used to understand the evolution of the Friuli Carbonate Platform across the Cenomanian-Turonian, a critical interval of the Late Cretaceous. The facies evolution and depositional settings were reconstructed based on facies analyses and sedimentological observations, allowing for the identification of seven lithofacies associations deposited in a shallow subtidal to more open lagoonal environment. A precise chronostratigraphic framework was developed using biostratigraphy, together with $\delta^{13}C$ and $^{87}Sr/^{86}Sr$ stratigraphy which constrained the studied section to the upper Cenomanian-middle Turonian interval.

Using $\delta^{18}O$ analysis on well-preserved bulk rock and rudist shell material, it was possible to build a high-resolution paleotemperature curve and to estimate the paleotemperature minima and maxima in shallow water carbonates. The results suggest a close match between the results presented herein and the SSTs reconstructed in the open ocean sites with increased warming from the late Cenomanian to the Early Turonian and a subsequent cooling phase. In the studied section, the Early Turonian warmest interval (KTM) reached temperatures as high as 41-45 °C (according to different $\delta^{18}O_{seawater}$ values), specifying the timing of the KTM in the peri-Adriatic area. Temperature changes from the late Cenomanian to Early Turonian had a magnitude >7 °C and a rate of changes of around 10 °C in less than 1Ma.

Paleontological data show that benthic foraminifera and rudists evolution follows paleotemperature fluctuations and that their demise in the upper Cenomanian and reoccurrence in the Turonian strata was strongly modulated by temperature. The close match of the biotic record between the Friuli Carbonate Platform and the isolated Apennine Carbonate Platform suggests a common driving mechanism which is, most likely, temperature above other

environmental stressors. However, further studies from different carbonate neritic successions and a multidisciplinary methodology are required to confirm this hypothesis and infer causal-relationship between environmental factors and evolutionary trends of the biota.

4 Clumped isotope thermometry in the shallow water carbonates of Friuli region (NE Italy) and Istria (Croatia): evaluation of samples preservation and the case of solid-state reordering.

4.1 Introduction

High-resolution paleoclimatic reconstructions allow for detailed studies of biotic changes and determining possible causal relationships between biotic evolution and environmental fluctuations in carbonate platforms. However, such studies in deep time require pristine carbonate material for geochemical analyses, highlighting the importance of diagenetic alterations assessment. Late Cretaceous carbonate platforms developed extensively in the Tethyan realm, reaching up to 35 °N paleolatitude (Kiessling et al., 2003). In the shallow-marine environment of the carbonate platform tops and margins, rudist bivalves were one of the most significant carbonate producers (Kauffman and Johnson, 1988; Gili et al., 1995). Rudists incorporated oxygen isotopes into their thick outer low-Mg calcite shell layer at or near equilibrium with the ambient water (Steuber, 1999). As such, they have been extensively used as a proxy for Cretaceous paleoenvironmental and geochemical evolution, above all using the stable oxygen isotope ratio ($\delta^{18}O$) analysis of the outer shell layer of rudist fossils (Huck and Heimhofer, 2021; Schmitt et al., 2022; Steuber et al., 2005 among others). Furthermore, the possibility to evaluate environmental changes through the life of the animal (sclerochronological analysis) allows for unprecedented resolution of seasonal temperature variations during both the Early and Late Cretaceous (de Winter et al., 2017a, 2021; Huck and Heimhofer, 2021; Steuber et al., 2005b). However, the $\delta^{18}O$ paleothermometer suffers from a significant pitfall. The temperature is calculated using the measured $\delta^{18}O$ of the calcite, as well as the original $\delta^{18}O$ composition of the seawater; information missing for the deep time (*e.g.*, Came et al., 2007; Grossman, 2012).

Clumped isotope thermometer is a fairly novel tool for paleotemperature reconstructions (Ghosh et al., 2006; Schauble et al., 2006). It is based on the temperature-dependent clumping of the heavy carbon and oxygen isotopes (^{13}C and ^{18}O) into bonds with each other within the mineral lattice of carbonate minerals (Eiler, 2011, 2007). Compared to the widely used $\delta^{18}O$ thermometry, the main advantage of clumped isotope thermometry is that the bonding of the heavy carbon and oxygen isotopes in the carbonates is independent of the oxygen isotopic composition of ambient water (Eiler, 2011). Several studies use modern and fossil shells (down

to the Paleozoic) for clumped isotope thermometry (Came et al., 2007; Eagle et al., 2013; Henkes et al., 2013; Huyghe et al., 2022; Petersen et al., 2016; Petrizzo et al., 2014), with only a few studies performed on rudist shells to date (de Winter et al., 2021; Huck et al., 2012).

However, the clumped isotopes are susceptible to alteration as the original clumping of the heavy isotopes within the carbonates partially or completely resets to reflect higher temperatures during certain burial conditions (Henkes et al., 2014). Solid-state reordering of the C-O bonds can happen without influencing the apparent shell microstructure, $\delta^{13}C$ and $\delta^{18}O$ composition, or trace element concentrations (Henkes et al., 2014), the usual indicators used to assess the degree of post-depositional alteration (Allan and Matthews, 1982; Brand and Veizer, 1981; Cochran et al., 2010; Jarvis et al., 2011; Smith et al., 2022).

In this study, we present $\delta^{18}O$ and Δ_{47} analyses of several rudist bivalve samples, both shell fragments and whole specimens from the Upper Cretaceous carbonates of the Friuli (NE Italy) and Istria (Croatia) regions; Adriatic Carbonate Platform (AdCP). The selected rudist specimens belong to the same depositional environment but experienced different burial conditions allowing for testing the effect of elevated burial temperatures vs. the near-surface post-depositional conditions at sample preservation. All samples were screened for diagenetic alterations via a multidisciplinary approach of conventional petrographic methods and elemental analyses to assess if diagenesis might have influenced the isotopic results. Furthermore, the rudist specimens used in this study were preserved in the form of fragments as well as nearly complete specimens. Given that fossil fragments are found more frequently than whole fossil shells in the sedimentary record, testing whether there is a difference in the preservation of the original isotopic signal between fragments and nearly complete specimens is essential.

The research questions postulated in this paper are the following: 1. Are whole specimens more likely to preserve the original clumping of the C-O bonds within their shells than virtually well-preserved shell fragments? And 2. Are clumped isotope-derived paleotemperatures always reliable? How, and to what extent, elevated burial temperatures during the sediments' history influence the commonly applied diagenetic alteration indicators?

4.2 Geological settings

The samples used in this study come from two regions (Friuli and Istria) belonging to the Adriatic carbonate platform (AdCP), one of the largest Mesozoic carbonate platforms of the Perimediterranean regions (Vlahović et al., 2005; Fig.4.1). The AdCP represented an isolated

platform where shallow-water carbonates deposited from the Jurassic to Eocene (Del Viscio et al., 2022; Vlahović et al., 2005). The Devetachi section is located on a road cut on the way from Trieste to Gorizia (45.86 N, 13.57 E; for a detailed description of the geological settings of the area, please refer to Chapter 3).

The shallow water Upper Cretaceous successions of southern Istria show continuous sedimentation during the Albian-early Campanian (Moro, 1997; Polšak, 1964), and the Santonian peritidal limestones are overlaid by Paleogene deposits (Moro et al., 2002). At the beginning of the Alpine collision during the Paleogene, the Istrian Peninsula became part of the foreland area of the orogenic system (del Viscio et al., 2022 and reference therein). In the southern part of the Istrian Peninsula, a broad, NE-plunging anticline is present, composed of Upper Jurassic shallow-water carbonates at the nucleus and of Lower Cretaceous – Santonian deposits (Moro et al., 2002) on the flanks (Fig.4.1c).

Fragmented rudists (radiolitid) shell material was obtained from a well-dated shallow-marine section from the Friuli region (Devetachi; see Chapter 3) and complemented by two nearly complete rudist specimens from the locality Aurisina (Fig.4.1b). Additionally, results from four nearly complete rudist specimens obtained from the localities Medulin, Punta secca, and Punta secca Vinjole, Istria, are presented in this study, (Fig.4.1c). Given the different tectonic evolution resulting from the relative position of the Friuli and Istria regions with respect to the SW migrating Dinaric fold-and-thrust belt (indicated in Korbar, 2009), different burial histories of the two regions can be expected.

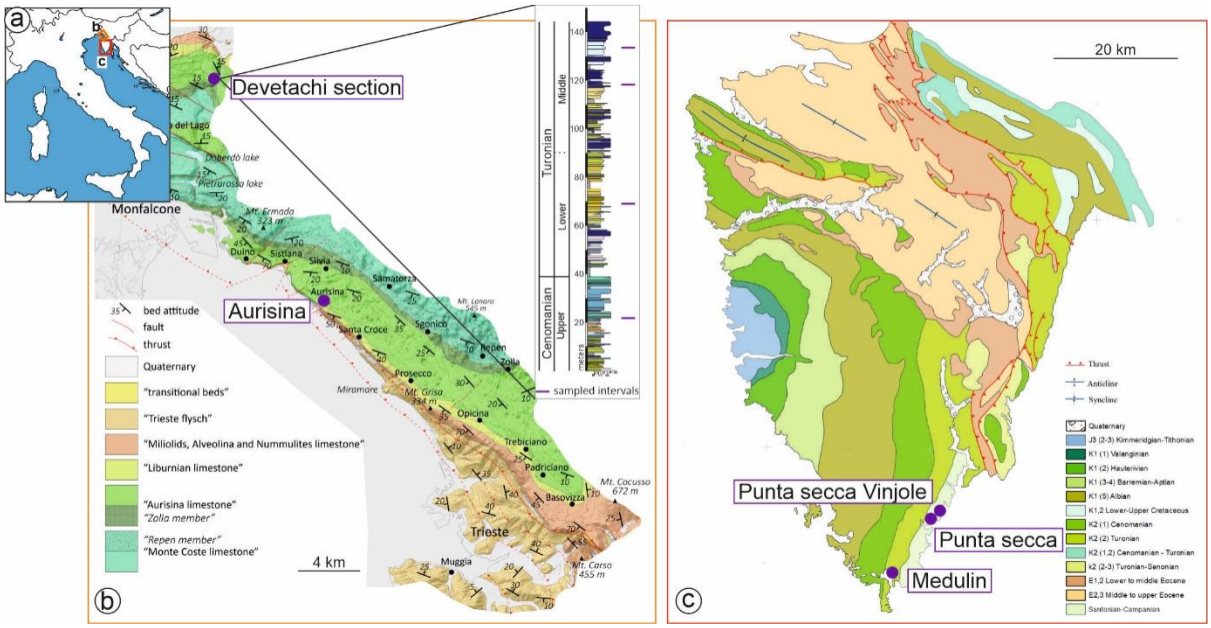

Fig.4.1 Locations of the studied specimens. **a.** Locations of Friuli Karst in NE Italy and Istria, Croatia. **b.** Geological map of the Trieste Karst area simplified from Jurkovšek et al. (2016) with marked sampled locations of Aurisina and Devetachi. The stratigraphic log of the latter is reported in the inlet showing the four sampled intervals for this study. **c.** Geological map of the Istrian Peninsula, with three localities discussed in this study, marked. Simplified after Velić and Vlahović (2009).

4.3 Material and methods

Clumped isotope and oxygen isotope analyses were performed on four shell fragments of radiolitid rudists and surrounding micritic matrix (Devetachi section; Friuli region; Fig.4.1b) corresponding to upper Cenomanian, Lower, and middle Turonian. All results from the two stratigraphic levels belonging to the middle Turonian were merged to obtain single data point for the given substage. Two nearly complete specimens of rudist bivalves from the Friuli region, *Vaccinites* cf. *cornuvaccinum* and *Hippurites nabresinensis* (Fig.4.2e, f; Tab.1) come from the Aurisina locality (Friuli region; Fig.4.1b). From the Istria region, four rudist specimens are analyzed in this study: *Praeradiolites ciryi* (Punta secca Vinjole), *Biradiolites stoppanianus* (Punta secca Vinjole), *Hippurites incisa* (Medulin), *Miloranovicia herakii* (Punta secca; Fig.4.2a-d). Additionally, micritic matrix (without a sparite content where possible) filling or surrounding all the rudist specimens was sampled. The nearly complete rudist specimens from both regions were provided by the Museum of Natural History of Trieste.

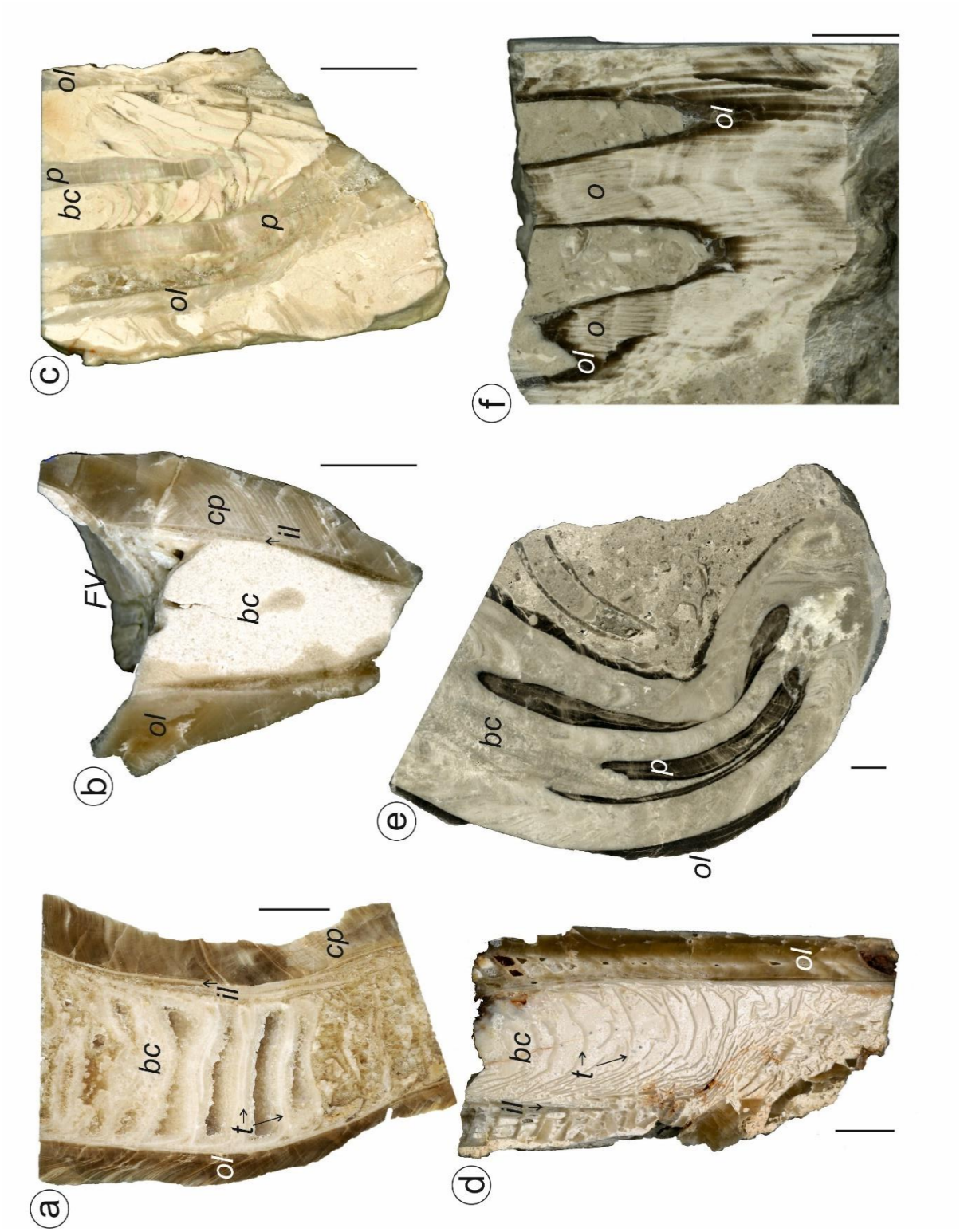

Fig.4.2. Studied nearly complete rudist specimens. **a.** *Praeradiolites ciryi*, **b.** *Biradiolites stoppanianus*, **c.** *Hippurites incisa*, **d.** *Miloranovicia herakii*, **e.** *Vaccinites cf. cornuvaccinum*, **f.** *Hippurites nabresinensis*. *bc* – body cavity; *cp* – cellulоprismatic structure of the outer shell layer; FV – free (upper) valve; *il* – inner shell layer; *o* – oscules, formed by infolding of the valve margin; *ol* – outer shell layer; *p* – pillars; *t* – tabulae. Scales equal 1cm.

Tab.4.1. Rudist specimens from the Museum of Natural History in Trieste and rudist fragments from the Devetachi section analyzed in this study. Reported chronostratigraphy is based on rudist and benthic foraminifera biostratigraphy in the nearly complete specimens, and from chemostratigraphic data ($\delta^{13}C$ and Sr-isotope stratigraphy) in the radiolitid fragments from the Devetachi section (*) (see Chapter 3).

Species	**Country**	**Region**	**Locality**	**Chronostratigraphy**
Hippurites incisa	Croatia	Istria	Medulin Punta secca	Turonian
Praeradiolites ciryi	Croatia	Istria	Vinjole Punta secca	Upper Coniacian
Biradiolites stoppanianus	Croatia	Istria	Vinjole	Coniacian
Miloranovicia herakii	Croatia	Istria	Punta secca	Santonian
Hippurites nabresinensis	Italy	Friuli	Aurisina TS	Coniacian – Santonian
Vaccinites cf. cornuvaccinum	Italy	Friuli	Aurisina TS	Coniacian – Santonian
Radiolitid fragment	Italy	Friuli	Devetachi	Upper Cenomanian*
Radiolitid fragment	Italy	Friuli	Devetachi	Lower Turonian*
Radiolitid fragment	Italy	Friuli	Devetachi	middle Turonian*

The studied specimens were cut and polished in the laboratories at Utrecht University (for the detailed methodology of sample preparation see Chapter 2.1). The selected areas of the thick outer shell layers of the studied specimens, and fragments showing the well-preserved prismatic structure were drilled using a tungsten carbide drill bits of 0.3 and 0.5 mm in diameter.

$\delta^{18}O$, $\delta^{13}C$, and clumped isotope analyses were performed at the Stable Isotope Lab at Utrecht University (For details on the analytical procedure refer to Chapter 2.3). Carbonate aliquots (70-150 µg) were reacted with nominally anhydrous (103%) phosphoric acid at 70°C for 300s using Kiel IV carbonate devices. The gas samples were purified using two liquid nitrogen-cooled cryogenic traps (−196°C) and a PoraPak™ Q trap (Merck KGaA, Darmstadt, Germany) kept at −150°C. The analysis was performed using MAT 253 or 253 Plus IRMS. Clumped isotope values were corrected to the Intercarb-Carbon Dioxide Equilibrium Scale (I-CDES) using measurements of ETH standards (ETH-1, -2, and -3) and their accepted Intercarb values (Bernasconi et al., 2021). The results of the clumped isotope analysis are expressed as Δ_{47} in ‰ units and the results of stable oxygen and carbon stable isotope analyses are expressed as $\delta^{18}O$ and $\delta^{13}C$ respectively, in ‰ units relative to VPDB. SSTs were calculated using the latest clumped isotope thermometer calibration performed by Anderson et al. (2021) and for the $\delta^{18}O$-

based paleotemperatures, the equation of Anderson and Arthur (1983) was used, assuming the $\delta^{18}O$ value of the seawater of -1 ‰ relative to VSMOW.

In total, 472 aliquots of carbonate powders were measured, 50 belonging to rudist shell fragments and 33 to bulk rock from the Devetachi section, 324 belonging to the nearly complete rudist specimens and 46 to the matrix and 19 to sparite cement filling the body cavities of the rudists.

To evaluate the reliability of the measurements, several variables were screened through each run. Sample measurements were excluded from further interpretations based on the elevated mass 49 (above 0.05‰), suggesting contamination of the sample (*e.g.*, Kluge et al., 2015). Similarly, any measurements showing standard deviation on Δ_{47} above 0.15‰ per aliquot and/or if signal intensity was outside the range of 10000-25000 were not included in the final dataset (after Agterhuis et al., 2022). The resulting number of aliquots after this syn-analytical screening was reduced to 450 in total.

To further corroborate age determination and to get insight into the preservation of the samples, the six complete rudist specimens were analyzed for $^{87}Sr/^{86}Sr$ and elemental content at the University of Bochum (Germany). Finally, to fully understand the elemental distribution in the bivalve shells and to screen for aberrant trace element concentrations that could point towards recrystallization (de Winter and Claeys, 2016), two specimens were selected and analyzed via µXRF methods by the Analytical, Environmental and Geochemistry research group at the Vrije Universiteit Brussel in Belgium, using Tornado M4 micro-X-ray fluorescence (µXRF) scanner (Bruker nano GmbH, Berlin, Germany) equipped with an Rh source and two X Flash 430 Silicon Drift detectors. The XRF source was operated at 50 kV and 600 µA without source filters for optimal X-ray signal intensity. Semi-quantitative XRF maps with short (1 ms) integration time per pixel were made to image the relative distribution of trace elements (Sr, Mn and Fe) for sample screening purposes (de Winter and Claeys, 2016). Quantitative XRF line scans were produced by point-by-point analyses with longer dwell times sufficient to reach reproducible accuracy and precision of trace element results (de Winter et al., 2017b; Vansteenberge et al., 2020). Quantitative XRF analyses were calibrated using measurements on a range of matrix-matched carbonate standards, following methodology in de Winter et al. (2020) and Vellekoop et al. (2022).

4.4 Results

4.4.1 Clumped isotope analysis

The clumped isotope results of the outer shell layers of nearly complete rudist specimens and the radiolitid fragments show a large difference in Δ_{47} values between the Friuli (Devetachi, Aurisina; Fig.4.1b) and Istria (Punta secca, Punta secca Vinjole, and Medulin; Fig.4.1c) regions (Fig.4.3). In the Friuli region, the analyzed shell fragments yield an average value of 0.443±0.011 ‰ (errors are reported as 95 % confidence limits), n=50 (number of aliquots measured per sample), and the average bulk rock has a Δ_{47} of 0.485±0.016 ‰, n=31. The Δ_{47} analysis of two nearly complete specimens from the Friuli region resulted in values of 0.486±0.028 ‰, n=17 (shell) and 0.519±0.096 ‰, n=4 (bulk rock) in *Vaccinites* cf. *cornuvaccinum*, and 0.473±0.029 ‰, n=14 (shell) and 0.476±0.138 ‰, n=3 in *Hippurites nabresinensis*.

In contrast, the specimens from the Istria region show results between Δ_{47} 0.550±0.024 ‰, n=34 (*B. stoppanianus*) and 0.576±0.021 ‰, n=33 (*H. incisa*) of the shell analysis and between Δ_{47} 0.579±0.044 ‰, n=14 (*P. ciryi*) and 0.603±0.028 and 0.043 ‰, n=13 (*M. herakii* and *B. stoppanianus* respectively) of the micritic bulk rock with sparite content. Despite the large errors on the bulk rock values in *V.* cf. *cornuvaccinum* and *H. nabresinensis* caused by the low number of repetitions of the measurements (Fig.4.3), the large offset between the Δ_{47} values in the Friuli and Istria regions is clear. Averaged Δ_{47} values of the shell material from the Friuli region is 0.105 ‰ (representing ~50 °C) higher than the shells from Istria. Similarly, the averaged bulk rock Δ_{47} results from Friuli are 0.107 ‰ (representing ~44.6 °C) higher than the results from the Istria region. The matrix Δ_{47} values are substantially higher than the values recorded in the shells of the same specimens.

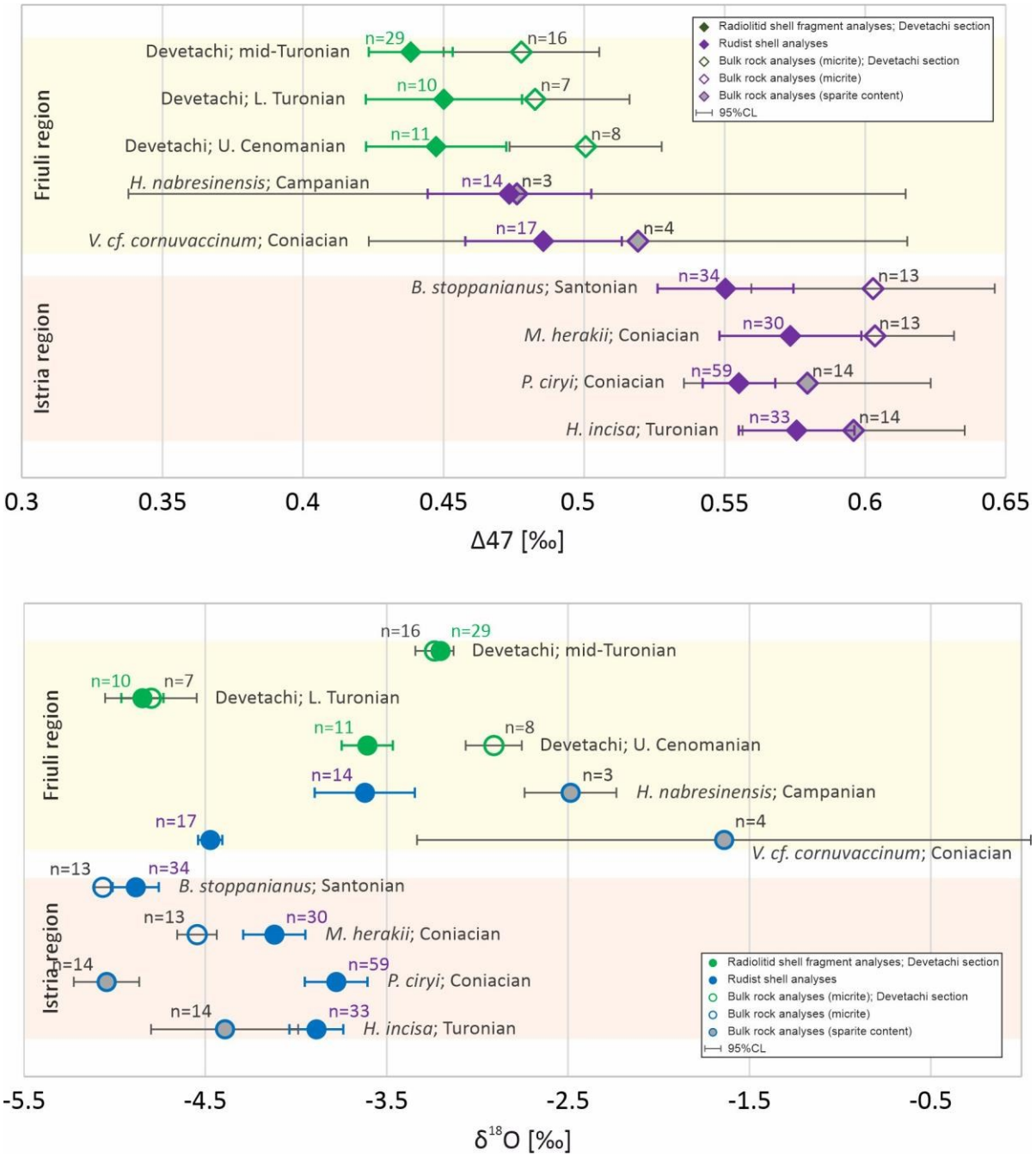

Fig.4.3. Clumped isotope and stable oxygen isotope analyses of the studied rudist shell fragments (Devetachi section) and of the complete rudist specimens from Friuli (Devetachi and Aurisina) and Istria (Punta secca, Punta secca Vinjole, and Medulin; Tab.1) regions. n, number of aliquots measured per data point.

4.4.2 Oxygen isotope analysis

The results of oxygen isotope analysis are more similar between the Friuli and Istria regions compared to the clumped isotope analysis (Fig.4.3). The shell material averaged $\delta^{18}O$ values are -3.80±0.14 ‰ in Friuli, and -4.11±0.11 ‰ in the Istria region, whereas the $\delta^{18}O$ results of the bulk rock are -3.23±0.32 ‰ in Friuli, and -4.77±0.13 ‰ in Istria. The results of the shell material as well as bulk rock show higher values in the Friuli region. The difference of average

$\delta^{18}O$ values in Friuli and Istria regions is small in the shell material, 0.31 ‰, representing ~1.5 °C. Contrarily, the difference of the results of bulk rock material from the two studied regions is larger, $\delta^{18}O$ of 1.54 ‰, representing ~7.6 °C.

4.4.3 µXRF analysis

Two nearly complete rudist specimens were analyzed by µXRF, Campanian *H. nabresinensis* from the Friuli region (locality Aurisina) and mid-Coniacian specimen *P. ciryi* from the Istria region (locality Punta secca Vinjole). The results of the analysis of Sr, Mn, and Fe concentrations are shown in Fig 4.4. Maps of relative elemental distributions, as well as point-by-point measurements, were generated. The relatively high Sr values in the map scans of both specimens clearly outline the outer shell layer of the rudist specimens (Fig.4.4b and d, in grey).

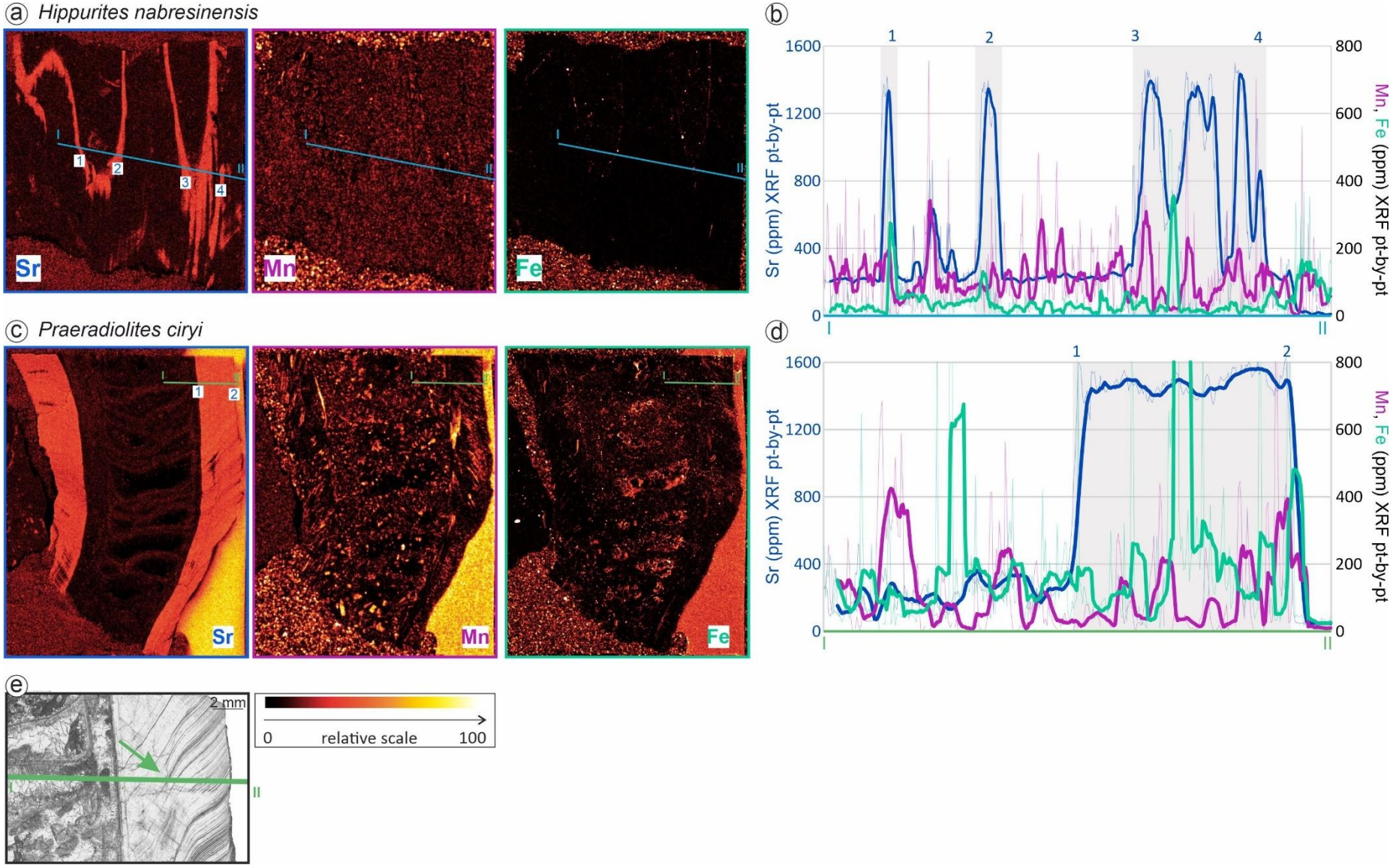
ⓐ Hippurites nabresinensis
Sr
Mn
Fe
ⓒ Praeradiolites ciryi
Sr
Mn
Fe
ⓑ
Sr (ppm) XRF pt-by-pt
Mn, Fe (ppm) XRF pt-by-pt
1600
1200
800
400
0
800
600
400
200
0
1
2
3
4
I
II
ⓓ
Sr (ppm) XRF pt-by-pt
Mn, Fe (ppm) XRF pt-by-pt
1
2
ⓔ
2 mm
0
relative scale
100

Fig.4.4. **a.** Results of µXRF analysis of *Hippurites nabresinensis* (Friuli region, locality Aurisina). Maps of relative elemental distributions show the relative content of Sr, Mn, and Fe from left to right. **b.** Results of point-by-point analysis through *H. nabresinensis* shell transect, thick line represents 10 points moving average of the element concentrations, and the shell wall areas are marked in grey. **c.** Maps of relative elemental distributions of *Praeradiolites ciryi* (Istria region, locality Punta secca Vinjole). **d.** Results of point-by-point analysis through transect of *P. ciryi*, thick line represents 10 points moving average of the element concentrations, and the shell wall area is marked in grey. The Sr point-by-point analysis marks the thick outer shell layer in both rudist specimens (1, 2 in *P. ciryi*, 1, 2, 3-4 in *H. nabresinensis*) by the elevated Sr content (blue lines). The major peak of Fe concentration shown within the shell wall of *P. ciryi* corresponds to the micro-crack observed in the thin section (**e.** bottom rectangle, marked by an arrow).

The µXRF line scan of *H. nabresinensis* crosses the outer shell layer in three places (marked 1, 2, and 3-4 in Fig.4.4a, b). The average Sr content of the shell material is 979 ppm with standard deviation (s.d.) 391 ppm. Two drops of the Sr concentration below 800 ppm are marked within the shell (Fig.4.4b 3-4), reflecting a fold of the shell wall in the lower part of the valve and hence corresponding to the Sr concentration of the bulk rock surrounding the shell. The Mn and Fe concentration is generally low with an average value of 104, s.d. 120 ppm, and 57, s.d.117 ppm respectively. The peaks of maximum Mn and/or Fe concentrations coincide with a drop in Sr content, likely reflecting the fold of the shell wall (between 3 and 4, Fig.4.4b). The micritic bulk rock filling the shell of *H. nabresinensis* (between 1, 2 and 3, Fig.4.4b) shows Sr concentrations of 254 ppm with s.d. 100 ppm; low compared to the shell material. The Mn concentrations of the bulk rock (116 ppm) are comparable to those of the shell material, whereas the Fe concentrations of the bulk rock are slightly lower (38 ppm) than in the shell.

In the outer shell layer of *P. ciryi* (edges marked 1 and 2 in Fig.4.4c, d), the average Sr content is 1461 ppm with s.d. of 97 ppm according to the line scans. The average Mn content is 109 ppm, with s.d. 157. The high s.d. in the Mn is caused by small cracks or impurities in the shell, that are visible on the map of the relative Mn distribution (Fig.4.4c). Several peaks in the Mn content (above 300 ppm) occur throughout the line scan of *P. ciryi*, one of which is depicted by the smoothed line and is located near the outer surface of the shell (Fig.4.4d). This peak corresponds to relatively elevated Mn concentration, visible in the map scan (Fig.4.4c). The average Fe content is generally low in the outer shell layer of *P. ciryi* (342 ppm), interrupted by five peaks, one of which being as large as over 12000 ppm. Indeed, the map of relative Fe abundance within the shell wall of *P. ciryi* shows isolated areas with elevated Fe content in the middle of the shell transect, one of which (as large as 12000 ppm) corresponds to a crack within

Tab.2. Results of Strontium-isotope analyses and stratigraphy, and elemental concentrations of the studied specimens.

Sample	Locality	Sr-isotope analyses			age				elemental analyses					
		$^{87}Sr/^{86}Sr$ measured*	± 2 s mean	$^{87}Sr/^{86}Sr$ corrected	min	pref.	max	chronostratigraphy	**Ca** [ppm]	**Mg** [ppm]	**Sr** [ppm]	**Fe** [ppm]	**Mn** [ppm]	**Ba** [ppm]
B. stoppanianus	Punta secca Vinjole	0.707436	0.000005	0.707434	85.3	**85.258**	85.2	Santonian	n.d.	n.d.	n.d.	n.d.	n.d.	n.d.
H. incisa	Medulin	0.707687	0.000009	0.707685	inconclusive			n.d.	n.d.	n.d.	n.d.	n.d.	n.d.	n.d.
H. incisa	Medulin	0.707670	0.000010	0.707663	inconclusive			n.d.	408970	2230	196	92.4	2.6	2.1
H. nabresinensis	Aurisina	0.707475	0.000005	0.707468	82.8	**82.632**	82.5	lower Campanian	410530	1377	1448	3.2	0.9	0.7
M. herakii	Punta Vinjole	0.707403	0.000006	0.707401	86.6	**86.564**	86.5	Coniacian	402090	1275	1263	11.2	0.6	1.2
P. ciryi	Punta secca Vinjole	0.707397	0.000005	0.707395	86.8	**86.772**	86.7	middle Coniacian	401930	1151	1160	4.0	0.5	0.8
V. cf. cornuvaccinum	Aurisina	0.707356	0.000005	0.707349	88.3	**88.341**	88.3	Coniacian	407640	1709	1500	1.7	0.4	0.7

the shell structure observed in thin section (Fig.4.4e). The locally elevated average values in Mn and Fe content are likely not indicative of a significant diagenetic overprinting of the shell of *P. ciryi* since recrystallization leads to a drop in Sr content accompanying the increase in Mn and Fe content (Brand and Veizer, 1981); not observed in the presented dataset. The line scans of the bulk rock material filling the shell of *P. ciryi* show relatively lower Sr content compared to the shell material (230 ppm on average with s.d. 101 ppm), whereas the Mn and Fe average values of the inner infill (126 and 342 ppm respectively) do not differ from the average shell values.

4.4.4 Strontium isotope and elemental concentration analyses

All the nearly complete rudist specimens were analyzed for $^{87}Sr/^{86}Sr$ (Tab.2) to further constrain their age, preliminarily based on biostratigraphy (Tab.1). Areas of sampling the low-Mg outer shell layers of the studied rudist specimens were selected based on petrographic screening, only shell portions with preserved visible growth lines and/or without apparent recrystallization were sampled. To control for the non-apparent diagenetic alteration of the sampled areas, analysis of the elemental concentrations (Sr, Mn, and Fe) was performed on the split powders of the same sample.

The results of the strontium isotope analysis range from 0.707356 to 0.707475 and are reported in Table 2. The chronostratigraphy (based on C- and Sr-isotope stratigraphy) of the shell fragments from the Devetachi section is reported in Table 1; for the preservation of the samples, see Chapter 3.

The Sr content varies from 196 ppm in *H. incisa* to 1500 ppm in *V.* cf. *cornuvaccinum*, and the Fe content in all the specimens is generally low (from 1.7 to 11.2 ppm) but shows one exceptionally high value of 196 ppm in *H. incisa*. Measured Mn concentrations show values below detection limits for all the specimens except for *H. incisa* (2.6 ppm).

The specimens from the Friuli region yield $^{87}Sr/^{86}Sr$ ratios of 0.707356 and 0.707468 for *V. cf. cornuvaccinum* and *H. nabresinensis* respectively. The ages derived from the look-up table (V 6) of McArthur and Horwath (2020) give a Coniacian and lower Campanian age for *V. cf. cornuvaccinum* and *H. nabresinensis* respectively. The result of *V. cf. cornuvaccinum* is in accordance with the biostratigraphy-derived age reported in Tab.1, whereas the results of SIS for *H. nabresinensis* give an older age than the biostratigraphic assumptions for this specimen (Tab.1 and 2).

The specimens from the Istria region, *M. herakii,* and *P. ciryi* yield $^{87}Sr/^{86}Sr$ values of 0.707403 and 0.707397, both translating in a Coniacian age (McArthur and Howarth, 2020; Tab.2). The Sr ratio of 0.707436 for the of *B. stoppanianus* points to Santonian (McArthur and Howarth, 2020), an age slightly older than suggested by the biostratigraphic data (Tab.1). However, the SIS age determination must be considered with a high level of uncertainty due to the slight recrystallization of the shell of *B. stoppanianus* (see below).

In specimen *H. incisa*, the results of SIS are, inconclusive. Biostratigraphic evidence indicates a Turonian age. Nonetheless, the results of repeated $^{87}Sr/^{86}Sr$ analysis show values of 0.707685 and 0.707663, which would correspond to upper Campanian. This age seems unrealistic for several reasons. No upper Campanian deposits have been reported in the literature from the sampled locality (see the geological map in Fig.4.1b), and the elemental composition of the shell shows a clear sign of diagenetic alteration (see below). For this reason, we do not rely on the SIS age for this specimen, but we follow the biostratigraphic age determination (Tab.1).

The radiolitid shell fragments from the Devetachi section were dated based on the biostratigraphy, and chemostratigraphy ($\delta^{13}C$, $^{87}Sr/^{86}Sr$; see Chapter 3).

4.5 Discussion

4.5.1 Clumped isotope thermometer and $\delta^{18}O$ of the seawater

Taking into consideration the results of the clumped and stable isotope analyses of the radiolitid shell fragments and nearly complete rudist specimens, a large difference between the clumped isotope analysis results accompanied by comparably small differences in $\delta^{18}O$ is apparent (Fig.4.3). When averaged, the Δ_{47} values for Friuli and Istria regions differ by 0.105 ‰, which corresponds to ~50 °C, whereas the $\delta^{18}O$ results differ by 0.31 ‰, corresponding to ~1.5 °C (using equations of Anderson et al., 2021 and Anderson and Arthur, 1983 respectively; Fig.4.5). Furthermore, when comparing the specimens/fragments of rudists from the same stratigraphic interval, the difference in the Δ_{47} is even more apparent. The Lower and middle Turonian radiolitid shell fragments from the Devetachi section (Friuli region) yield Δ_{47} values of 0.450±0.028 ‰ (92.1±17.1 °C) and 0.438±0.015 ‰ (100.5±11.3 °C), whereas Turonian specimen *H. incisa* from the Istria region yields Δ_{47} 0.576±0.021 ‰ (33.5±7.7 °C; errors are given as 95%CL on the averages). Similarly, the results of Δ_{47} analysis of the Coniacian specimens from the Friuli and Istria regions differ significantly. In Friuli, the specimen *V. cornuvaccinum* shows Δ_{47} of 0.486±0.028 ‰ (73.4±15 °C), whereas, in Istria, *P. ciryi* shows Δ_{47} of 0.555±0.013 ‰ (41.1±5.8 °C), and *M. herakii* shows Δ_{47} of 0.573±0.025 ‰ (35.5±10.7 °C). The maximum SST estimates for mid-Cretaceous based on TEX_{86} are above 35 °C, and range between 17 and 36 °C between the onset of the global cooling (Coniacian) and the end of the Cretaceous (O'Brien et al., 2017). These estimates are in accordance (within error) with the Δ_{47}-based paleotemperature calculations for the Istrian rudist shells presented herein. Contrarily, the Δ_{47}-based paleotemperature calculations for the Friuli region are markedly higher than plausible temperatures for low-mid latitudes Cretaceous seawater (reaching over 70 °C; Fig.4.5), as no recent multicellular organisms live in waters with temperatures above 50 °C (Brock, 1985).

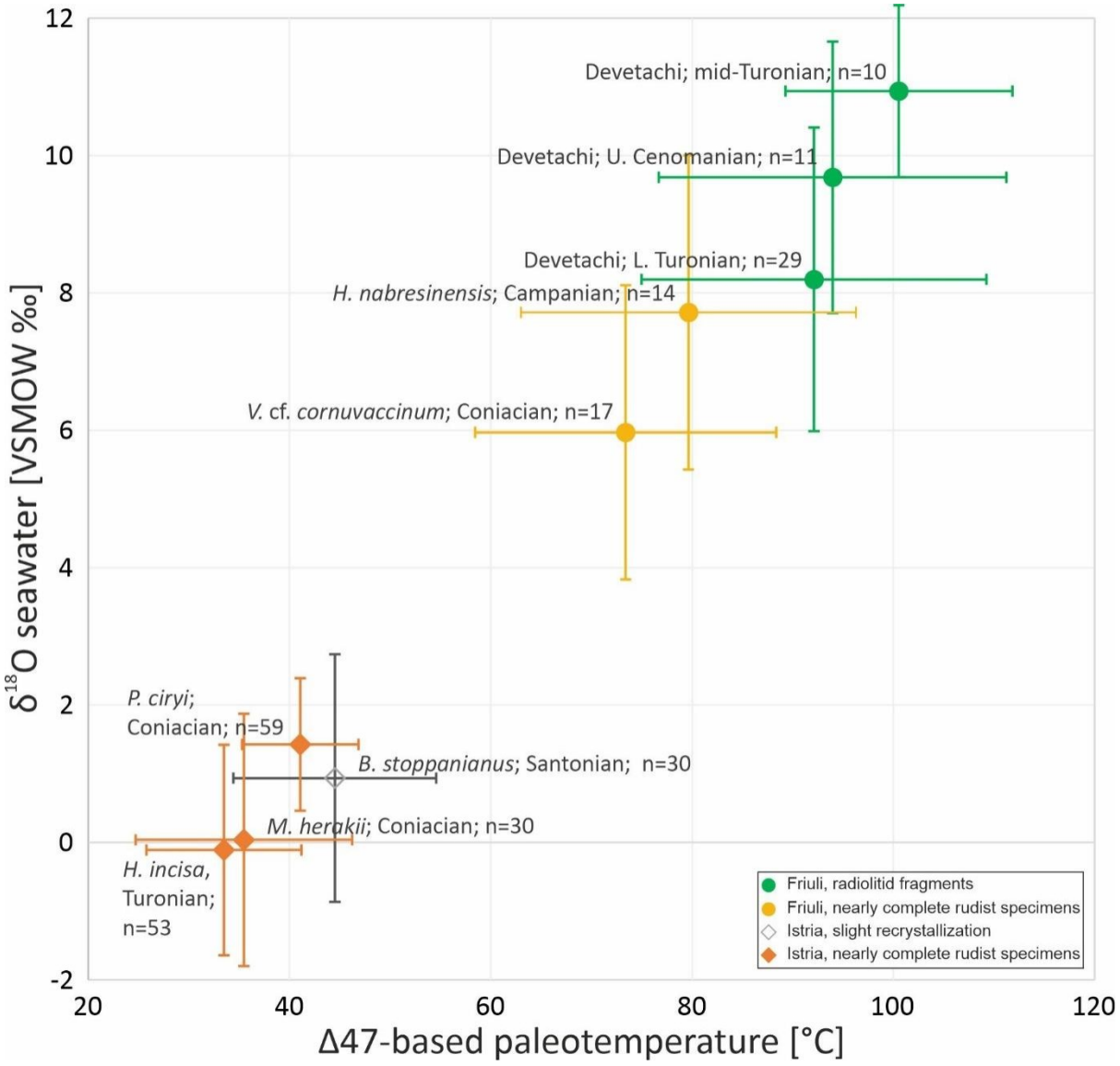

Fig.4.5. Results of paleotemperature calculations based on Clumped isotope analysis compared to $\delta^{18}O_{seawater}$. The paleotemperatures based on Clumped isotope analysis were calculated using the equation of Anderson et al. (2021; the errors represent 95 %CLs), and the $\delta^{18}O_{seawater}$ was calculated based on the Δ_{47}-temperatures and $\delta^{18}O$ results of the same aliquots (the error is calculated using Monte Carlo statistical method). In the Friuli region, the Δ_{47}-based paleotemperatures are above those suitable for the life of multicellular organisms. Similarly, the calculated values of $\delta^{18}O_{seawater}$ are significantly above the $\delta^{18}O$ modeled for the Mesozoic oceans (see Discussion).

The Δ_{47}-based temperatures combined with measured $\delta^{18}O$, allowed for calculating the $\delta^{18}O_{seawater}$, albeit with large uncertainty (using the equation of Anderson and Arthur, 1983; Fig.4.5). In the Istria region, where the Δ_{47}-based paleotemperatures are plausible (between ~34 and 45 °C), the calculated $\delta^{18}O_{seawater}$ is within the $\delta^{18}O_{seawater}$ variations reported from the modern restricted marine environment (*e.g.*, the Arctic Ocean, and the Mediterranean and Red Sea; ~-2 to +2 ‰; Grossman 2012, and references therein). The calculated $\delta^{18}O_{seawater}$ is -0.11±1.53 ‰ in the Turonian *H. incisa*, 1.43±0.97 ‰ in the middle Coniacian *P. ciryi*,

0.04±1.84 ‰ in the Coniacian *M. herakii*, and 0.94±1.8 ‰ in the Santonian *B. stoppanianus* (Fig.4.5).

The $\delta^{18}O_{seawater}$ suggested for the Late Cretaceous ice-free oceans is -1 ‰ (*e.g.*, Grossman and Joachimski, 2022). Nevertheless, the processes near shore are likely to affect the local $\delta^{18}O_{seawater}$ in shallow-marine environments. Enhanced precipitation or proximity of a source of freshwater can lower the local $\delta^{18}O_{seawater}$, whereas evaporation often increases the $\delta^{18}O_{seawater}$ value (Grossman, 2012; Pearson, 2012). The different $\delta^{18}O_{seawater}$ calculated for well-preserved specimens from different ages/localities in the Istria region (Fig.4.5) can be explained by the local evaporation-precipitation balance affecting the shallow-marine environment at around 30 °paleoN which caused deviation of the local $\delta^{18}O_{seawater}$ value from the average $\delta^{18}O_{seawater}$ of the open ocean. This further highlights the importance of using thermometers independent of the $\delta^{18}O_{seawater}$ variations, such as clumped isotope thermometry, especially in the shallow-marine environment that is likely susceptible to local $\delta^{18}O_{seawater}$ variations. Moreover, by better constraining the $\delta^{18}O_{seawater}$ in a given time and locality, absolute paleotemperatures can be calculated more reliably based on the widely used $\delta^{18}O$ analysis, and therefore, the potential of the $\delta^{18}O$ thermometry can be fully applied.

4.5.2 Diagenetic screening

The difference in the Δ_{47} results between Friuli and Istria regions could be attributed to the different preservation of the specimens/radiolitid fragments due to the diagenetic overprinting. Carbonates can be altered through a variety of reactions that partially or completely modify the original isotopic signal (Fernandez et al., 2021). Several mineralogical and geochemical tools have been developed to detect the signs of diagenetic alterations caused by dissolution and recrystallization (*e.g.*, Ullmann and Korte, 2015). All the radiolitid shell fragments from the Devetachi section analyzed for this study were carefully screened for diagenetic alteration (see Chapter 3). The diagenetic screening of the nearly complete specimens presented in this study is discussed below.

Several lines of research proved that the preservation of the original geochemical signature of biogenic low-Mg rudist bivalves is also matched by the good preservation of the original shell microstructure (Frijia et al., 2015 and references therein). The material from the nearly complete rudist specimens analyzed in this study (Δ_{47}, $\delta^{18}O$, and Sr-isotope analyses) was obtained from the selected shell areas showing good preservation of the original shell microstructure under the microscope (illustrated in Fig.4.6a,b). Furthermore, a

multidisciplinary approach that combines petrographic screening, and geochemical methods (stable isotope and elemental analyses, μXRF) is generally used to discern the degree of preservation of rudist shells (de Winter and Claeys, 2016; Frijia et al., 2015; Schmitt et al., 2022; Steuber et al., 2005 among others). Meteoric diagenesis of low-Mg biotic calcite typically results in Mn and Fe enrichment and coincident Sr (and Mg) depletion (Al-Aasm and Veizer, 1986; McArthur, 1994; Steuber, 1999). In well-preserved rudist shells, the Sr concentration is usually reported to range between 800 and 1500 ppm, whereas the Fe and Mn concentrations are more variable (upper limits are 150-300 ppm for Fe and 50-200 ppm for Mn; e.g., Steuber, 1999; Frijia et al 2015; Schmitt et al., 2022). In this study, the Fe and Mn thresholds are set to the upper limits, 300 and 200 ppm respectively.

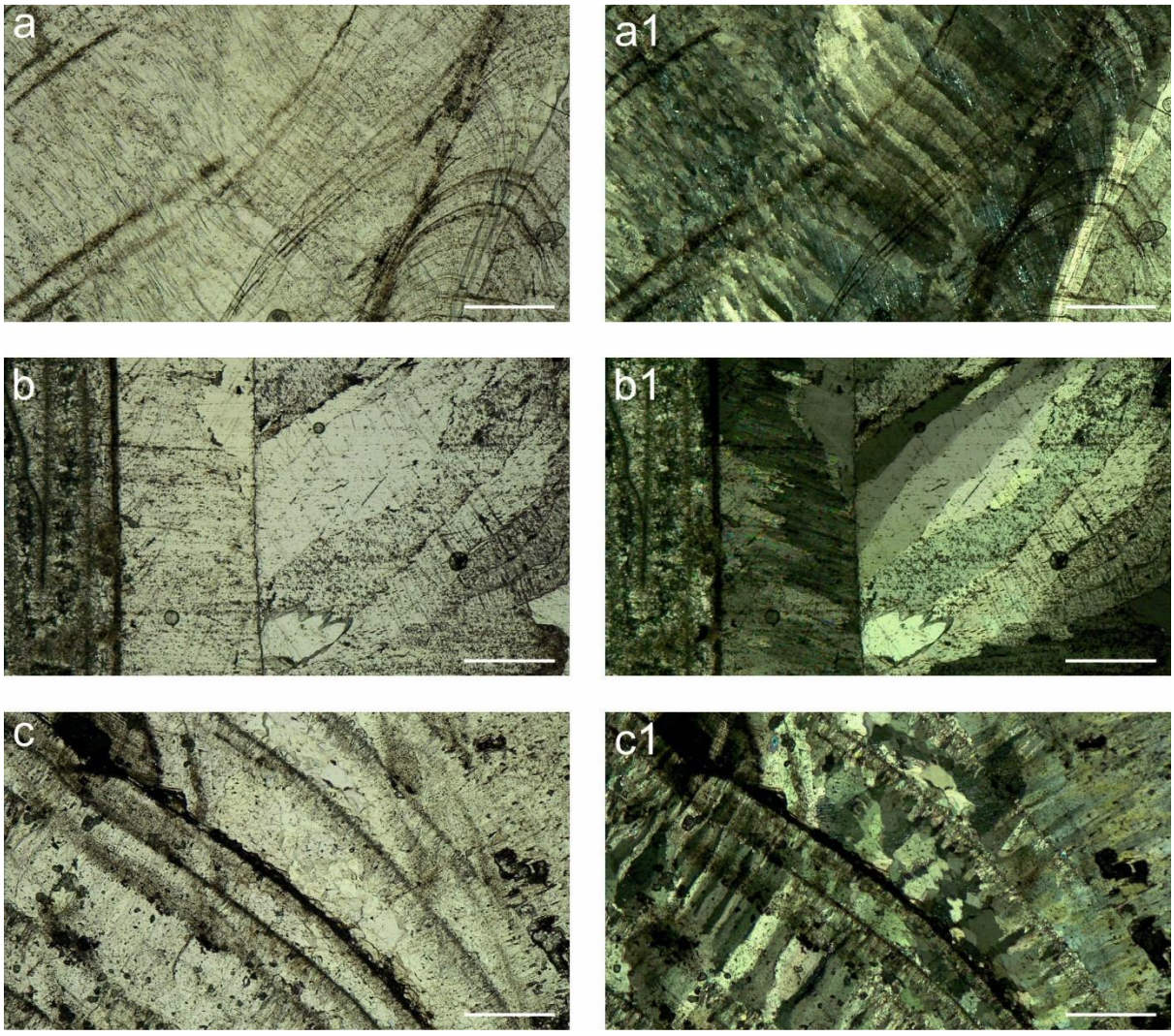

Fig.4.6. Thin sections of the studied specimens. Plane polarized light (a-c), and cross-polarized light (a1-c1). **a.** *Praeradiolites ciryi*, plane polarized light, outer shell layer with distinct growth laminae, **a1.** *P. ciryi*, cross-polarized light, note the prismatic microstructure of the shell suggesting the well-preservation of the outer shell layer. **b.** *Miloranovicia herakii*, well-preserved outer shell layer is visible on the right, the inner portion of the

shell filled by matrix, and diagenetic calcite on the right. **b1.** The prismatic microstructure of the shell suggests the well-preservation of the outer shell layer (on the right) when viewed in the crossed polarized light **c.** *Biradiolites stoppanianus*, plane polarized light, outer shell layer shows distinct growth lamellae but shows secondary cements well visible in the crossed polarized light (**c1**).

To evaluate the possible degree of diagenetic alteration, Mn, Fe, and Sr concentrations were measured using different methods (µXRF and ICP-AES). µXRF analysis was performed on shells of two rudist specimens, *H. nabresinensis* (Friuli region, Aurisina locality) and *P. ciryi* (Istria region, Punta secca Vinjole; Fig.4.4).

The results of the µXRF point-by-point analysis performed on *H. nabresinensis* show an average Sr content of 979 ppm (Fig.4.4b), which differs from the results of the elemental analysis which is 1448 ppm (Tab.2). Nevertheless, both values are well within the range reported for well-preserved rudists. The results of the µXRF analysis of Mn and Fe elemental concentrations are 104 and 57 ppm respectively, whereas the results of elemental analysis yield concentrations of Mn 0.9 ppm and Fe 3.2 ppm; both elements show concentrations well below the limits for preserved rudist shells. The high Mg concentration shown by elemental analysis (Tab.2) further supports the conclusion that the shell of the Friuli rudist specimen, *H. nabresinensis*, is well-preserved.

The results of µXRF line scans clearly show the thick outer shell layer of *P. ciryi* by an increase in Sr concentration (Fig.4.4c, 1-2). The average Sr concentration of 1461 ppm resulting from the µXRF analysis, as well as the result of elemental analysis (1160 ppm) are within the range reported for well-preserved rudist specimens (see above). µXRF line scan (Fig.4.4d) shows generally low Mn and Fe concentrations, apart from one peak in Mn and five peaks in Fe concentrations. Therefore, the average values of the µXRF line scan for Mn 109 ppm and Fe 342 ppm significantly differ from the results of the elemental analysis: 0.5 ppm for Mn and 4.0 for Fe. Inclusions with higher concentrations are well visible in the µXRF element concentration maps (Fig.4.4c). These inclusions generally indicate altered parts of the shell. The elongated shapes of these inclusions (Fig.4.4c) most likely represent microscopic cracks filled with secondary calcite cement. Overall, the good preservation of the shell of *P. ciryi* (Istria) is documented by generally low Mn and Fe content, and high Sr concentration accompanied by a high content of Mg (a result of the elemental analysis, 1151 ppm). To conclude, the µXRF analysis shows no evidence of diagenetic overprinting of the Friuli specimen *H. nabresinensis*, compared to the Istria specimen *P. ciryi*, which could explain the difference in the Δ47-based paleotemperatures between the regions.

To further assess the preservation of the remaining rudist specimens, the elemental analysis was performed to complement the optical screening and the μXRF analysis (Tab.2). The remaining rudist specimen from the Friuli region, *V.* cf. *cornuvaccinum*, shows values well within the range for well-preserved rudist specimens (see above).

In the specimens from the Istria region, good shell preservation is suggested by the elemental analysis results for *M. herakii* (Fig.4.7b, Tab.4.2). The Fe content is very low (11.2 ppm), whereas the Mg and Sr concentrations are in the range of the values reported for well-preserved rudists. In *B. stoppanianus*, the elemental analyses were not performed as petrographic observation showed a partial recrystallization of the shell (Fig.4.6c). For this specimen, $\delta^{18}O$ and $\delta^{13}C$ cross-plot and $^{87}Sr/^{86}Sr$ vs. $\delta^{18}O$ and $\delta^{13}C$ were used to assess the possible reliability of the isotopic data (Fig.4.7). The isotopic composition of *B. stoppanianus* plots away from the other analyzed samples, which composition overlaps with the field of well-preserved rudists (Fig.4.7; Steuber et al.,2005; Schmidt et al: 2023). Considering that the negative $\delta^{13}C$ value is associated with one of the most negative $\delta^{18}O$ values argues for a slight recrystallization of the shell of *B. stoppanianus*.

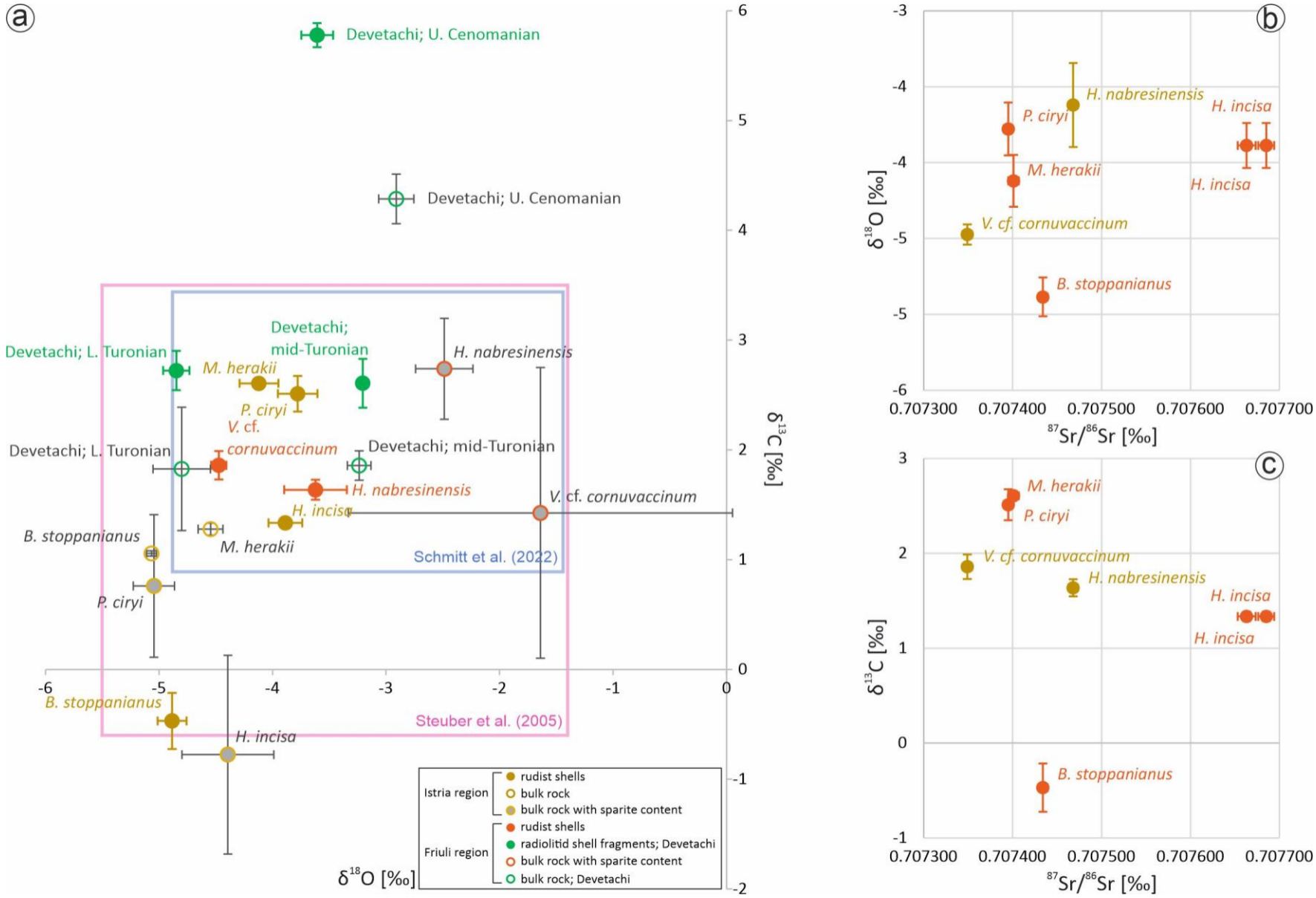
a
Devetachi; U. Cenomanian
Devetachi; U. Cenomanian
Devetachi; L. Turonian
Devetachi; mid-Turonian
M. herakii
P. ciryi
V. cf. cornuvaccinum
H. nabresinensis
H. incisa
B. stoppanianus
Schmitt et al. (2022)
Steuber et al. (2005)
δ18O [‰]
δ13C [‰]
Istria region
rudist shells
bulk rock
bulk rock with sparite content
Friuli region
rudist shells
radiolitid shell fragments; Devetachi
bulk rock with sparite content
bulk rock; Devetachi
b
δ18O [‰]
87Sr/86Sr [‰]
c
δ13C [‰]
87Sr/86Sr [‰]

Fig.4.7.**a.** Cross-plot of average values of $\delta^{18}O$ and $\delta^{13}C$ of the analyzed rudist specimens and rudist fragments. The blue rectangle represents the range of well-preserved radiolitids from the study of Schmitt et al. (2022), and the pink rectangle represents the range of well-preserved Upper Cretaceous rudists from Steuber et al. (2005). The error bars for each symbol show 95% confidence limits for both $\delta^{18}O$ and $\delta^{13}C$. The shell analyses of all studied complete specimens fall within the range of well-preserved rudists, the shell of *B. stoppanianus* is depleted in $\delta^{13}C$ likely due to slight recrystallization of its shell. Shell fragments from the Devetachi section show good preservation within both ranges of well-preserved rudists, apart from the Upper Cenomanian sample, which corresponds to the enrichment in $\delta^{13}C$ during the Cenomanian-Turonian boundary event (OAE2). The data points representing the matrix (possibly with sparite content) mostly show a large 95%CL. **b.** Cross-plot of $^{87}Sr/^{86}Sr$ and $\delta^{18}O$. **c.** Cross-plot of $^{87}Sr/^{86}Sr$ and $\delta^{13}C$, both showing no correlation and a narrow range of Sr isotope values for all the analyzed rudists except for *H. incisa*.

In *H. incisa*, despite the isotopic composition ($\delta^{18}O$ and $\delta^{13}C$) showing values within the range of the other analyzed specimens, the $^{87}Sr/^{86}Sr$ results yield values markedly different from the rest of the dataset (Fig.4.7b, c). It may suggest either a very different (younger) age than biostratigraphy suggests, or a diagenetic overprinting of the shell. Usually, diagenesis lowers the Sr concentration and increases the Sr-isotope values (Steuber et al., 2005; Frijia et al 2015). The Sr concentration in *H. Incisa* is very low (196 ppm), accompanied by considerably higher Fe content compared to the other specimens (92.4 ppm), and by the highest $^{87}Sr/^{86}Sr$ value. These findings suggest that the area of the shell drilled for the $^{87}Sr/^{86}Sr$, and elemental analysis was diagenetically altered. Nonetheless, the results of $\delta^{18}O$ and $\delta^{13}C$ analyses of the bulk shell material fall well within the range of well-preserved rudist specimens (Fig.4.7a), which suggests that these results reflect the original isotopic signal of the seawater.

The $\delta^{18}O$ results of rudist specimens/fragments from both, Istria and Friuli regions, show results between -2.48 and -5.29 ‰; values comparable to the $\delta^{18}O$ ranges of the Santonian-Campanian rudists from the Tethyan realm reported by Steuber (1996; ~-2 to -4.5 ‰) and by Steuber (1996; -2.69 to -5.28 ‰).

To conclude, the shell material of the nearly complete rudist specimens from the Friuli and Istria regions show no signs of recrystallization that could explain the difference in the Δ_{47} results. Apart from one sample (*B. stoppanianus*), all samples show no signs of recrystallization when observed under the microscope (Fig.4.6, Chapter 3) and fall within the range of values reported for well-preserved Cretaceous rudists (Fig.4.7a). Furthermore, one specimen from each region analyzed for the elemental composition (µXRF) shows no recrystallization of the shell material; no difference possibly explaining the difference in the Δ_{47} results observed between Friuli and Istria regions. Consequently, our data suggest that the difference in the Δ_{47}

results between Friuli and Istria regions is not accompanied by a significant shift in $\delta^{18}O$ results and more likely corresponds to regional differences in diagenetic evolution, rather than to the differences in the preservation of fragmented vs. complete fossil material.

4.5.3 The Friuli region – case of solid-state reordering?

Some diagenetic alterations-related processes involve no mass transfer and thus do not affect trace element or stable isotope (C and O) compositions, yet they can partially or completely reset clumped isotope compositions (*e.g.*, Fernandez et al., 2021; Henkes et al., 2014; Stolper and Eiler, 2015). These bond-reordering reactions proceed in the solid-state, resulting in a relative motion of carbon and oxygen atoms with respect to each other within the lattice of carbonate minerals (Affek, 2012). Partial or complete reordering occurs when carbonates are exposed to elevated burial temperatures high enough to break the kinetic energy barrier for O and C movement within the carbonate lattice (Stolper and Eiler, 2015). The model of Henkes et al. (2014; Fig.4.8) illustrating the threshold behavior of carbonate clumped isotope reordering, suggests that the burial temperatures must reach a threshold of 100°C before significantly starting to influence the resulting Δ_{47}-based temperatures. Consequently, it is possible to find samples with pristine textures, stable isotope signatures, and trace element concentrations but with strongly altered Δ_{47} results (Fernandez et al., 2021; Henkes et al., 2014; Smith et al., 2022). The results of our study point out that alteration of the Δ_{47} results in the Friuli region is not accompanied by obvious changes in $\delta^{18}O$, nor in 87Sr/86Sr (Fig.4.3, 4.7, Tab.2.).

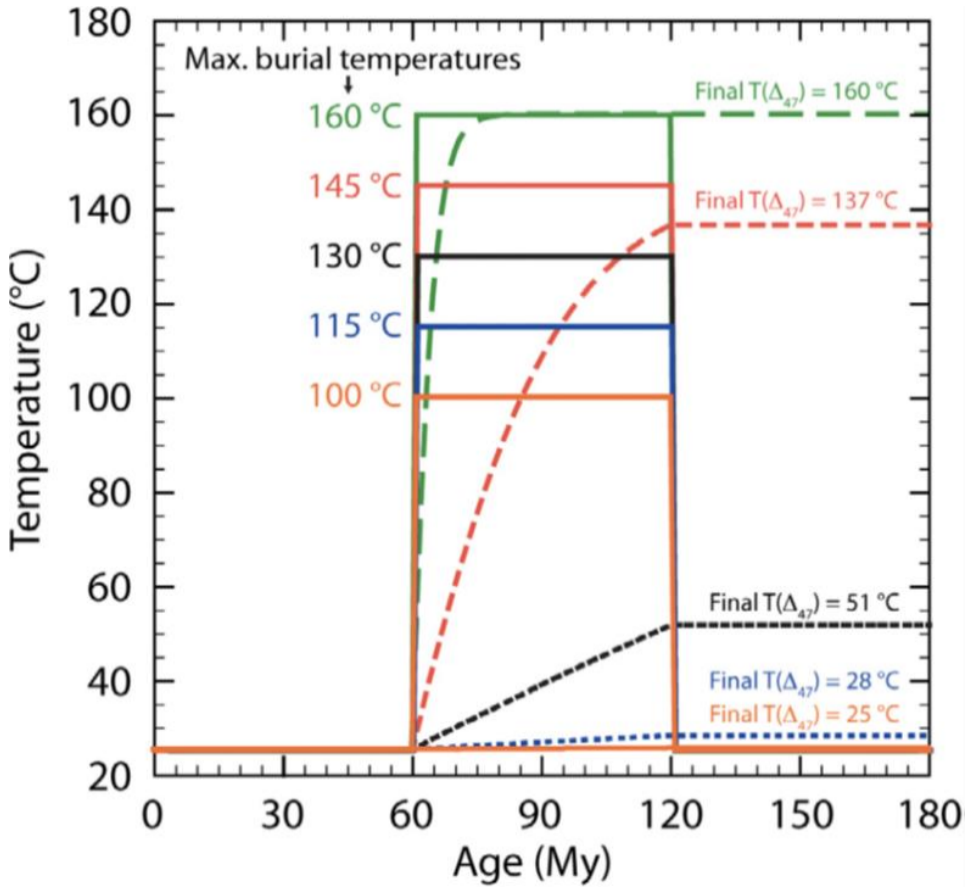

Fig.4.8. Threshold behavior of carbonate clumped isotope reordering illustrated for heating scenarios lasting 60Ma. The solid lines show the temperature forcing in 15°C increments from 100 to 160°C. Dashed and dotted lines represent the model response at each time step. At 100°C maximum burial temperature, there is no evidence of change from the initial Δ_{47} temperature, whereas, at 160°C maximum burial temperature, the model predicts complete reordering. From Henkes et al. (2014).

Following the hypothesis of solid-state reordering explaining the regional Δ_{47} differences between the Istria and Friuli, we attempt to reconstruct the burial history of the two regions. Commonly, the temperature-time histories of sedimentary rocks are reconstructed using models calibrated by paleothermometric data. Apart from, for example, the study of fluid inclusions, vitrinite reflectance, or conodont color alteration index (Henkes et al., 2014), these data are obtained by studying the thickness, lithologies, and ages of overlying stratigraphic formations, and by assumptions on heat flow (Shenton et al., 2015). Defining thermal history is necessary for reconstructing the effects of burial temperatures on the clumped isotope composition of fossils. Uniform time steps (one million years long) are found to be sufficiently short for accurate modeling of reordering progress (Henkes et al., 2014). Not always, though, are the paleothermometric data available.

Unfortunately, available literature data on this topic concerning the Friuli region is scarce, as most of the data sources are unpublished industry reports. The thermal maturity (and therefore the maximum burial depth) of the organic matter in the Cretaceous carbonates of the Friuli region has been inferred from the compilation of vitrinite reflectance data by Rainer et al. (2016; Fig.4.9). The Friuli localities, Devetachi and Aurisina, fall within the area that underwent a modeled burial temperature reaching maxima of 150-190 °C. Our results show Δ_{47}-based paleotemperatures of 92-101 °C in the rudist fragments (Devetachi), and 73-80 °C in the nearly complete rudist specimens (Aurisina), arguing for (incomplete; see below) resetting of the original clumped isotope signal due to the solid-state reordering regardless of whether the fossil material is preserved in the form of fragments or as nearly complete specimens.

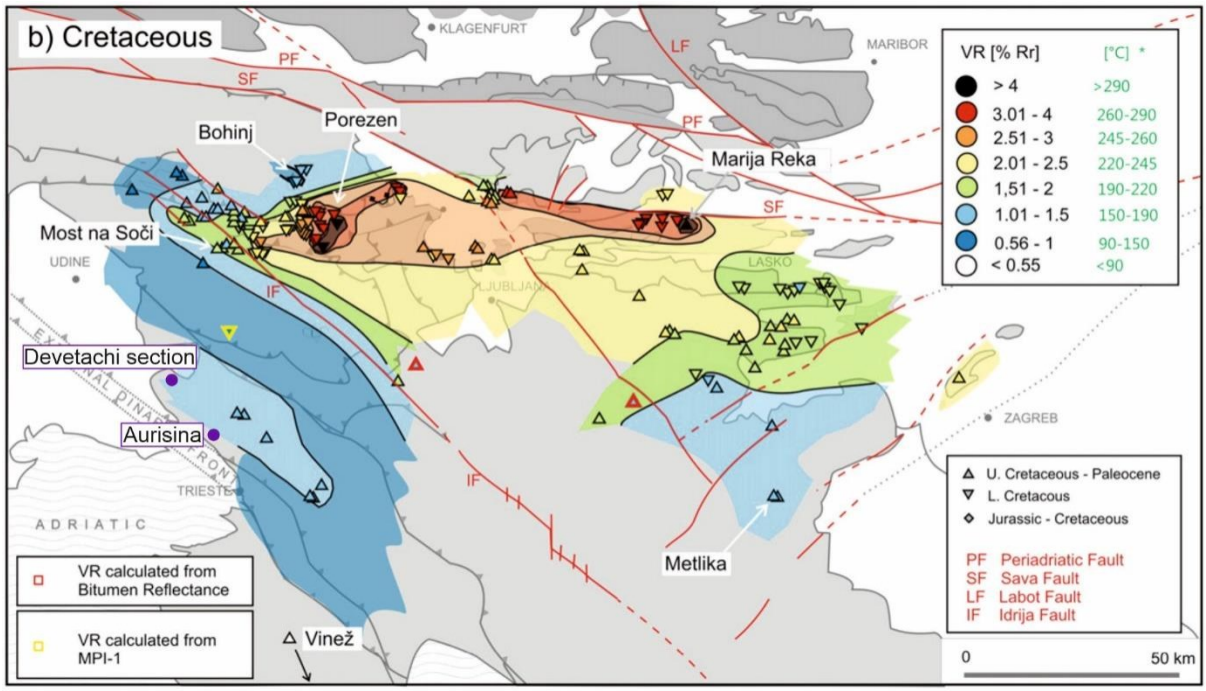

Fig.4.9. Thermal maturity map for Cretaceous rocks within the Alpine-Dinaric Transition Zone (including the Friuli region on the western edge of the map) based on the vitrinite reflectance (VR) data. Modified after Reiner et al. (2016). Two localities from the Friuli region, Devetachi section and Aurisina, are marked (purple points) within the area where the Upper Cretaceous sediments underwent the maximum burial temperatures between 150 and 190 °C (light blue).

There is no published information on the thermal maturity of the Istria region. Nevertheless, the difference in Δ_{47} signal between the reordered Δ_{47} composition in Friuli and the Δ_{47} results from the Istria region showing lower reconstructed temperatures suggests a different burial history of the peri-Adriatic Cretaceous platform carbonates, possibly due to the different

tectonic evolution of the two regions during the Cenozoic. Both regions were part of the large Mesozoic Adriatic Carbonate Platform, which passive margin stage ended with the onset of the Alpine collision in the Paleogene (Posenato et al., 2020 and references therein). Consequently, part of the AdCP (including the Friuli region and Istrian Peninsula) started acting as the foreland of the orogenic system with a regional flexure and uplift. In the Eocene, part of the previous foreland started to subside gradually becoming a foredeep, due to the SW migration of the Dinaric fold-and-thrust belt, and the carbonate successions were overlain by flysch deposits (del Viscio et al., 2022 and references therein). Due to the complicated orogenic evolution and different angles of the migration of the compressional front (Korbar, 2009), different thicknesses of the overburden Cenozoic synorogenic and post-orogenic deposits have been deposited in Friuli and Istria. Unpublished data consider the preserved Palaeocene-Eocene limestones and Eocene flysch deposits to show an increase in thickness toward NE with a maximum post-Cretaceous overburden thickness difference of ~1500 m between Istria and the Friuli Karst region without considering possibly eroded younger sedimentary successions (S. Venturini, unpublished data; Fig.4.10, personal communication). Their presence seems to be indicated by unpublished thermal maturity data from the Prealpine region of Friuli (S. Venturini personal communication).

Considering an average geothermal gradient of 30 °C/km, this sediment thickness difference would translate into possible maximum burial temperatures difference between the Friuli and Istria regions of around 40 °C, indicating maximum burial temperatures in the Istria region between 110 and 150 °C. Nonetheless, the Δ_{47}-based temperatures in the Istria region (Fig.4.5) suggest good preservation of the original Δ_{47} composition in Istria, suggesting that the burial temperatures did not exceed 110 °C for more than ~30 Ma (Henkes et al., 2014). On the other hand, the Δ_{47} results from the Friuli region suggest solid-state reordering of the original C-O bonds.

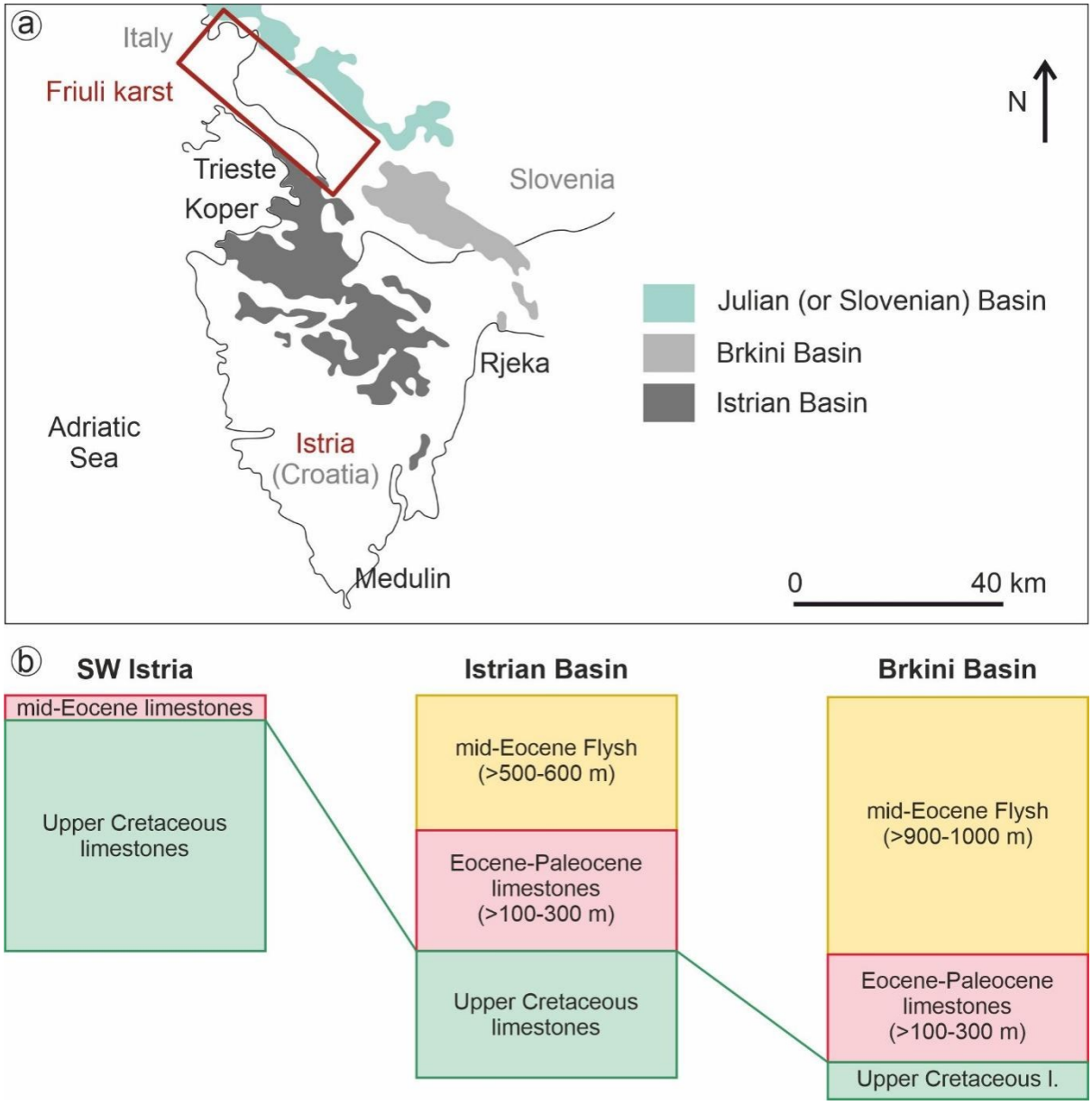

Fig.4.10. Estimated sedimentary cover overlaying the Upper Cretaceous sediments in Western Istria and Friuli karst (near Brkini Basin). **a.** Simplified map of the studied regions. **b.** In the Friuli region (Carso), approximately 1500 m of flysh overlie the Upper Cretaceous limestones. Unpublished figure from S. Venturini, 2023.

The maximum calculated Δ_{47}-based paleotemperatures found in the Friuli samples analyzed in this study are lower than the maximum burial temperatures experienced by the Cretaceous deposits in the region (Fig.4.5, 4.9). Burial temperatures between 150 and 190 °C indicated by Rainer et al. (2016) would correspond to complete solid-state reordering if the maximum burial temperatures reaching over 160 °C lasted for at least ~20 Ma according to the model of Henkes et al. (2014). The maximum Δ_{47}-based paleotemperatures in the studied material from the Friuli region (Devetachi section) reach 101 °C. Either the studied material did not reach thermal equilibrium at the maximum burial temperature due to the short burial period (under ~3 Ma at

over 160 °C, or the temperatures were 'locked in' at lower temperatures during the exhumation of the region as described in the model of Henkes (2014). Due to the lack of published data that would enable reconstructing the thermal history, especially in the Istria region, it is not possible to reliably distinguish the extent to which these factors control the apparent Δ_{47}-based temperatures. Nevertheless, our data imply that the temperature limit for reordering the C-O bonds within rudist calcite lies somewhere between 110 and 150 °C, considering the lowest maximum burial temperature indicated for the Istria and Friuli regions.

Since different carbonate components can differ in the rate by which the clumped isotope composition is reordered due to variations in primary mineralogy and porosity (brachiopods, crinoids, cements, etc.), variable potential for C-O bond reordering kinetics can be expected (Shenton et al., 2015). The apparent Δ_{47} composition results from the initial temperature, the temperature, timing, and range of recrystallization, and the possible extent of solid-state reordering (Shenton et al., 2015). Some studies argue that the relative temperature differences are preserved when samples experience a common burial history because the solid-state reordering shifts the original Δ_{47} values by about the same amounts (*e.g.*, Cummins et al., 2014). However, as pointed out by Fernandez et al. (2021) this remains a hypothesis, that has not yet been tested in measuring reordered natural fossil calcite. Thus, more studies on rudist bivalves from localities with well-constrained thermal histories are needed to assess the order-specific response to elevated burial temperatures.

Meaningful environmental reconstructions based on clumped isotope composition of various fossil materials are limited to sedimentary basins with relatively shallow burial histories (Henkes et al., 2014). This is a concern in areas around the deformation fronts of the orogenic belts. In this study, both regions are located in the Adriatic foreland of the External Dinarides (Korbar, 2009). The difference in the position of the studied localities relative to the sediment (flysh) source area is what most likely causes the difference in the preservation of the original Δ_{47} composition in the samples from the Istria region and the solid-state reordering of the Friuli samples.

4.6 Conclusions

Four nearly complete rudist specimens from the Istria region (*Praeradiolites ciryi*, *Biradiolites stoppanianus*, *Hippurites incisa*, *Miloranovicia herakii*), and two complete specimens (*Vaccinites* cf. *cornuvaccinum*, *Hippurites nabresinensis*) and four radiolitid fragments from the Friuli region were analyzed for Δ_{47} and $\delta^{18}O$ composition. The resulting Δ_{47}-based

temperatures in the Istria region are in accordance with those obtained by $\delta^{18}O$ analysis and are comparable to previously published Late Cretaceous SSTs. Contrarily, in the Friuli region, they show a considerable offset towards as much as 101 °C. Regardless of the size and completeness of the analyzed rudist fragments or specimens, the Δ_{47}-based paleotemperatures (the lowest being 73 °C) are above the maxima for recent multicellular organisms (50 °C; Brock, 1985).

Thorough diagenetic screening (petrographic observations, $\delta^{18}O$ and $\delta^{13}C$ comparison to previously reported well-preserved calcite, and μXRF) was performed to determine the extent of the diagenetic alteration of the stable and clumped isotopic composition in the studied samples. The results show that neither of the methods of diagenetic screening applied to the presented dataset detects any difference in the preservation of the studied specimens between the Friuli and Istria regions. The main factor controlling the preservation of the Δ_{47} original isotopic signal in the presented rudist specimens is the burial history of the Istria and Friuli regions. The solid-state reordering of the shells from the Friuli region is not reflected in any of the diagenetic screening methods used in this study, apart from the Δ_{47} composition of the samples. Our results support the importance of a thorough investigation of thermal history and/or the burial history of samples of interest, which should preclude the performance of the clumped isotope analysis.

5 The $\delta^{18}O$ of the seawater and seasonal temperature fluctuations in the Late Cretaceous rudist bivalves from the Adriatic Carbonate Platform (Istria, Croatia): Stable isotope analysis and clumped carbonate thermometry

5.1 Introduction

Paleoclimatic reconstructions of past greenhouse climate stages provide unique insight into Earth's climate system and a possibility to enhance understanding of the effects of globally rising temperatures on the biosphere (Burgener et al., 2019; Tierney et al., 2020). During the Cretaceous, greenhouse conditions prevailed (Huber et al., 2002), with a warming peak in the Early Turonian (see Chapter 3), marking one of the warmest climates of the past 140 million years (Linnert et al., 2014 and references therein). Despite that the Late Cretaceous general climate trends are well-established (Friedrich et al., 2012; Huber et al., 2018; O'Brien et al., 2017), estimating the absolute temperatures, as well as seasonal temperature variations, remains challenging. The understanding of the evolution of Cretaceous sea surface temperatures (SSTs) is mostly based on oxygen isotope analysis of planktonic and benthic foraminifera (Grossman, 2012), or bulk rock fine-fraction carbonates, mainly from the pelagic environment (*e.g.*, Clarke and Jenkyns, 1999). Unlike foraminifera, well-preserved shells of marine bivalves can record local environmental fluctuations in growth increments of their shells (de Winter et al., 2020, 2017a; Steuber et al., 2005b), allowing for estimating not only the average paleotemperatures but also seasonal temperature variations.

Upper Cretaceous shallow-water carbonate platforms were dominated by rudist bivalves (Kauffman and Johnson, 1988; Gili et al., 1995; Steuber et al., 2016). Rudist shells have been extensively used for $\delta^{18}O$-based paleoclimate studies, including seasonal temperature variation estimates (de Winter et al., 2020, 2017a; Immenhauser et al., 2016, 2005; Steuber et al., 2005b; Walliser and Schöne, 2020).

Despite a large number of studies dedicated to paleotemperature reconstructions in deep time, the $\delta^{18}O$-based SST estimates remain problematic in their absolute values. This results from the main limitation of the $\delta^{18}O$ paleothermometer. The relationship between the $\delta^{18}O_{calcite}$ and temperature depends on $\delta^{18}O_{seawater}$ which, in turn, depends on the amount of polar ice and local evaporation-precipitation balance (Grossman, 2012; Pearson, 2012), both of which are difficult

to independently constrain in the sedimentary record (Cummins et al., 2014; see Chapter 1.2.1). Therefore, the unknown and possibly variable original oxygen isotopic composition of past oceans is the major issue hampering reliable calculations of the $\delta^{18}O$-based paleotemperatures (Song et al., 2019a).

Clumped isotope thermometry (Ghosh et al., 2006; Schauble et al., 2006), has become increasingly used in combination with $\delta^{18}O$ paleothermometry (Cummings et al., 2014). This thermometer is based on ordering (clumping) of the ^{13}C–^{18}O atoms into bonds with each other within a carbonate mineral lattice – as the formation temperature decreases, the clumping of heavy isotopes into a single carbonate ion increases (Schauble et al., 2006; see Chapter 1.2.2). Consequently, the clumped isotope composition of carbonate is independent of the $\delta^{18}O$ of the ambient water and, as such, it can be used to calculate the $\delta^{18}O$ of the water from which the calcite was precipitated (Cummings et al., 2014).

In this study, we address the issue of the Late Cretaceous paleotemperature and seasonal changes in shallow-marine environments using two well-preserved specimens from Istria (Croatia); Turonian *Hippurites incisa* and mid-Coniacian *Praeradiolites ciryi*. The thick, outer shell layers of these specimens were analyzed for bulk shell clumped isotope composition, and detail growth profiles were analyzed for stable isotope (C and O) composition. Combining the clumped and oxygen isotope analyses resulted in absolute and seasonal paleotemperature estimates and allowed for inferring the $\delta^{18}O_{seawater}$ for mid-Cretaceous shallow-water habitats at around 30 °paleoN.

5.2 Geological settings

This study is based on analyses of two rudist specimens from two localities in Istria (Croatia) (Fig.5.1a) : Punta secca Vinjole in SE of Istria, and Medulin at the southern tip of the Istrian Peninsula. For the geological settings and detailed geological evolution of Istria, the reader is referred to Chapter 4.

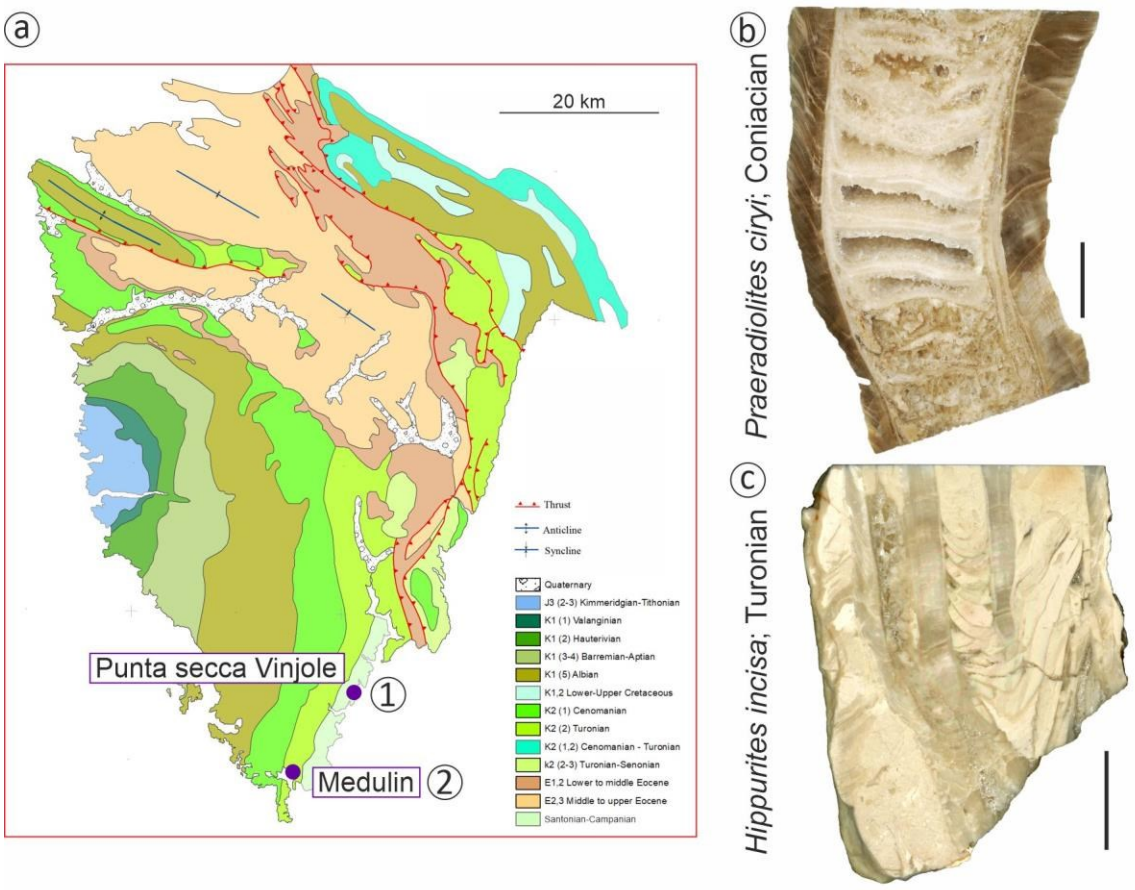

Fig.5.1. **a.** Location of the localities Punta secca Vinjole (a1) and Medulin (a2) on the geological map of the Istrian Peninsula (simplified from Jurkovšek et al. (2016), and the studied specimens. **b.** middle Coniacian specimen *Praeradiolites ciryi* and **c.** Turonian specimen *Hippurites incisa*. Scales equal 1cm.

5.3 Material and Methods

The two rudist specimens used in this study were provided by the Museum of Natural History in Trieste. The samples were selected after preliminary visual inspection (using a binocular microscope) of the shell structures, showing a high degree of preservation of the compact low-Mg calcite outer shell with visible prismatic structures and the growth increments (see Fig.4.5). The study was performed on the lower (attached) valves of rudists *Hippurites incisa*, and *Praeradiolites ciryi* (Fig.5.2). To obtain the most reliable dataset and avoid possibly diagenetically altered portions of the shells, different areas of shells in both specimens were drilled (Fig.5.2). The initial Shell tests (rough sampling from transversal cuts (*H. incisa*), and outer shell layer in *P. ciryi*; Fig.5.2, in blue) were complemented by Bulk shell sub-datasets for both shells (Fig.5.2, in green). Furthermore, growth profiles were sampled in both shells, starting with coarse-resolution sampling through darker and lighter areas/growth increment sets (Fig.5.2, in grey) and resulting in detailed sampling through the entire sclerochronological profiles (Fig.5.2, in pink) of the outer shell layer in *P. ciryi* and of a pillar in *H. incisa*. The

results, therefore, yield four sub-datasets for both shells, three of which were used for interpretations in this study.

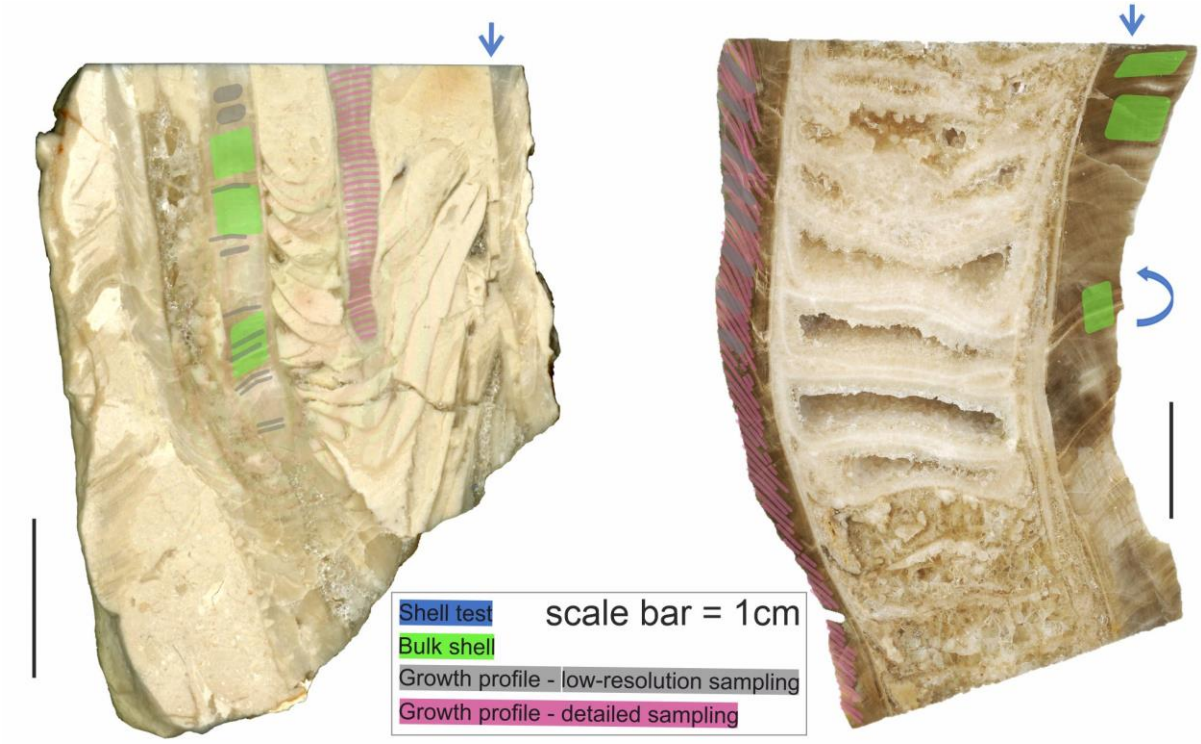

Fig.5.2. Different areas of the studied specimens drilled for Clumped and stable isotope analyses in *Hippurites incisa* (left) and *Praeradiolites ciryi* (right). The Shell test drilling areas (in blue) indicate a point-drilling on the surface of the transects in both specimens, and additional point-drilling on the shell surface in *P. ciryi*.

Clumped isotope and simultaneous $\delta^{18}O$ and $\delta^{13}C$ measurements were performed at Utrecht University (for methodology, see Chapter 2.3). 213 aliquots of the shell material were analyzed in total. The resulting dataset was screened, and outliers were removed (methodology is described in Chapter 4). Results of clumped isotope analysis were averaged per drilling area in each sample, and sample areas showing standard deviation (SD) larger than that shown by the Growth profile-detailed sampling sub-dataset were excluded from further interpretations (see Supplementary information 1). In total, 155 aliquots of the shell material were used for further interpretations. The detailed sampling of the growth profiles did not provide enough shell material to measure each of the drilled growth lines for the Δ_{47} composition. Therefore, 77 aliquots in total were measured for $\delta^{18}O$ and $\delta^{13}C$ composition only, at the University of Ferrara (for the methodology, see Chapter 2.2). Results of $\delta^{18}O$ and $\delta^{13}C$ are reported in ‰VPDB, and the errors on stable isotope and clumped isotope analyses are reported as 95% confidence limits (95%CLs). The $\delta^{18}O_{seawater}$ is reported relative to VSMOW, and errors on the $\delta^{18}O_{seawater}$ values are calculated using Monte Carlo statistical approach (nr. of repetitions ≈10 000).

The ages of the specimens are discussed in the previous Chapter (4).

5.4 Results

5.4.1 $\delta^{18}O$ and $\delta^{13}C$ analyses of the sclerochronological profiles of the studied specimens

In *Hippurites incisa*, detailed sclerochronological sampling was performed on one of the pillars (infolding of the outer shell; Figs.5.2 and 5.3) resulting in a 12.1 mm-long profile. A total of 42 aliquots were measured for $\delta^{18}O$ and $\delta^{13}C$. The $\delta^{13}C$ record shows low amplitude fluctuations between 0.94 and 1.50 ‰ with an average of 1.24 ‰. These small fluctuations appear throughout the profile, but no significant cyclicity is visible. The $\delta^{18}O$ profile, on the other hand, shows fluctuations as large as 2.14 ‰. The analyzed profile begins with values close to the average value of the entire profile, -3.77 ‰ which drops toward the minimum value of -4.63‰ between mm 5 and 6. A steep rise towards the maxima of the profile (-2.49 ‰) (mm 10-12), and the successive continuous drop (mm 12-16) towards the average $\delta^{18}O$ of the profile follows. The growth profile of *H. incisa* suggests the preservation of one cycle, possibly corresponding to one year of the duration of the growth profile (see Steuber, 1999). Nevertheless, a sharp increase in $\delta^{18}O$ values from ~ -4 to ~ -2.5 ‰ at around mm 11 suggests a cease of growth of the shell during the year. The isotopic profile shows resuming of the shell growth at $\delta^{18}O$ values of ~ -2.5 ‰. Interestingly, the minimum $\delta^{18}O$ values along the growth profile correspond to the lighter bands within the analyzed profile, whereas the maximum $\delta^{18}O$ values correspond to the darker bands, which are considerably shorter (~3mm vs. 6mm; Fig.5.3).

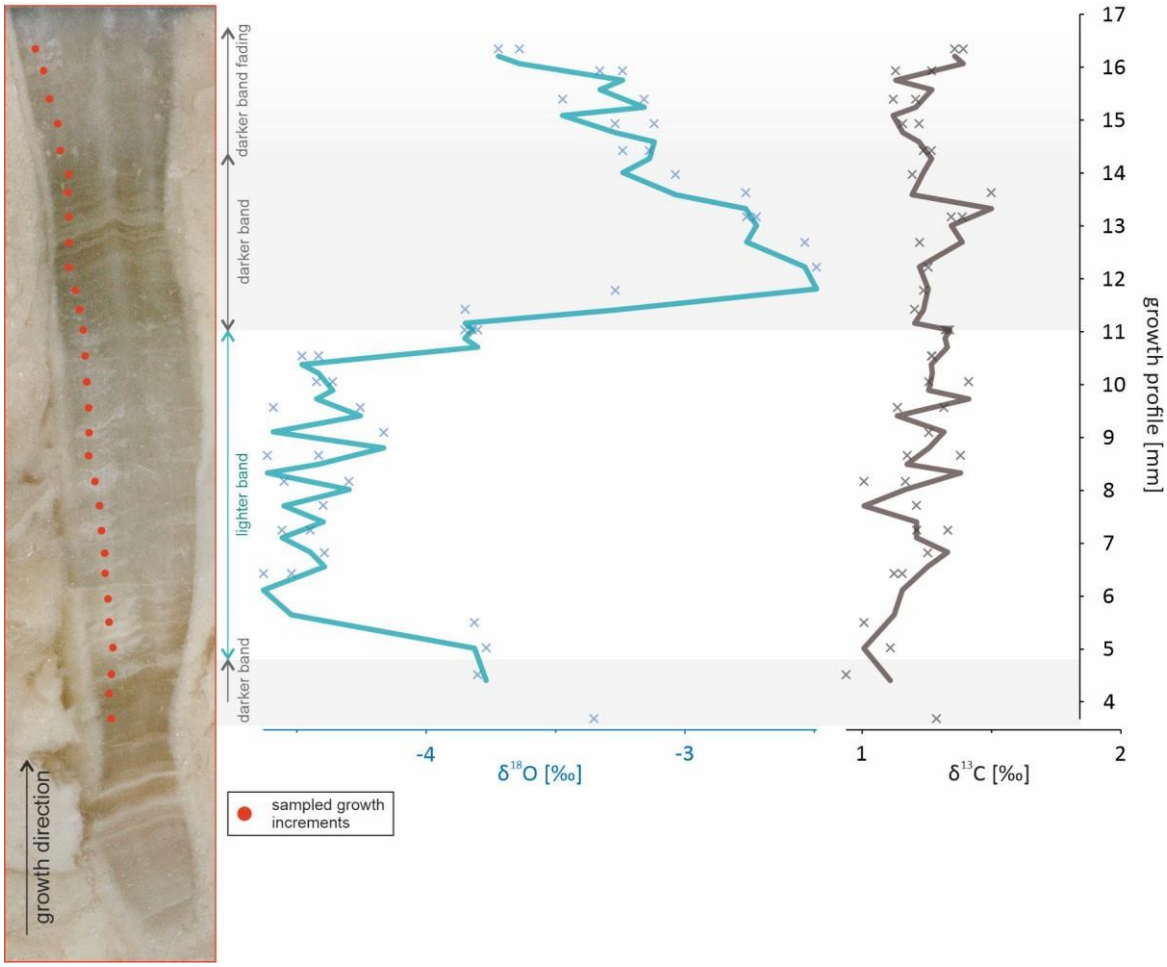

Fig.5.3. Stable isotope analyses along the growth profile of *H. incisa*. The growth increments sampled for analyses are marked along the pillar (left), and $\delta^{18}O$ and $\delta^{13}C$ results are reported. Note the correspondence between negative/positive $\delta^{18}O$ fluctuations and darker and lighter shell growth lines. Dashed lines represent 3 point moving average.

In *Praeradiolites ciryi*, detailed sclerochronological sampling was performed along its outer shell layer (Fig.5.4). In total, 98 aliquots were measured for $\delta^{18}O$ and $\delta^{13}C$, resulting in a 57.1 mm long profile. The $\delta^{13}C$ profile shows fluctuations of 2.22‰ (1.79-4.01 ‰), with an average $\delta^{13}C$ of 2.94 ‰, organized in cycles. The $\delta^{13}C$ profile begins with values close to its minimum and subsequently rises toward the maximum value. A steep drop follows and for the next ~14mm, the $\delta^{13}C$ values slightly fluctuate (± 0.25‰) around the average value of ~3‰. A successive rise of ~0.5 ‰ is the last positive excursion followed by a continuous drop toward values around ~2.20 ‰. The three growth increments measured on the very top of the sampled profile suggest that a rise in $\delta^{13}C$ values would likely follow (the highest among these last aliquots reaches 3.18 ‰). The $\delta^{18}O$ analysis resulted in an average of -3.52 ‰, showing fluctuations of ~2.17 ‰ (-4.62- -2.45 ‰). The $\delta^{18}O$ profile mirrors the $\delta^{13}C$ profile, especially in the upper half of the sampled profile. The $\delta^{18}O$ record begins with maximum values of -2.45

‰, followed by a drop toward the minima. Subsequent rise and fall in the $\delta^{18}O$ values show a similar amplitude as those described above for the $\delta^{13}C$ record. The $\delta^{18}O$ and $\delta^{13}C$ profiles show preservation of one complete and one incomplete cycle, suggesting a year and ~3/4 of the duration of the growth profile (see Steuber, 1999). Despite the growth increments are well-visible in *P. ciryi*, no lighter or darker bands were observed to show pattern corresponding to the $\delta^{13}C$ and $\delta^{18}O$ profiles.

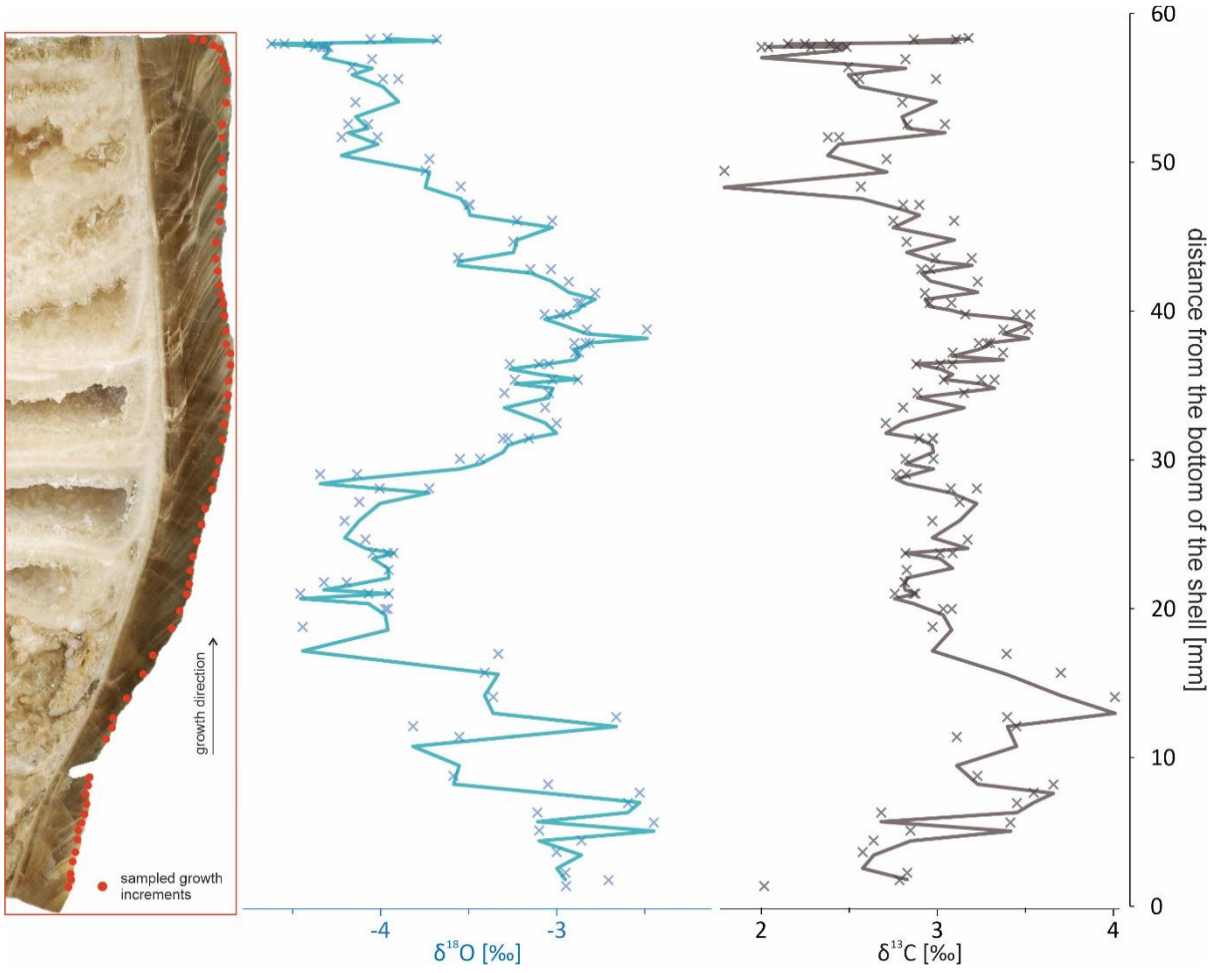

Fig.5.4. Stable isotope analyses along the growth profile of *P. ciryi*. The growth increments sampled for analyses are marked along the pillar (left), and $\delta^{18}O$ and $\delta^{13}C$ results are reported. Note the positive correlation between $\delta^{13}C$ and $\delta^{18}O$ profiles. Dashed lines represent 3 point moving average.

5.4.2 Clumped isotope analysis

The presented dataset (after data filtering; see Methods and Supplementary information 1) yields average values of all the shell material of 0.567±0.018 ‰ for *H. incisa*, and 0.577±0.014 ‰ for *P. ciryi* (uncertainty is given as 95 %CL). Based on the fluctuating $\delta^{18}O$ record throughout the growth profiles in both specimens, the results of the Growth profile sub-datasets were divided in 'seasons' (see Discussions). In *H. incisa*, the cooler season shows Δ_{47} value of

0.541±0.074 ‰, whereas the warmer season yields Δ_{47} result of 0.560±0.048 ‰. In *P. ciryi*, the Δ_{47} results are 0.639±0.043 ‰ and 0.579±0.34 ‰ for the cooler and warmer season respectively.

5.5 Discussion

5.5.1 Preservation of the original clumped and oxygen isotope signal

Even though equilibrium fractionation of oxygen isotopic signal is assumed for rudist bivalves (Steuber, 1996), the subsequent syn- and post-depositional diagenetic alteration of the fossil-bearing sediment can cause diagenetic overprinting of the fossil (*e.g.*, Huck and Heimhofer, 2015). An unintended sampling of an altered portion of the fossil can result in an overestimation of the paleotemperature (Walliser and Schöne, 2020). A particular type of diagenetic alteration affects the clumped isotope composition of carbonates, so-called solid-state reordering (Affek, 2012; Henkes et al., 2014). It is caused by increased burial temperatures, resulting in relative movement of the heavy and light carbon and oxygen isotopes within the solid lattice of the carbonate mineral (See Chapter 1.2.2) without changing other geochemical or structural characteristics of the shells. Solid state reordering had not significantly affected the locality of the studied specimens, as discussed in the previous Chapter (4).

The thick outer shell layer of rudist bivalves composed of low-Mg calcite which is considered to be relatively resistant to diagenetic alteration (Walliser and Schöne, 2020) makes the rudist shells a suitable material for isotope analyses. Nevertheless, diagenetic screening must preclude any paleotemperature reconstructions performed using the $\delta^{18}O$ or clumped isotope paleothermometers (*e.g.*, Affek, 2012; Walliser and Schöne, 2020). Numerous criteria are commonly employed to control for the diagenetic alteration of the original stable isotopic signal, including the preservation of macro- and micro-growth increments, preservation of cyclicity in $\delta^{18}O$ record through the growth profile of the shells, comparison of stable isotope results to values found in a coeval time interval and fossils, or element concentrations (commonly Mn, Fe, Sr) analysis (Brand and Veizer, 1981, 1980; Ivany, 2012; Steuber, 1999; Walliser and Schöne, 2020). Growth increment preservation and element concentrations (Mn, Fe, and Sr), in the studied specimens, are presented and discussed in the previous Chapter (4), proving no significant diagenetic overprinting of the shells presented in this study.

Differences between the isotopic signals of the two studied specimens arise when the $\delta^{18}O$ and $\delta^{13}C$ results are compared (Fig.5.5). The $\delta^{18}O$ variations within sclerochronological profiles of

the studied specimens (data subsets: Growth profile-detailed sampling) are compared to other rudists from coeval time intervals. A fairly large database of Cretaceous rudist seasonal $\delta^{18}O$ and $\delta^{13}C$ ranges is provided by Steuber et al. (2005). Two specimens of Turonian and middle Coniacian age showing the largest seasonal span of the stable isotope results were selected for comparison with the presented dataset. Maxima and minima in stable isotope composition of all Late Cretaceous rudist sclerochronological profiles (Steuber et al., 2005b) were further compared to the stable isotope composition of the studied specimens (Fig.5.5). Additionally, seasonal $\delta^{18}O$ and $\delta^{13}C$ ranges of late Turonian/early Coniacian rudist, *H. resectus* (Walliser and Schöne, 2020), are compared with the presented Turonian specimen (Fig.5.5).

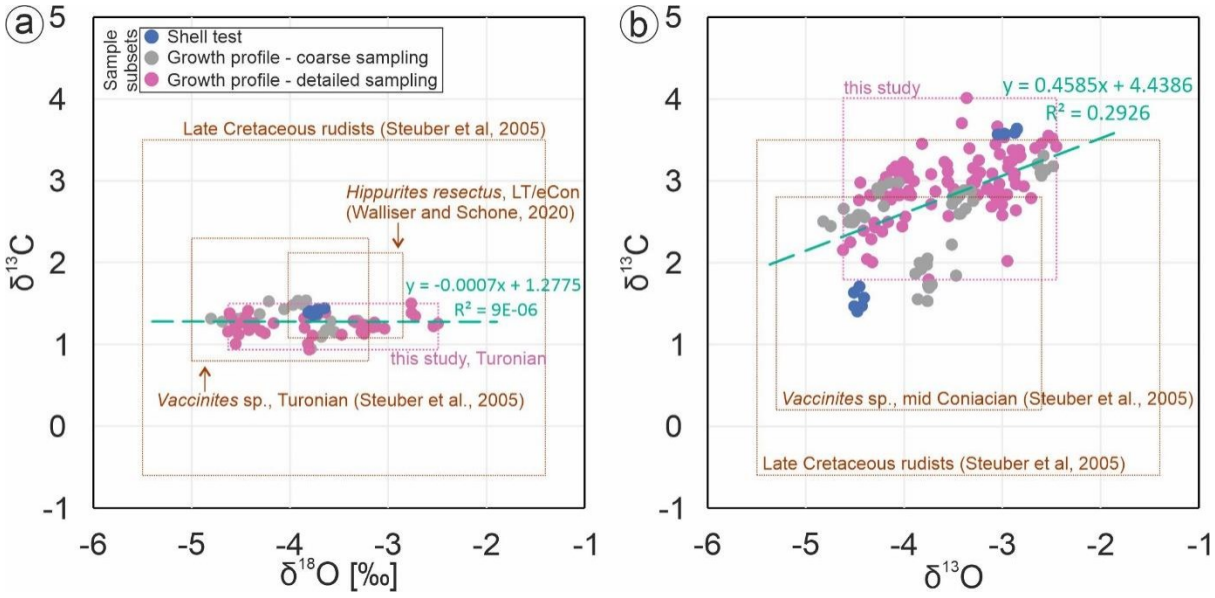

Fig.5.5. Results of $\delta^{18}O$ and $\delta^{13}C$ analysis of the shell material of the studied rudist specimens. **a.** *Hippurites incisa*, Turonian. No covariance of the carbon and oxygen isotope results is observed ($R^2 = 9*10^{-6}$). Seasonal $\delta^{18}O$ range of *H. incisa* (based on Growth profile-detailed sampling data subset; pink rectangle) is compared to the maxima and minima in $\delta^{18}O$ for the Late Cretaceous rudist sclerochronological profiles (Steuber et al., 2005), and to seasonal $\delta^{18}O$ ranges of Turonian *Vaccinites* sp. (Atzlgraben, Austria, 27.4 °paleoN; Steuber et al., 2005) and Late Turonian/earliest Coniacian *H. resectus* (Atzlgraben, Austria, ~27.4 °paleoN; Walliser and Schöne, 2020). **b.** *Praeradiolites ciryi*, middle Coniacian. The trendline shows a degree of covariance in the dataset, this finding is discussed below. Seasonal $\delta^{18}O$ range of *P. ciryi* (based on Growth profile-detailed sampling data subset; pink rectangle) is compared to the maxima and minima in $\delta^{18}O$ for the Late Cretaceous rudist sclerochronological profiles (Steuber et al., 2005), and to seasonal $\delta^{18}O$ ranges of middle Coniacian *Vaccinites* sp. (Keratovouno, Greece, 18.4 °paleoN; Steuber et al., 2005).

In *H. incisa*, the $\delta^{18}O$ seasonal range is between -4.63 and -2.49 ‰, and the $\delta^{13}C$ varies very little, between 0.94 and 1.50 ‰ (Fig.5.3). Seasonal ranges of both isotopes fall more or less in the center of the stable isotope span shown by Late Cretaceous rudists (Fig.5.5a). However,

compared to the seasonal $\delta^{18}O$ range of other Turonian rudists, *H. incisa* shows more positive $\delta^{18}O$ results within the growth profile. $\delta^{18}O$ profile of *Vaccinites* sp. (Steuber et al., 2005b) yields a maximum value of -3.2 ‰, in paleolatitude comparable to *H. incisa* (~27 and ~28 °paleoN respectively). This difference is possibly due to local differences in salinity and/or evaporation-precipitation balance between the locations and time of the shell growth or it is simply due to paleotemperature differences between the two locations or in time. Strontium isotope stratigraphy is inconclusive in *H. incisa* (see Chapter 4), and therefore, it is not possible to determine a precise stratigraphic correlation of *H. incisa* (Istria region) and *Vaccinites* sp. (from Atzlgraben, Austria). The $\delta^{18}O$ seasonal range of *H. incisa* was further compared to the stable isotope sclerochronological profile of *H. resectus* (Walliser and Schöne, 2020), revealing a difference of ~0.5 ‰ between $\delta^{18}O$ minima, as well as maxima (Fig.5.5a). Apart from the difference of ~10 ° in paleolatitude between *H. incisa* and *H. resectus*, other, above-mentioned reasons may have caused the difference in these $\delta^{18}O$ seasonal ranges.

In *P. ciryi*, the $\delta^{18}O$ seasonal range is between -4.62 and -2.45 ‰, and the $\delta^{13}C$ shows larger variations (compared to *H. incisa*), between 1.80 and 4.01 ‰ (Fig.5.4). The shell material shows a rather high correlation between the $\delta^{18}O$ and $\delta^{13}C$ ($R^2 = 0.29$). The largest subset of the *P. ciryi* shell dataset is the Growth profile-detailed sampling subset (n=98; Fig.5.2), showing correlation between the $\delta^{18}O$ and $\delta^{13}C$ cyclicity within the sclerochronological profile (Fig.5.3). The well-developed $\delta^{18}O$ and $\delta^{13}C$ cyclicity in *P. ciryi* implies preservation of the original stable isotopic signal driven by seasonal variations in the paleoenvironment (Ivany, 2012; Steuber, 1999; Walliser and Schöne, 2020), despite the slightly elevated $\delta^{13}C$ values compared to other Late Cretaceous rudists (Fig.5.5b).

5.5.2 Δ_{47}-based paleotemperature and $\delta^{18}O_{seawater}$ calculations

Based on the well-preserved shell datasets, average Δ_{47} values were calculated per specimen. In Turonian *Hippurites incisa*, the average Δ_{47} value is 0.567±0.018 ‰, corresponding to 37.7±7.6 °C (Tab.1, bulk shell). This result is comparable to the SST estimates of 31-37°C for the Late Cenomanian and early Turonian in the tropical western Atlantic Ocean based on $\delta^{18}O$ analyses of planktic foraminifera, reported by (Forster et al., 2007). Furthermore, O'Brien et al. (2017) reported temperatures over 35 °C for the late Cenomanian-Turonian interval in the equatorial Atlantic, mid-latitude North Atlantic, and offshore Tanzania based on $\delta^{18}O$ analyses of planktic foraminifera and TEX_{86} analyses. Despite that the $T(\Delta_{47})$ for *H. incisa* is higher than this estimate, the error (±7.6 °C) on $T(\Delta_{47})$, as well as the bathymetry of the rudist habitats, need to be taken into consideration. Rudist bivalves were sediment dwellers living in a very

shallow marine environment, generally between near-surface and 15 meters of water depth (Gili et al., 1995; Immenhauser et al., 2005). An assemblage of *H. resectus* (used for comparison with the presented dataset; Fig.5.5) and other hippuritids and radiolitids is reported from a water depth of 2-10 m (Walliser and Schöne, 2020). In restricted/semi-closed basins and platforms, the water can be unusually warm and seasonal compared to the open ocean sites (even at the same latitude), due to the smaller size of the water bodies and common seasonal stratification. Thus, the surface of the greenhouse epeiric seas (such as the Late Cretaceous margins of the Tethys ocean) can warm faster and more strongly (Judd et al., 2020).

Table 1. Results of Clumped and stable (oxygen and carbon) isotope analyses. Distance from the bottom of the shell is reported as a mean of the portion of the given growth profile corresponding to a given season. n = number of aliquots. **A.** Resulting averages of Δ_{47} and $\delta^{18}O$ are based on the very same aliquots, measured simultaneously. The bulk shell average Δ_{47} (calculated based on all the aliquots of shell material that passed the diagenetic screening) were translated into temperatures ($T(\Delta_{47})$) using the equation of Anderson et al. (2021). Combining the $T(\Delta_{47})$ and $\delta^{18}O$ results per specimen, $\delta^{18}O_{seawater}$ was calculated using the paleotemperature equation of Anderson and Arthur (1983). Dividing the data subsets Growth profile-detailed sampling based on $\delta^{18}O$ analysis yielded one summer and one winter subgroup in *H. incisa*, and two summer and two winter subgroups in *P. ciryi*. In the latter, $\delta^{18}O_{seawater}$ was calculated for summers and winters. $\delta^{18}O$-based temperatures ($T(\delta^{18}O)$) were calculated per season using the $\delta^{18}O_{seawater}$ calculated per specimen, and, in *P. ciryi*, additional $T(\delta^{18}O)$ were calculated using the $\delta^{18}O_{seawater}$ calculated per season. **B.** Stable isotope analysis results of the Growth profile-detailed sampling subsets, including the additional stable isotope analysis complementing the previous results of A. Clumped isotope analysis (see Methods). $T(\delta^{18}O)$ and $T(\delta^{18}O)$ maxima and minima were calculated the same way as in A.

	distance from the bottom of the shell [mm]	A. Clumped isotope analysis					T(δ18O) [° C]		B. Stable isotope analysis of growth profile						
		n	Δ47 [‰]	T(Δ47) [° C]	$\delta^{18}O$ [‰ VPDB]	$\delta^{18}O$ seawater [‰ VPDB]	$\delta^{18}O$ seawater constant	$\delta^{18}O$ seawater seasonal variations	n	$\delta^{18}O$ [‰ VPDB]	T($\delta^{18}O$) [° C] $\delta^{18}O$ seawater constant	T($\delta^{18}O$) [° C] min-max T [° C]	T($\delta^{18}O$) [° C] $\delta^{18}O$ seawater seasonal variations	T($\delta^{18}O$) [° C] min-max T [° C]	$\delta^{13}C$ [‰ VPDB]
H. incisa (Turonian)															
bulk shell	-	53	**0.567**±0.018	**37.7**±7.6	**-3.89**±0.14	0.69±1.36	-	-	-	-	-	-	-	-	-
summer I	4-11.4	12/20	**0.560**±0.048	**40.8**±19.7	**-4.35**±0.21	-	**40.1**±1.2	-	24/41	**-4.26**±0.13	**39.7**±0.7	**37.0**-41.7	-	-	**1.22**±0.05
winter I	11.8-17	8/20	**0.541**±0.074	**50.5**±37.7	**-3.25**±0.23	-	**34.3**±1.2	-	17/41	**-3.11**±0.19	**33.6**±1.0	**30.5**-36.8	-	-	**1.26**±0.05
P. ciryi (middle Coniacian)															
bulk shell	-	102	**0.577**±0.014	**34.4**±5.3	**-3.73**±0.13	**0.21**±0.51	-	-	-	-	-	-	-	-	-
summer I	-	11/43	**0.593**±0.048	**27.9**±17.0	**-4.06**±0.17	-	**36.1**±0.9	**33.5**±0.9	21/98	**-4.04**±0.12	**36.0**±0.6	-	**33.5**±0.6	-	**2.95**±0.07
summer II	-	12/43	**0.566**±0.570	**39.9**±22.3	**-4.30**±0.13	-	**37.3**±0.7	**34.8**±0.7	23/98	**-4.12**±0.12	**36.4**±0.6	-	**33.8**±0.6	-	**2.55**±0.16
winter I	17-31		-	-	-	-	-	-	18/98	**-3.06**±0.20	**31.0**±1.0	-	**14.7**±0.8	-	**3.15**±0.26
winter II	48-63	20/43	**0.639**±0.043	**14.8**±14.2	**-3.08**±0.12	-	**31.0**±0.6	**14.8**±0.5	36/98	**-3.07**±0.08	**31.0**±0.4	-	**14.8**±0.3	-	**3.08**±0.08
summers (I+II)	0-17		**0.579**±0.034	**34.2**±13.0	**-4.18**±0.11	**-0.27**±1.76	-	-	44	**-4.08**±0.08	**36.2**±0.4	**32.8**-39.1	**33.7**±0.4	**30.4**-36.5	-
winters (I+II)	31-48		-	-	-	**-3.37**±1.84	-	-	54	**-3.07**±0.08	**31.0**±0.4	**27.9**-34.8	**14.8**±0.3	**12.3**-17.9	-

Using the Δ_{47}-based temperature average ($T(\Delta_{47})$) and the average $\delta^{18}O$ measured during the same process (see Methods), the $\delta^{18}O_{seawater}$ was calculated, yielding a value 0.69±1.36 ‰ for the Turonian specimens, *H. incisa* (Fig.5.6, Tab.1). This result is roughly in line with the $\delta^{18}O_{seawater}$ -0.5 ‰ (almost within the uncertainty), but the more commonly used $\delta^{18}O_{seawater}$ -1 ‰ (Grossman, 2012; Walliser and Schöne, 2020) is not in agreement with the presented dataset. Similarly to $\delta^{18}O_{seawater}$ variations in modern oceans (LeGrande and Schmidt, 2006, see Fig.1.6), the $\delta^{18}O_{seawater}$ likely varied in the Late Cretaceous oceans as well. Surface $\delta^{18}O_{seawater}$ can vary depending on latitude (the difference between low and high latitudes can reach 1.5 ‰) and/or between the open ocean and marginal seas (difference as high as 3 ‰; Zachos et al., 1994 and references therein). To reduce the effect of the $\delta^{18}O_{seawater}$ latitudinal gradient, an equation describing $\delta^{18}O_{seawater}$ as a function of latitude was suggested (Zachos et al., 1994). However, this expression does not account for differences between global ocean mean, marginal seas- or coastal waters-specific $\delta^{18}O_{seawater}$. The $T(\delta^{18}O)$, calculated from the $\delta^{18}O_{\textit{H. incisa}}$ using this latitude-adjusted $\delta^{18}O_{seawater}$ value, is within the uncertainty of the $T(\delta^{18}O)$ using the $\delta^{18}O_{seawater}$ presented result (0.69 ‰; Fig.5.6). Local variations in the mid-Cretaceous (Albian-Turonian) $\delta^{18}O_{seawater}$ were modeled by Zhou et al. (2008), who found similar variations to those in modern oceans, even though with a smaller decrease in low- and middle-latitude surface $\delta^{18}O_{seawater}$, and larger variations in the Arctic. For the Tethys ocean, the modeled $\delta^{18}O_{seawater}$ is +0.3 in low latitudes and +0.5 ‰ at around 30°paleo-N. Using this modeled $\delta^{18}O_{seawater}$ +0.5 ‰ to calculate $T(\delta^{18}O)$ based on the $\delta^{18}O$ measured in *H. incisa*, the temperatures are within the error (Fig.5.6), corroborating the model of Zhou et al. (2008).

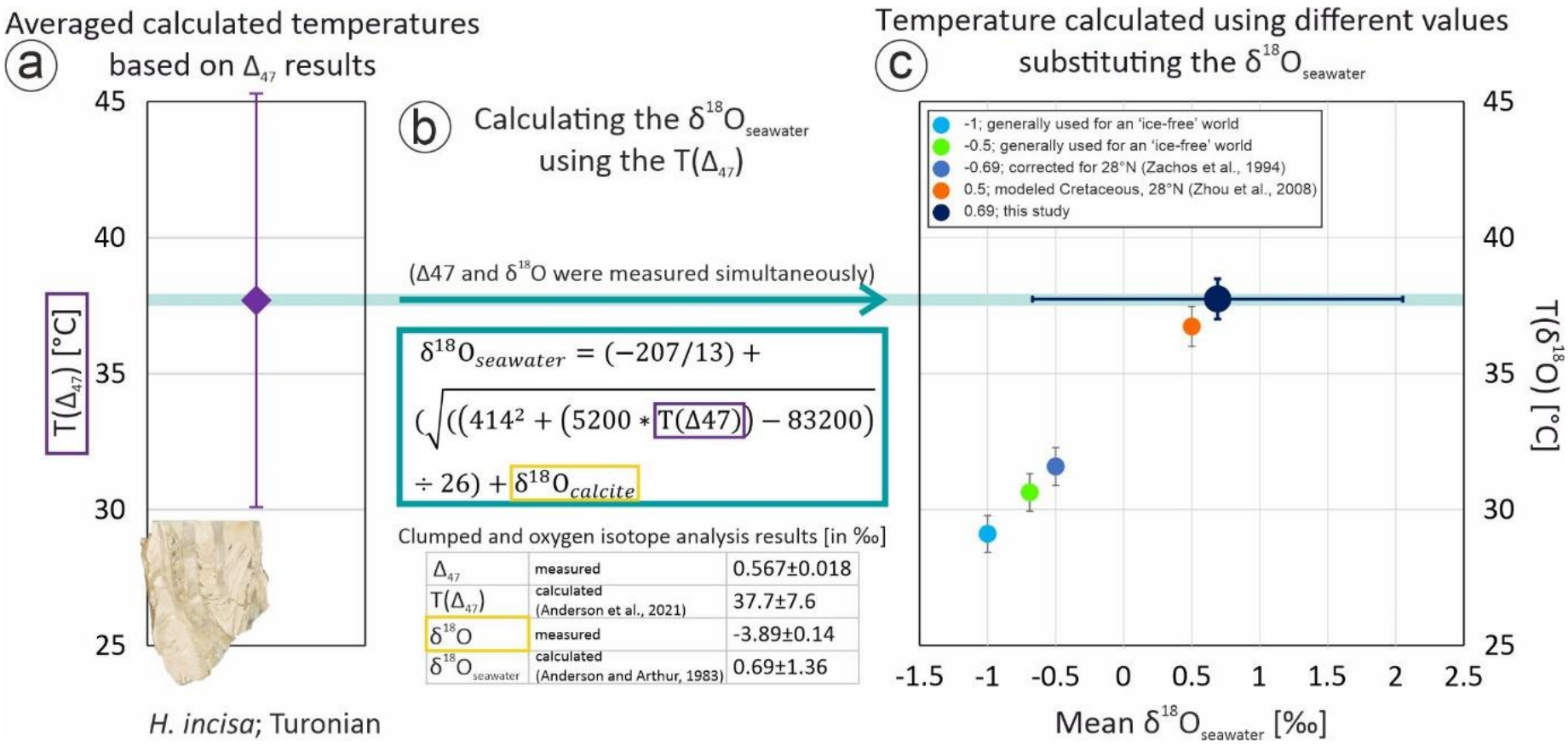
Averaged calculated temperatures
a
based on Δ_{47} results
45
40
35
30
25
$T(\Delta_{47})$ [°C]
H. incisa; Turonian
b
Calculating the $\delta^{18}O_{seawater}$ using the $T(\Delta_{47})$
(Δ47 and $\delta^{18}O$ were measured simultaneously)
$\delta^{18}O_{seawater} = (-207/13) + (\sqrt{((414^2 + (5200 * T(\Delta47)) - 83200)} \div 26) + \delta^{18}O_{calcite}$
Clumped and oxygen isotope analysis results [in ‰]
Δ_{47} measured 0.567±0.018
$T(\Delta_{47})$ calculated (Anderson et al., 2021) 37.7±7.6
$\delta^{18}O$ measured -3.89±0.14
$\delta^{18}O_{seawater}$ calculated (Anderson and Arthur, 1983) 0.69±1.36
Temperature calculated using different values substituting the $\delta^{18}O_{seawater}$
c
-1; generally used for an 'ice-free' world
-0.5; generally used for an 'ice-free' world
-0.69; corrected for 28°N (Zachos et al., 1994)
0.5; modeled Cretaceous, 28°N (Zhou et al., 2008)
0.69; this study
45
40
35
30
25
$T(\delta^{18}O)$ [°C]
-1.5 -1 -0.5 0 0.5 1 1.5 2 2.5
Mean $\delta^{18}O_{seawater}$ [‰]

Fig.5.6. $\delta^{18}O_{seawater}$ calculation for Turonian *H. incisa*. **a.** T(Δ_{47}) calculated from all well-preserved shell material. **b.** The equation used for calculating the $\delta^{18}O_{seawater}$ (based on the paleotemperature equation of Anderson and Arthur (1983)) and measured and calculated results of clumped and $\delta^{18}O$ analyses (same aliquots, measured simultaneously) are reported. **c.** Measured $\delta^{18}O$ used for T($\delta^{18}O$) calculations using the $\delta^{18}O_{seawater}$ calculated from the presented T(Δ_{47}) (dark blue) compared to measured $\delta^{18}O$ used for T($\delta^{18}O$) calculations using the $\delta^{18}O_{seawater}$ reported by previous studies.

In the middle Coniacian specimen, *P. ciryi*, the Δ_{47} analysis of the shell material results in 0.577±0.014 ‰, and the calculated T(Δ_{47}) is 34.4±5.3 °C (Tab.1). Lower calculated paleotemperature compared to the previously discussed specimen corresponds to the general paleotemperature trend of global cooling onset during the Coniacian, with paleotemperature range between 17 and 36 °C (O'Brien et al., 2017).

Using the T(Δ_{47}) and simultaneously measured $\delta^{18}O$ in *P. ciryi*, the $\delta^{18}O_{seawater}$ was calculated, resulting in a value of 0.21±0.51 ‰ (Fig.5.7). This result rejects the commonly used $\delta^{18}O_{seawater}$ of -1 ‰. Applying the correction for paleolatitude (Zachos et al., 1994), the resulting T($\delta^{18}O$) plots close, nevertheless, outside of the error, of the presented results (Fig.5.7).

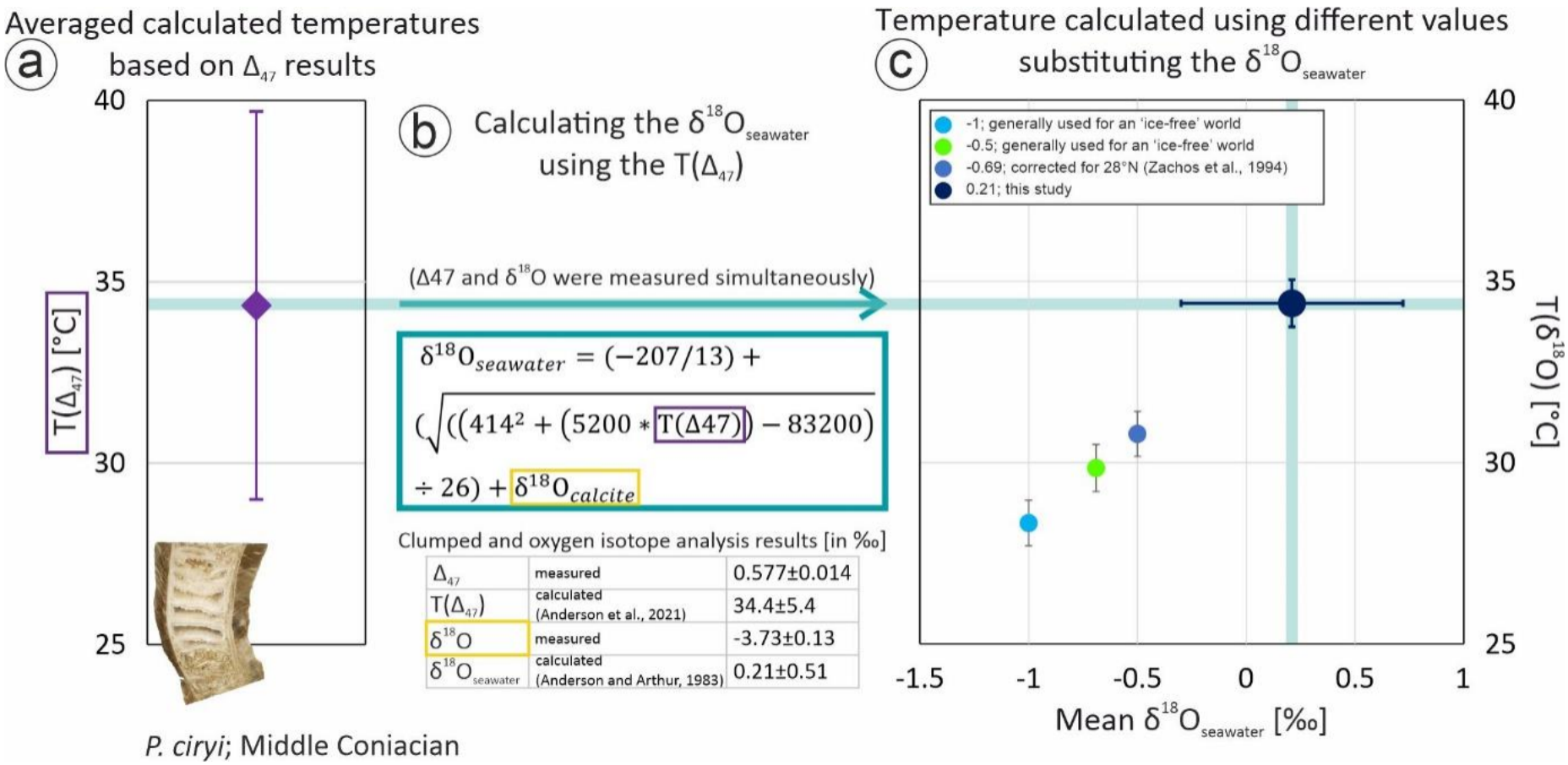

P. ciryi; Middle Coniacian

Fig.5.7. Same as Fig.5.6., for middle Coniacian *P. ciryi*.

The discrepancy between the calculated $\delta^{18}O_{seawater}$ values of the studied specimens and the $\delta^{18}O_{seawater}$ value commonly assumed for the Late Cretaceous oceans is possible to link to: 1. local and/or temporal variations in $\delta^{18}O_{seawater}$ due to the variations in evaporation-precipitation balance in the shallow-marine environment, 2. The difference in the global $\delta^{18}O_{seawater}$ value from the widely accepted value of -1 ‰ for the Late Cretaceous ice-free world.

Rudists inhabited shallow marine environments, and therefore, recorded geochemical properties of near-surface habitats to a water depth of around 15 m (Immenhauser et al., 2005). The shallow marginal marine environments are more prone to local differences in evaporation-precipitation balance and/or influenced by proximity to freshwater runoff and therefore could reflect regional differences rather than open ocean values (Grossman, 2012; Jimenez et al., 2019). Brand et al. (2009) concluded that the oxygen isotope composition of epeiric seas and open ocean low-Mg calcite fossils are decoupled during the mid-late Paleozoic, and Zachos et al. (1994) report the $\delta^{18}O_{seawater}$ values between the open ocean and marginal seas to vary by up to 3 ‰ (corresponding to our dataset). Furthermore, Zhang and Petersen (2023), have shown that even if the $\delta^{18}O_{seawater}$ is measured directly in modern seawater, it can give a biased mean $\delta^{18}O$-temperature as well as biased seasonal extreme temperatures when shells were collected further from the $\delta^{18}O_{seawater}$ measuring point.

In light of the above-mentioned, we interpret our data to favor the assumption nr. 1, which assumes local variations in $\delta^{18}O_{seawater}$ differing from the open ocean value. Our dataset is not sufficient to assess the assumption nr. 2; more studies performed on different types of fauna from different palaeoceanographic settings using the $\delta^{18}O_{seawater}$ independent paleothermometers are needed to address this issue. However, the presented study points out the applicability of the clumped isotope thermometer in shallow-water settings, and its benefits for paleoclimatological studies. Additionally, this study highlights the importance of precise constraints of the local $\delta^{18}O_{seawater}$ for $\delta^{18}O$-based paleotemperature reconstructions in shallow-water environments.

5.5.3 Seasonal variations observed at 28° paleo-N

If a constant $\delta^{18}O_{seawater}$ is assumed (0.69 ‰, calculated using the $T(\Delta_{47})$ and $\delta^{18}O$ results), the maximum seasonal difference based on the $\delta^{18}O$ analysis of the Turonian specimen *H. incisa* is $\delta^{18}O$ 2.14 ‰ at a paleolatitude of 28 °paleoN, which translates into seasonal temperature difference of 10.3 °C. A comparable seasonal $\delta^{18}O$ range of 2.25 ‰ (11.1 °C) is reported from

late Turonian-earliest Coniacian rudist shells from NW Tethys (Walliser and Schöne, 2020). The $\delta^{18}O$ sclerochronological profile of *H. incisa* shows fluctuations likely corresponding to seasonal temperature variations (Fig.5.8a), allowing for dividing the profile into summer and winter seasons. The $\delta^{18}O$ results cluster in two groups (Fig.5.8b), around -4.4 and -3.3 ‰ (Tab.1) with a possible boundary between summer and winter seasons set to ~3.5 ‰. When the Δ_{47} results are divided according to the seasons, the resulting number of aliquots within the summer (12) and winter (8) seasons is too low to give a reasonable error on the averaged Δ_{47} values: 0.560±0.048 ‰ (corresponding to 40.8±19.7 °C) for the summer, and 0.541±0.074 ‰ (50.5±37.7 °C; Tab.1, Fig.5.8a,c). These results do not allow for tackling the question of seasonal $\delta^{18}O_{seawater}$ variations, however, the overall number of aliquots of the well-preserved shell material analyzed for Δ_{47} (n=53), allows for the seasonal paleotemperature variations as well as a good average $T(\Delta_{47})$ and $\delta^{18}O_{seawater}$ estimates (Tab.1, Fig.5.8c,d).

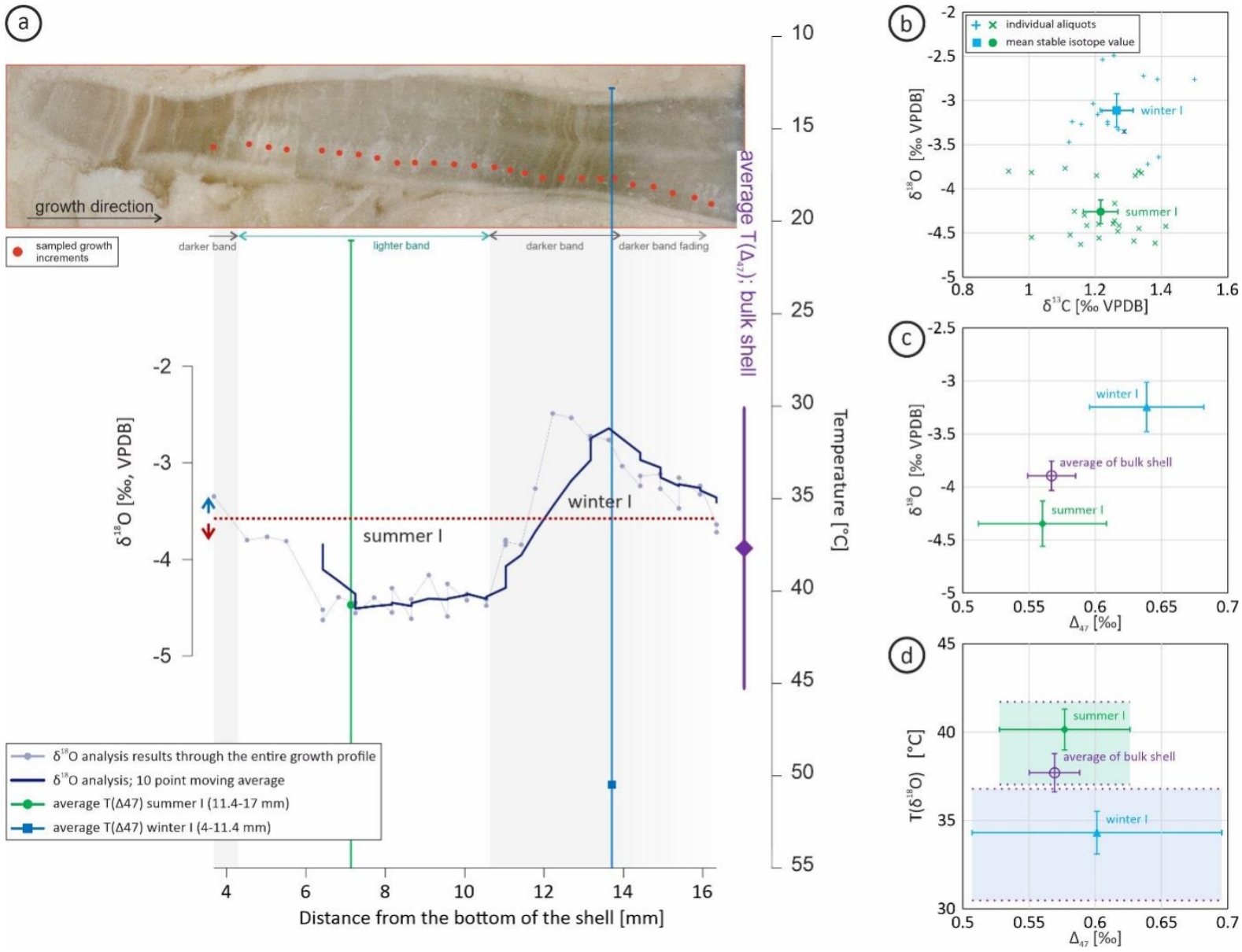
a
growth direction
sampled growth increments
darker band
lighter band
darker band
darker band fading
average T(Δ47); bulk shell
δ18O [‰, VPDB]
summer I
winter I
Temperature [°C]
δ18O analysis results through the entire growth profile
δ18O analysis; 10 point moving average
average T(Δ47) summer I (11.4-17 mm)
average T(Δ47) winter I (4-11.4 mm)
Distance from the bottom of the shell [mm]
b
individual aliquots
mean stable isotope value
winter I
summer I
δ18O [‰ VPDB]
δ13C [‰ VPDB]
c
winter I
average of bulk shell
summer I
δ18O [‰ VPDB]
Δ47 [‰]
d
summer I
average of bulk shell
winter I
T(δ18O) [°C]
Δ47 [‰]

Fig.5.8. Geochemical results, and paleotemperature and $\delta^{18}O_{seawater}$ calculations in Turonian *H. incisa*. **a.** Growth profile with marked locations of drilling the Growth profile-detailed sampling subset. $\delta^{18}O$ results through the growth profile are translated to paleotemperature based on the $T(\Delta_{47})$ results and calculated $\delta^{18}O_{seawater}$ (0.69 ‰). **b.** Results of stable isotope analysis, showing clustering of the data points below and above $\delta^{18}O$ -3.5 ‰, suggesting seasonal differences in temperatures. **c.** Δ_{47} and simultaneously measured $\delta^{18}O$ results of the summer and winter values measured throughout the Growth profile-detailed sampling subset (note that the number of aliquots is lower than in b., as not all the subset yielded enough material to perform the Δ_{47} analysis; Tab.1). The average is based on all the shell material measured in *H. incisa*. **d.** same as c., translated into paleotemperature. Seasonal temperature ranges (dashed lines) are based on the $\delta^{18}O$ results of the summer and winter values measured throughout the Growth profile-detailed sampling subset.

The growth of the shell of *H. incisa* does not seem to be continuous throughout the year, after ~4 mm recording the summer maximum temperatures, a rather sharp decrease in temperature occurs (10.4 °C in ~1.7 mm), followed by a gradual temperature increase for the following ~4.2 mm (Fig.5.8a). This suggests a decrease in calcite accretion after the summer temperature maxima, followed by its increase after the temperature minima. Discontinuous growth throughout the year is often the case for marine bivalves and is interpreted to reflect environmental and/or reproductive stress (Judd et al., 2018; Schöne et al., 2005).

Interestingly, the darker and lighter bands visible in the growth profile of *H. incisa* correspond to lower and higher temperatures respectively, yet the darker band seems to slightly preclude the drop in temperatures (Fig.5.8a).

Assuming constant $\delta^{18}O_{seawater}$ calculated in *P. ciryi* (0.21 ‰, calculated using the $T(\Delta_{47})$ and $\delta^{18}O$ results, Fig.5.7), the maximum seasonal difference within the $\delta^{18}O$ profile is 2.17 ‰, translated into max. seasonal $T(\delta^{18}O)$ difference of 11.1 °C (Fig.5.9). This suggests increasing seasonality at 28 °paleoN between Turonian (previous specimen, 10.3 °C) and mid-Coniacian. Fluctuations in the $\delta^{18}O$ profile of *P. ciryi* follow a pattern likely corresponding to seasonal temperature variations (Fig.5.9.a). Plotting the stable isotope analysis results of the Growth profile-detailed sampling data subset, the $\delta^{18}O$ results cluster in two groups (below and above -3.5 ‰), interpreted as summer and winter temperatures (Fig.5.9.b). In contrast, averaged seasonal $\delta^{13}C$ (summers vs. winters) show an almost negligible difference (summer I nearly overlap with winter II; Fig.5.9b, Tab.1), even though the $\delta^{13}C$ profile shows seasonal variations corresponding to those of $\delta^{18}O$ (Fig.5.4). Comparing the Δ_{47} values of the summer and winter portions of the growth profile shows a difference of 0.06 ‰ (Tab.1, Fig.5.9c). Despite the large error on the averaged Δ_{47} per season, calculating the $\delta^{18}O_{seawater}$ for averaged summer and winter was attempted. Using the calculated $T(\Delta_{47})$ and simultaneously measured $\delta^{18}O$, the

$\delta^{18}O_{seawater}$ was calculated as -0.27 ‰ for the summer season and -3.37 ‰ for the winter season in *P. ciryi*. Nonetheless, these results need to be considered with a high degree of uncertainty, since the errors of the seasonal average T(Δ_{47}) values overlap (Fig.5.9d), the same as those of the calculated $\delta^{18}O_{seawater}$ values. A further reason for a careful approach towards these $\delta^{18}O_{seawater}$ seasonal calculations is that the averaged T(Δ_{47}) of all the shell material of *P. ciryi* (including, but not limited to the Growth profile-detailed sampling subset, n=102) coincides with the T(Δ_{47}) averaged for the summers, instead of lying in the middle, between the averaged summer and winter T(Δ_{47}). Similarly, the calculated $\delta^{18}O_{seawater}$ in both, summers and winters, is lower than the $\delta^{18}O_{seawater}$ calculated using the average T(Δ_{47}) of all the shell material.

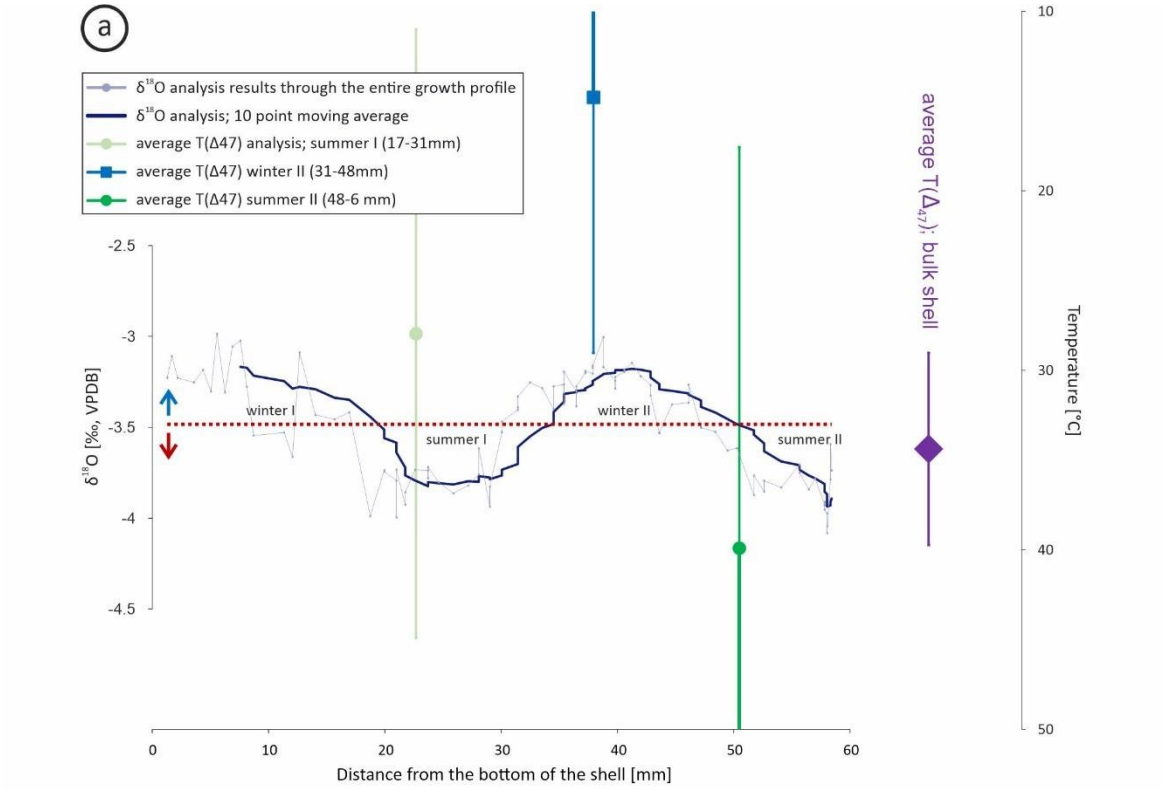
a
δ18O analysis results through the entire growth profile
δ18O analysis; 10 point moving average
average T(Δ47) analysis; summer I (17-31mm)
average T(Δ47) winter II (31-48mm)
average T(Δ47) summer II (48-6 mm)
δ18O [‰, VPDB]
winter I
summer I
winter II
summer II
average T(Δ47); bulk shell
Temperature [°C]
Distance from the bottom of the shell [mm]

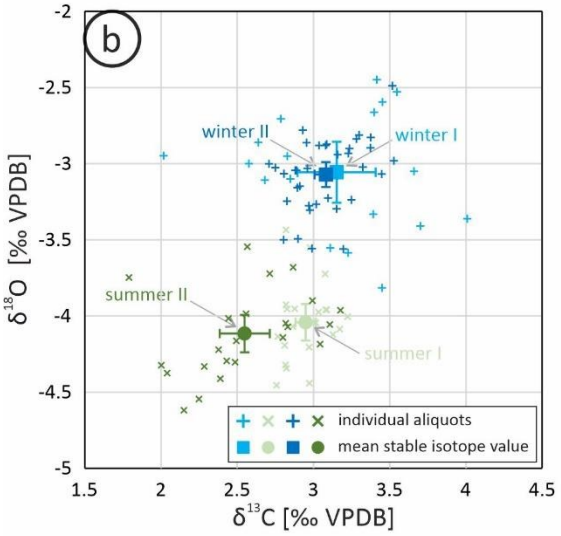
b
winter II
winter I
summer II
summer I
individual aliquots
mean stable isotope value
δ18O [‰ VPDB]
δ13C [‰ VPDB]

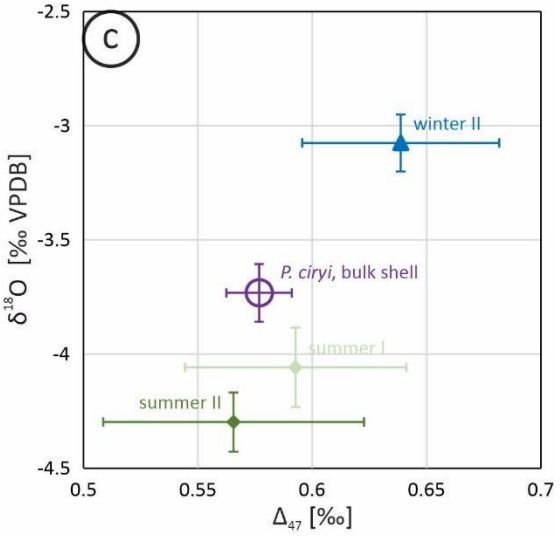
c
winter II
P. ciryi, bulk shell
summer I
summer II
δ18O [‰ VPDB]
Δ47 [‰]

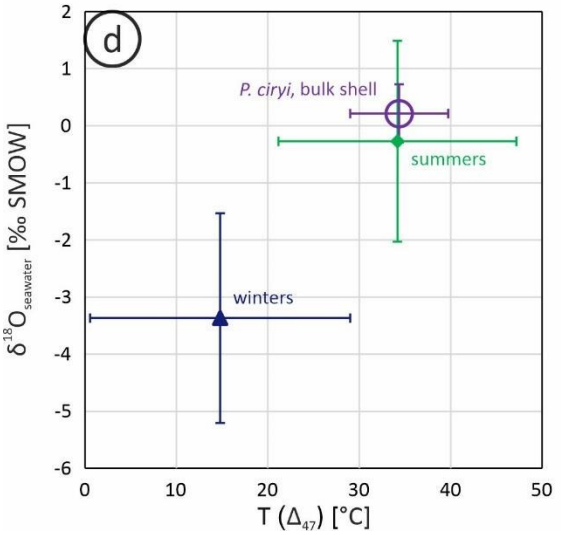
d
P. ciryi, bulk shell
summers
winters
δ18Oseawater [‰ SMOW]
T (Δ47) [°C]

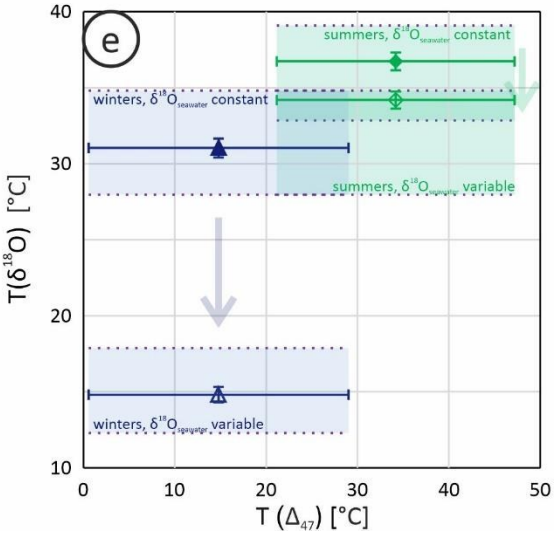
e
summers, δ18Oseawater constant
winters, δ18Oseawater constant
summers, δ18Oseawater variable
winters, δ18Oseawater variable
T(δ18O) [°C]
T (Δ47) [°C]

Fig.5.9. Geochemical results, and paleotemperature and $\delta^{18}O_{seawater}$ calculations in middle Coniacian *P. ciryi*. **a.** $\delta^{18}O$ results through the Growth profile-detailed sampling subset are translated to paleotemperature based on the $T(\Delta_{47})$ results and calculated $\delta^{18}O_{seawater}$ (0.21 ‰). **b.** Results of stable isotope analysis, showing clustering of the data points below and above $\delta^{18}O$ -3.5 ‰, suggesting seasonal differences in temperatures. **c.** Δ_{47} and simultaneously measured $\delta^{18}O$ results of the summer and winter values measured throughout the Growth profile-detailed sampling subset (note that the number of aliquots is lower than in b., as not all the samples within the subset yielded enough material to perform the Δ_{47} analysis; Tab.1). The average is based on all the shell material measured in *H. incisa*. **d.** $\delta^{18}O_{seawater}$ calculations, based on the $T(\Delta_{47})$ results. The bulk shell data point represents the averaged shell material, whereas the summers and winters $\delta^{18}O_{seawater}$ was calculated based on averaged $T(\Delta_{47})$ results per season. **e.** Shifts in resulting paleotemperatures when using the $\delta^{18}O_{seawater}$ calculated based on the entire shell dataset (constant; 0.21 ‰) and the $\delta^{18}O_{seawater}$ calculated per season (-0.27 and -3.37 ‰ for summers and winters respectively).

Having calculated the $\delta^{18}O_{seawater}$ using the average $T(\Delta_{47})$ and simultaneously measured $\delta^{18}O$ of all the shell material in *P. ciryi* (Fig. 5.7), it is possible to use this $\delta^{18}O_{seawater}$ (0.21 ‰) to calculate the paleotemperatures throughout the Growth profile of the shell, based solely on the $\delta^{18}O$ results. Dividing the Growth profile-detailed sampling subset into two groups corresponding to summer ($\delta^{18}O$ below -3.5) and winter ($\delta^{18}O$ below -3.5) seasons, average summer (36.7 °C) and winter temperatures can be calculated (31 °C; Fig.5.9e). Following the scenario in which the $\delta^{18}O_{seawater}$ seasonally varies, the summer average $T(\delta^{18}O)$ lowers to 33.7 °C and the winter average $T(\delta^{18}O)$ lowers significantly, to 14.8 °C compared to the previous scenario (Fig.5.9e).

As debated above, the limited possibility of measuring enough material throughout the growth profile for the Δ_{47} composition results in inaccurate estimates of the 'winter' and 'summer' $T(\Delta_{47})$ in the Turonian *H. incisa* (Fig.5.8a). Nevertheless, the $T(\Delta_{47})$ results of the middle Coniacian *P. ciryi* averaged per season (even though with a certain degree of uncertainty) suggest that the $\delta^{18}O_{seawater}$ possibly seasonally varied for as much as 3 ‰ (Tab.1, Fig.5.9d). Restricted marine waters, such as epeiric seas during greenhouse climates, were most likely chemically different from the open ocean due to the possible influence of freshwater runoff and/or evaporation-precipitation balance (Jimenez et al., 2019), likely being warmer and more seasonal than their open-ocean counterparts (Judd et al., 2020).

To address the question of oxygen isotopic seasonal variations in Late Cretaceous carbonate platforms using thermometers independent of $\delta^{18}O_{seawater}$, such as clumped isotope analysis in marine bivalves, further studies performed on larger specimens with longer and/or thicker growth profiles than those presented in this study (Fig.2) are needed. Larger areas of the outer

shell layer accessible to sampling provide more powder material per sample, allowing for measuring more Δ_{47} aliquots per season and thus lowering the error on the seasonal averaged $T(\Delta_{47})$ and hence, on the calculated $\delta^{18}O_{seawater}$.

5.6 Conclusions

The outer shell layers of the lower (attached) valves of two well-preserved rudist specimens from Istria, Croatia (28 °paleoN) were analyzed for stable and clumped isotope analysis. In the Turonian specimen, *Hippurites incisa*, analysis of the Δ_{47} and simultaneously measured $\delta^{18}O$ gave results of 0.567±0.018 and -3.89±0.14 ‰ respectively. The $T(\Delta_{47})$ 37.7±7.6 °C value was then used to calculate the $\delta^{18}O_{seawater}$, resulting in 0.69±1.36 ‰. A detailed sampling through the growth profile of *H. incisa* (1.7 mm) yielded a seasonally fluctuating $\delta^{18}O$ profile. The calculated $\delta^{18}O_{seawater}$ was then used to calculate paleotemperatures throughout the profile, resulting in maximum seasonal temperature variations of 10.4 °C, and average 'summer' and 'winter' temperatures of 39.7 and 33.6 °C.

The middle Coniacian specimen, *Praeradiolites ciryi*, gave results of Δ_{47} and simultaneously measured $\delta^{18}O$ 0.577±0.014 ‰ and -3.73±0.13 ‰ respectively. The resulting $T(\Delta_{47})$ is 34.4±5.3 ‰, and the calculated $\delta^{18}O_{seawater}$ is 0.21±0.51 ‰. Translating the seasonally fluctuating 57.1 mm-long $\delta^{18}O$ profile of the specimen into paleotemperatures using the calculated $\delta^{18}O_{seawater}$ resulted in the maximum seasonal temperature range of 11.1 °C with averaged 'summer' and 'winter' temperatures of 36.2 and 31 °C respectively. A relatively large number of aliquots measured for Δ_{47} composition through the growth profile allowed for calculating 'summer' and 'winter' $\delta^{18}O_{seawater}$ (-0.27 and -3.37 ‰ respectively). However, the Δ_{47} results per season show rather large errors, and therefore, these seasonal $\delta^{18}O_{seawater}$ differences need to be considered with some degree of uncertainty. Nevertheless, the results presented in this study suggest the possibility of seasonal $\delta^{18}O_{seawater}$ variations in the shallow-marine environment at 28 °paleoN.

The $\delta^{18}O_{seawater}$ calculated in both specimens differs from the widely accepted Late Cretaceous (ice-free) value -1 ‰. This is likely due to the local paleoenvironmental variations in $\delta^{18}O_{seawater}$, due to locality-specific precipitation-evaporation balance and/or stratification and faster heat-up of shallow-water rudist habitats, that caused the local $\delta^{18}O_{seawater}$ to differ from the open ocean value.

6 General Conclusions

In this thesis, shallow-water carbonates of the Late Cretaceous age from the Adriatic carbonate platform were investigated. The first study involved a continuous Cenomanian-Turonian section cropping out in the Karst area of the Friuli region (NE Italy). The Devetachi section was investigated for its stratigraphy, geochemistry, and faunal evolution (benthic foraminifera and rudists) to understand the evolution of the Friuli carbonate platform across the Cenomanian-Turonian, a critical interval of the Late Cretaceous. A precise stratigraphic framework was developed by applying bio- and chemostratigraphic analyses (benthic foraminifera distribution, $\delta^{13}C$- and Sr-isotope stratigraphy). Using $\delta^{18}O$ analysis on well-preserved bulk rock and rudist shell material, it was possible to build high-resolution paleotemperature curves and estimate paleotemperature minima and maxima in shallow-water carbonates. In the studied section, the Early Turonian interval records the warmest temperatures as high as 41-45 °C (according to the different assumptions of $\delta^{18}O_{seawater}$). Temperature changes from the Late Cenomanian to early Turonian had a magnitude >7 °C and a rate of changes of around 10 °C in less than 1Myr. Paleontological data show that benthic foraminifera and rudist evolution follow paleotemperature fluctuations and that their demise in the Upper Cenomanian and reoccurrence in the Turonian strata was strongly modulated by temperature.

In the second study, rudist fragments from the Devetachi section along with two complete rudist specimens from the Friuli carbonate platform, and four complete specimens from the southern Istria region (Croatia) were analyzed by Clumped isotope and $\delta^{18}O$ isotope analyses. The resulting Δ_{47}- and $\delta^{18}O$-based paleotemperatures yield similar results for the Istria region, whereas, in the Friuli region, the Δ_{47}-based paleotemperatures show an offset towards temperatures of as much as over 100 °C. Diagenetic screening applying the commonly used methods shows no difference in the preservation of the studied specimens between the Friuli and Istria regions. However, the exceptionally high Δ_{47}-temperatures recorded in the Friuli region suggest that the original Δ_{47} signal is not preserved, due to a particular type of diagenetic alteration. The solid-state reordering involves a reorganization of the original C-O bonds driven by elevated temperatures during the burial history of the Friuli region. The different burial histories experienced by the Istria and Friuli sectors of the Cretaceous Adriatic Carbonate Platform suggest that the exceptionally high Δ_{47}-temperatures are linked to the higher burial temperatures in the Friuli region.

The final study presented in this thesis attempts to estimate seasonal temperature fluctuations and possibly the $\delta^{18}O_{seawater}$ in the AdCP. For this purpose, two lower (attached) valves of two well-preserved rudist specimens from southern Istria (Croatia) were analyzed for Δ_{47} and $\delta^{18}O$. The $\delta^{18}O$ analyses of the growth profiles of the studied shells show temperature fluctuations of ~10 °C in Turonian and Coniacian, suggesting modern-scale seasonal variations even during the hothouse climate stage. Furthermore, the resulting Δ_{47} paleotemperatures were compared with those obtained by the $\delta^{18}O$ paleothermometer. When the $\delta^{18}O_{seawater}$ of -1 ‰ (VSMOW; generally used for an ice-free Cretaceous world) was applied, the temperatures obtained by the $\delta^{18}O$ paleothermometer differ from the Δ_{47}-based average paleotemperatures by 8.9 °C in Turonian, and by 6.6 °C in Coniacian. These differences can be attributed to the local variations in $\delta^{18}O_{seawater}$, caused by the variations in evaporation-precipitation balance in shallow-marine environments. The reconstructed $\delta^{18}O_{seawater}$ using the Δ_{47} results from the Istria region is 0.21 ‰ for Turonian and 0.69 ‰ (relative to VSMOW) for Coniacian. To date, it is the first $\delta^{18}O_{seawater}$ reconstruction for shallow water settings of the northwestern Tethys, opening new opportunities for understanding the Cretaceous climatic changes from neritic areas.

The high-resolution stratigraphic framework established for the Devetachi section (Friuli region) enabled tackling the long-lasting questions about the timing of the Late Cretaceous temperature maximum in the shallow-water environments and its impact on the biota (Chapter 1). The temperature maximum identified in the Lower Turonian (above the Cenomanian-Turonian Boundary Event) correlates with the disappearance of rudists and most benthic foraminifera from the sedimentary record. This suggests that despite other stress factors, the temperature played a major role in modulating the biota evolution. Further detailed studies such as the one presented in this thesis from other critical intervals of the Earth history are needed to fully confirm the results presented herein. Even though the studied Devetachi section bears a pristine stable isotopic signature of the bulk rock and fossils ($\delta^{13}C$ and $\delta^{18}O$, $^{87}Sr/^{86}Sr$), the original clumped isotopic signal was overprinted by a specific type of diagenetic alteration, the solid-state reordering of the clumped isotopic composition. This finding highlights the importance of a thorough reconstruction of the burial and temperature histories of areas of research interest, prior to attempting the absolute temperature estimates using the clumped isotope thermometry. In fact, rudist fossils from an area not paleogeographically distant from the studied section that was not subject to the solid-state reordering of the original clumped isotopic signal (Istria region) enabled reconstructing absolute Δ_{47}-based paleotemperatures, as well as seasonal temperature variations recorded by two rudist specimens. The

sclerochronological profile of Turonian *H. incisa* (Istria) yields maximum paleotemperatures of 41.7 °C, comparable to the temperature maxima of 41-45 °C identified in the Devetachi section (Lower Turonian; Friuli region) using the $\delta^{18}O$ thermometer.

The results presented in this thesis suggest that, when preserved, the clumped isotopic composition of the rudist shells can be used for absolute paleotemperature estimates. However, a careful approach must be used as it has been shown that the commonly applied methodology for diagenetic alteration assessment is not always indicative of the preservation of the original clumped isotopic signal (see above; Chapter 4). Moreover, as shown in the presented datasets, a relatively large number of measurement replicates need to be performed in order to obtain reliable Δ_{47} results. Hence, in a general routine, the Δ_{47} analysis alone is insufficient to study seasonal temperature changes throughout a sclerochronological profile of rudist shells. However, when the Δ_{47} analysis is combined with a detailed stable oxygen isotopic profile, it can yield absolute seasonal paleotemperature estimates, as demonstrated in Chapter 5.

Finally, the presented thesis reports that shallow-water carbonates have the potential to record global climatic fluctuations, regardless of the superimposed local isotopic signature (Chapter 3). However, reliable estimates of the $\delta^{18}O$-paleotemperatures are hampered by the unknown $\delta^{18}O_{seawater}$ in the deep time, and by the local $\delta^{18}O_{seawater}$ variations, causing the shallow-water oxygen isotopic composition to differ from the open-ocean values. The combination of $\delta^{18}O$ and Δ_{47} analyses enables calculating the local $\delta^{18}O_{seawater}$ value. Knowing these values for specific regions/sections, the full potential of the $\delta^{18}O$ paleothermometer can be applied to reliably estimate long-term, as well as seasonal temperature fluctuations. Moreover, obtaining the shallow-water $\delta^{18}O_{seawater}$ values different from those assumed for the Late Cretaceous open oceans highlights the importance of further studies aiming to model (reconstruct) precise local $\delta^{18}O_{seawater}$ values. Such data may help improve the climatic models in the Earth history and understanding of the $\delta^{18}O_{seawater}$ variability of shallow-water environments during hothouse climate stages, as is the case of the Late Cretaceous.

7 Bibliography

Affek, H.P., 2012. Clumped Isotope Paleothermometry: Principles, Applications, and Challenges. The Paleontological Society Papers 18, 101–114.

Agterhuis, T., Ziegler, M., De Winter, N.J., Lourens, L.J., 2022. Warm deep-sea temperatures across Eocene Thermal Maximum 2 from clumped isotope thermometry. Commun Earth Environ 3, 39. https://doi.org/10.1038/s43247-022-00350-8

Al-Aasm, I.S., Veizer, J., 1986. Diagenetic stabilization of aragonite and low-Mg calcite. I. Trace elements in rudists. Journal of Sedimentary Petrology 56, 763–770.

Allan, J.R., Matthews, R.K., 1982. Isotope signatures associated with early meteoric diagenesis. Sedimentology 29, 797–817. https://doi.org/10.1111/j.1365-3091.1982.tb00085.x

Anderson, N.T., Kelson, J.R., Kele, S., Daëron, M., Bonifacie, M., Horita, J., Mackey, T.J., John, C.M., Kluge, T., Petschnig, P., Jost, A.B., Huntington, K.W., Bernasconi, S.M., Bergmann, K.D., 2021. A Unified Clumped Isotope Thermometer Calibration (0.5–1,100°C) Using Carbonate-Based Standardization. Geophysical Research Letters 48. https://doi.org/10.1029/2020GL092069

Anderson, T.F., Arthur, M.A., 1983. Stable isotopes of oxygen and carbon and their application to sedimentologic and paleoenvironmental problems. Stable Isotopes in Sedimentary Geology, SEPM Short Course No. 10. SEPM 10, 1–151.

Arriaga, M., Frijia, G., Parente, M., Caus, E., 2016. Benthic foraminifera in the aftermath of the Cenomanian-Turonian boundary extinction event in the carbonate platform facies of the southern Apennines (Italy). The Journal of Foraminiferal Research 46, 9–24.

Barrier, E., Vrielynck, J., Brouillet, J.F., Brunet, M.F., 2018. Atlas DARIUS PDF - Paleotectonic Reconstruction of the Central Tethyan Realm.

Bice, K.L., Birgel, D., Meyers, P.A., Dahl, K.A., Hinrichs, K.-U., Norris, R.D., 2006. A multiple proxy and model study of Cretaceous upper ocean temperatures and atmospheric CO 2 concentrations: CRETACEOUS MULTIPLE PROXY STUDY. Paleoceanography 21, n/a-n/a. https://doi.org/10.1029/2005PA001203

Boix, C., Frijia, G., Vicedo, V., Bernaus, J.M., Di Lucia, M., Parente, M., Caus, E., 2011. Larger foraminifera distribution and strontium isotope stratigraphy of the La Cova limestones (Coniacian–Santonian, “Serra del Montsec”, Pyrenees, NE Spain). Cretaceous Research 32, 806–822. https://doi.org/10.1016/j.cretres.2011.05.009

Bornemann, A., Norris, R.D., Friedrich, O., Beckmann, B., Schouten, S., Damsté, J.S.S., Vogel, J., Hofmann, P., Wagner, T., 2008. Isotopic Evidence for Glaciation During the Cretaceous Supergreenhouse. Science 319, 189–192. https://doi.org/10.1126/science.1148777

Brand, U., Tazawa, J. -i., Sano, H., Azmy, K., Lee, X., 2009. Is mid-late Paleozoic ocean-water chemistry coupled with epeiric seawater isotope records. Geology 37, 823–826. https://doi.org/10.1130/G30038A.1

Brand, U., Veizer, J., 1981. Chemical Diagenesis of a Multicomponent Carbonate System -2: Stable Isotopes. SEPM JSR Vol. 51. https://doi.org/10.1306/212F7DF6-2B24-11D7-8648000102C1865D

Brand, U., Veizer, J., 1980. Chemical Diagenesis of a Multicomponent Carbonate System-1: Trace Elements. SEPM JSR Vol. 50. https://doi.org/10.1306/212F7BB7-2B24-11D7-8648000102C1865D

Brock, T.D., 1985. Life at High Temperatures. Science 230, 132–38.

Burgener, L., Hyland, E., Huntington, K.W., Kelson, J.R., Sewall, J.O., 2019. Revisiting the equable climate problem during the Late Cretaceous greenhouse using paleosol carbonate clumped isotope temperatures from the Campanian of the Western Interior Basin, USA. Palaeogeography, Palaeoclimatology, Palaeoecology 516, 244–267. https://doi.org/10.1016/j.palaeo.2018.12.004

Burgener, L., Hyland, E., Reich, B.J., Scotese, C., 2023. Cretaceous climates: Mapping paleo-Köppen climatic zones using a Bayesian statistical analysis of lithologic, paleontologic, and geochemical proxies. Palaeogeography, Palaeoclimatology, Palaeoecology 613, 111373. https://doi.org/10.1016/j.palaeo.2022.111373

Came, R.E., Eiler, J.M., Veizer, J., Azmy, K., Brand, U., Weidman, C.R., 2007. Coupling of surface temperatures and atmospheric CO2 concentrations during the Palaeozoic era. Nature 449, 198–201. https://doi.org/10.1038/nature06085

Chiocchini, M., Pampaloni, M.L., Pichezzi, R.M., 2012. Microfacies and microfossils of the Mesozoic carbonate successions of Latium and Abruzzi (Central Italy). Memorie per Servire alla Descrizione della Carta Geologica D'Italia, ISPRA, Dipartimento Difesa del Suolo 17, 1–269.

Clarke, L.J., Jenkyns, H.C., 1999. New oxygen isotope evidence for long-term Cretaceous climatic change in the Southern Hemisphere. Geology 27, 699. https://doi.org/10.1130/0091-7613(1999)027<0699:NOIEFL>2.3.CO;2

Cochran, J.K., Kallenberg, K., Landman, N.H., Harries, P.J., Weinreb, D., Turekian, K.K., Beck, A.J., Cobban, W.A., 2010. Effect of diagenesis on the Sr, O, and C isotope composition of late Cretaceous mollusks from the Western Interior Seaway of North America. American Journal of Science 310, 69–88. https://doi.org/10.2475/02.2010.01

Consorti, L., Arbulla, D., Bonini, L., Fabbi, S., Fanti, F., Franceschi, M., Frijia, G., Pini, G.A., 2021. The Mesozoic palaeoenvironmental richness of the Trieste Karst. GFT 13, 1–40. https://doi.org/10.3301/GFT.2021.06

Consorti, L., Boix, C., Caus, E., 2016. Pseudorhapydionina bilottei sp. nov., an endemic foraminifera from the post-Cenomanian/Turonian boundary (Pyrenees, NE Spain). Cretaceous Research 59, 147–154. https://doi.org/10.1016/j.cretres.2015.10.021

Consorti, L., Schlagintweit, F., 2021. A new Vandenbroeckia Marie, 1958 (Peneroplidae) adds further data on the survival of shallow-water benthic Foraminifera through the Cenomanian-Turonian boundary. Cretaceous Research 126, 104910. https://doi.org/10.1016/j.cretres.2021.104910

Cramer, B.D., Jarvis, I., 2020. Carbon Isotope Stratigraphy, in: Geologic Time Scale 2020. Elsevier, pp. 309–343. https://doi.org/10.1016/B978-0-12-824360-2.00011-5

Cucchi, F., Pirini Radrizzani, C., Pugliese, N., 1987. The carbonate stratigraphic sequence of the Karst of Trieste (Italy)., in: Proceedings of "International Symposium on Evolution of the Karstic Carbonate Platform." Mem. Soc. Geol. Ital., Trieste.

Cummins, R.C., Finnegan, S., Fike, D.A., Eiler, J.M., Fischer, W.W., 2014. Carbonate clumped isotope constraints on Silurian ocean temperature and seawater δ18O. Geochimica et Cosmochimica Acta 140, 241–258. https://doi.org/10.1016/j.gca.2014.05.024

de Winter, N.J., Claeys, P., 2016. Micro X-ray fluorescence (μXRF) line scanning on Cretaceous rudist bivalves: A new method for reproducible trace element profiles in bivalve calcite. Sedimentology 64, 231–251.

de Winter, N.J., Goderis, S., Dehairs, F., Jagt, J.W.M., Fraaije, R.H.B., Van Malderen, S.J.M., Vanhaecke, F., Claeys, P., 2017a. Tropical seasonality in the late Campanian (late Cretaceous): Comparison between multiproxy records from three bivalve taxa from Oman. Palaeogeography, Palaeoclimatology, Palaeoecology 485, 740–760. https://doi.org/10.1016/j.palaeo.2017.07.031

de Winter, N.J., Goderis, S., Van Malderen, S.J.M., Sinnesael, M., Vansteenberge, S., Snoeck, C., Belza, J., Vanhaecke, F., Claeys, P., 2020. Subdaily-Scale Chemical

Variability in a *Torreites Sanchezi* Rudist Shell: Implications for Rudist Paleobiology and the Cretaceous Day-Night Cycle. Paleoceanography and Paleoclimatology 35. https://doi.org/10.1029/2019PA003723

de Winter, N.J., Müller, I.A., Kocken, I.J., Thibault, N., Ullmann, C.V., Farnsworth, A., Lunt, D.J., Claeys, P., Ziegler, M., 2021. Absolute seasonal temperature estimates from clumped isotopes in bivalve shells suggest warm and variable greenhouse climate. Commun Earth Environ 2, 121. https://doi.org/10.1038/s43247-021-00193-9

de Winter, N.J., Sinnesael, M., Makarona, C., Vansteenberge, S., Claeys, P., 2017b. Trace element analyses of carbonates using portable and micro-X-ray fluorescence: performance and optimization of measurement parameters and strategies. J. Anal. At. Spectrom. 32, 1211–1223. https://doi.org/10.1039/C6JA00361C

Dechaseaux, C., C., Coogan, A.H., Perkins, B.F., 1969. Superfamily Hippuritacea Gray, 1848., in: Moore, R.C. (Ed.), Treatise on Invertebrate Paleontology, Part N, Mollusca 6, Bivalvia 2. Geological Society of America, Boulder, CO, and The University of Kansas, pp. N749–N817.

Del Viscio, G., Frijia, G., Posenato, R., Singh, P., Lehrmann, D.J., Payne, J.L., Al-Ramadan, K., Struck, U., Jochum, K.P., Morsilli, M., 2021. Proliferation of Chondrodonta as a proxy of environmental instability at the onset of OAE1a: Insights from shallow-water limestones of the Apulia Carbonate Platform. Sedimentology 68, 3191–3227. https://doi.org/10.1111/sed.12887

Del Viscio, G., Morsilli, M., Posenato, R., Frijia, G., Moro, A., Mezga, A., 2022. Proliferation of Chondrodonta in upper Cenomanian shallow-water limestones of the Adriatic Carbonate Platform (Croatia) as a proxy of environmental instability. Cretaceous Research 134, 105151. https://doi.org/10.1016/j.cretres.2022.105151

Dennis, K.J., Cochran, J.K., Landman, N.H., Schrag, D.P., 2013. The climate of the Late Cretaceous: New insights from the application of the carbonate clumped isotope thermometer to Western Interior Seaway macrofossil. Earth and Planetary Science Letters 362, 51–65. https://doi.org/10.1016/j.epsl.2012.11.036

Eagle, R.A., Eiler, J.M., Tripati, A.K., Ries, J.B., Freitas, P.S., Hiebenthal, C., Wanamaker, A.D., Taviani, M., Elliot, M., Marenssi, S., Nakamura, K., Ramirez, P., Roy, K., 2013. The influence of temperature and seawater carbonate saturation state on ^{13}C-^{18}O bond ordering in bivalve mollusks. Biogeosciences 10, 4591–4606. https://doi.org/10.5194/bg-10-4591-2013

Eiler, J.M., 2011. Paleoclimate reconstruction using carbonate clumped isotope thermometry. Quaternary Science Reviews 30, 3575–3588. https://doi.org/10.1016/j.quascirev.2011.09.001

Eiler, J.M., 2007. "Clumped-isotope" geochemistry—The study of naturally-occurring, multiply-substituted isotopologues. Earth and Planetary Science Letters 262, 309–327. https://doi.org/10.1016/j.epsl.2007.08.020

Elrick, M., Molina-Garza, R., Duncan, R., Snow, L., 2009. C-isotope stratigraphy and paleoenvironmental changes across OAE2 (mid-Cretaceous) from shallow-water platform carbonates of southern Mexico. Earth and Planetary Science Letters 277, 295–306. https://doi.org/10.1016/j.epsl.2008.10.020

Epstein, S., Buchsbaum, R., Lowenstam, H.A., Urey, H.C., 1953. Revised Carbonate-Water Isotopic Temperature Scale. GSA Bulletin 64, 1315–1326. https://doi.org/10.1130/0016-7606(1953)64[1315:RCITS]2.0.CO;2

Fernandez, A., Korte, C., Ullmann, C.V., Looser, N., Wohlwend, S., Bernasconi, S.M., 2021. Reconstructing the magnitude of Early Toarcian (Jurassic) warming using the reordered clumped isotope compositions of belemnites. Geochimica et Cosmochimica Acta 293, 308–327. https://doi.org/10.1016/j.gca.2020.10.005

Forster, A., Schouten, S., Moriya, K., Wilson, P.A., Sinninghe Damsté, J.S., 2007. Tropical warming and intermittent cooling during the Cenomanian/Turonian oceanic anoxic event 2: Sea surface temperature records from the equatorial Atlantic: Tropical Cenomanian/Turonian SST Records. Paleoceanography 22, PA1219. https://doi.org/10.1029/2006PA001349

Friedrich, O., Norris, R.D., Erbacher, J., 2012. Evolution of middle to Late Cretaceous oceans—A 55 m.y. record of Earth's temperature and carbon cycle. Geology 40, 107–110. https://doi.org/10.1130/G32701.1

Frijia, G., 2006. Stratigrafia integrata (bio- e chemostratigrafia) nelle successioni carbonatiche di mare basso del Cretacico Superiore dell'Appennino meridionale. (Ph.D. thesis). University of Naples Federico II, Naples, Italy.

Frijia, G., Forkner, R., Minisini, D., Pacton, M., Struck, U., Mutti, M., 2019. Cyanobacteria Proliferation in the Cenomanian-Turonian Boundary Interval of the Apennine Carbonate Platform: Immediate Response to the Environmental Perturbations Associated With OAE-2? Geochem. Geophys. Geosyst. 20, 2698–2716. https://doi.org/10.1029/2019GC008306

Frijia, G., Parente, M., 2008. Strontium isotope stratigraphy in the upper Cenomanian shallow-water carbonates of the southern Apennines: Short-term perturbations of marine $^{87}Sr/^{86}Sr$ during the oceanic anoxic event 2. Palaeogeography, Palaeoclimatology, Palaeoecology 261, 15–29. https://doi.org/10.1016/j.palaeo.2008.01.003

Frijia, G., Parente, M., Di Lucia, M., Mutti, M., 2015. Carbon and strontium isotope stratigraphy of the Upper Cretaceous (Cenomanian-Campanian) shallow-water carbonates of southern Italy: Chronostratigraphic calibration of larger foraminifera biostratigraphy. Cretaceous Research 53, 110–139. https://doi.org/10.1016/j.cretres.2014.11.002

Frijia, G., Parente, M., Mutti, M., 2014. The distribution of rudist-rich beds in the Upper Cretaceous of the Apennine Carbonate Platform (southern Italy): just a local pattern? Presented at the Tenth International Congress on Rudist Bivalves, Bellaterra.

Galeotti, S., Rusciadelli, G., Sprovieri, M., Lanci, L., Gaudio, A., Pekar, S., 2009. Sea-level control on facies architecture in the Cenomanian–Coniacian Apulian margin (Western Tethys): A record of glacio-eustatic fluctuations during the Cretaceous greenhouse? Palaeogeography, Palaeoclimatology, Palaeoecology 276, 196–205. https://doi.org/10.1016/j.palaeo.2009.03.011

Garrabou, J., Coma, R., Bensoussan, N., Bally, M., Chevaldonné, P., Cigliano, M., Diaz, D., Harmelin, J.G., Gambi, M.C., Kersting, D.K., Ledoux, J.B., Lejeusne, C., Linares, C., Marschal, C., Pérez, T., Ribes, M., Romano, J.C., Serrano, E., Teixido, N., Torrents, O., Zabala, M., Zuberer, F., Cerrano, C., 2009. Mass mortality in Northwestern Mediterranean rocky benthic communities: effects of the 2003 heat wave. Global Change Biology 15, 1090–1103. https://doi.org/10.1111/j.1365-2486.2008.01823.x

Ghosh, P., Adkins, J., Affek, H., Balta, B., Guo, W., Schauble, E.A., Schrag, D., Eiler, J.M., 2006. $^{13}C–^{18}O$ bonds in carbonate minerals: A new kind of paleothermometer. Geochimica et Cosmochimica Acta 70, 1439–1456. https://doi.org/10.1016/j.gca.2005.11.014

Gili, E., Götz, S., 2018. Paleoecology of Rudists. Treatise online, Part N 1, 1–29.

Gili, E., Masse, J.-P., Skelton, P.W., 1995. Rudists as gregarious sediment-dwellers, not reef-builders, on Cretaceous carbonate platforms. Paleogeography Paleoclimatology Paleoecology 118, 245–267.

Gillikin, D.P., Wanamaker, A.D., Andrus, C.F.T., 2019. Chemical sclerochronology. Chemical Geology 526, 1–6. https://doi.org/10.1016/j.chemgeo.2019.06.016

Gradstein, F.M., Ogg, J.G., Schmitz, M.D., Ogg, G.M. (Eds.), 2020. Geologic Time Scale 2020. Elsevier.

Gröcke, D.R., Gillikin, D.P., 2008. Advances in mollusc sclerochronology and sclerochemistry: tools for understanding climate and environment. Geo-Mar Lett 28, 265–268. https://doi.org/10.1007/s00367-008-0108-4

Grossman, E.L., 2012. Applying Oxygen Isotope Paleothermometry in Deep Time. Paleontol. Soc. pap. 18, 39–68. https://doi.org/10.1017/S1089332600002540

Grossman, E.L., Joachimski, M.M., 2022. Ocean temperatures through the Phanerozoic reassessed. Sci Rep 12, 8938. https://doi.org/10.1038/s41598-022-11493-1

Grotzinger, J.P., Fike, D.A., Fischer, W.W., 2011. Enigmatic origin of the largest-known carbon isotope excursion in Earth's history. Nature Geosci 4, 285–292. https://doi.org/10.1038/ngeo1138

Haq, B.U., 2014. Cretaceous eustasy revisited. Global and Planetary Change 113, 44–58. https://doi.org/10.1016/j.gloplacha.2013.12.007

Hasenberg, C., 2018. Hasenberg, C., 2018. Oxygen isotope analysis in Paleoclimatology. In The Geological Newsletter, News of the Geological Society of the Oregon Country. 86, 27-32. News of the Geological Society of the Oregon Country 86, 27–32.

Hay, W.W., 2008. Evolving ideas about the Cretaceous climate and ocean circulation. Cretaceous Research 29, 725–753. https://doi.org/10.1016/j.cretres.2008.05.025

Hay, W.W., Floegel, S., 2012. New thoughts about the Cretaceous climate and oceans. Earth-Science Reviews 115, 262–272. https://doi.org/10.1016/j.earscirev.2012.09.008

Henkes, G.A., Passey, B.H., Grossman, E.L., Shenton, B.J., Pérez-Huerta, A., Yancey, T.E., 2014. Temperature limits for preservation of primary calcite clumped isotope paleotemperatures. Geochimica et Cosmochimica Acta 139, 362–382. https://doi.org/10.1016/j.gca.2014.04.040

Henkes, G.A., Passey, B.H., Wanamaker, A.D., Grossman, E.L., Ambrose, W.G., Carroll, M.L., 2013. Carbonate clumped isotope compositions of modern marine mollusk and brachiopod shells. Geochimica et Cosmochimica Acta 106, 307–325. https://doi.org/10.1016/j.gca.2012.12.020

Hernandez, J.O., 2011. Rudists. Geology Today 27, 74–77.

Huber, B.T., MacLeod, K.G., Watkins, D.K., Coffin, M.F., 2018. The rise and fall of the Cretaceous Hot Greenhouse climate. Global and Planetary Change 167, 1–23. https://doi.org/10.1016/j.gloplacha.2018.04.004

Huber, B.T., Norris, R.D., MacLeod, K.G., 2002. Deep-sea paleotemperature record of extreme warmth during the Cretaceous. Geol 30, 123. https://doi.org/10.1130/0091-7613(2002)030<0123:DSPROE>2.0.CO;2

Huck, S., Heimhofer, U., 2021. Early Cretaceous sea surface temperature evolution in subtropical shallow seas. Sci Rep 11, 19765. https://doi.org/10.1038/s41598-021-99094-2

Huck, S., Heimhofer, U., 2015. Improving shallow-water carbonate chemostratigraphy by means of rudist bivalve sclerochemistry: RUDIST BIVALVE CHEMOSTRATIGRAPHY. Geochem. Geophys. Geosyst. 16, 3111–3128. https://doi.org/10.1002/2015GC005988

Huck, S., Steuber, T., Bernasconi, S., Weissert, H., Dhabi, A., 2012. Clumped isotope geochemistry of mid-Cretaceous (Barremian-Aptian) rudist shells: paleoclimatic and paleoenvironmental implications, in: Geophysical Research Abstracts. Presented at the EGU General Assembly 2012.

Huyghe, D., Daëron, M., de Rafelis, M., Blamart, D., Sébilo, M., Paulet, Y.-M., Lartaud, F., 2022. Clumped isotopes in modern marine bivalves. Geochimica et Cosmochimica Acta 316, 41–58. https://doi.org/10.1016/j.gca.2021.09.019

Immenhauser, A., Nägler, T.F., Steuber, T., Hippler, D., 2005. A critical assessment of mollusk 18O/16O, Mg/Ca, and 44Ca/40Ca ratios as proxies for Cretaceous seawater temperature seasonality. Palaeogeography, Palaeoclimatology, Palaeoecology 215, 221–237. https://doi.org/10.1016/j.palaeo.2004.09.005

Immenhauser, A., Schöne, B.R., Hoffmann, R., Niedermayr, A., 2016. Mollusc and brachiopod skeletal hard parts: Intricate archives of their marine environment. Sedimentology 63, 1–59. https://doi.org/10.1111/sed.12231

Ivany, L.C., 2012. Reconstructing Paleoseasonality from Accretionary Skeletal Carbonates—Challenges and Opportunities. Paleontol. Soc. pap. 18, 133–166. https://doi.org/10.1017/S108933260000259X

Jarvis, I., Lignum, J.S., Gröcke, D.R., Jenkyns, H.C., Pearce, M.A., 2011. Black shale deposition, atmospheric CO 2 drawdown, and cooling during the Cenomanian-Turonian Oceanic Anoxic Event: CO_2 Drawndown and Cooling during OAE2. Paleoceanography 26, PA3201. https://doi.org/10.1029/2010PA002081

Jarvis, I., Trabucho-Alexandre, J., Gröcke, D.R., Uličný, D., Laurin, J., 2015. Intercontinental correlation of organic carbon and carbonate stable isotope records: evidence of

climate and sea-level change during the Turonian (Cretaceous). Depositional Rec 1, 53–90. https://doi.org/10.1002/dep2.6

Jenkyns, H.C., Gale, A.S., Corfield, R.M., 1994. Carbon- and oxygen-isotope stratigraphy of the English Chalk and Italian Scaglia and its palaeoclimatic significance. Geol. Mag. 131, 1–34. https://doi.org/10.1017/S0016756800010451

Jimenez, M.Y., Ivany, L.C., Judd, E.J., Henkes, G., 2019. Low and seasonally variable salinity in the Pennsylvanian equatorial Appalachian Basin. Earth and Planetary Science Letters 519, 182–191. https://doi.org/10.1016/j.epsl.2019.04.051

Johnson, C.C., Kauffman, E.G., 1990. Originations, radiations and extinctions of Cretaceous rudistid bivalve species in the Caribbean Province, in: Kauffman, Erle G., Walliser, O.H. (Eds.), Extinction Events in Earth History, Lecture Notes in Earth Sciences. Springer-Verlag, Berlin/Heidelberg, pp. 305–324. https://doi.org/10.1007/BFb0011154

Johnson, C.C., Sanders, D., Kauffman, E.G., Hay, W.W., 2001. Patterns and Processes Influencing Upper Cretaceous Reefs. SEPM Special Publication 72, 549–585.

Judd, E.J., Bhattacharya, T., Ivany, L.C., 2020. A Dynamical Framework for Interpreting Ancient Sea Surface Temperatures. Geophys. Res. Lett. 47. https://doi.org/10.1029/2020GL089044

Judd, E.J., Wilkinson, B.H., Ivany, L.C., 2018. The life and time of clams: Derivation of intra-annual growth rates from high-resolution oxygen isotope profiles. Palaeogeography, Palaeoclimatology, Palaeoecology 490, 70–83. https://doi.org/10.1016/j.palaeo.2017.09.034

Jurkovšek, B., Biolchi, S., Furlani, S., Kolar-Jurkovšek, T., Zini, L., Jež, J., Tunis, G., Bavec, M., Cucchi, F., 2016. Geology of the Classical Karst Region (SW Slovenia–NE Italy). Journal of Maps 12, 352–362. https://doi.org/10.1080/17445647.2016.1215941

Kauffman, E.G., Johnson, C.C., 1988. The Morphological and Ecological Evolution of Middle and Upper Cretaceous Reef-Building Rudistids. PALAIOS 3, 194. https://doi.org/10.2307/3514530

Kiessling, W., Flügel, E., Golonka, J., 2003. Patterns of Phanerozoic carbonate platform sedimentation. Lethaia 36, 195–225. https://doi.org/10.1080/00241160310004648

Kluge, T., John, C.M., Jourdan, A.-L., Davis, S., Crawshaw, J., 2015. Laboratory calibration of the calcium carbonate clumped isotope thermometer in the 25–250 °C temperature range. Geochimica et Cosmochimica Acta 157, 213–227. https://doi.org/10.1016/j.gca.2015.02.028

Korbar, T., 2009. Orogenic evolution of the External Dinarides in the NE Adriatic region: a model constrained by tectonostratigraphy of Upper Cretaceous to Paleogene carbonates. Earth-Science Reviews 96, 296–312. https://doi.org/10.1016/j.earscirev.2009.07.004

Korbar, T., Glumac, B., Tesovic, B.C., Cadieux, S.B., 2012. Response of a carbonate platform to the Cenomanian-Turonian Drowning and OAE 2: a case study from the Adriatic Platform (Dalmatia, Croatia). Journal of Sedimentary Research 82, 163–176. https://doi.org/10.2110/jsr.2012/17

LeGrande, A.N., Schmidt, G.A., 2006. Global gridded data set of the oxygen isotopic composition in seawater. Geophys. Res. Lett. 33, L12604. https://doi.org/10.1029/2006GL026011

Linnert, C., Robinson, S.A., Lees, J.A., Bown, P.R., Pérez-Rodríguez, I., Petrizzo, M.R., Falzoni, F., Littler, K., Arz, J.A., Russell, E.E., 2014. Evidence for global cooling in the Late Cretaceous. Nat Commun 5, 4194. https://doi.org/10.1038/ncomms5194

Lohmann, K.C., 1988. Geochemical Patterns of Meteoric Diagenetic Systems and Their Application to Studies of Paleokarst, in: James, N.P., Choquette, P.W. (Eds.), Paleokarst. Springer New York, New York, NY, pp. 58–80. https://doi.org/10.1007/978-1-4612-3748-8_3

Lowenstam, H.A., Epstein, S., 1954. Paleotemperatures of the Post-Aptian Cretaceous as Determined by the Oxygen Isotope Method. The Journal of Geology 62, 207–248.

MacLeod, K.G., Huber, B.T., Berrocoso, Á.J., Wendler, I., 2013. A stable and hot Turonian without glacial δ18O excursions is indicated by exquisitely preserved Tanzanian foraminifera. Geology 41, 1083–1086. https://doi.org/10.1130/G34510.1

Marcilly, C.M., Torsvik, T.H., Conrad, C.P., 2022. Global Phanerozoic sea levels from paleogeographic flooding maps. Gondwana Research 110, 128–142. https://doi.org/10.1016/j.gr.2022.05.011

Marshall, J., 1992. Climatic and oceanographic isotopic signals from the carbonate rock record and their preservation. Geological Magazine 129, 143–160.

Martinis, B., 1962. Ricerche geologiche e paleontologiche sulla regione compresa tra il t. Iudrio e il f. Timavo (Friuli orientale). Rivista italiana di paleontologia e stratigrafia.

McArthur, J.M., 1994. Recent trends in strontium isotope stratigraphy. Terra Nova 6, 331–358. https://doi.org/10.1111/j.1365-3121.1994.tb00507.x

McArthur, J.M., Horwath, R.J., 2020. Strontium isotope stratigraphy: Lowess Version 6: Best-fit to the marine Sr-isotope curve for 0 to 509 Ma and accompanying look-up table for deriving numerical age.

Melis, R., Colizza, E., Pugliese, N., 2000. Eventi cenomaniani e turoniani nell'abisso di Trebiciano (Carso triestino). Accad. Naz. Sci. Lett. Arti di Modena, Collana di Studi 21, 169–176.

Miller, K.G., Sugarman, P.J., Browning, J.V., Kominz, M.A., Olsson, R.K., Feigenson, M.D., Hernández, J.C., 2004. Upper Cretaceous sequences and sea-level history, New Jersey Coastal Plain. Geo. Society Am. Bull. 116, 368. https://doi.org/10.1130/B25279.1

Moro, A., 1997. Stratigraphy and paleoenvironments of rudist biostromes in the Upper Cretaceous (Turonian-upper Santonian) limestones of southern Istria, Croatia. Palaeogeography, Palaeoclimatology, Palaeoecology 131, 113–131. https://doi.org/10.1016/S0031-0182(96)00144-7

Moro, A., Skelton, P.W., Ćosović, V., 2002. Palaeoenvironmental setting of rudists in the Upper Cretaceous (Turonian–Maastrichtian) Adriatic Carbonate Platform (Croatia), based on sequence stratigraphy. Cretaceous Research 23, 489–508. https://doi.org/10.1006/cres.2002.1017

O'Brien, C.L., Robinson, S.A., Pancost, R.D., Sinninghe Damsté, J.S., Schouten, S., Lunt, D.J., Alsenz, H., Bornemann, A., Bottini, C., Brassell, S.C., Farnsworth, A., Forster, A., Huber, B.T., Inglis, G.N., Jenkyns, H.C., Linnert, C., Littler, K., Markwick, P., McAnena, A., Mutterlose, J., Naafs, B.D.A., Püttmann, W., Sluijs, A., van Helmond, N.A.G.M., Vellekoop, J., Wagner, T., Wrobel, N.E., 2017. Cretaceous sea-surface temperature evolution: Constraints from TEX_{86} and planktonic foraminiferal oxygen isotopes. Earth-Science Reviews 172, 224–247. https://doi.org/10.1016/j.earscirev.2017.07.012

O'Connor, L.K., Robinson, S.A., Naafs, B.D.A., Jenkyns, H.C., Henson, S., Clarke, M., Pancost, R.D., 2019. Late Cretaceous Temperature Evolution of the Southern High Latitudes: A TEX_{86} Perspective. Paleoceanography and Paleoclimatology 34, 436–454. https://doi.org/10.1029/2018PA003546

Oehlert, A.M., Swart, P.K., 2019. Rolling window regression of $\delta^{13}C$ and $\delta^{18}O$ values in carbonate sediments: Implications for source and diagenesis. Depositional Rec 5, 613–630. https://doi.org/10.1002/dep2.88

Otoničar, B., 2007. Upper Cretaceous to Paleogene forbulge unconformity associated with foreland basin evolution (Kras, Matarsko podolje and Istria; SW Slovenia and NW Croatia). Acta Carsologica 36, 101–120.

Parente, M., Frijia, G., Di Lucia, M., Jenkyns, H.C., Woodfine, R.G., Baroncini, F., 2008. Stepwise extinction of larger foraminifers at the Cenomanian/Turonian: A shallow-water perspective on nutrient fluctuations during Oceanic Anoxic Event 2 (Bonarelli Event). Geology 39, 715–718.

Paul, C.R.C., Lamolda, M.A., Mitchell, S.F., Vaziri, M.R., Gorostidi, A., Marshall, J.D., 1999. The Cenomanian-Turonian boundary at Eastbourne (Sussex, UK): A proposed European reference section. Palaeogeography, Palaeoclimatology, Palaeoecology 150, 83–121.

Pearson, P.N., 2012. Oxygen Isotopes in Foraminifera: Overview and Historical Review. Paleontol. Soc. pap. 18, 1–38. https://doi.org/10.1017/S1089332600002539

Petersen, S.V., Tabor, C.R., Lohmann, K.C., Poulsen, C.J., Meyer, K.W., Carpenter, S.J., Erickson, J.M., Matsunaga, K.K.S., Smith, S.Y., Sheldon, N.D., 2016. Temperature and salinity of the Late Cretaceous Western Interior Seaway. Geology 44, 903–906. https://doi.org/10.1130/G38311.1

Petrizzo, D.A., Young, E.D., Runnegar, B.N., 2014. Implications of high-precision measurements of 13 C– 18 O bond ordering in CO 2 for thermometry in modern bivalved mollusc shells. Geochimica et Cosmochimica Acta 142, 400–410. https://doi.org/10.1016/j.gca.2014.07.017

Petrizzo, M.R., Amaglio, G., Watkins, D.K., MacLeod, K.G., Huber, B.T., Hasegawa, T., Wolfgring, E., 2022. Biotic and Paleoceanographic Changes Across the Late Cretaceous Oceanic Anoxic Event 2 in the Southern High Latitudes (IODP Sites U1513 and U1516, SE Indian Ocean). Paleoceanog and Paleoclimatol 37. https://doi.org/10.1029/2022PA004474

Philip, J.M., Airaud-Crumiere, C., 1991. The demise of the rudist-bearing carbonate platforms at the Cenomanian/Turonian boundary: a global control. Coral Reefs 10, 115–125. https://doi.org/10.1007/BF00571829

Picotti, V., Cobianchi, M., Luciani, V., Blattmann, F., Schenker, T., Mariani, E., Bernasconi, S.M., Weissert, H., 2019. Change from rimmed to ramp platform forced by regional and global events in the Cretaceous of the Friuli-Adriatic Platform (Southern Alps, Italy). Cretaceous Research 104, 104177. https://doi.org/10.1016/j.cretres.2019.07.007

Pohl, A., Laugié, M., Borgomano, J., Michel, J., Lanteaume, C., Scotese, C.R., Frau, C., Poli, E., Donnadieu, Y., 2019. Quantifying the paleogeographic driver of Cretaceous carbonate platform development using paleoecological niche modeling. Palaeogeography, Palaeoclimatology, Palaeoecology 514, 222–232. https://doi.org/10.1016/j.palaeo.2018.10.017

Polšak, A., 1964. Geologija južne Istrie s osobitim obzirom na biostratigraliju krednih naslaga (Géologie de l'lstrie méridiohale specialement par rapport a la biostrutigraphie des couches cretacdes). Geologia Croatica 18, 415–509.

Pons, J.M., Vicens, E., 2008. The structure of the outer shell layer in radiolitid rudists, a morphoconstructional approach. Lethaia 41, 219–234. https://doi.org/10.1111/j.1502-3931.2007.00048.x

Posenato, R., Frijia, G., Morsilli, M., Moro, A., Del Viscio, G., Mezga, A., 2020. Paleoecology and proliferation of the bivalve Chondrodonta joannae (Choffat) in the upper Cenomanian (Upper Cretaceous) Adriatic Carbonate Platform of Istria (Croatia). Palaeogeography, Palaeoclimatology, Palaeoecology 548, 109703. https://doi.org/10.1016/j.palaeo.2020.109703

Pucéat, E., Lécuyer, C., Donnadieu, Y., Naveau, P., Cappetta, H., Ramstein, G., Huber, B.T., Kriwet, J., 2007. Fish tooth δ18O revising Late Cretaceous meridional upper ocean water temperature gradients. Geol 35, 107. https://doi.org/10.1130/G23103A.1

Rainer, T., Sachsenhofer, R.F., Green, P.F., Rantitsch, G., Herlec, U., Vrabec, M., 2016. Thermal maturity of Carboniferous to Eocene Sediments of the Alpine–Dinaric Transition Zone (Slovenia). International Journal of Coal Geology 157, 19–38. https://doi.org/10.1016/j.coal.2015.08.005

Ravelo, A.C., Hillaire-Marcel, C., 2007. Chapter Eighteen The Use of Oxygen and Carbon Isotopes of Foraminifera in Paleoceanography, in: Developments in Marine Geology. Elsevier, pp. 735–764. https://doi.org/10.1016/S1572-5480(07)01023-8

Rohling, E.J., 2013. PALEOCEANOGRAPHY, PHYSICAL AND CHEMICAL PROXIES | Oxygen Isotope Composition of Seawater, in: Encyclopedia of Quaternary Science. Elsevier, pp. 915–922. https://doi.org/10.1016/B978-0-444-53643-3.00293-4

Sanders, D., 2001. Burrow-mediated carbonate dissolution in rudist biostromes (Aurisina, Italy): implications for taphonomy in tropical, shallow subtidal carbonate environments. Palaeogeography, Palaeoclimatology, Palaeoecology 168, 39–74. https://doi.org/10.1016/S0031-0182(00)00249-2

Schauble, E.A., Ghosh, P., Eiler, J.M., 2006. Preferential formation of 13C–18O bonds in carbonate minerals, estimated using first-principles lattice dynamics. Geochimica et Cosmochimica Acta 70, 2510–2529. https://doi.org/10.1016/j.gca.2006.02.011

Schlagintweit, F., Cvetko Tešović, B., 2017. Braciana jelaskai n. gen., n. sp., a new larger benthic foraminifer from the Upper Cretaceous (Santonian?–lower Campanian) of the Dinaric-Hellenic realm. Cretaceous Research 72, 32–38. https://doi.org/10.1016/j.cretres.2016.12.005

Schlagintweit, F., Kołodziej, B., Qorri, A., 2015. Foraminiferan-calcimicrobial benthic communities from Upper Cretaceous shallow-water carbonates of Albania (Kruja Zone). Cretaceous Research 56, 432–446. https://doi.org/10.1016/j.cretres.2015.04.009

Schlagintweit, F., Septfontaine, M., 2022. SIPHOPFENDERINA GEN. NOV. (Type-Species Arenobulimina Geyikensis Solak, 2022), A Primitive Pfenderinid Foraminifera from the Cretaceous of Neothethys. Acta pal rom 53–60. https://doi.org/10.35463/j.apr.2023.01.06

Schlagintweit, F., Yazdi-Moghadam, M., 2021. Moncharmontia De Castro 1967, benthic foraminifera from the middle-upper Cenomanian of the Sarvak Formation of SW Iran (Zagros Zone): a CTB survivor taxon. mpal 67, 19–29. https://doi.org/10.47894/mpal.67.1.03

Schmidt, C., Titelboim, D., Brandt, J., Herut, B., Abramovich, S., Almogi-Labin, A., Kucera, M., 2016. Extremely heat tolerant photo-symbiosis in a shallow marine benthic foraminifera. Sci Rep 6, 30930. https://doi.org/10.1038/srep30930

Schmitt, K.E., 2019. Early Cretaceous Shoal Water Carbonates from the Central Apennines; Sedimentology, Chemostratigraphy and Sclerochemistry (Dissertation). Faculty of Natural Sciences, University of Hannover, Hannover.

Schmitt, K.E., Huck, S., Krummacker, M., De Winter, N.J., Godet, A., Claeys, P., Heimhofer, U., 2022. Radiolitid rudists: an underestimated archive for Cretaceous climate reconstruction? LET 55, 1–21. https://doi.org/10.18261/let.55.4.4

Schöne, B.R., Fiebig, J., Pfeiffer, M., Gleβ, R., Hickson, J., Johnson, A.L.A., Dreyer, W., Oschmann, W., 2005. Climate records from a bivalved Methuselah (Arctica islandica, Mollusca; Iceland). Palaeogeography, Palaeoclimatology, Palaeoecology 228, 130–148. https://doi.org/10.1016/j.palaeo.2005.03.049

Schroeder, R., Neumann, M. (Eds.), 1985. Les grands foraminiféres du Crétacé moyen de la région méditerraniénne., Geobios Mém. Spec.

Scotese, C.R., Song, H., Mills, B.J.W., van der Meer, D.G., 2021. Phanerozoic paleotemperatures: The earth's changing climate during the last 540 million years. Earth-Science Reviews 215, 103503. https://doi.org/10.1016/j.earscirev.2021.103503

Seuront, L., Nicastro, K.R., Zardi, G.I., Goberville, E., 2019. Decreased thermal tolerance under recurrent heat stress conditions explains summer mass mortality of the blue mussel Mytilus edulis. Sci Rep 9, 17498. https://doi.org/10.1038/s41598-019-53580-w

Shenton, B.J., Grossman, E.L., Passey, B.H., Henkes, G.A., Becker, T.P., Laya, J.C., Perez-Huerta, A., Becker, S.P., Lawson, M., 2015. Clumped isotope thermometry in deeply buried sedimentary carbonates: The effects of bond reordering and recrystallization. Geological Society of America Bulletin B31169.1. https://doi.org/10.1130/B31169.1

Skelton, P.W., 2018. Shell Structure, Anatomy, and Evolution. Treatise online, Part N 1, 1–37.

Skelton, P.W., 2003. Rudist Evolution and Extinction — A North African Perspective, in: Gili, E., Hédi Negra, M., Skelton, Peter W. (Eds.), North African Cretaceous Carbonate Platform Systems. Springer Netherlands, Dordrecht, pp. 215–227. https://doi.org/10.1007/978-94-010-0015-4_13

Skelton, P.W., Gili, E., 2002. Palaeoecological classification of rudist morphotypes., in: Sladić-Trifunović, M. (Ed.), Proceedings – First International Conference on Rudists – Beograd, 1988. Union of Geological Societies of Yugoslavia, Memorial Publication, pp. 265–285.

Smith, M.E., Moore, E.W., Swart, P.K., 2022. Constraining diagenesis within shallow water carbonate environments: Insights from clumped and sulfur isotopes. Chemical Geology 614, 121183. https://doi.org/10.1016/j.chemgeo.2022.121183

Song, Haijun, Kemp, D.B., Tian, L., Chu, D., Song, Huyue, Dai, X., 2021. Thresholds of temperature change for mass extinctions. Nat Commun 12, 4694. https://doi.org/10.1038/s41467-021-25019-2

Song, Haijun, Wignall, P.B., Song, Huyue, Dai, X., Chu, D., 2019a. Seawater Temperature and Dissolved Oxygen over the Past 500 Million Years. J. Earth Sci. 30, 236–243. https://doi.org/10.1007/s12583-018-1002-2

Song, Haijun, Wignall, P.B., Song, Huyue, Dai, X., Daoliang, C., 2019b. Song, H., Wignall, P.B., Song, H. et al. Seawater Temperature and Dissolved Oxygen over the Past 500 Million Years. J. Earth Sci. 30, 236–243 (2019). https://doi.org/10.1007/s12583-018-1002-2. Journal of Earth Sciences 30, 236–243.

Steuber, T., 2003. Strontium isotope stratigraphy of Cretaceous hippuritid rudist bivalves: rates of morphological change and heterochronic evolution. Palaeogeography, Palaeoclimatology, Palaeoecology 200, 221–243. https://doi.org/10.1016/S0031-0182(03)00452-8

Steuber, T., 1999. Isotopic and chemical intra-shell variations in low-Mg calcite of rudist bivalves (Mollusca-Hippuritacea): disequilibrium fractionations and late Cretaceous seasonality. International Journal of Earth Sciences 88, 551–570. https://doi.org/10.1007/s005310050284

Steuber, T., 1996. Stable isotope sclerochronology of rudist bivalves: Growth rates and Late Cretaceous seasonality. Geol 24, 315. https://doi.org/10.1130/0091-7613(1996)024<0315:SISORB>2.3.CO;2

Steuber, T., Korbar, T., Jelaska, V., Gušić, I., 2005a. Strontium-isotope stratigraphy of Upper Cretaceous platform carbonates of the island of Brač (Adriatic Sea, Croatia): implications for global correlation of platform evolution and biostratigraphy. Cretaceous Research 26, 741–756. https://doi.org/10.1016/j.cretres.2005.04.004

Steuber, T., Löser, H., Mutterlose, J., Parente, M., 2023. Biogeodynamics of Cretaceous marine carbonate production. Earth-Science Reviews 238, 104341. https://doi.org/10.1016/j.earscirev.2023.104341

Steuber, T., Mitchell, S.F., Buhl, D., Gunter, G., Kasper, H.U., 2002. Catastrophic extinction of Caribbean rudist bivalves at the Cretaceous-Tertiary boundary. Geol 30, 999. https://doi.org/10.1130/0091-7613(2002)030<0999:CEOCRB>2.0.CO;2

Steuber, T., Rauch, M., Masse, J.-P., Graaf, J., Malkoč, M., 2005b. Low-latitude seasonality of Cretaceous temperatures in warm and cold episodes. Nature 437, 1341–1344. https://doi.org/10.1038/nature04096

Steuber, T., Schlüter, M., 2012. Strontium-isotope stratigraphy of Upper Cretaceous rudist bivalves: Biozones, evolutionary patterns and sea-level change calibrated to numerical ages. Earth-Science Reviews 114, 42–60. https://doi.org/10.1016/j.earscirev.2012.04.004

Steuber, T., Scott, R.W., Mitchell, S.F., Skelton, P.W., 2016. Stratigraphy and Diversity Dynamics of Jurassic–Cretaceous Hippuritida (Rudist Bivalves). Treatise online, Part N 1.

Stoll, H.M., Schrag, D.P., 2000. High-resolution stable isotope records from the Upper Cretaceous rocks of Italy and Spain: Glacial episodes in a greenhouse planet? Geological Society of America Bulletin.

Stolper, D.A., Eiler, J.M., 2015. The kinetics of solid-state isotope-exchange reactions for clumped isotopes: A study of inorganic calcites and apatites from natural and experimental samples. American Journal of Science 315, 363–411. https://doi.org/10.2475/05.2015.01

Swart, P.K., Oehlert, A.M., 2018. Revised interpretations of stable C and O patterns in carbonate rocks resulting from meteoric diagenesis. Sedimentary Geology 364, 14–23. https://doi.org/10.1016/j.sedgeo.2017.12.005

Tierney, J.E., Poulsen, C.J., Montañez, I.P., Bhattacharya, T., Feng, R., Ford, H.L., Hönisch, B., Inglis, G.N., Petersen, S.V., Sagoo, N., Tabor, C.R., Thirumalai, K., Zhu, J., Burls, N.J., Foster, G.L., Goddéris, Y., Huber, B.T., Ivany, L.C., Kirtland Turner, S., Lunt, D.J., McElwain, J.C., Mills, B.J.W., Otto-Bliesner, B.L., Ridgwell, A., Zhang, Y.G., 2020. Past climates inform our future. Science 370, eaay3701. https://doi.org/10.1126/science.aay3701

Tsikos, H., Jenkyns, H.C., Walsworth-Bell, B., Petrizzo, M.R., Forster, A., Kolonic, S., 2004. Carbon-isotope stratigraphy recorded by the Cenomanian-Turonian Oceanic Anoxic Event: Correlation and implications based on three key localities. Journal of the Geological Society of London 161, 711–719.

Ullmann, C.V., Korte, C., 2015. Diagenetic alteration in low-Mg calcite from macrofossils: a review. GQ. https://doi.org/10.7306/gq.1217

Urey, H.C., 1947. The thermodynamic properties of isotopic substances. J. Chem. Soc. 562. https://doi.org/10.1039/jr9470000562

Urey, H.C., Lowenstam, H.A., Epstein, S., McKinney, C.R., 1951. Measurement of Paleotemperatures and Temperatures of the Upper Cretaceous of England, Denmark, and the Southeastern United States. Bulletin of the Geological Society of America 62, 399–416.

van der Meer, D.G., van den Berg van Saparoea, A.P.H., van Hinsbergen, D.J.J., van de Weg, R.M.B., Godderis, Y., Le Hir, G., Donnadieu, Y., 2017. Reconstructing first-order changes in sea level during the Phanerozoic and Neoproterozoic using strontium isotopes. Gondwana Research 44, 22–34. https://doi.org/10.1016/j.gr.2016.11.002

Vansteenberge, S., De Winter, N.J., Sinnesael, M., Xueqin, Z., Verheyden, S., Claeys, P., 2020. Benchtop μXRF as a tool for speleothem trace elemental analysis: Validation, limitations and application on an Eemian to early Weichselian (125–97 ka) stalagmite from Belgium. Palaeogeography, Palaeoclimatology, Palaeoecology 538, 109460. https://doi.org/10.1016/j.palaeo.2019.109460

Veizer, J., Prokoph, A., 2015. Temperatures and oxygen isotopic composition of Phanerozoic oceans. Earth-Science Reviews 146, 92–104. https://doi.org/10.1016/j.earscirev.2015.03.008

Velić, I., 2007. Stratigraphy and Palaeobiogeography of Mesozoic Benthic Foraminifera of the Karst Dinarides (SE Europe). Geologia Croatica 60, 1–113.

Velić, I., Vlahović, I., 2009. Geological Map of the Republic of Croatia. Scale 1: 300.000. explanatory notes HGI-CGS.

Vellekoop, J., Kaskes, P., Sinnesael, M., Huygh, J., Déhais, T., Jagt, J.W.M., Speijer, R.P., Claeys, P., 2022. A new age model and chemostratigraphic framework for the Maastrichtian type area (southeastern Netherlands, northeastern Belgium). nos 55, 479–501. https://doi.org/10.1127/nos/2022/0703

Vlahović, I., Tišljar, J., Velić, I., Matičec, D., 2005. Evolution of the Adriatic Carbonate Platform: Palaeogeography, main events and depositional dynamics. Palaeogeography, Palaeoclimatology, Palaeoecology 220, 333–360. https://doi.org/10.1016/j.palaeo.2005.01.011

Walliser, E.O., Schöne, B.R., 2020. Paleoceanography of the Late Cretaceous northwestern Tethys Ocean: Seasonal upwelling or steady thermocline? PLoS ONE 15, e0238040. https://doi.org/10.1371/journal.pone.0238040

Watkins, J.M., Hunt, J.D., Ryerson, F.J., DePaolo, D.J., 2014. The influence of temperature, pH, and growth rate on the δ18O composition of inorganically precipitated calcite. Earth and Planetary Science Letters 404, 332–343. https://doi.org/10.1016/j.epsl.2014.07.036

Wierzbowski, H., 2021. Advances and Challenges in Palaeoenvironmental Studies Based on Oxygen Isotope Composition of Skeletal Carbonates and Phosphates. Geosciences 11, 419. https://doi.org/10.3390/geosciences11100419

Wiese, F., Voigt, S., 2002. Late Turonian (Cretaceous) climate cooling in Europe: faunal response and possible causes Phase de refroidissement au Turonien supérieur (Crétacé) en Europe : réaction de la faune et causes possibles.

Yazdi-Moghadam, M., Schlagintweit, F., 2021. Cenomanian “orbitoliniform” foraminifera—State of the art and description of Ebrahimiella dercourti (Decrouez and Moullade, 1974) gen. et comb. nov. (family Coskinolinidae) from the Sarvak Formation (SW Iran, Zagros Zone). Cretaceous Research 126, 104885. https://doi.org/10.1016/j.cretres.2021.104885

Zachos, J.C., Stott, L.D., Lohmann, K.C., 1994. Evolution of Early Cenozoic marine temperatures. Paleoceanography 9, 353–387. https://doi.org/10.1029/93PA03266

Zhang, J.Z., Petersen, S.V., 2023. Clumped and oxygen isotope sclerochronology methods tested in the bivalve Lucina pensylvanica. Chemical Geology 620, 121346. https://doi.org/10.1016/j.chemgeo.2023.121346

Zhou, J., Poulsen, C.J., Pollard, D., White, T.S., 2008. Simulation of modern and middle Cretaceous marine δ1O with an ocean-atmosphere general circulation model: Modern, Mid-Cretaceous Seawater $\delta^{18}O$. Paleoceanography 23. https://doi.org/10.1029/2008PA001596

8 Appendices

Appendix 1

Supplementary information 1

Hippurites incisa

The average Δ47 value in *H. incisa* shell material is 0.560±0.016 ‰. Calculating the temperature, this value represents 43.6±8.2 °C. Keeping in mind the seasonal temperature variations indicated by the $\delta^{18}O$ analysis of the growth profile of the specimen (~11 °C), the resulting maximum annual temperature would equal almost 50 °C. Such temperatures are approaching the temperature limits for any multicellular organism; no modern multicellular organisms can live at temperatures above 50 °C (Brock, 1985). Fig.S1c shows that the average Δ47 and hence the T(Δ47) of the *H. incisa* shell material is dragged towards lower Δ47 (and therefore, higher T(Δ47)) by one of the sub-datasets (*i.e.*, drilling areas, Fig.S1a); the Bulk shell subset. The Bulk shell subset was included in the dataset in order to enlarge the number of aliquots from which the average shell Δ47 was calculated (and to lower the error (95%CL) of that average), and therefore, the drilling area was rather large, enhancing the possibility of unintended sampling of a recrystallized portion of the shell (Fig.S1a), resulting in the opposite effect on the error than intended. This interpretation is further supported by the large standard deviation (SD) on the Δ47 average of the Bulk shell subset, which is higher than the SD on Δ47 of the Growth profile-detail sampling subset. Given that the Growth profile-detailed sampling subset covers the maximum seasonal temperature span (see Results), the SD higher than the SD of the Growth profile-detailed sampling subset likely represents a scatter caused by other reasons than the seasonal environmental oscillations, probably by recrystallization of a portion of the drilling area.

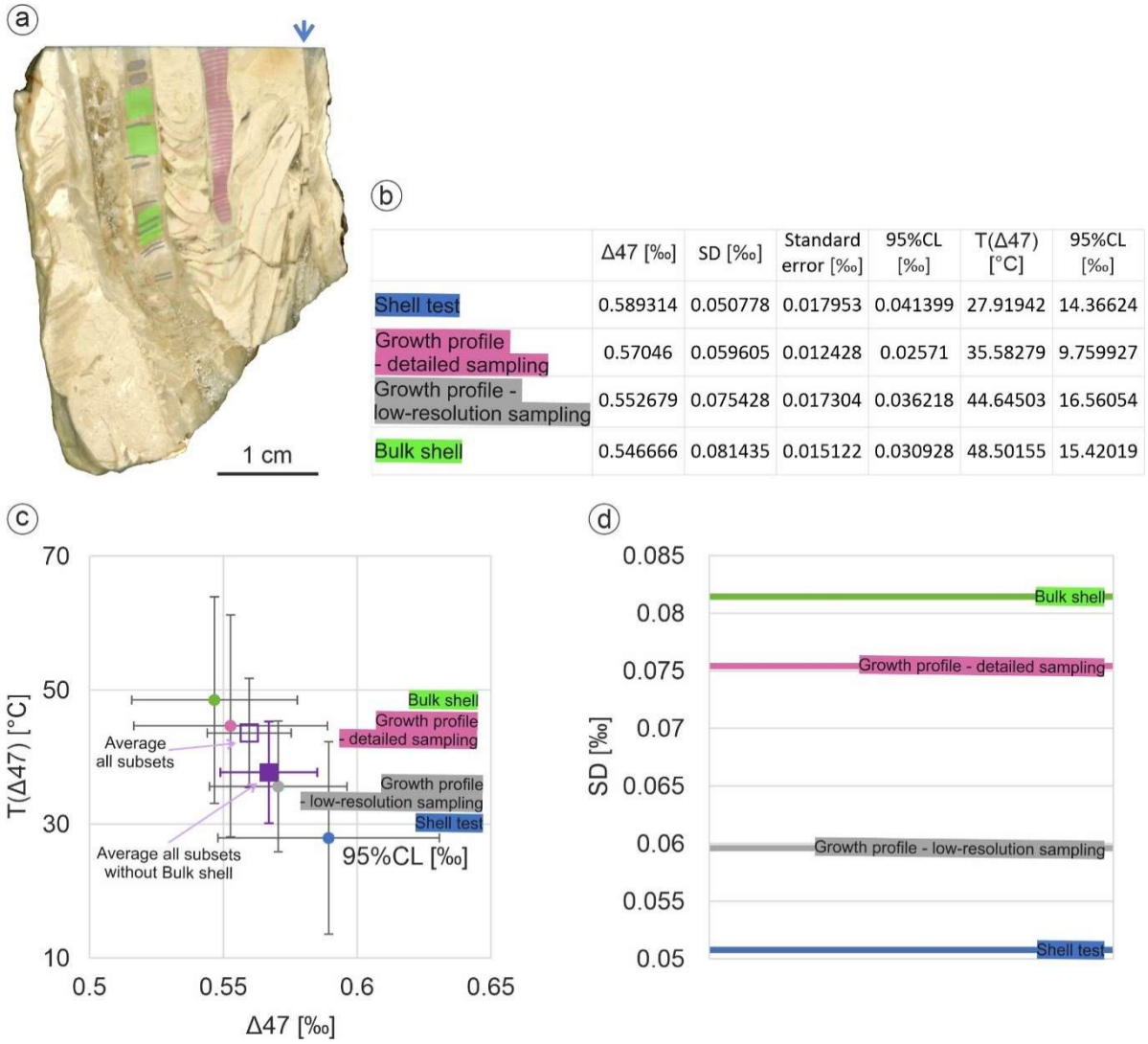

	Δ47 [‰]	SD [‰]	Standard error [‰]	95%CL [‰]	T(Δ47) [°C]	95%CL [‰]
Shell test	0.589314	0.050778	0.017953	0.041399	27.91942	14.36624
Growth profile - detailed sampling	0.57046	0.059605	0.012428	0.02571	35.58279	9.759927
Growth profile - low-resolution sampling	0.552679	0.075428	0.017304	0.036218	44.64503	16.56054
Bulk shell	0.546666	0.081435	0.015122	0.030928	48.50155	15.42019

Fig.S1. **a.** Drilling areas in *Hippurites incisa*, yielding four sub-datasets. The shell test drilling area (blue arrow) is located on the top of the specimen, on transect more or less perpendicular to growth axis. **b.** Results of Δ47 analysis and temperature calculations (using equation from Anderson et al., 2021). **c.** same as b., subsets plotted separately, the average Δ47 is calculated for all the shell material including/excluding the Bulk shell subset. **d.** Standard deviation on average Δ47 value per subset.

Excluding the Bulk shell subset when calculating the average Δ47 value of the shell material in *H. incisa*, the resulting Δ47 average is 0.567±0.018 ‰, which corresponds to 37.7±7.6 °C. This result is in better agreement with the previously reported Turonian paleotemperature maxima, *e.g.*, TEX_{86} and $\delta^{18}O_{\text{planktic foraminifera}}$-derived late Cenomanian-Turonian SSTs of over 35 °C (O'Brien et al., 2017).

Taking into consideration the above-mentioned reasons, the Bulk shell subset was excluded from further interpretations.

Praeradiolites ciryi

The average Δ47 value in *P. ciryi* shell material is 0.571±0.016 ‰. Calculating the temperature, this value represents 39.2±7.1 °C. Evaluating the internal consistency of the dataset, it becomes apparent that one subset (the Bulk shell drilling area; Fig.S2a) plots away from the rest of the subsets, enlarging the error on the Δ47 average and dragging the resulting T(Δ47) towards higher values (Fig.S2e). Same as above, the Bulk shell subset was included in the dataset in order to enlarge the number of aliquots from which the average Δ47 was calculated. Therefore, the drilling area was rather large, enhancing the possibility of unintended sampling of a recrystallized portion of the shell (Supp.Fig.2a).

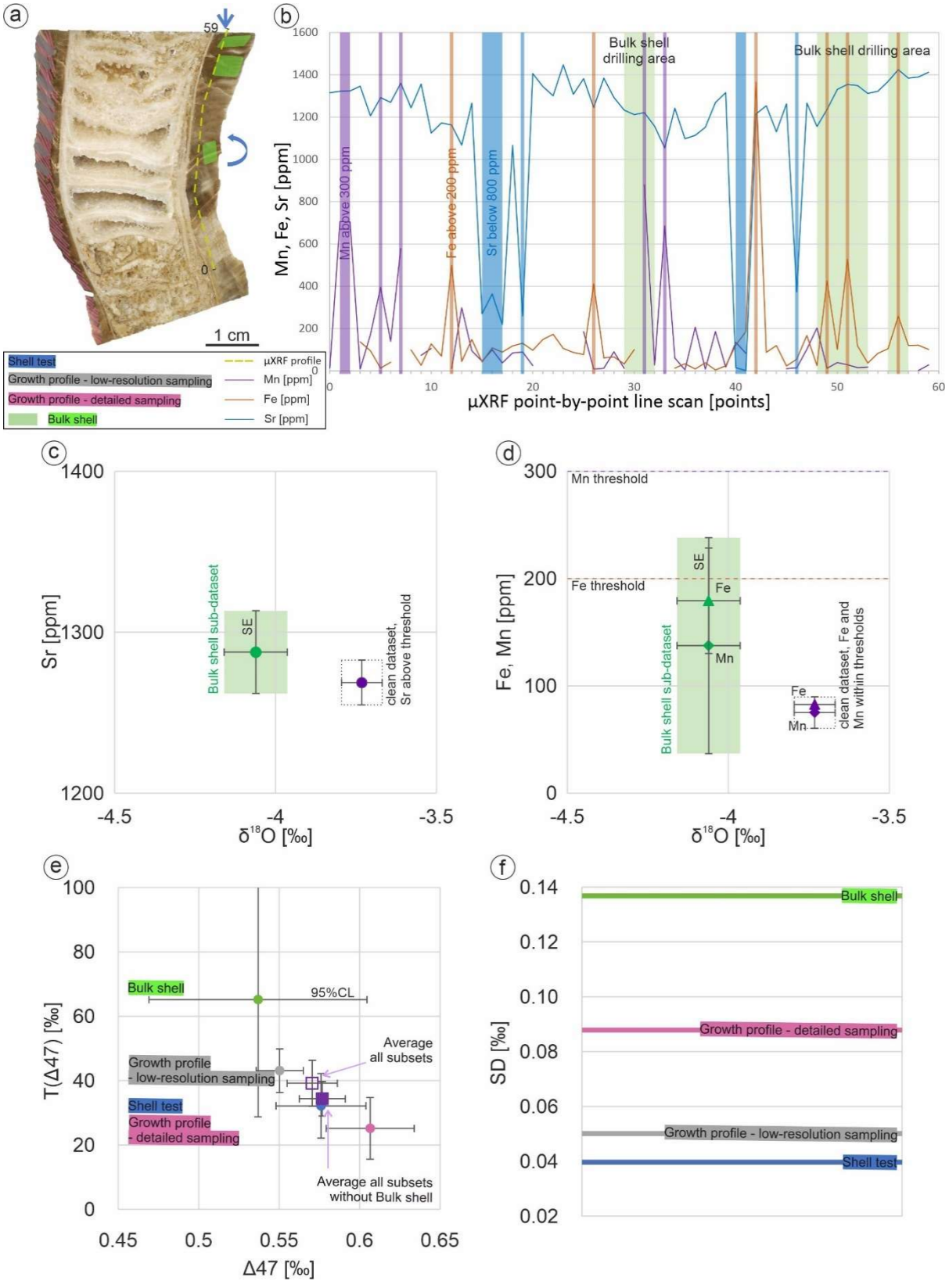

Fig.S1. **a.** Drilling areas in *Praeradiolites ciryi*, yielding four sub-datasets (Tab.S1). The shell test drilling areas (blue arrows) are located on the top of the specimen, on transect more or less perpendicular to growth axis, and on cleaned outer surface of the shell. **b.** Results of µXRF point-by-point coarse-resolution line scan crossing the Bulk shell drilling area (green rectangles). Peaks in Mn and Fe above thresholds (300 and 200 ppm respectively)

and drops in Sr content (below 800 ppm) are marked. The peaks in Mn or Fe correspond to Bulk shell drilling areas, suggesting at least partial recrystallization of the Bulk shell drilled area. **c.** Sr data plotted vs. $\delta^{18}O$ results. The clean-dataset datapoint represents an average of $\delta^{18}O$ results of all remaining subsets (except for the Bulk shell) and all Sr results of µXRF line scan that fall above the threshold of 800 ppm, suggested for well-preserved rudist shells (Frijia et al., 2015). **d.** same as c., for Fe and Mn. **e.** Results of individual subsets plotted separately, the average Δ47 is calculated for all the shell material including/excluding the Bulk shell subset. The temperatures are calculated using equation from Anderson et al. (2021). **f.** Standard deviation on average Δ47 value per subset.

Tab.S1. Results of Δ47 analysis and temperature calculations (using equation from Anderson et al., 2021).

	Δ47 [‰]	SD [‰]	Standard error [‰]	95%CL [‰]	T(Δ47) [°C]	95%CL [‰]
Shell test	0.575957	0.039679	0.012548	0.027958	32.16438	10.00271
Growth profile - detailed sampling	0.606538	0.087882	0.01356	0.027366	25.1575	9.582723
Growth profile - low-resolution sampling	0.550291	0.050129	0.007312	0.01471	43.1118	6.771169
Bulk shell	0.536875	0.136773	0.032238	0.067729	65.16739	36.4078

This assumption is supported by the results of µXRF point-by-point line scan, which shows peaks in Mn or Fe corresponding to the Bulk shell drilling areas (Fig.S2b, around points 30, 50, and 55). The peaks in Mn and Fe as well as the drop in Sr values between point 1 and 20 (Fig.S2b) correspond to the cellulo prismatic structure of the shell wall visible in the lower portion of the specimen (Fig.S2a). The averaged $\delta^{18}O$ results of the Bulk shell subset differ from the clean dataset by ~0.5 ‰ (Fig.S2c, d), and the Fe content differs by ~97 ppm (Fig.S2d), whereas the averaged Sr and Mn content of the clean dataset falls within the uncertainty (95%CL) of the Bulk shell subset (Fig.2c, d). Even though all the averaged subset-trace element contents (Bulk shell and clean) fall above the Sr threshold (800 ppm), and below the Mn (300) and Fe maximum levels (Mn uncertainty exceeding the limit), the relatively elevated Fe levels (Fig.S2d) and peaks in Fe or Mn (Fig.S2b) in averaged Bulk shell subset suggest diagenetic alteration (Frijia et al., 2015 and references therein) of at least part of the drilled area.

Furthermore, comparing the Δ47 and $\delta^{18}O$ results of the Bulk shell subset with the average of all other (well-preserved) subsets (drilling areas), it is apparent that the Bulk shell subset plots away from the rest of the subsets (Fig.S2d,e). Additionally, as in case of the previously discussed *H. incisa*, the SD of the Bulk shell subset is higher than the SD of the Growth profile-detailed sampling subset. This suggests that the Bulk shell drilling area in *P. ciryi* is, at least partially, recrystallized. Therefore, it has been excluded from further interpretations.

Bibliography

Anderson, N.T., Kelson, J.R., Kele, S., Daëron, M., Bonifacie, M., Horita, J., Mackey, T.J., John, C.M., Kluge, T., Petschnig, P., Jost, A.B., Huntington, K.W., Bernasconi, S.M., Bergmann, K.D., 2021. A Unified Clumped Isotope Thermometer Calibration (0.5–1,100°C) Using Carbonate-Based Standardization. Geophysical Research Letters 48. https://doi.org/10.1029/2020GL092069

Brock, T.D., 1985. Life at High Temperatures 230.

Frijia, G., Parente, M., Di Lucia, M., Mutti, M., 2015. Carbon and strontium isotope stratigraphy of the Upper Cretaceous (Cenomanian-Campanian) shallow-water carbonates of southern Italy: Chronostratigraphic calibration of larger foraminifera biostratigraphy. Cretaceous Research 53, 110–139. https://doi.org/10.1016/j.cretres.2014.11.002

O'Brien, C.L., Robinson, S.A., Pancost, R.D., Sinninghe Damsté, J.S., Schouten, S., Lunt, D.J., Alsenz, H., Bornemann, A., Bottini, C., Brassell, S.C., Farnsworth, A., Forster, A., Huber, B.T., Inglis, G.N., Jenkyns, H.C., Linnert, C., Littler, K., Markwick, P., McAnena, A., Mutterlose, J., Naafs, B.D.A., Püttmann, W., Sluijs, A., van Helmond, N.A.G.M., Vellekoop, J., Wagner, T., Wrobel, N.E., 2017. Cretaceous sea-surface temperature evolution: Constraints from TEX86 and planktonic foraminiferal oxygen isotopes. Earth-Science Reviews 172, 224–247. https://doi.org/10.1016/j.earscirev.2017.07.012

Appendix 2
Stable isotope analysis (Devetachi section)

Matrix analyses

Meters from the base	$\delta^{13}C$ (VPDB)	$\delta^{18}O$ (VPDB)
0.3	**2.58**	**-2.87**
1.3	**2.39**	**-3.33**
1.5	**2.65**	**-2.56**
1.9	**2.60**	**-2.99**
2.5	**0.70**	**-2.51**
3.35	**2.53**	**-2.94**
3.85	**2.31**	**-3.62**
4.4	**2.42**	**-4.49**
5.1	**1.43**	**-3.11**
5.4	**2.89**	**-1.36**
5.4	**1.78**	**-3.07**
5.75	**2.65**	**-2.30**
6	**2.35**	**-2.82**
6.5	**2.81**	**-4.58**
6.8	**2.84**	**-3.05**
6.85	**1.80**	**-3.10**
7	**3.29**	**-1.69**
	1.57	**-3.44**
	2.21	**-4.19**
	2.41	**-4.43**
	2.35	**-4.31**
	2.20	**-3.17**
	2.97	**-3.50**
	2.58	**-3.71**
	2.70	**-3.36**
	3.21	**-2.48**
	2.99	**-3.40**
	2.97	**-4.00**
	3.21	**-3.62**
	3.24	**-3.16**
	3.73	**-2.60**
	3.86	**-3.42**
	4.60	**-3.58**
	4.38	**-3.52**
	4.37	**-3.55**
	4.42	**-3.47**
	4.69	**-3.09**
	4.27	**-3.51**
	4.24	**-3.87**
	4.30	**-3.95**
	4.32	**-4.27**
	4.46	**-3.75**
	4.67	**-3.58**
	4.58	**-3.50**
18	**5.14**	**-3.10**

Meters from the base	$\delta^{13}C$ (VPDB)	$\delta^{18}O$ (VPDB)
18.3	**4.19**	**-2.77**
19.8	**4.52**	**-3.22**
20.5	**4.02**	**-3.48**
21.7	**4.37**	**-2.85**
21.75	**4.42**	**-3.58**
22	**4.17**	**-3.49**
22.6	**3.94**	**-3.54**
22.8	**4.01**	**-3.52**
23.6	**3.93**	**-3.36**
23.85	**4.36**	**-2.95**
24.6	**4.68**	**-2.97**
25.3	**4.69**	**-2.53**
25.5	**4.08**	**-2.99**
25.8	**4.25**	**-2.66**
26.3	**4.40**	**-2.51**
26.9	**4.06**	**-2.77**
27.6	**4.09**	**-2.65**
28.3	**3.74**	**-2.79**
28.45	**3.79**	**-2.71**
29.1	**3.96**	**-2.52**
29.7	**4.36**	**-2.62**
30.2	**4.32**	**-2.70**
30.8	**4.34**	**-2.58**
30.8	**4.37**	**-2.78**
31.4	**4.06**	**-2.70**
32	**4.16**	**-2.52**
	3.83	**-2.79**
	4.10	**-2.61**
	4.18	**-2.77**
	4.52	**-2.74**
	4.21	**-2.97**
	4.28	**-2.91**
	4.10	**-2.62**
	4.36	**-3.15**
	3.94	**-3.92**
	4.19	**-3.86**
	4.20	**-4.33**
	4.20	**-3.51**
	4.50	**-4.76**
	3.93	**-4.00**
	4.80	**-4.51**
	2.29	**-4.49**
	3.35	**-4.08**
	3.95	**-4.49**
46	**3.50**	**-4.48**

Meters from the base	$\delta^{13}C$ (VPDB)	$\delta^{18}O$ (VPDB)
46.9	**3.09**	**-4.39**
47	**2.87**	**-4.56**
47.6	**3.08**	**-4.33**
48.8	**2.91**	**-4.63**
49.6	**2.88**	**-4.54**
49.9	**3.28**	**-3.54**
50.6	**2.77**	**-4.84**
50.8	**3.21**	**-4.56**
51.3	**3.00**	**-4.46**
52.8	**3.18**	**-4.88**
53.4	**2.57**	**-4.12**
53.7	**2.50**	**-3.95**
54.3	**2.66**	**-4.42**
54.7	**3.20**	**-4.27**
55.2	**3.36**	**-4.30**
55.8	**3.20**	**-4.44**
56.3	**3.97**	**-5.02**
57.5	**3.83**	**-4.48**
57.5	**3.45**	**-4.41**
58.1	**3.84**	**-5.75**
59.3	**3.04**	**-4.87**
59.9	**3.26**	**-6.09**
60.6	**3.34**	**-6.11**
61.1	**2.60**	**-4.13**
61.3	**2.49**	**-5.11**
62	**2.91**	**-4.85**
62.5	**2.81**	**-5.60**
63.1	**2.79**	**-5.17**
63.7	**2.38**	**-5.31**
63.8	**2.46**	**-5.28**
64.5	**2.89**	**-5.45**
64.9	**2.40**	**-4.53**
65.3	**2.13**	**-5.09**
65.4	**2.29**	**-5.93**
65.8	**2.40**	**-4.69**
66.3	**1.98**	**-4.01**
67.1	**1.78**	**-4.78**
67.5	**1.67**	**-5.63**
68	**1.03**	**-5.76**
68.5	**1.21**	**-5.40**
69.1	**1.36**	**-5.61**
69.5	**2.17**	**-5.23**
69.9	**2.22**	**-4.69**
70.6	**1.94**	**-4.95**
71.8	**2.09**	**-4.72**

Meters from the base	$\delta^{13}C$ (VPDB)	$\delta^{18}O$ (VPDB)
72.2	**2.19**	**-5.03**
73	**1.64**	**-4.40**
73.6	**1.39**	**-4.62**
74.1	**1.41**	**-4.75**
74.6	**2.14**	**-4.05**
74.8	**1.19**	**-4.58**
74.9	**1.55**	**-4.24**
75.4	**0.57**	**-4.72**
76.4	**1.32**	**-5.80**
77.4	**1.64**	**-5.30**
78.4	**1.36**	**-4.53**
78.5	**1.81**	**-4.36**
79.2	**1.52**	**-4.58**
79.5	**1.46**	**-4.46**
79.8	**1.01**	**-5.28**
80	**1.04**	**-5.28**
80.4	**2.00**	**-4.23**
80.7	**1.10**	**-4.70**
81.2	**1.69**	**-4.88**
81.3	**2.24**	**-4.78**
81.8	**1.35**	**-5.04**
81.85	**1.29**	**-4.40**
82.7	**0.89**	**-5.29**
82.75	**1.57**	**-4.74**
83.3	**1.69**	**-4.54**
83.35	**1.17**	**-3.92**
83.4	**1.35**	**-4.22**
84.4	**2.09**	**-4.47**
84.9	**1.15**	**-3.36**
85.5	**1.35**	**-4.96**
86	**2.20**	**-5.14**
86.1	**2.18**	**-3.15**
86.9	**1.59**	**-4.66**
87.9	**1.14**	**-3.46**
88.3	**2.33**	**-4.18**
89.1	**2.51**	**-4.81**
89.6	**2.41**	**-3.07**
89.7	**0.62**	**-4.72**
90.3	**3.13**	**-2.99**
90.8	**2.68**	**-3.40**
91.1	**2.63**	**-3.21**
91.5	**3.64**	**-3.32**
92.2	**3.85**	**-3.44**
92.7	**4.06**	**-3.22**
92.9	**3.18**	**-3.44**
93.4	**4.02**	**-3.58**
93.4	**4.34**	**-3.33**

Meters from the base	$\delta^{13}C$ (VPDB)	$\delta^{18}O$ (VPDB)
94.1	**4.06**	**-3.57**
95 95	**3.72**	**-4.00**
95.3	**3.64**	**-4.15**
96.1	**3.55**	**-3.38**
96.4	**2.36**	**-3.18**
97.1	**2.92**	**-3.83**
97.3	**2.42**	**-2.97**
97.6	**1.89**	**-3.86**
98.6	**2.36**	**-3.62**
99.4	**2.90**	**-3.49**
99.45	**1.67**	**-2.39**
99.45	**2.00**	**-2.88**
99.7	**2.10**	**-3.15**
99.9	**1.98**	**-1.62**
100.1	**1.78**	**-4.74**
100.2	**1.64**	**-3.38**
100.3	**1.75**	**-2.08**
100.4	**1.35**	**-3.83**
100.4	**1.27**	**-5.85**
100.7	**0.67**	**-5.71**
101.1	**2.01**	**-5.01**
101.4	**2.03**	**-4.07**
102	**0.61**	**-4.39**
102.3	**2.54**	**-4.62**
102.8	**1.93**	**-1.53**
102.8	**1.28**	**-2.42**
103.2	**6.55**	**-6.35**
103.2	**1.48**	**-1.84**
103.8	**0.15**	**-1.54**
103.9	**2.22**	**-4.62**
104	**3.00**	**-3.55**
104.4	**2.71**	**-4.19**
105.1	**0.86**	**-4.96**
105.4	**2.38**	**-4.66**
106.9	**3.23**	**-3.73**
107.5	**3.33**	**-4.05**
107.9	**2.61**	**-4.52**
108.4	**3.28**	**-4.97**
108.8	**3.02**	**-3.39**
109.9	**2.17**	**-4.08**
110.5	**3.14**	**-3.64**
110.6	**2.74**	**-4.19**
110.9	**3.00**	**-4.02**
111.2	**2.45**	**-4.29**
111.2	**1.27**	**-3.29**
111.2	**1.42**	**-3.27**
	0.66	**-3.75**

Meters from the base	$\delta^{13}C$ (VPDB)	$\delta^{18}O$ (VPDB)
112.2	**-3.37**	**-5.28**
112.2	**2.46**	**-4.17**
113.1	**2.69**	**-5.29**
113.8	**2.74**	**-4.18**
115.1	**2.93**	**-4.75**
115.9	**2.19**	**-4.14**
116.5	**2.18**	**-3.32**
117.5	**2.39**	**-3.60**
118.8	**2.46**	**-4.26**
119	**1.63**	**-4.60**
119.8	**1.63**	**-4.04**
121	**2.07**	**-4.56**
121.9	**2.51**	**-4.06**
122.4	**1.97**	**-5.15**
123	**2.22**	**-4.39**
123.2	**2.01**	**-5.73**
124.6	**1.39**	**-3.36**
124.6	**1.77**	**-3.57**
125.8	**2.24**	**-5.18**
127.7	**1.56**	**-4.19**
127.9	**2.16**	**-4.28**
128.9	**2.17**	**-3.96**
129.9	**1.88**	**-3.78**
130.4	**1.47**	**-2.83**
131.4	**1.80**	**-2.58**
132.4	**2.07**	**-1.99**
133.4	**1.83**	**-3.34**
134.4	**1.20**	**-2.54**
134.4	**0.82**	**-2.68**
134.6	**2.03**	**-2.72**
134.6	**1.79**	**-2.84**
136	**1.95**	**-2.73**
136.2	**1.79**	**-2.87**
137.4	**1.94**	**-3.49**
139.1	**1.76**	**-2.98**
139.8	**1.72**	**-3.26**
141	**1.78**	**-3.06**
141	**1.66**	**-3.34**
141.3	**1.66**	**-3.60**
142.4	**1.62**	**-2.90**
142.8	**1.66**	**-3.06**
142.8	**1.59**	**-3.06**
144	**1.65**	**-2.89**
144.4	**1.45**	**-2.84**

Shell analyses

Meters from the base	$\delta^{13}C$ (VPDB)	$\delta^{18}O$ (VPDB)
0.3	**2.57**	**-2.15**
0.3	**2.59**	**-2.27**
6.8	**2.44**	**-3.42**
6.8	**2.87**	**-2.51**
9.2	**2.47**	**-2.64**
10.5	**2.64**	**-1.69**
11	**2.84**	**-1.85**
14.8	**4.96**	**-3.47**
15.6	**5.02**	**-2.52**
15.6	**5.02**	**-2.68**
15.6	**5.01**	**-1.96**
15.6	**5.38**	**-2.21**
16.2	**5.28**	**-2.64**
19.8	**4.92**	**-2.04**
21.75	**5.55**	**-3.17**
21.75	**5.89**	**-3.18**
21.75	**6.07**	**-3.44**
22	**5.63**	**-3.38**
22.6	**4.84**	**-3.50**
25.3	**6.55**	**-3.83**
25.3	**6.26**	**-3.37**
25.5	**4.80**	**-3.96**
25.5	**4.88**	**-2.93**
25.8	**5.75**	**-3.30**
26.3	**5.26**	**-3.57**
27.6	**4.44**	**-4.45**
28.3	**6.16**	**-4.02**
28.45	**5.98**	**-3.81**
29.7	**5.00**	**-3.77**
30.2	**5.07**	**-3.71**
30.2	**5.37**	**-3.42**
30.8	**5.83**	**-4.02**
31.4	**4.89**	**-3.35**
31.4	**4.98**	**-3.89**
33	**3.50**	**-4.06**
33.4	**6.05**	**-3.12**
33.4	**4.86**	**-3.49**
35.4	**4.75**	**-4.52**
35.4	**4.46**	**-3.71**
35.8	**5.92**	**-3.62**
35.8	**5.03**	**-2.24**
36.4	**4.25**	**-2.92**
36.6	**5.15**	**-3.70**
36.6	**4.94**	**-3.43**
37.5	**7.53**	**-2.16**
38.2	**5.56**	**-3.90**
38.2	**4.19**	**-4.58**
39	**4.33**	**-3.72**
45.7	**4.60**	**-4.22**
45.7	**3.80**	**-4.33**
46.9	**4.14**	**-4.08**
46.9	**3.83**	**-4.72**
47.6	**3.53**	**-4.31**
47.6	**3.43**	**-3.50**
47.6	**4.04**	**-4.27**
49.6	**4.16**	**-4.14**
49.6	**4.39**	**-4.90**
50.8	**3.89**	**-4.27**
52.8	**4.59**	**-3.98**
53.4	**4.10**	**-4.22**
53.4	**3.50**	**-4.46**
56.3	**3.00**	**-4.71**
56.3	**3.05**	**-4.49**
57.5	**3.37**	**-4.32**
57.5	**2.95**	**-4.52**
59.9	**2.52**	**-5.59**
60.6	**3.81**	**-3.29**
67.5	**2.46**	**-4.89**
67.5	**2.64**	**-4.68**
69.1	**2.76**	**-4.91**
69.1	**2.15**	**-4.80**
74.9	**3.05**	**-3.58**
84.9	**1.81**	**-3.08**
84.9	**2.13**	**-3.18**
84.9	**2.44**	**-3.26**
85.5	**1.85**	**-2.46**
88.3	**2.32**	**-2.88**
89.3	**3.70**	**-1.88**
89.6	**2.76**	**-2.82**
93.3	**2.99**	**-3.18**
93.3	**3.33**	**-3.49**
93.3	**3.08**	**-3.13**
103.9	**2.91**	**-3.32**
104.4	**3.98**	**-3.53**
104.4	**4.22**	**-3.20**
104.4	**4.30**	**-3.56**
105.1	**3.23**	**-3.64**
105.1	**2.89**	**-3.36**
107.9	**2.71**	**-3.11**
117.5	**2.65**	**-3.27**
117.5	**2.42**	**-3.38**
119	**2.45**	**-3.15**
119	**2.28**	**-3.15**
119	**2.84**	**-3.13**
121	**2.75**	**-3.14**
121	**3.02**	**-3.10**
121	**3.35**	**-3.12**
127.9	**2.41**	**-2.99**
127.9	**2.99**	**-3.71**
127.9	**2.52**	**-3.85**
127.9	**2.27**	**-3.34**
129.9	**2.31**	**-3.95**
129.9	**1.73**	**-3.58**
133.4	**2.27**	**-2.66**
133.4	**2.06**	**-2.76**
134.6	**2.23**	**-3.76**
134.6	**2.39**	**-3.63**
134.6	**2.50**	**-3.39**
134.6	**1.86**	**-2.72**
136.2	**2.72**	**-2.48**
136.2	**3.95**	**-2.13**
136.9	**2.85**	**-3.08**
137.4	**2.39**	**-3.62**
139.1	**2.28**	**-2.93**
139.1	**1.93**	**-3.33**
139.1	**2.16**	**-2.99**
139.8	**1.74**	**-3.29**
139.8	**2.29**	**-3.25**
139.8	**2.24**	**-3.14**
141	**2.01**	**-3.28**
141	**1.74**	**-3.24**
141	**1.92**	**-3.46**
141.3	**2.02**	**-3.61**
142.4	**2.52**	**-3.28**
142.4	**1.64**	**-3.65**
142.4	**1.39**	**-3.90**
142.8	**1.79**	**-3.63**
142.8	**1.57**	**-4.01**
142.8	**1.86**	**-3.83**
144	**1.28**	**-3.61**
144	**2.84**	**-3.46**
144.4	**2.57**	**-2.81**
144.4	**2.45**	**-3.23**

Appendix 3
Clumped and stable isotope analyses of rudist specimens

Hippurites incisa

Shell test n=9

Label	Run	Sa m44	49 parameter	Δ47 SD	Final Δ47	Δ47-based paleotemperature	Final δ18O	Final δ13C
Shell test n=9								
TMH-A	169	20371.61	0.000478	0.098205	0.522	52.8	-3.65	1.44
TMH-A	169	17323.65	0.000603	0.112532	0.532	48.5	-3.71	1.44
TMH-A	169	19222.06	0.001389	0.108341	0.638	11.0	-3.79	1.41
TMH-A	173	15510.254	0.000569	0.1133573	0.592	25.6	-3.72	1.38
TMH-A	173	16919.193	0.000457	0.118885	0.609	19.9	-3.74	1.38
TMH-A	173	16597.323	0.001255	0.1206521	0.665	3.6	-3.76	1.36
TMH-A	173	18732.037	0.001408	0.1182925	0.634	12.1	-3.81	1.39
TMH-A	174	16427.719	0.000608	0.1262284	0.556	38.6	-3.75	1.39
TMH-A	174	18826.351	0.000874	0.0828725	0.555	39.2	-3.74	1.39
Growth profile (low-resolution sampling) n=24								
TMH-TAB	178	18300.515	0.001273	0.0833868	0.495	65.3	-4.80	1.31
TMH-TB	178	17276.7	0.000929	0.1158428	0.502	62.0	-3.63	1.17
TMH-2.TB	184	16152.599	0.000423	0.1159407	0.617	17.3	-3.68	1.09
TMH-2.TB	184	11930.904	0.000260	0.1372918	0.679	-0.1	-3.78	0.95
TMH-2.TB	184	11429.271	0.000386	0.1383679	0.516	55.5	-3.66	1.12
TMH-TC	178	15565.628	0.001008	0.115634	0.578	30.4	-3.58	1.28
TMH-2.TC	184	13814.722	0.000765	0.129575	0.558	37.8	-3.27	1.24
TMH-2.TC	184	14118.181	0.000229	0.1376346	0.530	49.4	-3.23	1.23
TMH-2.TC	184	13890.694	0.000637	0.1219874	0.460	84.4	-3.54	1.15
TMH-TD	178	12613.393	0.000164	0.1139145	0.586	27.6	-4.06	1.43
TMH-TE	178	14041.947	0.000542	0.117205	0.515	55.9	-4.69	1.28
TMH-TE	178	16719.473	0.001077	0.0922484	0.549	41.5	-4.52	1.25
TMH-2.TE	184	16937.784	0.000594	0.1189057	0.632	12.8	-4.48	1.32
TMH-2.TE	184	15528.073	0.000809	0.1184206	0.547	42.1	-4.53	1.31
TMH-2.TE	184	17317.859	0.000318	0.0995886	0.605	21.2	-4.54	1.31
TMH-2.TE	184	17311.213	0.000567	0.1023797	0.622	15.8	-4.31	1.37
TMH-TF	178	11157.474	0.000278	0.1298736	0.639	10.7	-3.30	1.28
TMH-TF	178	15300.988	0.000229	0.119272	0.507	59.4	-3.31	1.29
TMH-TG	178	12545.592	-0.000106	0.113523	0.616	17.7	-4.21	1.53
TMH-2.TG	184	21158.496	0.000834	0.1096225	0.596	24.3	-3.88	1.52
TMH-2.TG	184	16875.193	0.000220	0.0996119	0.584	28.4	-3.97	1.48
TMH-2.TG	184	16807.332	0.000336	0.1113336	0.591	25.9	-3.87	1.49
TMH-2.TG	184	21635.544	0.001325	0.082409	0.672	1.7	-3.83	1.54
TMH-2.TG	190	15354.344	0.001212	0.1176057	0.492	66.9	-3.92	1.53
Growth profile (detailed sampling) n=22/44								
TMH-P-15	649	17023.446	-0.015527	0.0921333	0.753	-17.7	-4.41	1.15
TMH-P-16	649	18773.901	-0.052489	0.1144115	0.553	40.0	-4.52	1.12
TMH-P-16	649	17384.578	-0.035726	0.1264542	0.427	105.3	-4.63	1.16
TMH-P-18	652	20103.393	0.005343	0.0818664	0.643	9.7	-4.45	1.33
TMH-P-20	652	21397.76	-0.036044	0.0834848	0.581	29.3	-4.55	1.01
TMH-P-21	652	21730.632	-0.014557	0.0880922	0.694	-4.1	-4.61	1.38
TMH-P-23	652	24457.529	-0.051493	0.0895584	0.593	25.2	-4.59	1.32
TMH-P-24	652	21080.518	-0.052261	0.0956833	0.542	44.4	-4.42	1.41
TMH-P-25	649	20085.143	-0.055723	0.087641	0.502	62.0	-4.42	1.27

Label	Run	Sa m44	49 parameter	Δ47 SD	Final Δ47	Δ47-based paleotemperature	Final δ18O	Final δ13C
TMH-P-25	649	19184.191	-0.037370	0.0927816	0.587	27.4	-4.48	1.27
TMH-P-26	649	18200	-0.039882	0.1015585	0.481	72.7	-3.80	1.33
TMH-P-26	649	16861.864	-0.049724	0.1185599	0.518	54.6	-3.85	1.32
TMH-P-26	651	21032.262	-0.006665	0.1081627	0.602	22.4	-3.82	1.34
TMH-P-30-31	288	19766.824	0.000575	0.0906168	0.627	14.2	-2.76	1.39
TMH-P-34	649	18707.495	-0.023475	0.1109756	0.379	144.0	-3.24	1.24
TMH-P-34	651	17752.415	0.050390	0.1177525	0.646	8.8	-3.14	1.27
TMH-P-34	651	17037.119	-0.156365	0.1122956	0.347	177.4	-3.38	1.15
TMH-P-35	651	16480.715	0.045901	0.1265087	0.538	45.8	-3.12	1.22
TMH-P-35	651	22404.699	-0.023458	0.0862342	0.568	34.2	-3.27	1.16
TMH-P-36	651	15057.331	-0.031029	0.1061653	0.527	50.7	-3.47	1.12
TMH-P-37	651	15658.688	-0.006187	0.1169783	0.553	39.9	-3.33	1.27
TMH-P-38	651	18313.266	-0.028852	0.098195	0.494	66.1	-3.64	1.39
TMH-P-10-11	-	-	----------	-	-	-	-3.35	1.29
TMH-P-12	-	-	-------	-	-	-	-3.80	0.94
TMH-P-13	-	-	-	-	-	-	-3.77	1.11
TMH-P-14	-	-		-	-	-	-3.81	1.01
TMH-P-17	-	-		-	-	-	-4.39	1.25
TMH-P-18	-	-		-	-	-	-4.56	1.21
TMH-P-19	-	-		-	-	-	-4.40	1.21
TMH-P-20	-	-		-	-	-	-4.30	1.17
TMH-P-21	-	-		-	-	-	-4.42	1.17
TMH-P-22	-	-		-	-	-	-4.16	1.26
TMH-P-23	-	-		-	-	-	-4.25	1.14
TMH-P-24	-	-		-	-	-	-4.36	1.26
TMH-P-27	-	-		-	-	-	-3.85	1.20
TMH-P-28	-	-		-	-	-	-3.27	1.24
TMH-P-29	-	-		-	-	-	-2.49	1.26
TMH-P-30	-	-		-	-	-	-2.54	1.22
TMH-P-31	-	-		-	-	-	-2.72	1.34
TMH-P-32	-	-		-	-	-	-2.76	1.50
TMH-P-33	-	-		-	-	-	-3.04	1.19
TMH-P-36	-	-		-	-	-	-3.16	1.21
TMH-P-37	-	-		-	-	-	-3.24	1.13
TMH-P-38	-	-		-	-	-	-3.72	1.36
Bulk shell n=34								
TMH-BI	651	19395.686	-0.022129	0.1031949	0.601	22.7	-3.51	1.27
TMH-BI	651	21077.677	0.000860	0.0706914	0.595	24.5	-3.36	1.25
TMH-BI	651	17831.158	-0.022792	0.0776688	0.567	34.7	-3.47	1.30
TMH-BI	287	17489.731	0.000498	0.1354982	0.526	50.9	-3.45	1.19
TMH-BI	287	17898.064	0.002007	0.1281585	0.351	172.6	-3.54	1.31
TMH-BI	287	18905.475	0.001605	0.0856231	0.565	35.4	-3.36	1.26
TMH-BI	287	17495.684	0.001512	0.1107427	0.411	116.8	-3.65	1.30
TMH-BI	287	16984.434	0.000870	0.0887215	0.546	42.6	-3.66	1.20
TMH-BI	287	17255.98	0.001396	0.1078752	0.519	54.0	-3.43	1.34
TMH-BI	287	18808.682	0.000573	0.1019088	0.383	140.2	-3.52	1.32
TMH-BI	287	21323.602	0.001531	0.0988513	0.324	207.1	-3.64	1.29

Label	Run	Sa m44	49 parameter	Δ47 SD	Final Δ47	Δ47-based paleotemperature	Final δ18O	Final δ13C
TMH-BII	651	19944.772	-0.022598	0.0913093	0.508	59.4	-3.81	1.42
TMH-BII	651	20090.353	0.007205	0.0967178	0.636	11.6	-3.93	1.38
TMH-BII	651	21882.337	0.012986	0.0869276	0.607	20.5	-3.73	1.43
TMH-BII	651	21605.099	0.002951	0.089974	0.630	13.6	-4.30	1.24
TMH-BII	287	18204.033	0.001212	0.1375323	0.579	30.0	-3.88	1.37
TMH-BII	287	18605.851	0.001961	0.1069241	0.574	31.9	-3.90	1.37
TMH-BII	287	18235.263	0.001282	0.1499339	0.240	401.0	-3.85	1.41
TMH-BII	287	19864.721	0.001234	0.1250173	0.623	15.7	-3.80	1.38
TMH-BII	287	18933.001	0.001867	0.1317269	0.452	89.1	-3.88	1.35
TMH-BII	287	16465.133	0.000223	0.1253613	0.599	23.3	-3.57	1.46
TMH-BII	287	17299.237	0.002152	0.1049831	0.585	28.1	-3.77	1.42
TMH-BII	287	20486.587	0.000728	0.1132675	0.509	58.9	-3.88	1.32
TMH-BIII	651	18396.466	-0.038380	0.103045	0.518	54.7	-3.56	1.43
TMH-BIII	651	24614.232	-0.000166	0.1055189	0.709	-7.7	-3.52	1.45
TMH-BIII	651	19422.72	-0.029859	0.1083711	0.581	29.3	-3.62	1.45
TMH-BIII	287	17460.257	0.001176	0.1441877	0.223	481.2	-3.60	1.32
TMH-BIII	287	19252.031	0.000592	0.1116643	0.538	45.8	-3.52	1.38
TMH-BIII	287	18896.129	0.001174	0.1413635	0.413	115.4	-3.56	1.42
TMH-BIII	287	17967.311	0.001240	0.1260901	0.560	37.3	-3.55	1.44
TMH-BIII	287	18065.409	0.000859	0.1191873	0.598	23.6	-3.59	1.38
TMH-BIII	287	20962.099	0.001421	0.1041905	0.532	48.5	-3.63	1.38
TMH-BIII	287	20624.017	0.000986	0.104673	0.558	38.1	-3.65	1.39
TMH-BIII	287	17619.109	0.001017	0.1348915	0.737	-14.1	-3.11	1.76
Matrix and Sparite n=14								
TMH-M	188	17406.902	0.000254	0.1200113	0.638	11.1	-3.65	0.62
TMH-M	188	18795.602	0.001039	0.1084744	0.611	19.2	-3.73	0.61
TMH-M	188	17140.907	0.000439	0.108237	0.588	27.0	-3.87	0.63
TMH-M	188	14305.382	0.000570	0.1476957	0.596	24.4	-3.87	0.64
TMH-M	189	17874.644	0.001167	0.122963	0.457	86.1	-3.74	0.67
TMH-M	189	16075.492	0.001562	0.1227634	0.454	88.1	-3.73	0.69
TMH-M	189	16209.82	0.000690	0.1244705	0.588	27.2	-3.62	0.72
TMH-S	188	18330.4	0.000676	0.1010533	0.664	3.7	-5.12	-2.13
TMH-S	188	19282.247	0.001012	0.0997012	0.635	11.9	-5.05	-2.72
TMH-S	188	20505.912	0.001531	0.1217929	0.626	14.6	-4.98	-2.34
TMH-S	188	23038.65	0.000949	0.1014736	0.680	-0.5	-5.05	-2.33
TMH-S	189	16265.374	0.001548	0.0865727	0.615	18.1	-5.04	-1.44
TMH-S	189	20206.227	0.000981	0.0850567	0.584	28.6	-5.00	-2.50
TMH-S	189	20881.85	0.001260	0.1022965	0.607	20.6	-5.06	-1.99

Praeradiolites ciryi

Label	Run	Sa m44	49 parameter	Δ47 SD	Final Δ47	Δ47-based paleotemperature	Final δ18O	Final δ13C
Shell test n=11								
TMP-P-AA	169	17100.61	-0.000193	0.110883	0.629	13.8	-2.98	3.57
TMP-P-AA	169	16447.05	0.000725	0.099913	0.599	23.2	-3.05	3.56
TMP-P-AA	173	19912.405	0.0012374	0.0903272	0.644	9.2	-2.87	3.58
TMP-P-AA	173	20007.491	0.0014579	0.0815766	0.565	35.3	-2.85	3.63
TMP-P-AA	174	21622.925	0.00101	0.097283	0.532	48.4	-2.85	3.63
TMP-P-AB	169	17585.97	0.000129	0.098951	0.522	52.8	-4.45	1.70
TMP-P-AB	169	20091.64	0.001008	0.106162	0.577	30.9	-4.51	1.63
TMP-P-AB	173	20851.342	0.0009152	0.1227575	0.600	22.9	-4.51	1.46
TMP-P-AB	174	19840.488	0.000619	0.102327	0.552	40.2	-4.43	1.47
TMP-P-AB	174	15879.577	0.0002786	0.1222907	0.578	30.4	-4.48	1.40
TMP-P-AB	174	19539.84	0.000887	0.106437	0.536	46.9	-4.41	1.57
Growth profile (low-resolution sampling) n=48								
TMP--L1S	181	14856.917	-4.9E-05	0.1160822	0.511	57.9	-4.46	2.58
TMP--L1S	181	17500.834	0.0007373	0.0912355	0.614	18.5	-4.57	2.50
TMP--L1S	181	22483.32	0.0008919	0.0818546	0.626	14.6	-4.55	2.52
TMP--L1S	182	11825.719	0.0005211	0.117157	0.551	40.8	-4.75	2.44
TMP--L1S	182	12782.726	0.0001149	0.0937137	0.536	46.8	-4.50	2.52
TMP--L1S	182	20112.406	0.0012717	0.0972887	0.518	54.4	-4.52	2.49
TMP--L1W	181	19971.603	0.0008536	0.1218419	0.579	30.3	-3.47	1.84
TMP--L1W	181	19099.533	0.0010257	0.1087869	0.554	39.4	-3.76	1.53
TMP--L1W	181	14683.409	0.0006681	0.1197702	0.573	32.4	-3.72	1.73
TMP--L1W	182	20118.529	0.0009882	0.0980062	0.564	35.8	-3.86	1.55
TMP--L1W	182	18027.643	0.0009045	0.1159525	0.525	51.5	-3.74	1.69
TMP--L1W	182	18267.608	0.001275	0.0944124	0.577	30.8	-3.76	1.72
TMP--L2S	181	14814.654	0.0006242	0.1114014	0.417	112.7	-2.48	3.18
TMP--L2S	181	21482.404	0.0008132	0.0882343	0.524	51.8	-2.58	3.31
TMP--L2S	181	21082.614	0.0017114	0.0895009	0.575	31.7	-2.61	3.10
TMP--L2S	182	14417.504	0.0002085	0.1226904	0.512	57.3	-2.56	3.13
TMP--L2S	182	20674.963	0.0012862	0.1101204	0.493	66.5	-2.64	3.20
TMP--L2S	184	17836.326	0.0008094	0.09303	0.606	21.0	-2.60	3.06
TMP--L2W	181	16973.08	0.0010833	0.1139306	0.440	96.7	-3.30	2.75
TMP--L2W	181	17657.156	0.0008992	0.1177564	0.561	36.9	-3.51	2.22
TMP--L2W	181	17509.698	0.0008194	0.1014138	0.581	29.4	-3.31	2.87
TMP--L2W	182	16361.414	0.0006421	0.1206162	0.540	45.0	-3.42	2.60
TMP--L2W	182	17789.084	0.000883	0.1174863	0.612	19.1	-3.44	2.59
TMP--L2W	182	19620.079	0.0015116	0.0986329	0.533	48.2	-3.38	2.66
TMP--L3S	182	17522.798	0.0006258	0.1033601	0.612	19.0	-3.81	1.95
TMP--L3S	181	21931.183	0.0005374	0.0880769	0.572	32.7	-3.47	2.77
TMP--L3S	181	18342.215	0.000837	0.10616	0.601	22.5	-3.49	2.78
TMP--L3S	181	17645.3	0.0015033	0.1199109	0.595	24.7	-3.51	2.72
TMP--L3S	182	19013.08	0.0006652	0.1048071	0.527	50.6	-3.39	2.88
TMP--L3S	182	16899.266	0.0008818	0.1191782	0.527	50.7	-3.43	2.84
TMP--L3S	182	17045.78	0.0006631	0.1099308	0.552	40.5	-3.46	2.84
TMP--L3W	181	17627.783	0.0011557	0.1275144	0.398	127.1	-3.76	2.05
TMP--L3W	181	18648.034	0.0007573	0.0939118	0.571	33.2	-3.77	1.97

Label	Run	Sa m44	49 parameter	Δ47 SD	Final Δ47	Δ47-based paleotemperature	Final δ18O	Final δ13C
TMP--L3W	181	19897.026	0.0006531	0.098953	0.551	40.9	-3.84	2.00
TMP--L3W	182	19774.022	0.0012972	0.1221801	0.523	52.2	-3.83	1.92
TMP--L3W	182	17595.197	0.0008825	0.1153072	0.519	54.1	-3.89	1.86
TMP--L4S	181	20059.231	0.0011562	0.1078731	0.526	51.2	-4.15	2.98
TMP--L4S	181	17172.94	0.0009474	0.085057	0.552	40.2	-4.27	2.91
TMP--L4S	181	18397.779	0.0010504	0.0812313	0.585	28.0	-4.05	2.98
TMP--L4S	182	15335.842	0.0006679	0.1095549	0.472	77.4	-4.21	2.69
TMP--L4S	182	14892.233	0.0002703	0.0935859	0.622	15.9	-4.26	2.85
TMP--L4S	182	18924.78	0.0007488	0.1094341	0.585	28.1	-4.22	2.93
TMP--L4W	181	17984.146	0.0006672	0.1167641	0.561	36.7	-4.42	2.58
TMP--L4W	181	18595.24	0.0007005	0.0958164	0.588	27.1	-4.53	2.49
TMP--L4W	181	15760.529	0.0012814	0.1236467	0.627	14.3	-4.40	2.55
TMP--L4W	182	15933.013	0.0007681	0.0953584	0.533	48.1	-4.61	2.66
TMP--L4W	182	18203.892	0.0012184	0.0982745	0.525	51.4	-4.49	2.55
TMP--L4W	182	15987.764	0.0007443	0.0950893	0.571	33.1	-4.82	2.50
Growth profile (detailed sampling) n=46/101								
TMP-P-16	288	18105.543	0.0011911	0.108	0.834	-33.4	-3.88	3.64
TMP-P-22	649	19912.046	-0.050667	0.0762895	0.554	39.6	-3.96	3.08
TMP-P-22	649	19775.058	-0.038313	0.0976751	0.612	19.0	-3.97	3.03
TMP-P-23	649	19173.852	-0.068627	0.1024274	0.487	69.6	-4.07	2.87
TMP-P-23	649	19695.602	-0.057769	0.1107615	0.565	35.1	-4.46	2.76
TMP-P-23	649	18467.661	-0.05451	0.0860463	0.522	52.7	-3.95	2.88
TMP-P-24	290	20032.136	0.0008766	0.1004523	0.666	3.2	-4.32	2.82
TMP-P-26	290	18349.523	0.0010448	0.1016249	0.524	51.8	-3.96	3.09
TMP-P-26	290	17521.172	0.0009243	0.1176968	0.645	9.1	-4.05	3.02
TMP-P-30	290	18452.048	0.0012412	0.097762	0.583	28.8	-4.00	3.22
TMP-P-31	290	19136.997	0.0012527	0.1111426	0.677	0.2	-4.34	2.82
TMP-P-32	290	20066.93	0.001107	0.1391224	0.684	-1.5	-3.55	2.98
TMP-P-33	290	17245.319	0.0012531	0.0955357	0.729	-12.4	-3.31	2.98
TMP-P-33	290	17813.97	0.0013233	0.1103731	0.761	-19.3	-3.28	2.97
TMP-P-36	290	17364.9	0.0013461	0.1035247	0.634	12.3	-3.30	3.15
TMP-P-37	290	17515.119	0.0011586	0.0862842	0.598	23.4	-3.02	3.32
TMP-P-37	290	19867.181	0.001292	0.1136016	0.668	2.7	-3.24	3.25
TMP-P-38	290	16096.975	0.0010834	0.111757	0.567	34.4	-3.10	3.09
TMP-P-38	290	19440.266	0.0012801	0.0992996	0.740	-14.9	-3.27	3.02
TMP-P-39	290	16864.361	0.0016058	0.129051	0.760	-19.1	-2.90	3.37
TMP-P-40	649	20920.622	-0.041145	0.0793335	0.490	68.0	-2.90	3.24
TMP-P-40	649	19298.171	-0.050191	0.1044782	0.537	46.4	-2.84	3.28
TMP-P-40	649	19238.27	-0.0355	0.0780354	0.451	89.8	-2.81	3.30
TMP-P-41	649	23201.389	-0.029333	0.0741191	0.614	18.3	-2.49	3.52
TMP-P-41	651	21552.064	-0.020345	0.0979178	0.567	34.6	-2.83	3.38
TMP-P-42	290	15650.465	0.0004521	0.1065823	0.678	0.0	-2.98	3.53
TMP-P-42	290	18373.205	0.0010912	0.0973749	0.630	13.4	-3.07	3.45
TMP-P-43	290	19260.343	0.0006868	0.0941142	0.694	-4.1	-2.88	3.08
TMP-P-46	290	19761.975	0.0014292	0.0977691	0.710	-7.9	-3.03	2.96
TMP-P-47	290	17237.87	0.0010084	0.1035007	0.736	-13.9	-3.56	3.20
TMP-P-48	290	18726.586	0.0013977	0.105	0.271	304.8	-3.37	3.10

Label	Run	Sa m44	49 parameter	Δ47 SD	Final Δ47	Δ47-based paleotemperature	Final δ18O	Final δ13C
TMP-P-49	290	18134.184	0.0007721	0.105108	0.640	10.5	-3.23	3.10
TMP-P-50	290	20445.278	0.0012013	0.1004482	0.570	33.4	-3.49	2.90
TMP-P-52	290	20919.907	0.0009095	0.101	0.932	-49.0	-3.87	1.98
TMP-P-54	290	19917.806	0.0011247	0.1106168	0.685	-1.7	-4.22	2.38
TMP-P-55	290	18410.92	0.0012425	0.0884045	0.676	0.5	-4.18	3.04
TMP-P-57	290	19797.342	0.0006124	0.0969153	0.604	21.7	-3.90	2.99
TMP-P-60	652	20664.746	-0.051007	0.1236492	0.488	69.1	-4.32	2.00
TMP-P-60	652	20183.12	-0.034938	0.1111169	0.544	43.3	-4.29	2.43
TMP-P-60	652	18030.848	-0.051691	0.1247977	0.476	75.2	-4.30	2.49
TMP-P-60	652	22372.656	-0.044559	0.0886616	0.616	17.7	-4.33	2.28
TMP-P-60	652	20608.82	-0.030156	0.0956407	0.573	32.2	-4.38	2.04
TMP-P-61	652	22736.919	-0.0027	0.103496	0.533	48.1	-4.41	2.39
TMP-P-61	652	17251.756	-0.075815	0.126201	0.434	100.9	-4.55	2.25
TMP-P-61	652	19252.344	-0.050012	0.1043844	0.485	70.3	-4.62	2.15
TMP-P-62	290	18423.047	0.0010353	0.0949489	0.672	1.5	-4.06	3.11
TMP-P-2	-	-	-	-	-	-	-2.95	2.02
TMP-P-3	-	-	-	-	-	-	-2.70	2.79
TMP-P-4	-	-	-	-	-	-	-2.95	2.83
TMP-P-6	-	-	-	-	-	-	-3.00	2.58
TMP-P-7	-	-	-	-	-	-	-2.86	2.64
TMP-P-8	-	-	-	-	-	-	-3.10	2.85
TMP-P-9	-	-	-	-	-	-	-2.45	3.42
TMP-P-10	-	-	-	-	-	-	-3.11	2.68
TMP-P-11	-	-	-	-	-	-	-2.60	3.45
TMP-P-12	-	-	-	-	-	-	-2.53	3.55
TMP-P-13	-	-	-	-	-	-	-3.05	3.66
TMP-P-14	-	-	-	-	-	-	-3.59	3.23
TMP-P-15	-	-	-	-	-	-	-3.55	3.11
TMP-P-16	-	-	-	-	-	-	-3.82	3.45
TMP-P-17	-	-	-	-	-	-	-2.66	3.40
TMP-P-18	-	-	-	-	-	-	-3.36	4.01
TMP-P-19	-	-	-	-	-	-	-3.41	3.70
TMP-P-20	-	-	-	-	-	-	-3.33	3.39
TMP-P-21	-	-	-	-	-	-	-4.44	2.97
TMP-P-24	-	-	-	-	-	-	-4.19	2.81
TMP-P-25	-	-	-	-	-	-	-3.95	2.83
TMP-P-26	-	-	-	-	-	-	-3.93	2.82
TMP-P-27	-	-	-	-	-	-	-4.09	3.17
TMP-P-28	-	-	-	-	-	-	-4.20	2.97
TMP-P-29	-	-	-	-	-	-	-4.12	3.13
TMP-P-30	-	-	-	-	-	-	-3.72	3.08
TMP-P-31	-	-	-	-	-	-	-4.13	2.77
TMP-P-32	-	-	-	-	-	-	-3.43	2.82
TMP-P-33	-	-	-	-	-	-	-3.16	2.90
TMP-P-34	-	-	-	-	-	-	-3.00	2.71
TMP-P-35	-	-	-	-	-	-	-3.07	2.81
TMP-P-36	-	-	-	-	-	-	-3.04	2.89

Label	Run	Sa m44	49 parameter	Δ47 SD	Final Δ47	Δ47-based paleotemperature	Final δ18O	Final δ13C
TMP-P-37	-	-	-	-	-	-	-2.88	3.04
TMP-P-38	-	-	-	-	-	-	-3.04	2.88
TMP-P-39	-	-	-	-	-	-	-2.87	3.09
TMP-P-42	-	-	-	-	-	-	-2.94	3.16
TMP-P-43	-	-	-	-	-	-	-2.86	2.96
TMP-P-44	-	-	-	-	-	-	-2.78	2.93
TMP-P-45	-	-	-	-	-	-	-2.93	3.23
TMP-P-46	-	-	-	-	-	-	-3.15	2.91
TMP-P-47	-	-	-	-	-	-	-3.56	2.99
TMP-P-48	-	-	-	-	-	-	-3.25	2.83
TMP-P-49	-	-	-	-	-	-	-3.03	2.75
TMP-P-50	-	-	-	-	-	-	-3.50	2.81
TMP-P-51	-	-	-	-	-	-	-3.55	2.57
TMP-P-52	-	-	-	-	-	-	-3.75	1.79
TMP-P-53	-	-	-	-	-	-	-3.72	2.71
TMP-P-54	-	-	-	-	-	-	-4.02	2.44
TMP-P-55	-	-	-	-	-	-	-4.07	2.83
TMP-P-56	-	-	-	-	-	-	-4.14	2.80
TMP-P-57	-	-	-	-	-	-	-3.99	2.56
TMP-P-58	-	-	-	-	-	-	-4.16	2.50
TMP-P-59	-	-	-	-	-	-	-4.05	2.82
TMP-P-62	-	-	-	-	-	-	-3.68	2.87
TMP-P-63	-	-	-	-	-	-	-3.96	3.18
Bulk shell n=19								
TMP-P-BI	288	19521.77	0.0014813	0.0889836	0.364	158.6	-4.26	2.79
TMP-P-BI	288	17988.211	0.0009424	0.1213808	0.644	9.5	-4.51	2.70
TMP-P-BI	288	18540.148	0.0028595	0.1157724	0.695	-4.3	-4.37	2.83
TMP-P-BI	288	19447.895	0.0015679	0.1175438	0.598	23.6	-4.37	2.81
TMP-P-BI	288	19368.58	0.0007009	0.0965941	0.684	-1.4	-4.31	2.90
TMP-P-BI	288	19268.002	0.0007525	0.0958471	0.439	97.5	-4.49	2.85
TMP-P-BI	288	19212.016	0.0010087	0.0966945	0.703	-6.3	-4.36	2.92
TMP--BII	288	19065.171	0.0011985	0.0884345	0.522	52.8	-4.21	3.04
TMP--BII	288	17137.243	0.0047825	0.1230978	0.551	40.5	-4.21	3.44
TMP--BII	288	19662.241	0.001197	0.119443	0.343	181.5	-4.25	3.04
TMP--BII	288	17946.892	0.0012834	0.1052666	0.356	166.9	-4.15	3.12
TMP--BII	288	21173.654	0.0011066	0.1121565	0.489	68.3	-4.25	3.14
TMP--BII	288	20197.985	0.0010323	0.0867674	0.629	13.7	-4.24	3.16
TMP--BII	288	17936.522	0.0010135	0.0959278	0.665	3.5	-4.14	3.23
TMP-B-BIII	288	20485.694	0.0010072	0.1095711	0.422	108.8	-3.46	3.17
TMP-B-BIII	288	17564.87	0.0016399	0.0998859	0.310	228.2	-3.32	3.25
TMP-B-BIII	288	20656.813	0.0009681	0.0970823	0.697	-4.7	-3.56	3.19
TMP-B-BIII	288	17903.194	0.0011732	0.114443	0.644	9.3	-3.21	3.40
TMP-B-BIII	288	20556.968	0.0015448	0.1036188	0.447	92.2	-3.50	3.29
Matrix and Sparite n=14								
TMP-MP-M	188	18413.008	0.0005207	0.1134391	0.474	76.6	-5.04	1.81
TMP-MP-M	188	16234.997	0.0003985	0.1184724	0.622	15.9	-5.08	1.74
TMP-MP-M	188	21167.681	0.001144	0.0947667	0.599	23.3	-4.60	1.84

Label	Run	Sa m44	49 parameter	Δ47 SD	Final Δ47	Δ47-based paleotemperature	Final δ18O	Final δ13C
TMP-MP-M	188	19717.785	0.0012014	0.083444	0.532	48.7	-4.41	1.85
TMP-MP-M	189	20019.387	0.0011354	0.1048687	0.693	-3.8	-5.02	1.75
TMP-MP-M	189	22229.673	0.0015714	0.1175203	0.541	44.7	-4.74	1.77
TMP-MP-M	189	18773.919	0.0012381	0.0841117	0.410	117.7	-4.91	1.82
TMP-MP-S	188	18534.235	0.0004235	0.1065065	0.613	18.7	-5.35	-0.44
TMP-MP-S	188	19461.668	0.000396	0.1042858	0.636	11.8	-5.32	-0.45
TMP-MP-S	188	19548.222	0.0007633	0.102541	0.579	30.1	-5.44	-0.32
TMP-MP-S	189	17140.104	0.0009142	0.1175129	0.649	7.9	-4.93	-0.04
TMP-MP-S	189	19172.896	0.0011595	0.1040776	0.619	16.9	-5.27	-0.28
TMP-MP-S	189	20944.481	0.0004965	0.1004199	0.565	35.4	-5.32	-0.43
TMP-MP-S	189	20766.757	0.0011873	0.0847455	0.582	29.3	-5.18	0.02

Miloranovicia herakii

Label	Run	Sa m44	49 parameter	Δ47 SD	Final Δ47	Δ47-based paleotemperature	Final δ18O	Final δ13C
Shell test n=15								
TMM-AA	169	17930.077	0.0009119	0.0898717	0.574	31.9	-4.63	2.64
TMM-AA	173	15859.5	0.0006019	0.1367661	0.408	118.9	-4.57	2.59
TMM-AA	173	21214.341	0.0008949	0.0894281	0.573	32.2	-4.62	2.57
TMM-AA	174	20729.252	0.0009677	0.0796239	0.591	25.9	-4.60	2.68
TMM-AA	178	16174.253	0.000355	0.0953205	0.577	30.7	-4.58	2.66
TMM-AA	178	14374.729	0.0006967	0.124426	0.593	25.3	-4.57	2.67
TMM-AA	178	14222.583	0.0005166	0.1044093	0.460	84.3	-4.58	2.82
TMM-AA	178	19779.182	0.0010478	0.1203538	0.592	25.5	-4.57	2.69
TMM-AA	178	16596.299	0.0005916	0.1041844	0.573	32.4	-4.62	2.63
TMM-AA	178	17791.443	0.0007235	0.092125	0.533	48.2	-4.49	2.61
TMM-AA	178	15497.586	0.0002406	0.112894	0.574	32.0	-4.50	2.65
TMM-AB	169	17658.11	0.0007548	0.110663	0.597	24.0	-4.45	2.57
TMM-AB	173	18374.64	0.000848	0.1156197	0.550	41.1	-4.39	2.57
TMM-AB	173	21331.171	0.0011989	0.1013872	0.557	38.2	-4.48	2.54
TMM-AB	174	20210.393	0.0008973	0.1290097	0.661	4.4	-4.41	2.55
Bulk shell n=15								
TMM-2.1	184	22069.516	0.0012354	0.0814504	0.633	12.7	-3.44	2.61
TMM-2.1	184	16545.101	0.0004517	0.1042324	0.529	49.8	-3.63	2.61
TMM-2.1	184	21016.208	0.0014125	0.098926	0.621	16.2	-3.78	2.51
TMM-2.1	187	16779.404	0.0002461	0.0974736	0.611	19.4	-3.56	2.51
TMM-2.2	184	20425.191	0.0010268	0.091225	0.638	11.2	-3.56	2.60
TMM-2.2	184	16622.269	0.0003861	0.1205133	0.664	3.8	-3.60	2.60
TMM-2.2	184	19309.783	0.0014393	0.0939386	0.430	103.3	-3.49	2.68
TMM-2.2	184	21214.331	0.0010459	0.1012333	0.684	-1.4	-3.61	2.64
TMM-2.2	190	21515.702	0.0019673	0.0986889	0.571	32.9	-3.50	2.73
TMM-2.3	184	21914.529	0.0010559	0.0939599	0.541	44.9	-4.01	2.51
TMM-2.3	184	17303.222	0.0008591	0.097103	0.594	25.1	-4.03	2.48
TMM-2.3	184	21310.21	0.0009074	0.093058	0.547	42.4	-3.90	2.46
TMM-2.3	184	20024.296	0.0019264	0.0824194	0.594	24.9	-3.81	2.65
TMM-2.3	187	16462.634	0.0007021	0.1275396	0.468	79.7	-3.97	2.60
Matrix n=13								
TMM-M	188	21373.705	0.0004527	0.1097129	0.587	27.2	-4.61	1.27
TMM-M	188	19182.422	0.0007034	0.1056989	0.608	20.4	-4.49	1.34
TMM-M	188	20079.368	0.0011158	0.0814185	0.625	15.0	-4.66	1.36
TMM-M	188	17557.351	0.0011743	0.0947112	0.561	36.8	-4.60	1.28
TMM-M	188	15700.718	0.0003086	0.1012824	0.678	-0.1	-4.57	1.14
TMM-M	188	20091.465	0.0006296	0.0894642	0.659	5.1	-4.69	1.06
TMM-M	189	18479.213	0.000892	0.0980157	0.637	11.5	-4.64	1.30
TMM-M	189	21316.575	0.000994	0.0760311	0.566	35.0	-4.55	1.35
TMM-M	189	20999.202	0.0009269	0.0711487	0.635	12.0	-4.63	1.33
TMM-M	189	15659.56	0.0008307	0.1201558	0.514	56.6	-4.53	1.27
TMM-M	189	18894.594	0.0018059	0.1032847	0.612	19.1	-4.70	1.30
TMM-M	189	21291.84	0.0015185	0.0793521	0.593	25.1	-4.54	1.37
TMM-M	189	20195.526	0.000609	0.0889865	0.570	33.3	-4.44	1.25

Biradiolites stoppanianus

Label	Run	Sa m44	49 parameter	Δ47 SD	Final Δ47	Δ47-based paleotemperature	Final δ18O	Final δ13C
Shell test n=12								
TMB-AA	169	21239.859	0.0005447	0.0977986	0.603	21.8	-4.33	0.45
TMB-AA	169	18778.627	0.0011768	0.1064206	0.488	68.9	-4.39	0.40
TMB-AA	173	19205.12	0.0007232	0.0927957	0.591	25.9	-4.30	0.45
TMB-AA	173	19066.827	0.0009715	0.1024182	0.649	7.8	-4.31	0.42
TMB-AA	173	21933.612	0.0016791	0.1085189	0.598	23.6	-4.30	0.43
TMB-AA	173	20896.737	0.0017579	0.0914739	0.603	22.1	-4.36	0.45
TMB-AA	173	21230.252	0.0018018	0.0857719	0.604	21.6	-4.38	0.39
TMB-AA	174	19077.277	0.0008575	0.0923375	0.572	32.6	-4.34	0.43
TMB-AA	174	18015.808	0.0009625	0.1009845	0.597	24.1	-4.33	0.46
TMB-AA	169	15381.398	0.0005709	0.1008247	0.575	31.7	-5.06	-1.12
TMB-AA	169	20940.436	0.000805	0.0678068	0.488	69.1	-5.00	-1.07
TMB-AA	174	16515.417	0.0005263	0.1123022	0.629	13.9	-5.09	-1.24
Matrix and Sparite n=13								
TMB-M	188	22783.155	0.0013145	0.0736907	0.548	41.7	-5.00	1.06
TMB-M	188	15044.128	0.0005315	0.1373798	0.601	22.6	-5.04	1.05
TMB-M	188	21614.192	0.0010919	0.1191017	0.513	56.8	-4.96	1.09
TMB-M	188	14790.883	8.593E-05	0.1184494	0.663	3.9	-5.11	1.00
TMB-M	188	20749.169	0.0005056	0.0996162	0.608	20.4	-5.08	1.02
TMB-M	188	21802.728	0.0010316	0.1030163	0.661	4.5	-5.11	1.07
TMB-M	189	20254.684	0.0010759	0.0996135	0.667	2.9	-5.09	1.00
TMB-M	189	14052.829	0.0011604	0.0971595	0.523	52.5	-5.17	1.04
TMB-M	189	17594.334	0.0008868	0.1211032	0.649	8.0	-5.05	1.12
TMB-M	189	20523.098	0.0016738	0.1124904	0.707	-7.2	-5.12	1.10
TMB-M	189	17938.159	0.0002281	0.0900723	0.651	7.3	-4.94	1.04
TMB-M	189	18273.29	0.0013394	0.0960935	0.528	50.3	-5.04	1.11
TMB-M	189	20058.367	0.0008173	0.0860394	0.517	54.9	-5.14	1.03
Bulk shell n=23								
TMB-L1S	187	16891.305	0.000186	0.0994655	0.612	18.9	-5.18	-2.20
TMB-L1S	187	16100.91	0.0009359	0.1450006	0.435	100.0	-5.18	-1.78
TMB-L1S	187	18774.822	0.0005264	0.0899582	0.577	30.9	-5.13	-2.00
TMB-L1W	187	18471.393	0.0010695	0.1335169	0.498	63.9	-5.13	-0.98
TMB-L1W	187	16486.054	0.0007881	0.1310544	0.587	27.2	-5.00	-0.93
TMB-L1W	187	15406.525	5.999E-05	0.1037329	0.596	24.2	-5.25	-1.06
TMB-L2S	187	19851.611	0.0008604	0.1325327	0.503	61.4	-5.17	-0.58
TMB-L2S	187	18468.602	0.000379	0.1130297	0.671	1.8	-5.22	-0.51
TMB-L2S	187	19853.578	0.0008181	0.1210107	0.450	90.4	-5.14	-0.41
TMB-L2W	187	22078.019	0.0009537	0.0985813	0.415	113.6	-5.15	-0.69
TMB-L2W	187	17639.849	0.0006883	0.1042576	0.530	49.5	-5.17	-0.94
TMB-L2W	187	15881.525	0.0002884	0.119069	0.495	65.4	-5.29	-0.32
TMB-L3S	187	17371.857	0.0009366	0.1066436	0.550	41.0	-5.21	-0.46
TMB-L3S	187	20632.74	0.0007224	0.1025902	0.491	67.6	-5.17	-0.22
TMB-L3S	187	18405.65	0.0005342	0.1161907	0.694	-4.0	-5.14	-0.30
TMB-L3W	187	16583.278	0.000515	0.123478	0.311	225.5	-5.20	-0.59
TMB-L3W	187	15515.655	0.0003189	0.1033335	0.541	44.7	-5.11	-0.73

Label	Run	Sa m44	49 parameter	Δ47 SD	Final Δ47	Δ47-based paleotemperature	Final δ18O	Final δ13C
TMB-L3W	187	18758.479	0.0008456	0.1058325	0.585	28.2	-5.17	-0.52
TMB-2.A	187	19278.673	0.0007709	0.1035913	0.496	64.8	-4.95	-0.35
TMB-2.A	187	12792.644	0.0005459	0.1271394	0.462	83.0	-4.80	-0.37
TMB-2.A	187	20285.051	0.000802	0.086536	0.500	63.0	-4.66	-0.06
TMB-2.A	187	16133.807	0.0004798	0.1063237	0.509	58.7	-4.84	-0.55
TMB-2.A	187	15133.955	0.0014464	0.1344469	0.514	56.4	-4.80	-0.44

Vaccinites cf. cornuvaccinum

Label	Run	Sa m44	49 parameter	Δ47 SD	Final Δ47	Δ47-based paleotemperature	Final δ18O	Final δ13C
Shell test n=17								
TMV-TA	281	19015.75	0.0010509	0.1024227	0.436	99.1	-4.43	1.67
TMV-TA	281	18559.693	0.0014764	0.0895205	0.542	44.3	-4.39	1.42
TMV-TA	647	18680.109	-0.016355	0.1049895	0.406	121.1	-4.48	1.75
TMV-TA	647	22819.799	-0.058623	0.094265	0.453	88.7	-4.46	1.67
TMV-TA	647	17533.943	-0.020088	0.0897393	0.506	60.2	-4.44	1.70
TMV-TA	647	16776.766	-0.011679	0.0913402	0.468	79.5	-4.52	1.71
TMV-TA	647	21856.046	-0.002948	0.1162753	0.455	87.4	-4.67	1.63
TMV-TA	647	18169.07	0.0113942	0.1073474	0.485	70.6	-4.57	1.65
TMV-TA	647	18280.931	0.0421729	0.0766704	0.398	127.2	-4.57	1.66
TMV-TB	281	17827.432	0.0011099	0.1200767	0.538	46.1	-4.35	2.17
TMV-TB	281	17173.683	0.0013577	0.1111212	0.559	37.7	-4.53	2.18
TMV-TB	647	20978.525	-0.0296	0.1049763	0.442	95.1	-4.32	2.01
TMV-TB	647	18224.996	-0.02005	0.1122669	0.453	88.3	-4.27	2.10
TMV-TB	647	22729.129	-0.007877	0.1093923	0.550	40.9	-4.72	1.96
TMV-TB	647	22211.425	-0.014836	0.1031619	0.483	71.7	-4.36	2.13
TMV-TB	647	19764.989	0.0325511	0.102267	0.527	50.7	-4.36	2.20
TMV-TB	647	19767.78	-0.018527	0.0990789	0.555	39.2	-4.59	1.99
Matrix and Sparite n=4								
TMV-M	281	17287.994	0.0007972	0.1031523	0.553	39.8	-2.35	1.93
TMV-M	281	17757.764	0.0015125	0.1051023	0.510	58.5	-2.48	2.13
TMV-S	281	10607.445	0.0020839	0.1267113	0.449	90.6	-1.09	0.64
TMV-S	281	12326.147	0.0016986	0.1237278	0.564	35.5	-0.63	0.99

Hippurites nabresinensis

Label	Run	Sa m44	49 parameter	Δ47 SD	Final Δ47	Δ47-based paleotemperature	Final δ18O	Final δ13C
Shell test n=14								
TMHN-TA	281	19522.312	0.0019521	0.1058045	0.544	43.7	-3.20	1.70
TMHN-TA	281	20288.604	0.0018516	0.0947363	0.548	41.8	-3.18	1.69
TMHN-TA	647	17857.43	-0.031112	0.102005	0.475	75.9	-3.32	1.70
TMHN-TA	647	16099.738	-0.030923	0.0943463	0.497	64.7	-3.22	1.72
TMHN-TA	647	17301.287	-0.008428	0.0967737	0.467	80.3	-3.27	1.68
TMHN-TA	647	20627.181	-0.006036	0.1005404	0.431	102.8	-3.21	1.72
TMHN-TA	647	17086.008	-0.017658	0.1088698	0.508	59.0	-3.36	1.64
TMHN-TA	647	20530.047	0.0324187	0.0859198	0.439	97.3	-3.21	1.68
TMHN-TAB	647	17659.607	0.0309143	0.1130416	0.455	87.2	-3.86	1.52
TMHN-TB	281	17950.727	0.0009825	0.098332	0.531	48.7	-4.22	1.99
TMHN-TB	281	20702.358	0.0020375	0.0916104	0.384	139.4	-4.19	1.45
TMHN-TB	281	18883.631	0.0014041	0.1357987	0.479	73.8	-4.00	1.54
TMHN-TB	647	21131.614	-0.046665	0.1196462	0.454	87.8	-4.28	1.45
TMHN-TB	647	22140.572	-0.013142	0.1268497	0.417	112.6	-4.16	1.42
Matrix and Sparite n=3								
TMHN-M	281	17948.267	0.0018564	0.0996814	0.485	70.6	-2.58	2.56
TMHN-S	281	20140.283	0.0013994	0.1145812	0.427	105.3	-2.47	2.81
TMHN-S	281	17837.32	0.0010866	0.1062133	0.517	55.3	-2.41	2.84

Appendix 4
Results of µXRF analysis

Praeradiolites ciryi

point	Mn 0	Fe	Sr
128.16 1		253.44	252.04
140.14 2		100.01	264.57
188.73 3		182.85	247.40
257.03 4		162.99	111.89
100.81 5		229.44	89.11
60.34 6		196.60	103.58
110.74 7		51.52	111.93
186.05 8		96.72	124.35
155.56 9		187.85	110.57
154.71		61.51	105.93
10	135.47	50.24	89.78
11	131.16	39.41	100.22
12	129.65	26.41	119.69
13	116.49	39.21	130.78
14	134.83	53.66	121.02
15	87.13	104.31	130.51
16	278.71	62.84	119.57
17	191.77	37.96	119.82
18	44.87	95.41	167.49
19	0.56	134.37	173.07
20		104.36	173.38
21	7.25	117.54	348.27
22	42.69	57.46	337.35
23	21.95	112.83	522.24
24	2.12	198.29	479.76
25	21.50	647.28	149.39
26	105.87	284.73	78.20
27	88.24	57.70	70.03
28	68.68	71.16	59.37
29	55.21	52.72	58.27
30	36.71	67.17	63.26
31	45.37	53.58	57.31
32	52.67	261.01	61.96
33	51.76	63.74	62.45
34	69.68	50.66	65.36
35	218.61	152.44	108.67
36	356.33	79.96	179.87
37	559.41	3.11	269.79
38	643.98		334.18
39	683.98		332.61
40	432.94	22.93	292.96
41	315.91	20.22	375.27
42	270.69	119.07	301.41
43	361.28	261.90	253.06
44	316.64	405.62	247.86
45	300.52	21.66	237.47
46	332.67	32.40	204.99
47	395.59	84.69	200.81

point	Mn 48	Fe	Sr
515.93 49		16.59	148.35
340.89 50		49.76	128.47
282.93 51		49.68	230.45
279.83 52		50.60	240.20
588.47 53		41.28	157.00
418.43 54		47.88	108.53
43.30 55		63.56	275.69
56		66.90	232.94
57	35.95	125.09	174.19
58	54.57	40.75	169.96
59	52.77	59.92	181.88
60	124.47	44.29	157.70
61	114.38	45.10	167.80
62	161.96	41.49	169.90
63	201.69	26.20	164.33
64	78.44	54.64	152.18
65	3.90	72.89	154.68
66	0.54	108.92	218.69
67	5.34	68.21	237.50
68	16.63	71.89	273.94
69		100.39	278.86
70		57.00	262.63
71	3.84	155.53	184.10
72	9.41	86.68	209.56
73	30.43	99.91	200.11
74	46.30	42.06	183.88
75	49.03	62.44	179.53
76	52.52	147.58	169.00
77	15.84	1020.25	169.22
78	36.26	133.91	139.68
79	180.83	51.14	125.34
80	143.43	45.13	120.43
81	167.23	78.60	134.34
82	92.34	50.66	127.62
83	49.32	35.40	114.03
84	22.76	94.05	110.68
85	11.09	66.17	98.46
86	23.37	4118.85	165.48
87		1502.50	178.91
88	11.51	46.86	208.46
89	37.07	71.38	234.12
90	6.66	215.39	218.60
91	2.28	105.44	239.41
92		101.21	221.72
93	0.38	100.35	184.51
94		134.81	194.91
95	1.15	353.37	295.34
		333.77	545.68

point	Mn	Fe	Sr 96
178.89	534.89 97	9.75	
123.62	307.92 98	3.33	
115.71	369.13 99	1.82	
225.85	357.69		
100	22.83	105.74	311.06
101	44.49	115.16	287.13
102	213.32	462.73	286.35
103	118.67	113.57	317.07
104	21.37	166.84	292.16
105	5.90	197.80	264.23
106	8.90	158.03	244.56
107		86.88	246.00
108	2.97	146.97	237.12
109	12.65	136.69	246.48
110	39.69	84.82	281.49
111	223.35	62.60	247.65
112	411.39	36.48	280.53
113	414.67	126.33	291.18
114	60.09	53.02	247.11
115	135.03	55.64	255.39
116	246.58	136.92	300.88
117	200.75	151.52	305.86
118	328.36	184.25	313.93
119	254.11	119.54	333.56
120	97.28	149.42	362.27
121	85.52	93.71	334.21
122	563.78	179.33	331.70
123	386.80	73.78	312.96
124	147.97	279.97	367.55
125	116.76	328.07	377.77
126	56.39	261.70	321.74
127	5.71	454.41	254.25
128		85.19	302.82
129		85.11	379.50
130	1.06	132.12	293.85
131	6.07	112.86	340.97
132	16.01	181.62	332.40
133	14.89	83.00	395.35
134	8.38	70.20	321.83
135		32.13	312.02
136	2.92	73.51	303.73
137	27.23	68.59	134.34
138	96.12	167.31	132.61
139	43.98	120.29	176.88
140	38.17	166.16	101.02
141	141.15	66.10	104.85
142	194.70	44.45	207.02
143	209.95	125.80	257.58
144	141.03	81.52	205.30

point	Mn	Fe	Sr
145	127.00	67.72	180.75
146	125.10	135.82	213.04
147	92.27	419.79	256.21
148	23.46	178.55	273.80
149	35.68	275.83	270.89
150	17.14	95.28	339.79
151	88.57	159.37	275.00
152	46.71	207.94	261.08
153	45.75	95.85	210.60
154	24.35	48.86	211.09
155	16.99	72.41	224.54
156	10.62	113.46	237.86
157	6.83	318.03	246.55
158		98.26	245.41
159	9.68	154.91	265.71
160	36.02	189.98	288.21
161	33.50	209.52	314.99
162	54.32	265.43	359.85
163	31.70	262.71	312.26
164		68.98	349.33
165		24.96	424.48
166		46.64	532.78
167		89.07	650.62
168	2.49	65.35	914.30
169	26.76	86.61	1008.29
170	29.43	97.06	1302.06
171	12.21	898.25	1599.73
172	16.53	154.35	1590.78
173	7.40	131.20	1552.43
174	26.48	82.18	1395.30
175	31.48	135.47	1353.71
176	77.22	116.95	1383.26
177	80.22	78.39	1430.67
178	71.68	84.65	1306.79
179	51.30	49.74	1256.13
180	40.37	36.48	1547.15
181	63.72	72.35	1531.68
182	40.52	34.14	1544.61
183	50.13	59.33	1462.48
184	45.75	46.40	1433.16
185	37.70	80.81	1424.35
186	17.16	63.78	1520.59
187		84.69	1429.80
188		91.55	1484.63
189		98.65	1424.90
190	0.69	73.74	1421.33
191		53.92	1444.83
192	37.35	108.78	1443.46
193	12.07	298.28	1445.65

point	Mn	Fe 118.35	Sr
194		78.58	1462.63
195		72.53	1456.57
196	34.04	106.18	1483.99
197	258.02	169.42	1498.96
198	291.11	85.00	1476.25
199	252.43	43.35	1458.47
200	218.55	39.25	1496.56
201	60.65	323.38	1526.42
202	21.87	63.86	1552.94
203	40.68	29.21	1524.24
204	70.89	121.26	1516.21
205	72.97	128.97	1429.82
206	92.17	917.72	1465.07
207	77.63	858.75	1491.05
208	46.17	60.72	1463.92
209	9.16	42.15	1464.65
210	3.94	31.85	1493.80
211	25.67	75.91	1442.73
212	25.37	26.64	1411.72
213	19.68	20.80	1427.61
214	19.40	27.18	1451.69
215	60.10	19.29 9.44	1411.19
216	92.29	56.47	1470.71
217	58.39	31.93	1388.05
218	63.73	26.89	1364.32
219	126.94	76.97	1403.01
220	181.76	61.51	1369.14
221	205.36	70.26	1360.67
222	283.78	282.27	1394.39
223	135.62	153.74	1424.33
224	65.11	7.91 62.64	1447.81
225	206.19	118.71	1451.41
226	439.32	161.56	1423.48
227	377.11	99.76	1433.06
228	153.79	241.59	1476.80
229	16.28	655.58	1460.62
230		545.17	1486.74
231		664.92	1486.70
232		189.66	1459.29
233		12064.51	1464.33
234	0.73	6084.32	1500.51
235	22.25	5276.52	1450.01
236	67.57	363.29	1564.82
237	41.48	237.25	1534.51
238	41.48	280.54	1532.34
239	40.30	182.92	1496.71
240	30.72		1458.82
241	37.80		1427.03
242	35.92		1406.12

point	Mn	Fe	Sr
243	49.21	187.07	1432.18
244	28.14	250.97	1445.27
245	20.44	361.08	1416.68
246	11.36	149.74	1428.43
247	8.49	206.63	1415.49
248	9.07	267.47	1404.10
249	7.77	227.26	1389.34
250	0.62	267.43	1383.11
251	6.51	341.29	1374.87
252	14.46	269.21	1386.19
253	33.83	183.98	1416.60
254	41.49	267.02	1409.08
255	62.07	1095.80	1418.72
256	165.40	97.81	1429.77
257	249.07	56.70	1513.09
258	190.46	85.18	1527.82
259	150.12	125.15	1513.00
260	36.12	374.64	1455.13
261	19.50	171.24	1376.57
262	3.72	124.16	1349.19
263	2.10	107.98	1384.65
264	2.56	150.50	1451.26
265	8.84	203.41	1450.44
266	17.75	177.52	1482.75
267	6.81	212.01	1512.66
268	7.24	348.44	1497.52
269	23.66	428.19	1488.87
270	55.88	142.54	1499.03
271	79.77	119.92	1510.06
272	5.95	141.65	1535.41
273		252.06	1495.17
274		66.70	1526.66
275		90.78	1571.37
276		167.87	1562.46
277	14.45	160.65	1572.62
278	193.39	51.31	1515.33
279	428.32	46.95	1528.12
280	445.19	135.26	1526.03
281	364.29	109.39	1585.08
282	78.18	97.49	1553.46
283	38.72	59.41	1534.98
284	196.98	90.81	1584.82
285	368.19	141.16	1576.26
286	211.85	97.68	1600.50
287	54.12	159.68	1583.40
288	26.05	170.28	1511.30
289	7.89	73.54	1526.53
290		37.05	1539.90
291	9.78	54.09	1562.23

point	Mn	Fe 67.74	Sr
292		1160.04	1605.11
293		970.92	1524.75
294		48.43	1565.14
295		54.88	1572.38
296	3.03	36.82	1543.02
297	101.14	43.09	1566.92
298	367.82	46.42	1493.04
299	383.34	67.46	1454.86
300	71.51	98.30	1452.50
301	24.64	46.58	1437.13
302	32.47	45.49	1434.29
303	284.40	30.47	1401.94
304	1026.84	34.49	1445.29
305	862.36	63.47	1426.24
306	338.92	29.23	1434.39
307	132.41	74.63	1521.53
308	103.60	156.12	1503.45
309	189.45	126.31	1525.14
310	396.23	310.66	1602.99
311	440.40	708.04	1624.92
312	159.22	1968.56	1436.24
313	24.71	203.73	1312.34
314	34.12	575.93	1048.42
315	92.27	646.69	482.18
316	457.19	38.98	120.99
317		49.52	62.95
318		43.93	48.49
319		41.56	55.03
320		45.88	45.04
321		46.96	49.72
322		17.08	48.85
323	19.52	33.15	50.35
324		30.77	38.42
325	9.00	29.59	54.40
326		42.74	53.51
327	14.68	8.14	36.79
328		29.06	45.60
329		25.63	60.65
330	3.52	18.86	48.29
331		2.86	45.63
332	17.72	17.75	47.30
333		23.98	41.90
334	10.48	39.19	34.64
335	4.62	30.06	52.67
336		34.79	49.00
337	5.88	13.79	48.78
338		28.89	48.86
339		30.43	45.02
340			47.11

point	Mn	Fe	Sr
341		44.90	44.43

Hippurites nabresinensis

point	Mn 0	Fe	Sr
136.30 1		26.72	197.36
81.00 2		20.55	213.57
102.35 3		17.89	208.77
166.85 4		4.59	211.75
227.01 5			196.68
332.21 6			201.60
291.81 7		5.98	194.25
162.36 8			197.12
151.70 9		2.92	211.41
104.18		2.73	211.08
10	24.30	52.76	208.50
11	49.24	58.62	210.73
12	54.38	35.16	233.08
13	73.23	0.96	238.01
14	162.81	3.75	220.65
15	105.29	10.17	208.00
16	40.56	39.80	210.78
17	16.84	104.65	221.74
18	59.94	7.23	215.60
19	266.23		212.68
20	142.04	21.12	218.48
21	47.06	38.94	243.34
22	138.84		238.35
23	273.60		215.89
24	143.40	7.97	216.04
25	120.67	13.12	211.45
26	235.79		199.30
27	44.79	0.62	218.48
28	37.19	9.08	216.92
29	43.96	16.74	226.45
30	226.18		250.31
31	405.54		238.99
32	144.15		213.75
33	44.76	29.43	185.83
34	71.76	90.94	189.87
35	42.74	27.58	201.55
36	46.84	4.09	188.62
37	33.03	7.00	184.36
38	41.33	11.36	194.43
39	59.80	2.07	202.58
40	64.78	12.48	199.26
41	183.49	12.27	209.31
42	112.90	11.53	218.67
43	96.23	25.09	213.71
44	53.26	24.04	241.11
45	48.80	18.20	238.25
46	28.95	16.49	216.85
47	54.95	16.94	212.47

point	Mn 48	Fe	Sr
128.79 49			212.72
285.27 50			229.17
346.63 51			211.38
210.81 52			198.27
127.51 53			218.56
147.21 54		0.51	232.47
40.03 55		55.08	240.83
100.72 56		35.25	234.41
117.49 57			231.95
256.60 58		3.71	219.29
191.24 59			212.64
191.58 60		3.72	201.20
54.19 61		47.68	191.20
8.30 62		48.04	203.91
22.28 63		55.83	219.37
34.55 64		10.13	221.35
140.75 65			231.11
139.98 66		10.57	218.89
180.35 67		8.70	231.33
165.48 68			228.51
116.32 69		14.46	224.83
55.80 70		33.93	206.47
39.23 71		10.56	218.56
166.25 72		7.96	218.84
300.24 73			192.76
186.96 74			187.90
203.49 75		6.70	183.20
130.27 76		17.91	196.95
143.70 77		18.92	199.77
156.98 78		30.61	209.76
99.56 79		0.34	222.97
159.10 80			242.47
100.10 81		1.71	478.70
111.19 82		0.63	1010.85
15.27 83		15.28	1134.76
3.54 84		7.59	1248.42
107.76 85		4.70	1338.57
394.81 86			1372.95
506.43 87		1.13	1329.79
289.09 88			1302.05
147.77 89			1301.78
100.45 90			1374.09
103.71 91		108.10	1418.07
263.83 92		435.80	1348.38
27.51 93		294.18	1310.93
8.83 94		356.93	1176.51
5.53		456.81	662.65
95	51.91	149.40	458.85

point	Mn	Fe	Sr
96	52.69	110.77	242.16
97	68.29	54.86	228.15
98	50.07	54.27	208.45
99	42.64	56.40	220.31
100	29.26	76.83	221.61
101	62.48	49.32	221.00
102	98.25	26.56	247.24
103	8.08	82.46	212.46
104	9.52	35.53	185.97
105	1.59	36.74	269.64
106	10.37	46.12	299.10
107	31.56	41.41	200.52
108	26.46	90.74	181.35
109	76.18	55.36	184.32
110	56.78	97.16	192.64
111	74.07	43.23	192.77
112	87.16	23.16	212.00
113	47.98	31.60	224.14
114	51.87	69.75	209.87
115	28.76	102.06	204.87
116	80.66	110.24	218.90
117	116.28	32.42	205.11
118	68.97	43.90	201.52
119	119.70	32.80	218.60
120	70.66	38.43	209.67
121	30.28	55.25	199.26
122	60.84	66.74	201.00
123	30.21	74.13	216.19
124	31.88	68.97	235.79
125	7.41	148.32	261.86
126	14.16	68.58	387.45
127	180.10	16.61	527.69
128	254.34		537.09
129	185.27	10.50	332.55
130	40.59	17.91	235.90
131	84.68	61.52	236.33
132	71.87	58.52	214.10
133	20.49	29.87	212.16
134	84.13	46.56	237.18
135	69.63	98.10	213.80
136	157.15	40.74	238.06
137	159.19	52.37	214.95
138	9.96	114.99	232.66
139	7.29	66.89	242.79
140	28.93	53.80	203.76
141	77.69	38.02	251.81
142	201.52	15.76	229.09
143	298.08		333.70
144	232.70		499.82

point	Mn	Fe	Sr
145	123.02	17.59	480.25
146	276.52	31.92	578.81
147	422.59		615.21
148	504.48		457.68
149	755.78		684.84
150	511.27		810.32
151	97.12		768.96
152	11.84	8.83	395.20
153	7.09	12.18	499.14
154	46.19	6.46	921.73
155	94.94		609.67
156	132.82	80.20	535.15
157	311.14	65.50	336.37
158	138.13	25.89	442.62
159	24.82	55.55	269.99
160	42.01	51.08	467.41
161	3.66	50.32	317.38
162	42.24	3.02	347.03
163	193.95	10.66	251.54
164	111.17		238.93
165	55.46	3.44	215.91
166	37.88	17.06	532.90
167	58.07	25.02	270.13
168	157.16	16.08	199.11
169	171.86	38.20	226.16
170	46.57	59.92	214.27
171	45.64	36.45	235.70
172	32.30	52.61	227.06
173	107.17	15.20	212.92
174	22.47	42.66	273.55
175	30.19	38.13	554.80
176	211.33		340.96
177	464.24		551.34
178	127.53	2.27	422.50
179	70.16	36.45	544.71
180	41.82	67.85	412.17
181	76.66	45.78	347.19
182	22.10	40.22	216.55
183	54.21	21.06	186.48
184	146.23	6.97	165.97
185	57.86	21.57	184.73
186	90.11	34.27	212.10
187	117.24	41.92	230.78
188	41.23	45.21	244.64
189	133.01	53.31	197.72
190	72.51	29.48	206.76
191	30.63	28.47	205.68
192	49.43	51.66	209.91
193	63.92	48.71	194.76

point	Mn	Fe	Sr
194	53.52	39.53	209.77
195	67.27	28.90	223.28
196	82.70	55.44	212.44
197	57.13	48.51	224.05
198	126.96	45.87	219.03
199	40.10	30.97	254.85
200	48.11	46.01	205.66
201	109.14	52.57	210.24
202	52.79	46.20	248.53
203	91.76	57.35	255.03
204	95.23	41.33	253.87
205	138.27	58.49	258.04
206	79.73	46.74	257.13
207	59.22	26.99	252.79
208	75.32	23.33	254.16
209	61.63	38.94	253.78
210	112.18	106.17	252.96
211	54.91	85.17	280.65
212	68.74	59.65	264.33
213	72.69	23.22	245.36
214	108.55	26.48	269.21
215	226.92	13.27	324.78
216	62.08	46.77	385.92
217	58.31	61.30	452.01
218	114.63	61.34	447.74
219	69.18	74.01	533.41
220	90.93	107.22	585.39
221	58.68	174.67	783.61
222	102.33	238.65	1009.47
223	148.37	204.37	1137.26
224	47.09		1310.45
225	96.08		1348.11
226	84.34	131.73	1325.07
227	58.19	11.18	1380.54
228	9.41	3.37	1386.64
229	65.69		1316.30
230	59.79	56.45	1329.82
231	165.81		1311.85
232	58.20	65.15	1331.90
233	183.21	31.12	1397.47
234	114.37		1345.84
235	31.83	0.10	1239.68
236	133.01	14.80	1157.27
237	170.59	87.37	1136.38
238	352.68	16.01	1118.80
239	138.67	20.12	1170.66
240	214.88		1183.95
241	48.42	23.05	1218.58
242	22.05	8.39	1198.61

point	Mn	Fe	Sr
243	68.39	8.68	1120.37
244	16.34	84.93	514.52
245	62.22	20.85	207.42
246	68.57	19.26	212.38
247	34.39	27.43	213.48
248	58.01	8.56	216.87
249	109.23		210.84
250	83.42	10.57	209.33
251	47.93	29.20	213.12
252	71.64	13.00	232.24
253	77.23	3.11	238.63
254	91.51	6.04	231.23
255	116.81	0.11	220.55
256	279.24		204.46
257	200.90		200.79
258	193.42		205.45
259	66.64	1.23	209.42
260	82.69	6.54	236.72
261	115.94	9.47	233.42
262	134.66	7.25	217.90
263	65.43	38.26	218.47
264	58.09	38.98	228.99
265	111.56	7.89	236.46
266	106.96	6.92	230.35
267	75.74	23.18	221.51
268	52.34	35.16	203.35
269	24.34	53.55	210.78
270	31.31	25.50	210.43
271	30.23	37.56	210.68
272	42.10	41.20	212.54
273	62.88	30.27	194.18
274	35.73	6.91	193.01
275	86.48	8.24	202.76
276	106.30	23.42	193.11
277	74.36	26.40	192.98
278	193.78	9.42	186.59
279	193.44		197.34
280	243.72		199.80
281	236.84		205.36
282	359.63		207.52
283	157.16	1.62	213.33
284	136.74		233.72
285	113.56	2.67	236.09
286	8.07	60.62	229.05
287	17.78	50.98	228.04
288	77.82	19.81	222.87
289	62.93	25.59	213.52
290	28.48	53.81	222.68
291	12.68	75.49	212.19

point	Mn	Fe	Sr
292	10.07	65.00	213.22
293	35.96	36.42	216.14
294	68.22	20.85	205.54
295	68.21	21.32	198.16
296	75.51	20.00	204.70
297	97.30	30.35	211.73
298	64.76	30.89	234.01
299	131.11		236.02
300	144.00		226.52
301	115.93	2.98	239.31
302	232.85		240.61
303	346.04		222.37
304	452.03		208.65
305	482.71		212.00
306	341.29		200.05
307	211.00		220.12
308	160.65		230.23
309	359.02		222.11
310	130.68	9.10	245.55
311	9.70	35.30	243.94
312	37.49	26.66	230.23
313	34.91	57.75	247.54
314	33.05	66.26	225.47
315	81.02	62.62	232.83
316	202.61		228.29
317	181.47		235.00
318	235.39		254.04
319	146.40		244.42
320	49.26	8.94	238.10
321	109.23	8.69	233.73
322	143.51		237.93
323	143.57		234.27
324	88.74	6.31	257.89
325	64.07	13.28	248.67
326	45.98	15.86	241.93
327	49.28	32.78	224.30
328	139.39		215.13
329	324.63		220.11
330	406.83		227.45
331	458.15		235.12
332	264.10		232.25
333	250.12		218.78
334	159.53	12.86	239.13
335	114.37	14.42	251.11
336	264.68		256.90
337	182.87		261.81
338	156.70		257.45
339	45.02	0.57	258.47
340	63.08	1.61	246.56

point	Mn	Fe	Sr
341	74.57	51.82	252.40
342	106.34	34.24	247.64
343	58.93	68.64	241.74
344	75.28	55.29	243.22
345	60.93	32.00	233.49
346	57.19	42.73	231.45
347	91.56	24.63	237.26
348	51.72	39.16	226.09
349	93.86	36.13	219.28
350	63.45	27.43	234.51
351	69.63	25.02	222.57
352	84.45	0.19	226.37
353	211.76		222.83
354	135.85	25.13	232.37
355	176.09	22.34	210.42
356	114.20	11.21	248.00
357	105.67	22.81	229.92
358	53.16	32.67	232.51
359	45.28	46.03	225.36
360	40.83	35.46	211.21
361	205.84		217.49
362	168.43		203.11
363	88.87		204.10
364	282.60		207.93
365	186.27		209.73
366	69.22		229.87
367	67.08	9.47	229.23
368	103.03	4.15	236.13
369	33.44	40.07	223.85
370	54.75	30.54	218.29
371	51.80	28.26	238.14
372	71.32		221.47
373	53.91		221.21
374	54.66		222.51
375	48.67		235.09
376	61.60	2.52	215.62
377	16.33	5.93	233.15
378	12.99	22.92	252.91
379	17.47	5.49	255.18
380	258.58		234.11
381	189.10		213.80
382	187.63	2.33	206.53
383	205.58	14.19	211.42
384	79.66		210.58
385	53.80		223.11
386	113.05		220.73
387	88.45		222.91
388	171.47		221.74
389	207.99		228.67

point	Mn	Fe	Sr
390	39.42		237.36
391	97.46	17.00	231.33
392	131.27	60.64	225.02
393	73.51	134.83	229.91
394	65.89	86.28	231.67
395	62.58	18.86	230.56
396	156.38	2.49	235.84
397	141.30	2.11	242.56
398	131.73		240.26
399	145.29		244.53
400	127.04		241.21
401	105.61	56.08	240.47
402	114.72	43.47	258.73
403	57.60	0.55	278.35
404	191.61		260.82
405	72.36	1.34	254.77
406	258.89		257.33
407	233.07		263.50
408	274.46	0.97	260.66
409	122.88	11.60	240.06
410	180.40		252.53
411	15.75	3.83	255.55
412	40.44	35.09	241.77
413	166.33		244.71
414	249.32		251.43
415	326.61	17.92	245.92
416	199.98	32.98	237.55
417	197.43	1.05	221.33
418	298.25		231.36
419	187.28	13.86	237.96
420	133.14		236.24
421	91.36	2.14	234.70
422	204.32	18.77	242.88
423	18.07	61.62	252.20
424	14.42	97.22	287.28
425	26.14	45.83	271.49
426	14.79	70.63	264.21
427	21.12	76.93	336.30
428	28.60	140.65	331.20
429	54.87	108.27	307.36
430	100.20	48.76	304.91
431	104.70	22.30	291.92
432	21.61	35.26	325.47
433	7.72	8.63	307.51
434	139.50	7.30	286.53
435	66.56	18.25	273.20
436	108.31	31.12	266.22
437	155.21	28.50	255.93
438	81.36	1.41	364.45

point	Mn	Fe	Sr
439	66.11	3.67	880.54
440	13.10	42.30	892.48
441	2.99	32.74	872.39
442	30.69	45.01	528.17
443	24.16	5.02	413.31
444	21.20	86.16	502.57
445	160.06	28.77	515.40
446	404.35		670.16
447	248.45		790.63
448	87.60		1014.54
449	258.84		982.16
450	213.73		1093.28
451	41.80		1188.87
452	237.50		1322.92
453	648.18		1317.64
454	450.85	50.75	1344.75
455	200.26		1365.33
456	357.32		1464.31
457	355.42		1315.39
458	331.20		1269.83
459	23.00	12.52	1399.40
460	12.01	9.86	1461.94
461	9.42	1.08	1412.01
462		5.66	1453.26
463		11.38	1416.39
464		6.68	1386.25
465		0.39	1337.55
466			1356.59
467	3.49	0.94	1276.64
468	17.18	5.50	1254.36
469	59.32		981.79
470	38.29	46.48	1335.28
471	84.69	32.54	1412.25
472	115.34		1315.64
473	37.32		1297.94
474	68.48	5.22	1418.76
475	72.17	51.12	1212.25
476	219.19	31.48	1042.87
477	28.68	31.07	957.46
478	53.60	26.77	851.22
479	93.86	15.87	862.21
480	65.73	19.23	802.54
481	43.25		813.90
482	40.44	24.42	774.76
483	9.44	4.96	576.69
484	13.60	6.59	502.74
485	17.08	2.45	520.27
486	13.51	9.34	547.98
487	20.52	10.34	537.61

point	Mn	Fe	Sr
488	27.79	82.23	553.43
489	27.51	377.07	561.20
490	17.61	540.06	658.93
491	13.10	553.06	659.80
492	16.99	545.53	621.52
493	16.51	554.03	639.27
494	8.94	514.02	671.95
495	35.87	298.20	747.71
496	75.09	53.99	618.74
497	18.12	37.28	646.03
498	9.41	16.80	707.40
499	10.57	15.13	669.09
500	10.98	15.90	680.61
501	10.31	19.18	697.42
502	17.18	17.03	748.48
503	7.08	8.55	784.90
504	35.75	1.33	890.32
505	145.91	3.31	859.19
506	171.34	17.87	914.10
507	192.17	6.34	847.86
508	177.09	2.34	911.41
509	151.98	23.77	1023.54
510	15.86	52.12	1132.35
511	22.33	62.59	1157.68
512	131.32	7.15	1125.15
513	17.65	0.06	1348.30
514	357.70	17.11	1428.08
515	576.95	6.71	1446.02
516	546.52		1399.80
517	316.89		1420.33
518	6.23	12.27	1298.76
519	37.59	4.14	1036.48
520	3.69	4.65	1175.86
521	13.79	51.84	1282.11
522	0.99	7.83	1376.98
523	0.60	0.89	1389.90
524	24.95	16.06	1378.81
525	114.20		1321.61
526	307.61		1377.56
527	43.56	8.71	1330.51
528	27.99	2.67	1352.78
529	7.70	54.74	1324.33
530	4.10	12.99	1394.61
531		8.42	1373.94
532		18.38	1348.35
533			1186.51
534	65.48		1275.34
535	94.43		1259.40
536	26.20	0.87	1220.13

point	Mn	Fe	Sr
537	18.06	11.48	1197.80
538	3.35		1157.54
539			1066.04
540	25.97	18.41	1006.06
541	3.49		977.38
542	13.86		1010.38
543	25.26	7.65	1042.88
544	8.51	1.25	1116.46
545	21.27	4.33	1187.53
546	113.99	3.63	1272.41
547	89.90	2.30	1413.59
548	83.45	0.13	1399.54
549	27.83	7.71	1432.37
550	86.82	2.02	1429.14
551	119.40	42.06	1403.08
552	81.75	28.13	1264.73
553	31.60		1035.81
554	29.52		861.69
555	137.85		921.68
556	107.39		664.95
557	54.05		424.05
558	44.56	4.94	406.47
559	78.26		335.94
560	140.88	6.15	223.96
561	104.16	14.86	192.26
562	47.47	50.48	217.54
563	32.58	35.30	210.06
564	119.40		215.17
565	153.08		218.37
566	130.69		229.97
567	71.21	5.26	272.49
568	104.81	20.51	288.58
569	216.74	3.80	351.06
570	233.13	35.22	360.99
571	150.46	43.36	501.83
572	133.85		621.25
573	313.10		262.44
574	41.55	3.02	326.90
575	22.72	4.92	261.71
576	26.83	69.38	241.70
577	43.82	112.75	256.13
578	71.18	33.99	314.65
579	97.50	22.69	395.89
580	165.10	18.35	571.47
581	166.34		1198.87
582	90.59	7.45	1395.69
583	321.64	7.11	1398.45
584	293.17		1499.42
585	249.27		1442.77

point	Mn	Fe	Sr
586	173.00		1443.94
587	111.87		1452.27
588	272.55		1432.98
589	113.06		1458.62
590	192.26		1407.66
591	119.55	1.17	1420.03
592	7.05	21.78	1364.93
593	4.03		1360.66
594	84.37		1328.94
595	2.24		1384.07
596	67.30	38.11	1330.43
597	67.12	54.00	1044.91
598	56.19	16.83	866.82
599	56.45	15.91	793.59
600	130.35	35.40	653.60
601	75.27	3.27	485.14
602	57.15	11.32	500.50
603	28.75	22.80	410.68
604	68.24	6.98	333.29
605	133.70	39.77	342.41
606	31.96	6.20	408.71
607	41.47	3.45	402.48
608	11.38	40.34	434.07
609	15.47	24.67	480.20
610	23.11		633.03
611	33.01		635.06
612	60.71	10.31	701.14
613	89.67		850.85
614	702.11		1027.93
615	193.62		1165.61
616	22.57		1169.61
617	35.04		789.29
618	77.10	14.20	834.68
619	48.66	20.99	684.33
620	83.40	2.47	741.68
621	176.56		342.43
622	119.22		307.36
623	68.88	10.65	294.30
624	67.56	84.68	285.39
625	68.56	49.84	268.26
626	147.35	5.47	263.81
627	299.13	48.50	267.81
628	324.76	96.49	255.75
629	147.65		257.36
630	37.77	85.95	238.43
631	21.91	91.78	256.95
632	34.06	65.43	255.23
633	53.32	71.98	251.98
634	88.49	76.58	244.17

point	Mn	Fe	Sr
635	140.38	133.17	262.99
636	106.53	67.32	252.52
637	54.24	48.37	252.29
638	19.84	20.64	237.82
639	86.33	33.69	228.07
640	82.70	30.63	212.05
641	32.54	30.16	219.56
642	40.39	37.43	224.24
643	50.08	43.24	219.56
644	66.65	16.25	216.37
645	53.08	13.98	210.01
646	61.06	39.60	213.19
647	90.67	35.62	210.32
648	112.12	18.57	214.71
649	174.92	27.99	213.67
650	160.25	26.66	203.98
651	134.83	16.60	219.98
652	112.65	20.92	220.99
653	119.32	16.18	228.30
654	126.08	12.55	232.38
655	70.05	1.99	249.99
656	17.84	87.50	247.66
657	17.26	154.46	262.99
658	18.61	68.02	290.54
659	1.27	16.51	296.98
660	26.92	13.82	336.70
661	14.00	55.77	316.90
662	0.63	18.89	106.97
663		13.25	64.54
664	2.46	76.45	52.84
665	1.65	81.89	40.15
666	3.28	73.73	26.20
667	0.16	6.51	25.24
668		16.81	27.71
669		97.24	44.92
670	0.99	336.95	51.61
671	3.85	258.91	35.80
672		120.20	9.87
673		150.18	5.95
674	19.40	67.79	5.04
675	31.32	24.56	13.22
676	50.59	44.99	20.17
677	89.74	297.61	29.57
678	139.79	145.15	27.72
679	560.33	210.92	25.06
680	298.15	55.95	28.90
681	4.02	154.10	46.54
682	2.08	368.49	52.90
683	8.25	131.24	13.53

point	Mn	Fe	Sr
684	22.09	70.48	7.86
685	16.01	83.96	6.80
686	104.74	81.31	3.81
687	163.85	115.08	3.83
688	273.35	70.46	7.90
689	149.65	176.83	6.39
690	13.87	354.01	16.49
691		139.47	10.37
692	12.43	127.70	6.85
693	12.95	131.63	6.22
694	23.69	93.03	26.42
695	201.90	56.21	21.50
696	232.59	78.46	12.85
697	181.04	115.71	10.24
698	127.16	78.09	10.10
699	40.35	72.23	16.23
700	44.32	56.34	63.17
701	55.93	69.20	28.05
702	64.92	170.50	12.36
703	62.90	106.17	6.49
704	21.07	123.30	5.25
705	23.93	193.35	4.99
706	11.43	135.26	3.03
707	2.23	54.78	0.27
708	0.26	50.07	
709	42.47	37.45	4.01
710	64.81	23.89	9.79
711	62.84	18.83	16.22
712	63.70	24.55	17.40
713	58.31	41.85	13.72
714	40.78	55.76	7.81
715	83.95	49.72	3.11
716	85.51	58.07	2.88
717	25.65	85.74	5.25
718	79.18	151.29	9.28
719	36.22	166.09	16.33
720	40.39	157.80	15.99